

Koopman with inputs and control for constitutive law identification

Emily Jayne Southern

Department of Mathematics
Imperial College London

Submitted in part fulfilment of the requirements for the degree of
Doctor of Philosophy in Mathematics of the University of London and
the Diploma of Imperial College, January 25, 2023

Abstract

Constitutive laws characterise the stress-strain relationship in a material. Determining a constitutive law experimentally typically involves subjecting the material to a prescribed deformation and measuring the force required to achieve it. There are numerous constitutive laws which have been developed to model the stress response of viscoelastic fluids, and the decision on which constitutive law should be fitted to data is largely based on the rheologist's knowledge about the fluid in relation to the catalogue of standard models appearing in the literature. In this thesis, we present an alternative approach for determining a viscoelastic fluid's constitutive law based on methods related to Koopman operator theory and Dynamic Mode Decomposition in the context of control. Our approach systematically extracts the material parameters that arise in stress-evolution equations of viscoelastic fluids directly from simulation or experimental data. We will present results from various applications of the framework that highlight its accuracy and robustness in identifying material parameters and reconstructing the underlying constitutive law. We will discuss how data should be supplied to the method, and also demonstrate how data from recently developed experimental protocols, as well as combined data from multiple experiments, can be used to improve resolution. Finally, we will show that our approach provides a natural way to utilise data from the nonlinear regime and extends to higher-dimensional data sets where spatial data within a sample is available.

Acknowledgements

I would firstly like to thank my supervisor, Dr. Eric E. Keaveny, for his constant support and encouragement over the past four years. I am incredibly grateful that he saw the potential in this project and pushed me to explore it further, and I commend his ability to keep me on track when I attempted to work on anything other than what I was meant to be working on.

I would like to thank the members of my group - Adam, Tim, Smitha, Madeleine, Hang, and Beth - for the camaraderie that they managed to make me feel even throughout a global pandemic. When we were actually allowed to work in the office, I'm thankful to Henry, Paul, Jacob, and everyone else who passed through HUX749 for the great conversations and the positive atmosphere. I am grateful to Dr. Prasun Ray and Prof. Demetrios Papageorgiou for their advice and comments during my early and late stage reviews. I am also greatly indebted to the many long conversations I had with Prof. Peter Schmid: whether they were about work, how to get second-years to think for themselves, or just generally putting the world to rights, I always left the office feeling inspired.

Outside of Imperial, the people I have met through Brixton Fencing Club have become like a second family to me and I am incredibly glad to have had them throughout my PhD. I would especially like to thank my coach, Pavel Rynes, for his patience and confidence in my abilities, and the strength & conditioning team at Imperial for getting me to do the exercises that I dislike. It has not been easy to train and compete internationally at a sport throughout the PhD process but I can't imagine it any other way.

Lastly, I would like to thank my parents and my sister for cheering me on through the good times and helping me to plough on through the hard ones. I wish that my Grandma and my Uncle Martin could have been around to see this completed. And I would like to dedicate this thesis to Mr. Paul Raymond, who taught me maths during a very hard time in my life, and who believed in me when very few others did.

Statement of Originality

The contents of this thesis is my own work and any assistance received in preparing this thesis have been acknowledged. This thesis has not been submitted for any degree or other purposes. Except where stated otherwise by reference or acknowledgment, the work presented is entirely my own.



The copyright of this thesis rests with the author. Unless otherwise indicated, its contents are licensed under a Creative Commons Attribution-Non Commercial 4.0 International Licence (CC BY-NC). Under this licence, you may copy and redistribute the material in any medium or format. You may also create and distribute modified versions of the work. This is on the condition that: you credit the author and do not use it, or any derivative works, for a commercial purpose. When reusing or sharing this work, ensure you make the licence terms clear to others by naming the licence and linking to the licence text. Where a work has been adapted, you should indicate that the work has been changed and describe those changes. Please seek permission from the copyright holder for uses of this work that are not included in this licence or permitted under UK Copyright Law.

Contents

Acknowledgements	5
1 Introduction	25
1.1 Thesis layout	28
2 Characterisation of constitutive laws for viscoelastic fluids	30
2.1 Constitutive laws	31
2.2 Viscoelastic fluids	36
2.3 Constitutive law frameworks	38
2.4 Rheometry	39
2.5 Oscillatory Rheometry	41
2.5.1 Linear oscillatory experiments	43
2.5.2 Nonlinear oscillatory experiments	46
2.5.3 More complex nonlinear oscillatory experiments	49
2.6 Summary	52

3	rheoKIC	53
3.1	The singular value decomposition and proper orthogonal decomposition	54
3.2	Dynamic Mode Decomposition	57
3.3	DMD with Control	61
3.4	Koopman decomposition	63
3.5	Koopman with inputs and control	65
3.6	Choice of observables	67
3.7	The rheoKIC method	70
4	Application to linear constitutive laws	73
4.1	The linear Maxwell model	73
4.2	Errors from time derivative approximation	76
4.3	Reduction of rheoKIC to DMDc	79
4.4	Inclusion of higher-order observables	81
4.4.1	Cause of redundancy for the cubic observables	84
4.5	Increasing the data complexity	87
4.5.1	Combined data sets from different experiments	87
4.5.2	Combining multiple SAOS data sets	91
4.6	Conclusions	92
5	Application to weakly nonlinear laws	95
5.1	Linear/Maxwell regime	97

5.1.1	Frequency-sweep MAOS	99
5.2	GNMM observables	101
5.3	Combined data sets	104
5.4	Sequential analysis	106
5.5	MAPS data	110
5.6	Effect of noise on rheoKIC	116
5.7	Conclusions	120
6	Applications to systems of nonlinear equations	122
6.1	Initial analysis	125
6.1.1	Effect of the viscosity term	128
6.2	Combined data sets	130
6.3	Sequential analysis	133
6.3.1	Combined data sets with sequential and thresholded analysis	137
6.4	MAPS data	140
6.5	Conclusions	143
7	Incorporating spatial inhomogeneity	145
7.1	Inducing shear banding	148
7.2	Methodology for interpreting spatial data	155
7.2.1	Interpreting the generalised coefficients	159
7.2.2	Determining the number of modes to keep	163

7.3	Effects of shear banding on rheoKIC	164
7.3.1	Applying rheoKIC to each band separately	169
7.4	Generalised coefficients for shear banding data	171
7.4.1	Analysis of Simulation 1	173
7.4.2	Analysis of Simulation 2	176
7.5	Conclusions	181
8	Conclusions and future work	184
8.1	Future work	187
8.1.1	Extensions within Rheology	187
8.1.2	Extensions within the methodology	188
8.2	Closing remarks	190
	Bibliography	190
A	GNMM equation	215
B	Full transformation of GNMM observables to Fourier basis functions	217

List of Tables

3.1	Terms present (marked with ‘x’) and absent (marked with ‘-’) for each of the elements of $\underline{\underline{\sigma}}$ making up the GNMM.	70
5.1	Approximated coefficients when concatenating the data sets used for ω -sweep MAOS. The ‘ 10^{-x} ’ entries indicate that the coefficients are of order $O(10^{-x})$ or smaller.	104
5.2	Approximated coefficients when concatenating data sets with a fixed frequency and $\dot{\gamma}_0 = [10^{-3}, 10^{-2}, 10^{-1}, 1, 10]$	105
5.3	Approximated coefficients for the higher order observables when applying sequential rheoKIC.	109
5.4	Final reconstructed constitutive law when applying rheoKIC using the sequential approach and two data sets $\omega = 1/\tilde{\lambda}$, $\dot{\gamma}_0 = 1, 10$	110
5.5	Reconstructed constitutive laws when applying rheoKIC to a single MAPS data set, then reducing the set of candidate observables based on the coefficients from the pseudo inverse step. $\lambda = G = 1$, $\beta = 0.4$, $[\omega_1, \omega_2, \omega_3] = [1, 4, 16]10^{-2}$ in all cases.	115
6.1	Final reconstructed equations for $\dot{\Sigma}_{xy}$ and $\dot{\Sigma}_{yy}$ when applying rheoKIC sequentially, then reducing the set of candidate observables based on the coefficients from the pseudo inverse step. $\lambda = G = 1$, $\beta = 0.4$	137

6.2	Final reconstructed equations from the last thresholding step in Fig. 6.10.	140
6.3	Final reconstructed equations for $\dot{\Sigma}_{xy}$ and $\dot{\Sigma}_{yy}$ when applying rheoKIC to a single MAPS data set, then reducing the set of candidate observables based on the coefficients from the pseudo inverse step. $\lambda = G = 1$, $\beta = 0.4$, $[\omega_1, \omega_2, \omega_3] = [5, 6, 9]$	143
7.1	Final reconstructed equations when using the combined data sets from the wall of the rheometer, where the fluid within the rheometer may be experiencing shear banding.	168
7.2	Reconstructed constitutive laws using spatially inhomogeneous data where the dimensions of the coefficients are enforced to be scalar.	170
7.3	Number of spatial modes required to represent each observable for Simulation 1 and Simulation 2, using $e = 0.99$ in both cases.	173
7.4	Spatial mode vector correlations and approximated scalar coefficients for each observable from Simulation 1.	175
7.5	Generalised coefficients for each observable for Simulation 1, alongside the original coefficient for that term in nRP equations.	175
7.6	Spatial mode vector correlations and predicted scalar coefficients for each observable from Simulation 2.	177
7.7	Generalised coefficients for each observable for Simulation 2, alongside the original coefficient for that term in nRP equations.	180

List of Figures

2.1	Left: Points represented on a two-dimensional Cartesian grid, e_1, e_2 . Right: The same points mapped onto a convected grid, e'_1, e'_2	33
2.2	Schematics for spring-dashpot models. (a) A spring with elastic modulus G ; (b) A linear dashpot with viscosity coefficient μ ; (c) The linear Maxwell model; (d) The generalised Maxwell model.	37
2.3	Common types of rotational rheometer. (a) Cone-plate; (b) Parallel plates; (c) Concentric cylinders (Couette).	40
2.4	Applied strain (top row) and resulting stress (bottom row) from commonly used experiments to probe the linear viscoelasticity of a material. (left) stress relaxation experiment; (right) constant shear rate experiment.	41
2.5	Illustration of an oscillatory shear experiment carried out in a parallel-plate model, with shear area A , gap width L , shear force F , and shear displacement s	42
2.6	Representative data from a small amplitude oscillatory shear test. (Left) Applied oscillatory shear (orange, dashed) and resulting stress (blue, solid). (Right) Breakdown of the stress signal into sine and cosine components, showing amplitudes of the different signals and the phase shift.	43

2.7	Alternative ways of representing data from a SAOS experiment. (a) Connections between δ , G' , G'' , and G^* . (b) Lissajous-Bowditch curve for a linearly elastic solid. (c) Lissajous-Bowditch curve for a linearly viscous fluid. (d) Lissajous-Bowditch curve for a linearly viscoelastic fluid.	45
2.8	Representative data of the stress response to an oscillatory shear experiment (top row) and its corresponding frequency spectrum (bottom row). (Left) SAOS; (Middle) MAOS; (Right) LAOS.	47
2.9	Examples of the applied shear for (left) a parallel superposition rheology scenario and (right) a MAPS scenario.	50
2.10	Example of the applied shear for a chirp experiment.	51
3.1	The SVD applied to (top row) a matrix with more columns than rows, and (bottom row) a matrix with more rows than columns. The rows and columns filled with zeros can be removed to produce the ‘compact’ SVD.	55
4.1	Representative data of the type typically produced by an oscillatory rheometer for a Maxwell fluid under small amplitude shear. $G = 1$ can be found as the value of G' for high frequencies, while $\lambda = 1$ can be found as the reciprocal of ω where G' and G'' coincide.	75
4.2	Values of the $\Phi = [\sigma, \dot{\gamma}]$ coefficients for the linear Maxwell model. (Solid line) Exact values using Eq. 4.11. (Dashed line) Taylor expansion with one term. (Dot-dashed line) Taylor expansion with two terms. Top: σ coefficient. Bottom: $\dot{\gamma}$ coefficient.	78
4.3	Predicted values for the coefficient multiplying each observable $\Phi = [\sigma, \dot{\gamma}]$, normalised k_1 and k_2 respectively. $G = \lambda = \dot{\gamma}_0 = 1$, data taken from one stationary period of data, 512 measurements taken per period.	79

4.4	The difference between the predicted observable coefficients \tilde{k}_1 and their actual values, alongside the predictions for λ and G compared to their actual values, computed using Eq. 4.14.	80
4.5	rheoKIC applied to data from the linear Maxwell model where $G = \lambda = \gamma_0 = 1$ and Φ is constructed according to Eq. 4.15.	82
4.6	rheoKIC applied to data from the linear Maxwell model where $G = \lambda = \gamma_0 = 1$ and Φ contains linear and cubic observables only.	83
4.7	Reconstruction error for rheoKIC when the set of candidate observables contains only σ and $\dot{\gamma}$, and when all cubic order combinations of σ and $\dot{\gamma}$ are also provided.	84
4.8	Data from the same scenario as in Fig. 4.6, but the SVD of Φ has been truncated to four.	85
4.9	Normalised approximations for observable coefficients where the data set is computed to resemble (left) data from a stress relaxation experiment with $\Phi = [\sigma \ \sigma^3]$ and (right) data from a constant shear rate experiment with $\Phi = [\sigma \ \dot{\gamma} \ \sigma^3, \ \sigma^2 \dot{\gamma}]$	89
4.10	Normalised approximations for observable coefficients where, at each frequency, the data set consists of data from a stress relaxation simulation, a constant shear rate simulation, and a SAOS simulation. (Left) Normalised values of $\tilde{\lambda}$ and \tilde{G} only, corresponding to the linear observables. (Right) Coefficients for all the observables in rheoKIC.	90
4.11	Approximations for λ (left) and G (right), normalised by their true values. The solid lines correspond to approximations where the provided data is only the data at that frequency, while the dashed lines correspond to approximations using data sets from all frequencies at once.	92
5.1	Stress response for a fluid governed by the SFM with fluid parameters $G = \lambda = 1$ and $\beta = 0.4$	96

- 5.2 rheoKIC applied to SAOS data where $\gamma_0 = 10^{-5}$ and $\omega = 10^{-2} - 10^2$, such that $\dot{\gamma}_0 = 10^{-7} - 10^{-3}$. The supplied observables are (left) σ and $\dot{\gamma}$, and (right) σ , $\dot{\gamma}$, and $\dot{\gamma}^2\sigma$ 98
- 5.3 Re-scaled approximations for k_3 where ω has been fixed while $\gamma_0 = 10^{-5} - 10$. The supplied observables are $\Phi = [\sigma, \dot{\gamma}, \dot{\gamma}^2\sigma]$ 99
- 5.4 rheoKIC applied to ω -sweep MAOS data using $\Phi = [\sigma, \dot{\gamma}, \dot{\gamma}^2\sigma]$. The legend in the top right describes the value of $\dot{\gamma}_0$ for all cases. Top left: Approximations for λ . Top left: Approximations for G . Bottom left: Approximations for β , $\dot{\gamma}_0 = 10^{-2} - 10$. Inset: σ for $\omega = 4$. Bottom right: Approximations for k_3 , $\dot{\gamma}_0 = 10^{-5} - 10^{-3}$ 100
- 5.5 rheoKIC applied to ω -sweep MAOS data using the full set of observables, The value of $\dot{\gamma}_0$ is fixed for each sweep. In all cases $G = \omega = 1$ and $\beta = 0.4$ 102
- 5.6 Approximations for SFM constitutive parameters when rheoKIC is applied to ω -sweep MAOS data using the full set of observables. 103
- 5.7 Stress response when $\dot{\gamma}_0 = 10$ and (top row) $\omega = 4$ and (bottom row) $\omega = 100$, and their corresponding power spectra. 108
- 5.8 RheoKIC applied to MAPS data where $[\omega_1, \omega_2, \omega_3] = [1, 4, 16]\omega_0$ 111
- 5.9 RheoKIC applied to MAPS data where $[\omega_1, \omega_2, \omega_3] = [5, 6, 9]\omega_0$ 112
- 5.10 Approximations for the SFM constitutive law parameters applied to MAPS data where (left) $[\omega_1, \omega_2, \omega_3] = [1, 4, 16]\omega_0$ and (right) $[\omega_1, \omega_2, \omega_3] = [5, 6, 9]\omega_0$. The full set of 7 GNMM observables has been provided in both cases. 113
- 5.11 Values for the coefficients C described in Eq. 5.13 using data from (left) MAPS data where $[\omega_1, \omega_2, \omega_3] = [1, 6, 14]\omega_0$ and (right) ω -sweep MAOS data. In both cases, $\dot{\gamma}_0 = 10^{-1}$ and the full set of 10 GNMM observables has been provided. . . 114

5.12	Approximated coefficients (normalised) as Gaussian white noise is added to both $\dot{\gamma}$ and σ to produce data with different SNR values. (Left) Oscillatory data analysed with the method developed in Section 5.4. (Right) MAPS data with thresholding applied during analysis.	118
5.13	MAPS data where $\omega = 0.01$, $\dot{\gamma}_0 = 1$, $[\omega_1, \omega_2, \omega_3] = [1, 4, 16]$, and with a SNR of 50.	118
6.1	Examples of Σ_{xy} and Σ_{yy} from the nRP model after 20 oscillatory periods have elapsed, for different values of $\dot{\gamma}_0$. In all cases $G = \lambda = \omega = 1$, $\beta = 0.4$, $\eta = 10^{-5}$	124
6.2	Predicted coefficients for observables using Φ_{xy} and Φ_{yy} from Eq. 6.8 and data from the nRP model where $G = \lambda = 1$, $\beta = 0.4$, $\eta = 10^{-5}$	127
6.3	The rank of Φ_{xy} where $K_{xy} = 11$ and data comes from the nRP model, for different strain rate magnitudes $\dot{\gamma}_0$	128
6.4	Predicted (red crosses) versus correct (blue circles) coefficients for observables where (top left) $\eta = 10^{-5}$, (top right) $\eta = 10^{-2}$, and (bottom) $\eta = 1$. In all cases $\omega = \dot{\gamma}_0 = 1$. The exact observables have been supplied for clarity.	129
6.5	Predicted (red crosses) versus correct (blue circles) coefficients for observables where the data has been concatenated from simulations where $\dot{\gamma}_0$ is fixed and ω is varied.	131
6.6	Predicted (red crosses) versus correct (blue circles) coefficients for observables where the data has been concatenated from simulations where ω is fixed and $\dot{\gamma} = [10^{-2}, 10^{-1}, 1, 10]$	132
6.7	Predicted (red crosses) versus correct (blue circles) coefficients when applying sequential rheoKIC to data representing an nRP fluid. The black dashed line is located at 10^{-1}	135

6.8	Predicted (red crosses) versus correct (blue circles) coefficients when the second step of sequential has been applied using only the observables with coefficients above the black dashed line in Fig 6.7.	136
6.9	Predicted (red crosses) versus correct (blue circles) coefficients from an application of rheoKIC where the results in the top row are as in Fig. 6.8, then rheoKIC is iteratively applied while the candidate observables for Σ_{xy} are removed based on the thresholds shown by the dashed lines.	136
6.10	Predicted (red crosses) versus correct (blue circles) coefficients from an application of rheoKIC using a combination of concatenated data sets, the sequential method, and thresholding.	139
6.11	Predicted (red crosses) versus correct (blue circles) coefficients from an application of rheoKIC on MAPS data where $n_j = [5, 6, 9]$	141
6.12	Predicted (red crosses) versus correct (blue circles) coefficients from an application of rheoKIC where the results in the top row are as in Fig. 6.11 for $\dot{\gamma}_0 = 1$, then rheoKIC is iteratively applied with reduced numbers of observables.	142
7.1	Illustration of the shear banding phenomenon in an oscillatory cell. (left) Homogeneous flow. (right) shear banding has separated the fluid's strain local rate into two regions in the gapwise direction.	146
7.2	Example flow curve for a constitutive law demonstrating shear banding. The dotted line illustrates the theoretical stress response produced by constitutive law with constrained spatial homogeneity, while the dashed line illustrates the type of stress response recorded from experiments.	148
7.3	Illustration of an oscillatory shear experimental protocol in two dimensions where the fluid response (dashed line) is assumed to be spatially homogeneous.	149

- 7.4 (l-r) Stress vs. strain rate, stress vs. strain, and velocity profiles for the nRP model in both the spatially homogeneous and inhomogeneous cases. Top row: $\beta = 0.4$, $\gamma_0 = 1$, $\omega = 10^{0.5}$. Bottom row: $\beta = 1$, $\omega = 1$, $\gamma_0 = 0.1 \cdot 10^{0.75}$. $J = 512$ when $\beta = 0.4$ and $J = 1024$ when $\beta = 1$. The symbols in the stress vs. strain curves correspond to the points in time where the velocity profiles have been plotted. 154
- 7.5 Predicted higher order coefficients (red crosses) in comparison to the coefficients from the homogeneous nRP equations (blue circles) when $\omega = \{10^{0.5}, 10\}$, the fluid is spatially homogeneous, and stress data is only recorded at the rheometer wall. The results are the same whether we use the imposed strain rate $\bar{\dot{\gamma}}$ or the local strain rate to construct the $\dot{\gamma}$ observable. 165
- 7.6 Predicted higher order coefficients (red crosses) and coefficients from the homogeneous nRP equations (blue circles) for the $\beta = 0.4$ fluid when $\dot{\gamma}_0 = 10$ and $\omega = [10^{0.5}, 10]$. We show the results when using the applied strain rate $\bar{\dot{\gamma}}$ (left) and the local strain rate $\dot{\gamma}$ for the shear rate observable. 166
- 7.7 Predicted higher order coefficients (red crosses) and coefficients from the homogeneous nRP equations (blue circles) for the $\beta = 1$ fluid when $\dot{\gamma}_0 = 10$ and $\omega = [10^{0.5}, 10]$. We show the results when using the applied strain rate (left) and the local strain rate for the $\dot{\gamma}$ observable. 167
- 7.8 First spatial modes for Σ'_{xy} , Σ'_{yy} , and $u(y)$ for the $\beta = 0.4$ fluid when $\omega = 10^{0.5}$ and $\dot{\gamma}_0 = 10^{1.75}$. (Left) The fluid is spatially homogeneous. (Right) The fluid has shear banding behaviour, with inset zoomed in to the high shear banding region. 169
- 7.9 Primary spatial modes needed to represent more than 99% of the Σ_{xy} and Σ_{yy} data for (top row) Simulation 1 and (bottom row) Simulation 2. 172
- 7.10 Spatial modes needed to represent more than 99% of the $\dot{\gamma}$ data for Simulation 1. 174
- 7.11 (Left) Reconstructed modes for the $\dot{\gamma}$ observable. (Right) Values for $\dot{\gamma}$ at each of the wall edges. 176

7.12	(Top-left) Reconstructed modes for the Σ_{yy} observable. (Top-right) Σ_{yy} recorded at each wall of the rheometer. (Bottom) First two projected spatial modes for Σ'_{yy} .	179
7.13	Reconstructed modes for the $\dot{\gamma}\Sigma_{yy}$ observable where each of the entries in the generalised coefficient has been multiplied by its corresponding entry in $\check{\mathbf{U}}_k^T \phi_k$.	181

Chapter 1: Introduction

Complex fluids are ubiquitous: in foods such as ketchup and chocolate [1], cosmetics like shampoo [2], industrial processing of materials like polymers and plastics [3, 4], in biological fluids including blood and mucus [5], and natural disasters such as volcanic lava and mudslides [6]. While they may all fall under the umbrella term of ‘fluids’ when in the state we model them, it is clear that they behave differently and require different equations in order to be modelled accurately. The difference lies in each fluid’s *constitutive law*: the equation required in addition to the standard momentum balance equation for fluid flow, which describes the relationship between the fluid’s stress and its deformation.

For a Newtonian fluid like water at a constant temperature, the shear stress and rate of strain are linearly proportional and the constant of proportionality is defined as the viscosity μ ,

$$\underline{\underline{\sigma}} = -p\mathbf{I} + 2\mu\underline{\underline{\mathbf{e}}}, \quad (1.1)$$

where \mathbf{I} is the identity matrix, p is the isotropic pressure, and $\underline{\underline{\mathbf{e}}} = \frac{1}{2}(\nabla\underline{\mathbf{u}} + (\nabla\underline{\mathbf{u}})^T)$ is the rate of strain tensor where $\underline{\mathbf{u}}$ is the velocity field. Meanwhile, constitutive laws for complex fluids can vary significantly, from simple modifications of Eq. 1.1 up to systems of highly nonlinear equations containing various invariants of the stress, strain and rate of strain tensors, and may also include other variables such as temperature, material aging, and so on.

Constitutive laws have been derived in both a bottom-up manner, from the kinetic theory of the fluid molecules which is then taken to a continuum limit, and in a top-down, phenomenological manner to describe the behaviour of a fluid observed during experiments. There is a catalogue

of constitutive laws that have been developed over decades in order to represent the dynamics of different complex fluids, and modifications can be made to these laws in order to better represent a given system, provided that physical constraints are still maintained [7]. Choosing an appropriate constitutive law involves balancing the benefits of a simple law that is easy to interpret in a given environment, with a complex law that can encapsulate all the properties of the fluid in question in a variety of scenarios, and also a level of reliance on the practitioner's own knowledge and experience.

Once a suitable constitutive law for a given fluid has been selected, the parameters for each of the terms in the law are determined by fitting it to rheological data recorded from experiments, with the assumption that the data is sufficiently detailed to identify the model parameters uniquely [8]. A classical rheometry experiment involves applying a deformation to the fluid and measuring its mechanical response. For example, in an oscillatory shear test, a Couette rheometer (or Couette cell) formed of two concentric cylinders is filled with the fluid, and then the inner cylinder is rotated while the force on the outer cylinder from the fluid is measured. Oscillating the cylinder at low amplitudes provokes a linear rheological response, while experiments taken at higher amplitudes can probe any nonlinear terms that are present in the fluid's constitutive law. The methods for analysing linear rheological data are well-established, while the analysis and interpretation of nonlinear rheological data is an active area of research.

An important assumption made during these experiments is that an affine deformation is carried out across the rheometer, meaning that the force measurements at the rheometer wall are sufficient to obtain the stress response of the entire fluid. Work in recent years has established the existence of a phenomenon known as shear banding, where the velocity is different in one or multiple subsections of the rheometer [9], and its importance in understanding the dynamics of a fluid undergoing large deformations. Shear banding can be indicated by analysing time-series data at the rheometer wall [10], and can be viewed fully when 2D or 3D images are taken during the experiment [11]. While the data for fitting a constitutive law and the data for analysing shear banding stems from the same experiments, they have so far been considered separately in the rheological community.

Broadly speaking, determining a fluid’s constitutive law is equivalent to finding the function which best relates the input to the experiment - the experimental parameters and the applied deformation - to the output - the forces measured on the rheometer or images taken during the experiment. This type of problem fits within the wider realm of ‘system identification methods’ [12], and we will seek solutions to this problem from a system identification perspective.

The family of methods we employ to achieve this goal stems from work in the 1930s by Bernard Koopman [13] and has had an explosion of interest in the past two decades. These methods are based on the idea of transforming a data set coming from a finite-dimensional, nonlinear dynamical system, into one coming from an infinite-dimensional, linear dynamical system, using the so-called *Koopman operator* [14]. The approach received renewed interest when Schmid introduced Dynamic Mode Decomposition (DMD) as a method to produce a finite-dimensional approximations to the Koopman operator [15]. DMD was originally developed for turbulence research to understand the dynamics of turbulent flow [16] - however, it has since been applied in a range of fields, such as monitoring power networks [17], modelling the spread of infectious diseases [18], and for the development of algorithmic trading strategies [19]. It is applicable to such disparate topics due to it being a *data-driven* method: any underlying dynamics are identified entirely based on features in the data that it has been provided. A huge number of variants and extensions to DMD have been proposed since this initial publication, of which we will discuss several in Chapter 3, with particular emphasis on a version of DMD called Koopman with inputs and control (KIC) [20].

In this thesis we present an application of KIC, which we will refer to as rheoKIC, that can be used as a system identification tool for both linear and nonlinear constitutive laws. We believe that this is the first time that a method based on Koopman operator theory has been used to analyse and identify the constitutive law of a complex fluid. Rather than fitting the parameters to a pre-selected constitutive law as is typical in the field, we instead aim to fit the entire stress evolution equation of the fluid, so that the data itself determines which constitutive law should be used. Given a dictionary of candidate terms that could be included in the constitutive law, rheoKIC computes a linear combination of them that optimally (with respect to the Frobenius norm) maps the input and output data from a rheometry experiment. We

use our knowledge of how constitutive laws are constructed to choose the initial dictionary of possible terms in the law, and investigate various techniques to balance the accuracy and simplicity of the resulting constitutive law during the rheoKIC process. We begin by looking at linear constitutive laws, and then systematically build on the problem complexity until we are dealing with systems of equations containing multiple nonlinear terms. We focus on data sources that align with the types of data extracted from rheometry and investigate how combinations of experimental data can aid in the identification of the terms and increase the accuracy of their approximated coefficients. Lastly, we show how the rheoKIC method naturally incorporates any spatial variation in the data when higher-dimensional data is provided.

1.1 Thesis layout

The structure of the thesis is as follows:

Chapter 2 We first establish the rheological background and scope of the fluid types that we will analyse. We discuss what a constitutive law should do and the physical laws it must follow, and specifically introduce the structure of constitutive laws of viscoelastic fluids. We additionally provide an explanation of the experimental protocols that we will simulate in order to generate the data used throughout the thesis.

Chapter 3 We establish the methodology behind Koopman operator theory and in particular DMD. We provide the specific extensions to DMD, namely Dynamic Mode Decomposition with control (DMDc) and Koopman with inputs and control (KIC), that serve as the main sources of inspiration to our method (rheoKIC). We then lay out the principal steps for applying rheoKIC to rheological data.

Chapter 4 We apply rheoKIC to data from the linear Maxwell model. We show that, for a specific choice of observables, rheoKIC applied to this data set reduces to DMDc. We compare our results to those from the analytic solution and analyse sources

of error. We show how to recognise that nonlinear terms are unnecessary when constructing the constitutive law, and we show the effects of using data sets from different types of simulations both in isolation and when combined.

Chapter 5 We show how rheoKIC can be applied to the simple/scalar fluidity model, which has a term that depends nonlinearly on the shear rate amplitude. We show that rheoKIC identifies a linear model when the shear rate amplitude of the provided data is not sufficiently high, but identifies the full, nonlinear model when the shear rate is large and/or the experimental data is appropriately complex. We introduce more complex data sets to investigate how this effects the performance of rheoKIC, and evaluate the effects of data noise on our results.

Chapter 6 We apply rheoKIC to the non-stretching Rolie-Poly model comprising a nonlinear system of two equations. We use combinations of experimental data to improve accuracy, and demonstrate various approaches to reducing the number of candidate observables that are initially supplied: by applying rheoKIC sequentially to data from different experiments; by combining data sets that demonstrate nonlinear behaviour; and by repeatedly applying rheoKIC while pruning any unused observables.

Chapter 7 We apply rheoKIC to nonlinear, spatially inhomogeneous rheological data which replicates a fluid demonstrating shear banding behaviour. We show that rheoKIC is still able to successfully reconstruct the constitutive law when provided only with measurements taken at the rheometer wall, and that rheoKIC can be used to determine any differences in the properties of the fluid within the two banded regions. Finally, we show that analysis using rheoKIC naturally extends to incorporate spatial inhomogeneity such as shear banding within the provided data, and that the coefficients generated by the method are generalised extensions to the fluid parameters that incorporate information about the spatially-varying response of the fluid.

Chapter 8 Conclusions and suggestions for future work.

Chapter 2: Characterisation of constitutive laws for viscoelastic fluids

Throughout the entirety of this thesis we will be looking at fluids that follow the momentum equation

$$\rho \frac{D\underline{u}}{Dt} = -\nabla \cdot \underline{\underline{\sigma}} + \underline{f} \quad (2.1)$$

for the Cauchy stress tensor $\underline{\underline{\sigma}}$ and body forces acting on the fluid \underline{f} . The stress tensor is symmetric under the assumption that there is no angular momentum within the fluid [21]. The operator $\frac{D\underline{x}}{Dt} = \frac{\partial \underline{x}}{\partial t} + \underline{u} \cdot \nabla \underline{x}$ is the material derivative which we will discuss further in Sec. 2.1. Eq. 2.1, along with the assumption that the fluid is incompressible,

$$\nabla \cdot \underline{u} = 0. \quad (2.2)$$

together form the incompressible Navier-Stokes equations for a Newtonian fluid. We assume that we are considering fluids where viscous effects dominate over any inertial effects, allowing us to reduce Eq. 2.1 and Eq. 2.2 to the Stokes equations for an incompressible fluid,

$$\nabla \cdot \underline{\underline{\sigma}} + \underline{\underline{f}} = 0, \quad (2.3a)$$

$$\nabla \cdot \underline{\underline{u}} = 0. \quad (2.3b)$$

The lack of inertial terms in comparison to the full Navier-Stokes equations means that Stokes flow, also known as ‘creeping flow’, is determined instantaneously from the effects of body forces. However, Eqs. 2.3 are not closed, as there is no equation that describes the dynamics of $\underline{\underline{\sigma}}$: this is the constitutive law which we must also provide. For a Newtonian fluid, the constitutive law is given by

$$\underline{\underline{\sigma}} = -p\underline{\underline{I}} + 2\mu\underline{\underline{e}}, \quad (2.4)$$

where $\underline{\underline{I}}$ is the identity tensor, μ is the fluid’s viscosity, and $\underline{\underline{e}}$ is the rate-of-strain tensor,

$$\underline{\underline{e}} = \frac{1}{2}(\nabla \underline{\underline{u}} + (\nabla \underline{\underline{u}})^T). \quad (2.5)$$

The dynamics of a Newtonian fluid in Stokes flow defined by Eq. 2.4 and Eqs. 2.3 are therefore entirely linear and can be solved using well-known methods for solving linear differential equations. For a complex fluid, Eq. 2.4 no longer holds and an alternative, possibly nonlinear, equation must be used in its place.

2.1 Constitutive laws

The constitutive law determines how the stress in the fluid will evolve over time and under the influence of applied forces. For a Newtonian fluid, the stress is linearly proportional to the rate of strain and the constant of proportionality is the shear viscosity, μ . The situation is less clear if the fluid is not Newtonian and this relation no longer holds. Constitutive laws for complex

fluids include extra terms that may be nonlinear in both the stress tensor and the rate of strain tensor, as well as their invariants.

While it is unquestionable that constitutive laws cannot violate the laws of thermodynamics, it was additionally noted by Oldroyd [22] that the evolution of the stress tensor should be independent of how it is observed and laid out a list of criteria to this end. In brief, a constitutive law should:

1. Remain the same despite a change in frame of reference;
2. Remain the same despite the fluid element under observation changing position, or its translational or rotational motion;
3. Remain the same despite any changes to nearby sections of the fluid (with the exception of enforcing boundary conditions for continuity).

If a constitutive law has all three of these properties then it is known as ‘rheologically invariant’ or ‘admissible’ [3]. The most convenient form for writing a constitutive law so that it can be checked for admissibility is within a convected coordinate system [23]. This is a coordinate system that is frame-invariant with respect to tensors, and as such the stress tensor will not appear to change if the frame of reference is changed. Similar to how the time derivative of the velocity vector is replaced by a material derivative for the Stokes equations in Eq. 2.3, we must replace the derivatives of our tensor with a *convected derivative* in a convected coordinate system [24] that deforms with the flow (represented in Fig. 2.1).

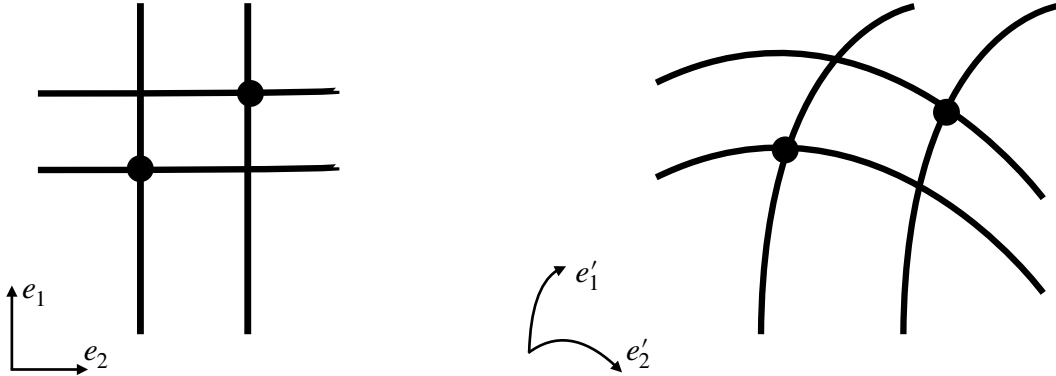


Figure 2.1: Left: Points represented on a two-dimensional Cartesian grid, e_1, e_2 . Right: The same points mapped onto a convected grid, e'_1, e'_2 .

The most commonly used frame-invariant derivatives are the upper-convected derivative,

$$\underline{\underline{\nabla}} \underline{\underline{\sigma}} = \frac{\partial \underline{\underline{\sigma}}}{\partial t} + \underline{u} \cdot \underline{\underline{\sigma}} - [(\nabla \underline{u})^T \cdot \underline{\underline{\sigma}} + \underline{\underline{\sigma}} \cdot (\nabla \underline{u})], \quad (2.6)$$

the lower-convected derivative [25],

$$\underline{\underline{\Delta}} \underline{\underline{\sigma}} = \frac{\partial \underline{\underline{\sigma}}}{\partial t} + \underline{u} \cdot \underline{\underline{\sigma}} + [(\nabla \underline{u})^T \cdot \underline{\underline{\sigma}} + \underline{\underline{\sigma}} \cdot (\nabla \underline{u})], \quad (2.7)$$

and the co-rotational, or ‘Jaumann’, derivative [3]

$$\overset{\circ}{\underline{\underline{\sigma}}} = \frac{\partial \underline{\underline{\sigma}}}{\partial t} + \underline{u} \cdot \underline{\underline{\sigma}} + \frac{1}{2}(\underline{\underline{\omega}} \cdot \underline{\underline{\sigma}} - \underline{\underline{\sigma}} \cdot \underline{\underline{\omega}}) \quad (2.8)$$

where $\underline{\underline{\omega}}$ is the vorticity tensor $\nabla \times \underline{u}$ and ‘ \times ’ denotes the cross product. The upper-convected derivative is used more regularly over the lower-convected derivative as it is able to produce the

well-known rod-climbing phenomenon, or ‘Weissenberg effect’ seen with some complex fluids: if a rod is rotated within a polymer suspension, the polymers will align with the circular streamlines around the rod and are ‘pushed’ upwards and out of the fluid [25]. Additionally, the Oldroyd-B model, which uses the upper-convected derivative, can be derived directly from the kinetic theory of a suspension of dumbbells, while the Oldroyd-A model, which uses the lower-convected derivative, cannot [26].

The well-known Oldroyd-B constitutive law can be derived in a bottom-up manner from modelling the kinetic theory of a suspension of non-interacting pairs of beads connected by Hookean springs [27]. Zhao *et al.* [28] were able to use a meso-scale particle dynamics simulation to learn the parameters to fit a generalised Newtonian fluid, which could then serve as the closure equation for a continuum-level model of a polymer solution. However, these models often require access to detailed information concerning the microstructure of the fluid, which may not be available, and their analysis is challenging except for in simple cases.

In contrast, other laws have been developed in a top-down, phenomenological manner by constructing models that match the behaviour of the fluid in question. For example, the Cross model, given by

$$\underline{\underline{\sigma}} = \mu(\underline{\underline{e}})\underline{\underline{e}}, \quad (2.9a)$$

$$\mu(\underline{\underline{e}}) = \mu_\infty + \frac{\mu_0 - \mu_\infty}{1 + (C\underline{\underline{e}})^m}, \quad (2.9b)$$

was designed to empirically fit data from a fluid that had two plateaus for its viscosity at low and high shear rates [29]. The ‘Cross time constant’ C and ‘Cross rate constant’ m are parameters that can be tuned to most accurately interpolate between the plateaus.

It is also possible to augment known constitutive laws with extra terms, along with fitting the model parameters, in order to represent the data more accurately [7]. Kim *et al.* [30] carried out experiments of a sphere settling in a Carbopol suspension that would typically be modelled with the Herschel-Bulkley constitutive law, and then compared the measured sphere

resistance with finite-element simulations that used the Herschel-Bulkley model directly. After quantifying the sources of error stemming from both experimental and model parameters, they found that the inclusion of a term in the constitutive law to represent slip on the sphere reduced the discrepancy between the sphere resistance predictions from 26% to 18%. The addition of the slip term produced a new model, not previously identified in the literature, that nevertheless fully satisfied the admissibility criteria and physical constraints of a constitutive law.

One issue with empirically fitting constitutive models to a data set is that multiple models can seemingly produce the same level of accuracy by using different sets of coefficients for the parameters. This was investigated by comparing the fits of various constitutive models commonly used for blood [8], and it was found that, if the experimental data did not cover a large enough range of shear rates, a wide range of parameter coefficients were capable of producing the same level of accuracy when fitting the data. Fluids modelled using these sets of parameter coefficients would then produce drastically different velocity profiles when used in a simulation with a different geometry, in this case a simulation of pressure-driven pipe flow.

Within materials science, the modified error in constitutive equation (MECE) [31–35] method has been developed to estimate parameters such as the elastic modulus of a material, while ensuring that the constitutive law always remains physically admissible as it is optimised. Parameters of the constitutive law are updated according to ‘reliable’ information (such as initial conditions) with rigid constraints such as Lagrange multipliers, and according to ‘unreliable’ information (such as the measured data itself) with less rigid constraints such as penalty terms. This method has the benefit of remaining equation-free by re-framing the problem as one of energy minimisation, but applications have so far been limited to problems such as truss structures where highly granular data is available.

An alternative system for deriving constitutive equations from physical laws is via the ‘General Equation for Non-Equilibrium Reversible-Irreversible Coupling’ (GENERIC) formalism [36]. Under this formalism, the evolution equations for the fluid are derived from a combination of a reversible equation, for the mechanical evolution, and an irreversible equation, describing the thermodynamic evolution of the fluid dynamics. The GENERIC method ensures that all

thermodynamic restrictions are observed and it has been shown to successfully produce well-known polymeric constitutive equations [37]; however, applications to data from simulations and experiments have so far been limited.

2.2 Viscoelastic fluids

Throughout this thesis we focus exclusively on analysing data from simulations of viscoelastic fluids. In contrast to ideally viscous fluids (such as water and oil) and ideally elastic solids (such as rubber), viscoelastic fluids demonstrate a combination of viscous and elastic behaviours. Gels are considered to be viscoelastic solids, while viscoelastic liquids have behaviour more aligned with viscous liquids, and include shampoos [2], glues [38], polymers [3, 4], micellar surfactant solutions [39], emulsions [40], and liquid crystals [41].

Viscoelastic fluids are produced by suspending macro-molecular chains, which have elastic behaviour, in a viscous liquid. As such, the constitutive law for a viscoelastic fluid has both a viscous part and an elastic part, the proportions of which are dependent on the microstructure of the fluid. Linear, one-dimensional models for describing fluids as a combination of viscous and elastic responses were first developed in the early 20th century [42]. The idea behind the simplest linear viscoelastic models is to combine the equation for a Hookean spring

$$\underline{\underline{\sigma}} = G \underline{\underline{\dot{\gamma}}} \quad (2.10)$$

to represent the non-instantaneous, elastic response from the macro-molecules (where $\underline{\underline{\dot{\gamma}}}$ represents the rate of strain tensor), with the equation for a linear dashpot:

$$\underline{\underline{\sigma}} = \mu \underline{\underline{\dot{\gamma}}}. \quad (2.11)$$

The dashpot represents the instantaneous, viscous response of the surrounding fluid and allows for the presence of a fluid memory. The constants G and μ refer to the elastic modulus and the

fluid viscosity, respectively. The typical diagrammatic representation of springs and dashpots are shown in Fig. 2.2. The springs and dashpots may be combined either in series or in parallel to produce spring-dashpot elements.

A single spring-dashpot element with one coefficient can be used to represent the fluid's relaxation rate, defined as the characteristic time scale for the fluid to return to its initial state after being deformed. A spring-dashpot element can be a viscoelastic model in its own right, such as the linear Maxwell model which is defined by one spring and one dashpot in series. Elements can be combined additively to produce other models - for example, the addition of a spring in parallel with a Maxwell element produces the standard linear model, also known as the Zener model [43]. Generalised models formed from many elements are able to represent fluids with multiple deformation time scales, such as suspensions of long polymer chains [44]. An example of this, the generalised Maxwell model, is shown in Fig 2.2. Increasing the number of modes increases the degrees of freedom in the generalised model, allowing for a closer fit to the data, but the subsequent increase in the model complexity can cause over-fitting of the model to the data [7].

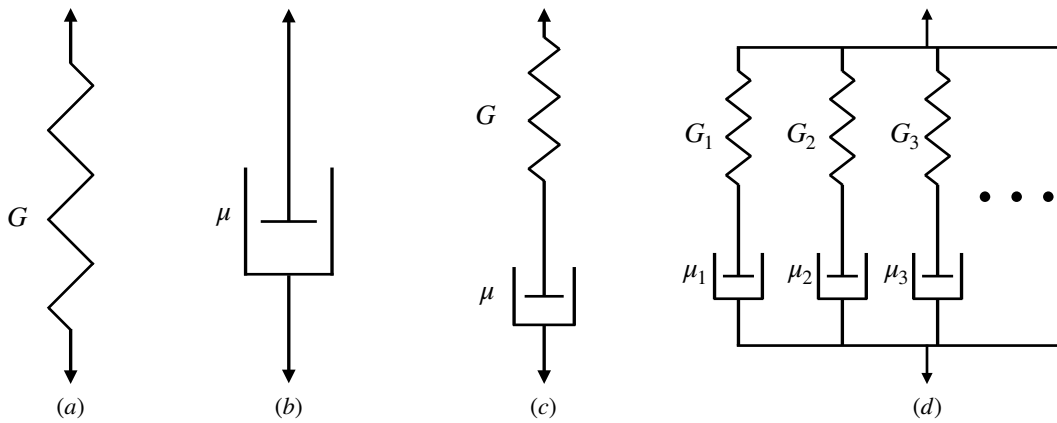


Figure 2.2: Schematics for spring-dashpot models. (a) A spring with elastic modulus G ; (b) A linear dashpot with viscosity coefficient μ ; (c) The linear Maxwell model; (d) The generalised Maxwell model.

2.3 Constitutive law frameworks

By restricting our scope to single-mode viscoelastic models that do not involve material aging or changes in temperature, the constitutive laws under examination may only contain frame-invariant combinations of the stress tensor and the rate of strain tensor, along with their spatial and temporal (convected) derivatives. As such, it is possible to develop frameworks for constitutive models by including all the combinations of permissible terms up to a given order. For example, the Oldroyd 8-constant model [45] contains all possible terms that are linear in $\underline{\underline{\sigma}}$, linear in $\underline{\underline{e}}$, and quadratic in $\underline{\underline{e}}$. The framework then reduces to well-known constitutive laws such as the Oldroyd-B model and the Johnson-Segalman model when setting different combinations of the 8 available coefficients to zero [46].

A recent extension to the Oldroyd 8-constant model, the generalised nonlinear Maxwell model (GNMM) [47], allows for all terms up to cubic order in both $\underline{\underline{\sigma}}$ and $\underline{\underline{e}}$. Starting with the multi-modal, corotational Jeffreys model:

$$\underline{\underline{\sigma}} + \lambda_1 \frac{\mathcal{D}\underline{\underline{\sigma}}}{\mathcal{D}t} = \eta_0 \left(\underline{\underline{\dot{\gamma}}} + \lambda_2 \frac{\mathcal{D}\underline{\underline{\dot{\gamma}}}}{\mathcal{D}t} \right) \quad (2.12)$$

where $\frac{\mathcal{D}\underline{\underline{x}}}{\mathcal{D}t} \equiv \frac{D\underline{\underline{x}}}{Dt} + \frac{1}{2}(\underline{\underline{\omega}} \cdot \underline{\underline{x}} - \underline{\underline{x}} \cdot \underline{\underline{\omega}})$ is the corotational derivative as described in Eq. 2.8, we add a term $F(\underline{\underline{\sigma}}, \underline{\underline{\dot{\gamma}}})$ which is a nonlinear function of $\underline{\underline{\sigma}}$ and $\underline{\underline{\dot{\gamma}}}$. With the additional constraints that the fluid is isotropic, incompressible, and undergoing simple shear, all possible terms in $F(\underline{\underline{\sigma}}, \underline{\underline{\dot{\gamma}}})$ can be enumerated up to a given order [48], which here we set as cubic. The cubic expansion contains twenty terms, of which some make use of the first $I(\underline{\underline{x}}) = \text{tr}(\underline{\underline{x}})$ and second $\underline{\underline{x}} : \underline{\underline{y}} = \text{tr}(\underline{\underline{x}} \cdot \underline{\underline{y}})$ tensor invariants. The full equation for the GNMM is [47]

$$\begin{aligned}
& \underline{\underline{\sigma}} + \frac{\mathcal{D}\underline{\underline{\sigma}}}{\mathcal{D}t} + \frac{1}{2}\mu_0\text{tr}(\underline{\underline{\sigma}})\dot{\underline{\underline{\sigma}}} - \frac{1}{2}\mu_1\{\underline{\underline{\sigma}} \cdot \dot{\underline{\underline{\sigma}}} + \dot{\underline{\underline{\sigma}}} \cdot \underline{\underline{\sigma}}\} + \frac{1}{2}\nu_1(\underline{\underline{\sigma}} : \dot{\underline{\underline{\sigma}}})\underline{\underline{I}} - \frac{\alpha_0}{\eta_0}\text{tr}(\underline{\underline{\sigma}})\underline{\underline{\sigma}} \\
& + \frac{\alpha_1}{\eta_0}\{\underline{\underline{\sigma}} \cdot \underline{\underline{\sigma}}\} + \frac{\beta_0}{\eta_0}\text{tr}(\underline{\underline{\sigma}})^2\underline{\underline{I}} - \frac{\beta_1}{2\eta_0}(\underline{\underline{\sigma}} : \underline{\underline{\sigma}})\underline{\underline{\delta}} - \frac{c_1\lambda_1}{\eta_0}(\underline{\underline{\sigma}} : \dot{\underline{\underline{\sigma}}})\underline{\underline{\sigma}} - c_2\lambda_1(\dot{\underline{\underline{\sigma}}} : \dot{\underline{\underline{\sigma}}})\underline{\underline{\sigma}} \\
& - \frac{c_3\lambda_1}{\eta_0^2}(\underline{\underline{\sigma}} : \underline{\underline{\sigma}})\underline{\underline{\sigma}} - \frac{d_1\lambda_1}{\eta_0}(\underline{\underline{\sigma}} : \underline{\underline{\sigma}})\dot{\underline{\underline{\sigma}}} - d_2\lambda_1(\underline{\underline{\sigma}} : \dot{\underline{\underline{\sigma}}})\dot{\underline{\underline{\sigma}}} - \frac{f_1\lambda_1}{\eta_0}\{\underline{\underline{\sigma}} \cdot \underline{\underline{\sigma}} \cdot \dot{\underline{\underline{\sigma}}} + \dot{\underline{\underline{\sigma}}} \cdot \underline{\underline{\sigma}} \cdot \underline{\underline{\sigma}}\} \\
& - f_2\lambda_1\{\underline{\underline{\sigma}} \cdot \dot{\underline{\underline{\sigma}}} \cdot \dot{\underline{\underline{\sigma}}} + \dot{\underline{\underline{\sigma}}} \cdot \dot{\underline{\underline{\sigma}}} \cdot \underline{\underline{\sigma}}\} - \frac{2f_3\lambda_1}{\eta_0^2}\{\underline{\underline{\sigma}} \cdot \underline{\underline{\sigma}} \cdot \underline{\underline{\sigma}}\} + \zeta\text{tr}(\underline{\underline{\sigma}})\underline{\underline{I}} \\
& = \eta_0\left(\dot{\underline{\underline{\sigma}}} + \lambda_2\frac{\mathcal{D}\dot{\underline{\underline{\sigma}}}}{\mathcal{D}t} - \mu_2\{\dot{\underline{\underline{\sigma}}} \cdot \dot{\underline{\underline{\sigma}}}\} + \frac{1}{2}\nu_2(\dot{\underline{\underline{\sigma}}} : \dot{\underline{\underline{\sigma}}})\underline{\underline{\delta}} + d_3\lambda_1(\dot{\underline{\underline{\sigma}}} : \dot{\underline{\underline{\sigma}}})\dot{\underline{\underline{\sigma}}} + 2f_4\lambda_1\{\dot{\underline{\underline{\sigma}}} \cdot \dot{\underline{\underline{\sigma}}} \cdot \dot{\underline{\underline{\sigma}}}\}\right).
\end{aligned} \tag{2.13}$$

The GNMM can also be readily extended to models with multiple relaxation times. All of the coefficients aside from η_0 and ζ have dimensions of time, while the specific physical description for each coefficient will be dependent on the model it is being used within. It encompasses 18 different constitutive laws and asymptotically approximates a further three constitutive laws. All of the constitutive laws contained within the model have three non-zero parameters η_0 , λ_1 , and λ_2 , corresponding to the linear terms and derivatives in the equation.

Working with the GNMM framework allows for great flexibility in modelling the fluid accurately but requires the cumbersome fitting of many parameters to the data and the entire framework should not to be used to fit a data set. Further, as is the case with the generalised spring-dashpot models described previously, including extra terms for diminishing gains of representing the fluid accurately can lead to overfitting to the data, which may cause the resulting model to be inaccurate when applied to data from the same fluid in a different scenario.

2.4 Rheometry

The process of carrying out experiments to analyse the properties of a complex fluid is known as rheometry, while the instruments for carrying out rheological experiments are called rheometers. In this thesis we will analyse data from simulations - however, to maintain that the approach we develop is transferable to experimental data, we set up our simulations to produce data that

mimic the outputs from rheometry.

We will be focusing our efforts on data from the shear type of rheometer, and primarily rotational rheometers. Some of the main types of rotational rheometer are laid out in Fig. 2.3 below. The rheometer is operated by prescribing the rotational speed or shear rate represented by the curved arrow. The shear stress or strain, depending on the type of scenario the rheologist is aiming to emulate, is then measured by the sensors positioned at the locations of the dashed red lines in the figure.

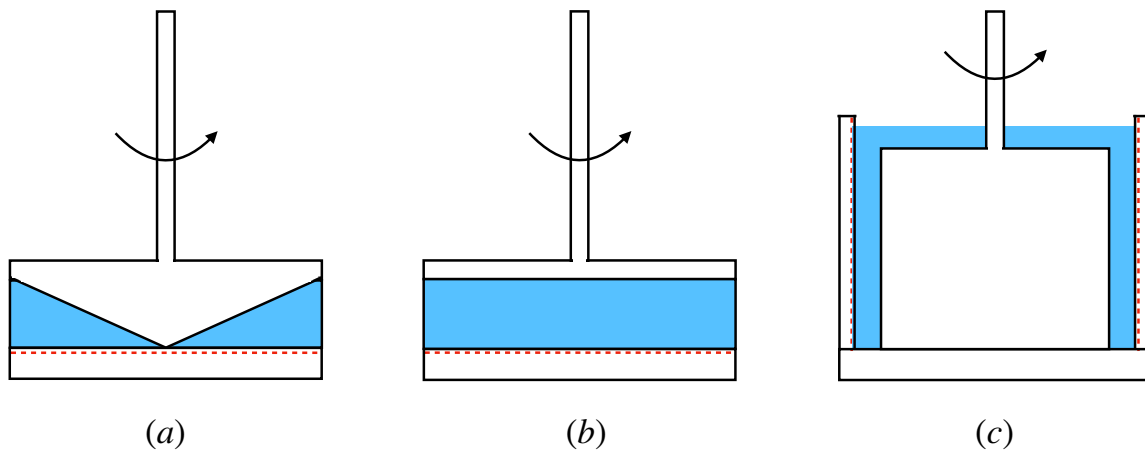


Figure 2.3: Common types of rotational rheometer. (a) Cone-plate; (b) Parallel plates; (c) Concentric cylinders (Couette).

Two common experiment types which probe the linear responses of a viscoelastic material are the stress relaxation experiment and the shear startup experiment. Representative data from both experiments are shown in Fig. 2.4.

When carrying out a stress relaxation experiment, shown in Fig. 2.4 (left), a constant shear is applied to an initially quiescent fluid, causing the stress to jump in value and then decay exponentially. The inverse of the stress relaxation experiment is the ‘creep experiment’, where instead a constant stress is applied and the strain is recorded. Measurements at very short intervals may be necessary in order to capture the fluid response if the relaxation time is small. For a shear startup experiment, shown in Fig. 2.4 (right), the shear is instead applied

at a constant rate while the stress is recorded until it settles. Multiple applications of a shear startup and a stress relaxation experiment can also be combined in series to produce a sawtooth pattern for the applied shear rate [49].

In both cases, for a Newtonian fluid the stress would respond instantaneously; any difference in the stress response from being linearly proportional to the shear rate is what sets the fluid apart from being Newtonian.

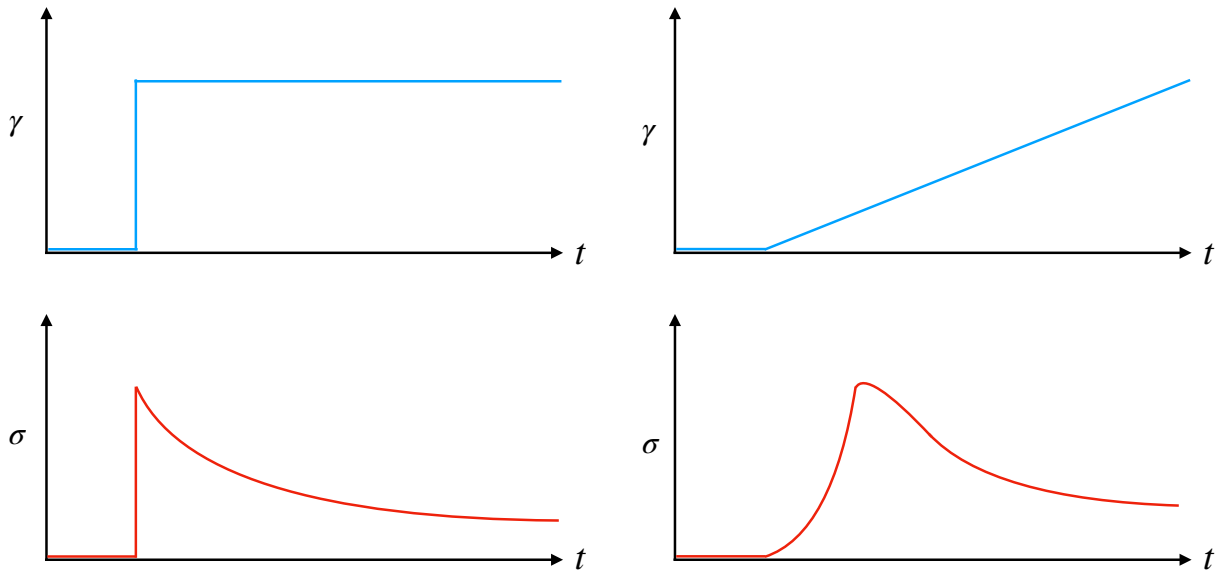


Figure 2.4: Applied strain (top row) and resulting stress (bottom row) from commonly used experiments to probe the linear viscoelasticity of a material. (left) stress relaxation experiment; (right) constant shear rate experiment.

2.5 Oscillatory Rheometry

Oscillatory rheometry is the most common method to capable of probing both the linear and nonlinear features of a viscoelastic fluid. A diagram of the dynamics involved in an oscillatory test is displayed in Fig. 2.5 where flow is assumed to be homogeneous in the z -direction. During oscillatory experiments, the applied deformation is time-dependent and oscillatory, with angular frequency ω and amplitude γ_0 . Oscillatory experiments are carried out in a rotational rheometer, which has two operational modes:

1. Enforce a prescribed rotational speed or shear rate on one of the plates and record the shear stress.
2. Enforce a prescribed torque or shear stress on one of the plates and record the shear rate.

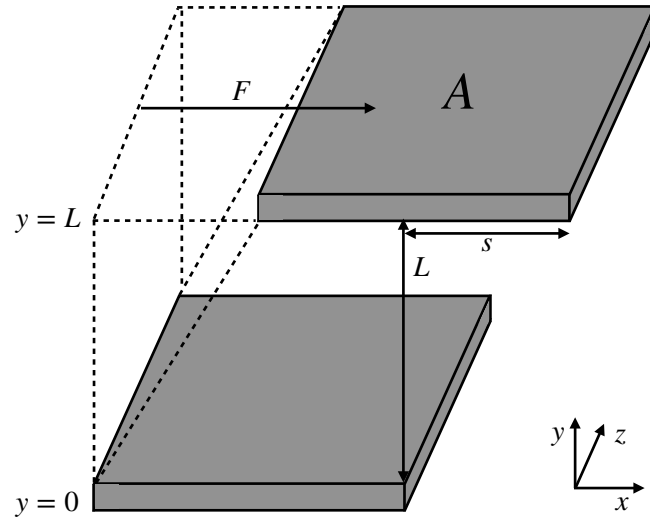


Figure 2.5: Illustration of an oscillatory shear experiment carried out in a parallel-plate model, with shear area A , gap width L , shear force F , and shear displacement s .

For a shear-controlled oscillatory test, a sensor on the moving plate in the rheometer records the off-diagonal component of the strain tensor as

$$\gamma_{xy} = \frac{s}{L} \quad (2.14)$$

where s is the displacement of the plate and L is the distance between the plates as indicated in Fig. 2.5. The sensor on the stationary plate then records the amount of force required to keep the plate in position without moving,

$$\sigma_{xy} = \frac{F}{A} \quad (2.15)$$

where A is the area of the plate. It is generally assumed that the gap L is small enough and that the deformation is controlled such that the dynamics across the rheometer are spatially homogeneous [50]. Later in this thesis we will look at the effects on a constitutive model if we incorporate the spatial inhomogeneity in the y -direction on the fluid.

2.5.1 Linear oscillatory experiments

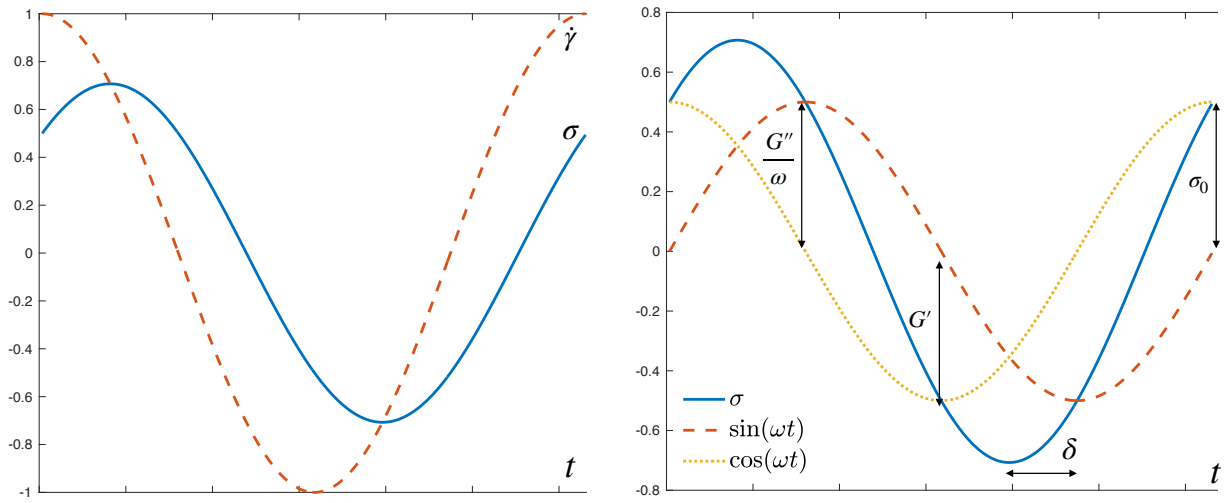


Figure 2.6: Representative data from a small amplitude oscillatory shear test. (Left) Applied oscillatory shear (orange, dashed) and resulting stress (blue, solid). (Right) Breakdown of the stress signal into sine and cosine components, showing amplitudes of the different signals and the phase shift.

Linear oscillatory tests use a shear amplitude γ_0 small enough to not disturb the fluid's microstructural state, causing any response to be linear. An example of the type of data extracted from a small amplitude test is shown in Fig. 2.6. For an experiment where a small amplitude oscillatory shear strain (SAOStrain) is applied in the x -direction, the applied shear is

$$\gamma_{xy}(t) = \gamma_0 \sin(\omega t) \quad (2.16)$$

and the corresponding shear rate is

$$\dot{\gamma}_{xy}(t) = \frac{\partial \gamma}{\partial t} = \gamma_0 \omega \cos(\omega t) = \dot{\gamma}_0 \cos(\omega t) \quad (2.17)$$

where $\dot{\gamma}_0 = \gamma_0 \omega$ is the shear rate amplitude. The shear stress response will be

$$\sigma_{xy}(t) = \sigma_0 \sin(\omega t + \delta). \quad (2.18)$$

The phase-shift angle, or mechanical loss angle, $\delta(\omega)$ defines the speed of the fluid's response to the applied strain rate, and is also depicted in Fig. 2.6. If the fluid is ideally elastic with no viscous part, then $\delta = 0$ and σ_{xy} is completely in-phase with γ_{xy} . If the fluid is ideally viscous with no elastic part, then $\delta = \pi/2$ and σ_{xy} is completely out-of-phase with γ_{xy} - it is in-phase with $\dot{\gamma}_{xy}$ instead. For a viscoelastic fluid, once any transients from initialisation of the experiment have died away, the shear stress response can be decomposed into a combination of a sine wave and a cosine wave, both with frequency ω (dropping subscripts),

$$\sigma(t) = G'(\omega) \sin(\omega t) + G''(\omega) \cos(\omega t) = G'(\omega) \gamma(t) + \frac{G''(\omega)}{\omega} \dot{\gamma}(t). \quad (2.19)$$

The elastic storage modulus $G'(\omega)$ represents the stored energy from the deformation while the viscous loss modulus $G''(\omega)$ represents the energy from the deformation that is dissipated via friction within the fluid. We can combine the storage and loss moduli and write them as the complex shear modulus $G^*(\omega) = G'(\omega) + iG''(\omega)$, which describes the entire linear viscoelastic behaviour of the fluid [51]. The relationship between $G^*(\omega)$, δ , $G'(\omega)$, and $G''(\omega)$, is shown in Fig 2.7(a). It can be seen that $\tan(\delta) = G''/G'$, and as such describes the ratio between the viscous and elastic behaviour. This relationship can also be shown via *Lissajous-Bowditch curves*, also shown in Fig. 2.7, where the stress and strain are used as axes to plot the data: an elastic solid will show a straight line, a viscous fluid will show a circle, while a linear viscoelastic fluid will show an ellipse rotated at an angle δ .

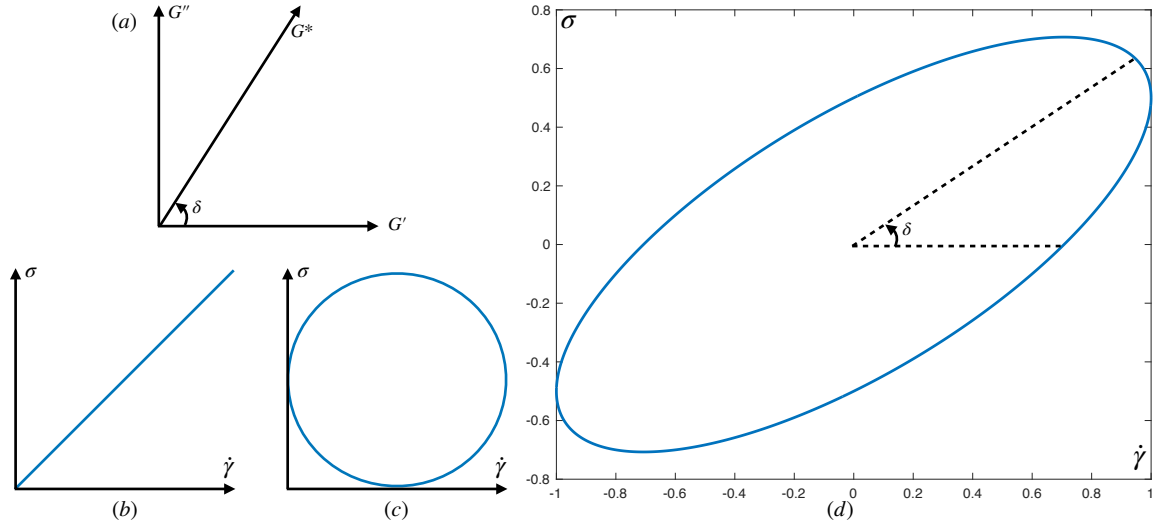


Figure 2.7: Alternative ways of representing data from a SAOS experiment. (a) Connections between δ , G' , G'' , and G^* . (b) Lissajous-Bowditch curve for a linearly elastic solid. (c) Lissajous-Bowditch curve for a linearly viscous fluid. (d) Lissajous-Bowditch curve for a linearly viscoelastic fluid.

The storage and loss moduli are *material functions*: intermediate values that depend on the experimental setup (in this case, the oscillatory frequency ω) rather than being intrinsically related to properties of the fluid. Other material functions include the dynamic viscosity

$$\eta(\sigma_{xy}) = \frac{\sigma_{xy}}{\dot{\gamma}_0} \quad (2.20)$$

and the first and second normal stress differences $N_1 = \sigma_{xx} - \sigma_{yy}$ and $N_2 = \sigma_{yy} - \sigma_{zz}$. Material functions serve to bridge the gap between a constitutive law and the measurements taken during an experiment: they can be calculated directly from the equations of a constitutive law, while also being straightforward to compute from measurements taken from an experiment due to their simple dependencies on experimental parameters. They are a useful conduit for checking whether a proposed constitutive law can accurately model the behaviour of the fluid under investigation. On the other hand, their usage is restricted to the type of experiment for which they are designed.

2.5.2 Nonlinear oscillatory experiments

Many nonlinear constitutive laws will produce identical linear behaviour under small enough deformations [46, 52]. It is therefore necessary to carry out large deformation experiments which probe the nonlinear response of the fluid in order to distinguish between constitutive laws in a given framework, and also to produce models that describe the fluid in a wider range of environments.

For a SAOS experiment, γ_0 is fixed at a small enough value to provoke a linear response in the fluid and separate experiments are carried out for a range of values of ω typically spanning several orders of magnitude. It is then possible to use plots of G' and G'' to extract parameters which appear in the constitutive law: for example, the characteristic relaxation time λ , first described in Section 2.2, can be found as the reciprocal of ω at which G' and G'' intersect [53].

Confirming that the fluid is no longer in the linear viscoelastic region can be done by fixing ω and carrying out experiments over a range values for γ_0 , then observing when G' and G'' are no longer independent of the deformation magnitude, or by observing where the Lissajous-Bowditch curves begin to deviate from the ellipse shape that is the signature of viscoelastic fluids [54]. The method which follows most directly from SAOS analysis is to compute the discrete Fourier transform (DFT) of the data, once any initial transients have decayed, according to

$$\sigma(t; \omega, \dot{\gamma}_0) = \sum_{n=1, \text{odd}}^{\infty} [a_n(\omega, \dot{\gamma}_0) \sin(n\omega t) + b_n(\omega, \dot{\gamma}_0) \cos(n\omega t)], \quad (2.21)$$

in a process known as FT-rheology [55]. The higher order frequencies appear only at odd harmonics since the stress response should be independent of shear direction but should change sign with the shear [56]. An example of stress response data from an oscillatory shear experiment, and its corresponding frequency spectrum, is shown in Fig. 2.8.

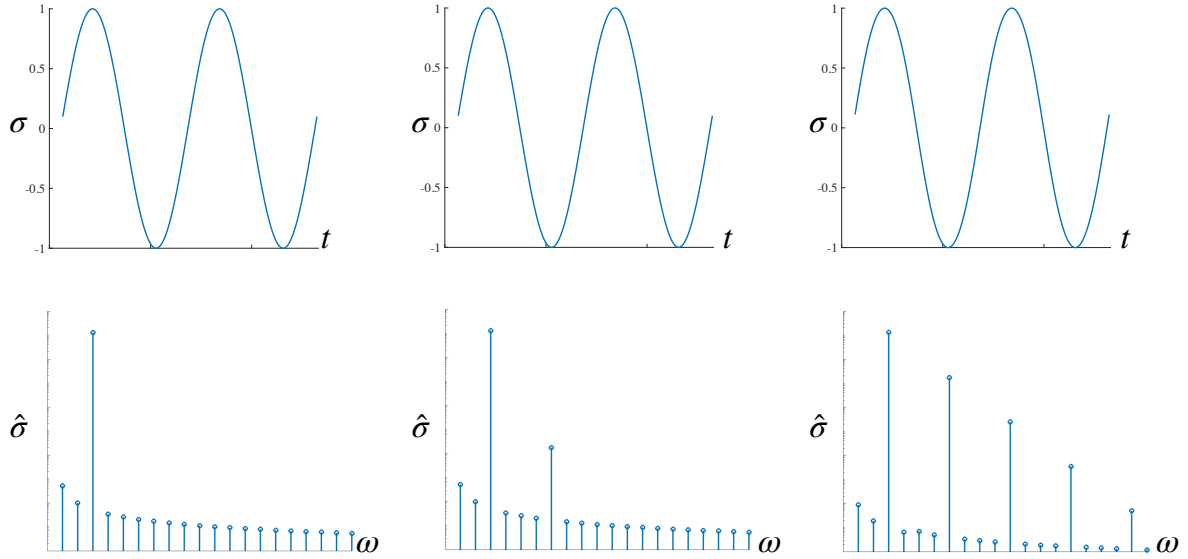


Figure 2.8: Representative data of the stress response to an oscillatory shear experiment (top row) and its corresponding frequency spectrum (bottom row). (Left) SAOS; (Middle) MAOS; (Right) LAOS.

If the stress response to the applied oscillatory strain is weakly nonlinear with non-trivial frequencies at the first and third harmonics only, the experiment is referred to as medium amplitude oscillatory shear (MAOS). A decidedly nonlinear response with non-trivial frequencies at harmonics higher than this is referred to as large amplitude oscillatory shear (LAOS). For the case of Fig. 2.8, the stress response looks very similar in all three simulations - it is only when the Fourier transform is applied that the higher order frequencies of the stress response can be observed.

While the analysis of viscoelastic fluids under linear oscillatory shear is well established, there are currently several competing theories for how to analyse nonlinear viscoelastic data [54,56–61] with no general consensus. These methods can be broadly described as determining a set of basis functions upon which the nonlinear stress response data can be decomposed. The ideal set of basis functions should be orthogonal and produced in a methodical manner, but at the same time be easily relatable to the physical attributes of the fluid. For example, the set of basis functions in FT-rheology is of course orthogonal, and it has the benefit that the classical SAOS analysis can be retrieved by setting $n = 1$ and therefore $a_n = \dot{\gamma}_0 G'(\omega)$, $b_n = \dot{\gamma}_0 G''(\omega)$. However, the resulting coefficients from directly applying FT-rheology to nonlinear data suffer

from a lack of physical interpretation.

An alternative method known as the ‘stress decomposition’ (SD) method [57] decomposes the stress data into a viscous response and an elastic response,

$$\sigma = \sigma' + \sigma'' \quad (2.22a)$$

$$\sigma' = \sum_{k=1}^{\infty} g'_{2k+1} (\gamma_0 \sin(\omega t))^{2k+1} = g'_1 \gamma_0 \sin(\omega t) + g'_3 \gamma_0^3 \sin^3(\omega t) + \dots \quad (2.22b)$$

$$\sigma'' = \sum_{k=1}^{\infty} g''_{2k+1} (\gamma_0 \cos(\omega t))^{2k+1} = g''_1 \gamma_0 \cos(\omega t) + g''_3 \gamma_0^3 \cos^3(\omega t) + \dots \quad (2.22c)$$

The benefit of this method is that the decomposition is unique and the coefficients can be directly related to viscous and elastic contributions. On the other hand, if straightforward polynomial regression is used to fit the coefficients as proposed in the initial paper [57], the coefficient values will change based on the chosen order of the truncation. An extension to the SD method resolves this issue by using Chebyshev coefficients for the fitting step instead [62]; however, the physical interpretation for higher order dynamics is not fully developed, and in theory an infinite number of these basis functions is necessary to fully represent the dynamics.

An approach which focuses on directly representing the fluid’s physical phenomena within the choice of basis terms was presented by Klein et al [59]. Here, the stress response is decomposed into the following characteristic functions: a sinusoidal function for the linear viscoelastic response; a rectangular function for strain softening; a triangular function for strain hardening; and a sawtooth function to represent wall slip and/or shear banding (discussed in further detail in Chapter 7). The ability to directly attribute each basis function to a characteristic of the fluid is useful, but the choice of functions is not uniquely determined and the proposed characteristic functions are not orthogonal.

All of the basis function decompositions listed above were developed with oscillatory experiments in mind. An exception to this is a recently developed framework where an orthogonal basis is constructed from invariants of the rate of strain tensor [63]. This decomposition is

agnostic to the experiment type, which allows coefficients determined in a steady flow to be generalised to model the fluid in more complex geometries, such as a contraction flow.

2.5.3 More complex nonlinear oscillatory experiments

Modifications to oscillatory experiments have been suggested as procedures to further probe the nonlinear features of a fluid. These often involve combining features from more standard linear experiments to form new experimental protocols.

Superposition rheometry, initially proposed by Tanner in 1968 [64], consists of superimposing an oscillatory shear on a steady-state shear flow. They are applied in the same direction during parallel superposition rheometry (PSR), and perpendicular to each other in the case of orthogonal superposition rheometry (OSR). It is possible to translate the results between PSR and OSR by writing the stress as a Fréchet series and combining the results from both as measure of flow anisotropy [65]. OSR requires data from simulations in at least two dimensions in order for both types of flow to be applied, but the effects from each flow are then easily separable. On the other hand, PSR can be carried out in one dimension with the caveat that there is a more direct interaction between the two types of shear. An example of the applied strain γ from a PSR experiment is shown in Fig. 2.9(a).

The PSR test reduces to the constant shear rate test as the oscillatory amplitude reduces to zero. The standard material functions $G'(\omega)$ and $G''(\omega)$ are not applicable to data from a PSR scenario: instead, linear perturbation analysis is carried out on the stress tensor to find their analogues $G'_{||}$ and $G''_{||}$ in integral form [66]. These cannot be converted to the standard storage and loss moduli, most notably because they both may become negative at high shear rates.

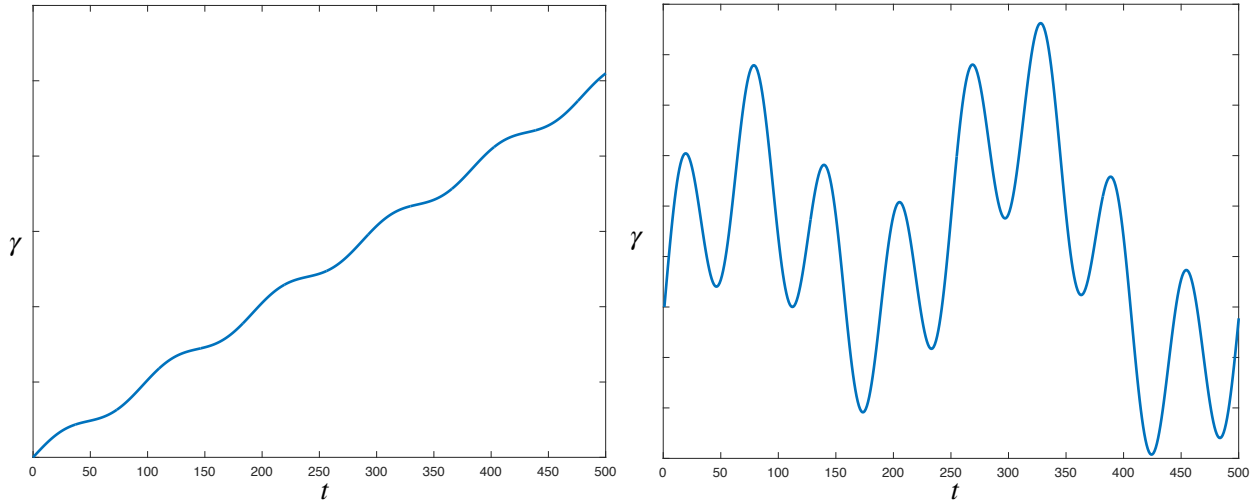


Figure 2.9: Examples of the applied shear for (left) a parallel superposition rheology scenario and (right) a MAPS scenario.

An alternative approach to superposition rheometry is to combine simultaneous oscillatory shear experiments at different frequencies, first proposed as ‘Fourier transform mechanical spectroscopy’ (FTMS) [67] or the ‘multiwave technique’ [68]. The applied shear becomes

$$\gamma(t) = \gamma_0 \sum_{j=1}^N \sin(n_j \omega^* t + \delta_j) \quad (2.23)$$

and an example waveform is shown in Fig. 2.9. Initial analysis from these types of experiments focused exclusively on identifying the fluid’s linear viscoelastic response [69]; recent work has involved finding sets of the n_j frequencies such that the stress response of the fluid will also show features at the intermediate frequencies between n_j values, via a process called ‘intermodulation’ [70, 71]. Setting $N = 3$ is sufficient to provoke the medium amplitude response, and the resulting method is known as the medium amplitude parallel superposition (MAPS) technique [47].

Similar to the PSR data, results from MAPS experiments cannot be directly compared to data from standard oscillatory shear experiments. In its place, the proposed method of interpretation involves expanding the stress response as a Volterra series [47] and projecting the resulting

coefficients onto a three-dimensional surface. The rich data set resulting from a MAPS protocol has also been shown to successfully identify a third-order constitutive model for a data set computed using the reptation-reaction (RR) model, which has a much more complex mathematical structure [72].

A final subset of more complex experiments to which there has recently been renewed interest involve running oscillatory tests with a fixed amplitude but exponentially increasing the oscillatory frequency over time. This procedure was initially inspired by the echolocation processes of bats [73] and dolphins [74], and these signals are known as ‘chirps’ [75] when applied to radar and acoustic measurements. The chirp signal is given by [76]

$$x(t) = x_0 \sin \left(\frac{\omega_1 T}{\log(\omega_2/\omega_1)} \left[\exp \left(\log(\omega_2/\omega_1) \frac{t}{T} \right) - 1 \right] \right) \quad (2.24)$$

where ω_1 and ω_2 are the initial and final frequencies of the chirp, respectively, and T is the total length of the signal. Using Eq. 2.24 directly as the value of the applied strain $\gamma(t)$, and its subsequent analysis, has been referred to as ‘optimal Fourier rheometry’ since it is both optimal in terms of the frequency resolution and the signal-to-noise ratio [68, 77]. An example of a chirp of this type is given in Fig. 2.10 where $x_0 = \omega_1 = 1$ and $\omega_2 = 10$.

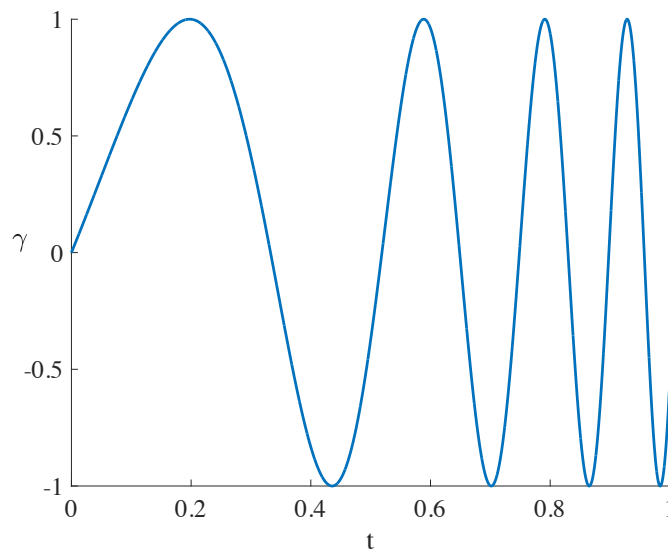


Figure 2.10: Example of the applied shear for a chirp experiment.

The typical process for analysing data from chirp experiments involves applying the discrete Fourier transform and then computing $G'(\omega)$ and $G''(\omega)$. However, the constant amplitude in Eq. 2.24 produces ripples, known as ‘Fresnel ripples’, in the frequency spectrum which muddies the data from experiments. The optimally windowed chirp (OWCh) experimental protocol [76] applies a chirp signal within a cosine-tapered window function designed to optimally reduce the effect of Fresnel ripples. The data from a single OWCh protocol produces measurements in around one hundredth of the time that a standard oscillatory frequency sweep would take in order to produce the same level of accuracy [78].

2.6 Summary

In this chapter we have detailed the stages of the standard process for fitting a constitutive model to a viscoelastic fluid. They can be broadly considered as follows:

1. Choose a rheometry process that probes the behaviour of the fluid that the model should be able to reproduce;
2. Choose a suitable constitutive model based on a combination of known information regarding the fluid and the rheologist’s own experience;
3. Fit the data to the model via the parameters in the chosen constitutive law.

In the following chapters, we seek to automate some of the decisions that must be made during this process and attempt to answer the following question: Given an appropriately-detailed rheological data set, are we able to directly infer both the coefficients and the terms in the constitutive law which produced the data?

Chapter 3: rheoKIC

We have identified that in a rheological experiment there is an unknown equation (the constitutive law) evolving the dynamics of the fluid, with known inputs (the experimental setup and applied shear strain) and measured outputs (one or more elements of the shear stress tensor). With all of this data to hand, we aim to identify the constitutive law in a data-driven and rheologically-informed manner.

We are seeking both the terms of the constitutive equation and the coefficients that scale them, rather than seeking purely the coefficients for a constitutive law that have already been determined. This problem has been broken down into two sub-problems within rheology [30] and quantitative biology [79]:

1. ‘Model-form uncertainty’ or ‘structural identifiability’: whether the correct underlying dynamics for the chosen model can be inferred from the data.
2. ‘Parametric uncertainty’ or ‘practical identifiability’: whether the model parameters can be computed correctly, given errors in measurement from noise or other issues regarding data quantity and quality.

This chapter covers some existing methods that tackle structural identifiability; the question of practical identifiability will arise repeatedly in the following chapters. We develop our approach based on modal decomposition methods, an area which has seen rapid growth within the fluids community in recent years. We will introduce the Koopman operator, followed by its most well-known successor Dynamic Mode Decomposition (DMD). We then move onto the most

recent developments of DMD that are suited to system identification for nonlinear rheological constitutive laws, in particular Koopman with Inputs and Control (KIC). We intersperse descriptions of the extensions and modifications to DMD and other Koopman-inspired methods that are most relevant to this work; however, this list is by no means exhaustive and research in this area is developing at a phenomenal rate. Recent and comprehensive reviews can be found here [80–82].

3.1 The singular value decomposition and proper orthogonal decomposition

As a precursor to the rest of the chapter, we will first formally introduce the singular value decomposition (SVD) as it will be used extensively throughout the methods described later.

The SVD is a matrix factorisation method that can be thought of as a generalisation of the eigenvalue decomposition to rectangular matrices. Given a matrix $\mathbf{X} \in \mathbb{R}^{n \times m}$, the SVD produces three matrices

$$\mathbf{X} = \mathbf{U}\mathbf{S}\mathbf{V}^T \tag{3.1}$$

with dimensions $\mathbf{U} \in \mathbb{R}^{n \times n}$, $\mathbf{S} \in \mathbb{R}^{n \times m}$, $\mathbf{V} \in \mathbb{R}^{m \times m}$, and using T to denote the matrix transpose. \mathbf{S} is a rectangular diagonal matrix where all of its entries are non-negative and its entries are the ‘singular values’ of \mathbf{X} . \mathbf{U} and \mathbf{V} are orthogonal matrices whose columns are the left and right ‘singular vectors’ of \mathbf{X} , respectively. Since the dimensions of the left and right singular vectors are different, they represent different bases: the columns of \mathbf{V}^T span the domain m , while the columns of \mathbf{U} span the range n .

If $n \neq m$, a ‘compact’ or ‘economy’ version of the SVD can be created by removing all rows and columns in \mathbf{U} and \mathbf{V} associated with the zero rows in \mathbf{S} , as illustrated in Fig. 3.1. The matrices are typically written so that the singular values are in descending order, ensuring that

the SVD is unique up to sign changes in \mathbf{U} and \mathbf{V} .

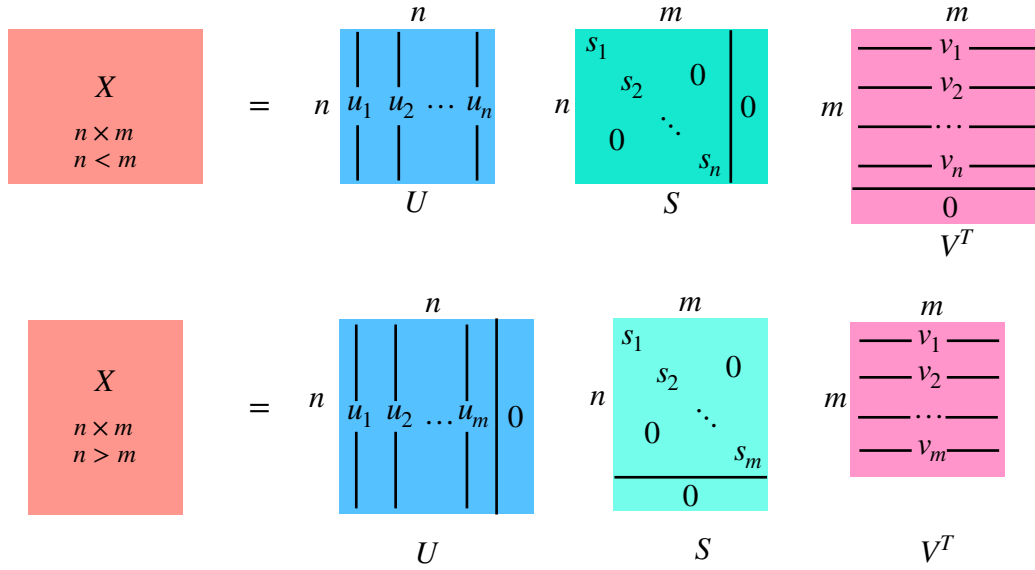


Figure 3.1: The SVD applied to (top row) a matrix with more columns than rows, and (bottom row) a matrix with more rows than columns. The rows and columns filled with zeros can be removed to produce the ‘compact’ SVD.

The rank of \mathbf{X} , R , will be at most $\min(n, m)$. If $R < \min(n, m)$, entries after the first R diagonal entries in \mathbf{S} will be zero, or at least close to zero when accounting for numerical precision. \mathbf{X} can then be reconstructed using the first R columns of \mathbf{U} , rows of \mathbf{V} , and diagonal entries of \mathbf{S} ,

$$\mathbf{X} = \sum_{i=1}^R s_i \mathbf{u}_i \mathbf{v}_i^T. \quad (3.2)$$

According to the Eckart-Young-Mirsky theorem [83], truncating the SVD to $r < R$ will produce the best possible rank- r approximation of \mathbf{X} with respect to the Frobenius norm

$$\|\mathbf{X}\|_F = \sqrt{\sum_{j=1}^m \sum_{i=1}^n x_{ij}^2}. \quad (3.3)$$

The SVD is fundamental for computing the proper orthogonal decomposition (POD) of a data

set. POD was first coined for applications within fluid dynamics by Lumley [84], however POD or very minor variants to it are also known as Principal Component Analysis (PCA), the Hotelling transform, the Karhunen–Loeve transform, quasi-harmonic modes, and empirical component analysis, across different fields of research [85]. Within rheology, POD has been applied to data from an Oldroyd-B fluid simulated within in a four-roll mill to interpret its transitions to different dynamics [86, 87].

The steps for carrying out POD are as follows: we first assume that we have captured data snapshots of a state \underline{x} , for example the velocity of a fluid, at n locations in space and at m regular intervals in time. The data from each snapshot can be formed into a column, so that we end up with an $\mathbf{X} \in \mathbb{R}^{n \times m}$ matrix of snapshots

$$\mathbf{X} = \begin{bmatrix} | & | & & | \\ \mathbf{x}_1 & \mathbf{x}_2 & \dots & \mathbf{x}_m \\ | & | & & | \end{bmatrix}. \quad (3.4)$$

The temporal mean is also removed from each column of \mathbf{X} . We may then compute the SVD, truncated to r , as described earlier. The first r columns from the left singular matrix \mathbf{U} are the POD modes of \mathbf{X} . They can be used to perform a Galerkin-type projection, which optimally [88] projects the data \mathbf{X} onto the reduced subspace spanned by \mathbf{U} such that

$$\sum_{i=1}^r \|\mathbf{u}_i \mathbf{u}_i^T \mathbf{x}_i - \mathbf{x}_i\|_2^2 \quad (3.5)$$

is minimised [89], where the norm here is the standard L_2 -norm. The accuracy of the truncation increases monotonically as r is increased. If the data contains incoherent noise, it will typically appear in the higher modes which are usually truncated, and as such POD is often used as a denoising tool and for data compression. POD was developed with data that has high spatial dimension but low temporal dimension in mind, $n \gg m$. The ‘method of snapshots’ [90] approach to POD circumvents computing the potentially costly application of the SVD to an $n \times m$ matrix by instead computing the eigendecomposition of $\mathbf{X}^T \mathbf{X} \in \mathbb{R}^{m \times m}$,

$$\mathbf{X}^T \mathbf{X} \boldsymbol{\phi}_i = \lambda_i \boldsymbol{\phi}_i, \quad i = 1, 2, \dots, m. \quad (3.6)$$

The same POD results as before can then be found with a simple linear transformation

$$\mathbf{u}_i = \frac{1}{\lambda_i} \mathbf{X}^T \mathbf{X} \boldsymbol{\phi}_i, \quad i = 1, 2, \dots, r. \quad (3.7)$$

If \underline{x} describes a velocity field, the magnitude of each λ_i will represent the amount of kinetic energy represented by each mode [80]. This may not always be beneficial, however, as important dynamical features in the flow are not necessarily those corresponding to the highest kinetic energy [81].

3.2 Dynamic Mode Decomposition

The SVD and POD can be used to identify underlying features on ‘static’ data sets, such as identifying the main features of an image from its pixels, without issue, but cannot also incorporate features that change over time, such as how a feature changes across time in a video clip. In other words, the matrix \mathbf{X} will have the same POD modes even if the columns \mathbf{x}_i are shuffled. Various extensions to POD exist which aim to resolve this issue, but either require computing adjoint equations [91, 92], which may not be feasible with experimental data, or are restricted to statistically stationary data sets [93].

In contrast, the Dynamic Mode Decomposition (DMD) was developed to identify dynamics of autonomous systems that vary over both space and time - it can be thought of as an ideal combination of both POD for interpreting the spatial domain and the Fourier transform for interpreting the temporal domain [94].

Since its introduction within the fluids community in 2008 [95] and subsequent paper in 2010 [15], DMD has been applied to a wide array of problems where complex spatiotemporal data is present, such as modelling the spread of infectious diseases [18] and the development

of algorithmic trading strategies [19]. A similar method in molecular dynamics, named ‘time-lagged independent component analysis’ (TICA), has also been independently developed for recognising the slow time scales in molecular dynamics simulations [96].

While the initial method for computing the DMD involved constructing a companion matrix of the data [81], a subsequent alternative method which utilises the SVD instead has been accepted as the standard approach, called the ‘method of snapshots’ [90]. This version has also been shown as more well-conditioned [15] than when using the companion matrix approach.

Consider data snapshots of a state $\mathbf{x}_i \in \mathbb{R}^{n \times 1}$ have been taken, $i = 1, 2, \dots, m$, which do not necessarily need to come from the same experiment [81]. We consider pairs of these snapshots $(\mathbf{x}_i, \mathbf{x}_{i+1})$ recorded at a time interval Δt apart and assume the relationship between them is approximately linear,

$$\mathbf{x}_{i+1} = \mathbf{A}\mathbf{x}_i, \quad i = 1, \dots, m-1, \quad (3.8)$$

where \mathbf{A} is a linear operator. We use the snapshots \mathbf{x}_i to form two $n \times m-1$ matrices

$$\mathbf{X} = \begin{bmatrix} | & | & & | \\ \mathbf{x}_1 & \mathbf{x}_2 & \dots & \mathbf{x}_{m-1} \\ | & | & & | \end{bmatrix}, \quad \mathbf{X}' = \begin{bmatrix} | & | & & | \\ \mathbf{x}_2 & \mathbf{x}_3 & \dots & \mathbf{x}_m \\ | & | & & | \end{bmatrix}, \quad (3.9)$$

such that Eq. 3.8 can then be rewritten in matrix form as

$$\mathbf{X}' = \mathbf{A}\mathbf{X}. \quad (3.10)$$

where $\mathbf{A} \in \mathbb{R}^{n \times n}$. We then take the SVD of \mathbf{X} as before, $\mathbf{X} = \mathbf{U}\mathbf{S}\mathbf{V}^T$. If the spatial dimension of the data n is large, we can approximate \mathbf{X} as described in Section 3.1 such that $\mathbf{X} \approx \hat{\mathbf{U}}\hat{\mathbf{S}}\hat{\mathbf{V}}^T$ where each matrix is truncated to produce a rank r approximation of \mathbf{X} . The number of truncated modes r is chosen as described in Section 3.1. An existing modification to the

method includes adding an \mathcal{L}_1 restriction so that a smaller number of modes are identified in the first place [97], although these new modes may not be dynamically optimal. It is also important to check that the energy content of the data set is not represented by so few modes that one mode can end up representing multiple frequencies [98], as this has implications on the ability of the method to represent data over long time scales. If the spatial dimension of \mathbf{X} is large, an initial projection step can be carried out on \mathbf{X} by using $\hat{\mathbf{U}}$. Taking advantage of the fact that the columns of $\hat{\mathbf{U}}$ are orthogonal,

$$\hat{\mathbf{U}}^T \mathbf{X}' = (\hat{\mathbf{U}}^T \mathbf{A} \hat{\mathbf{U}}) \hat{\mathbf{U}}^T \mathbf{X} \quad (3.11a)$$

$$\longrightarrow \hat{\mathbf{X}}' = \hat{\mathbf{A}} \hat{\mathbf{X}}, \quad (3.11b)$$

where $\hat{\mathbf{X}}, \hat{\mathbf{X}}' \in \mathbb{R}^{r \times m-1}$ and $\hat{\mathbf{A}} \in \mathbb{R}^{r \times r}$. If the initial projection step is not applied, then an $n \times n$ approximation of \mathbf{A} can be found by computing

$$\tilde{\mathbf{A}} = \mathbf{X}' \hat{\mathbf{V}} \hat{\mathbf{S}}^{-1} \hat{\mathbf{U}}^T. \quad (3.12)$$

If the projection from Eq. 3.11 has been applied, instead we have

$$\tilde{\mathbf{A}} = \hat{\mathbf{U}}^T \mathbf{X}' \hat{\mathbf{V}} \hat{\mathbf{S}}^{-1} \hat{\mathbf{U}}^T \hat{\mathbf{U}} \quad (3.13)$$

which produces an $r \times r$ approximation for \mathbf{A} instead. The eigendecomposition of $\tilde{\mathbf{A}}$,

$$\tilde{\mathbf{A}} \tilde{\mathbf{v}}_j = \mu_j \tilde{\mathbf{v}}_j, \quad (3.14)$$

has eigenvalues μ_j which are the same as the eigenvalues of \mathbf{A} , while the DMD modes

$$\mathbf{v}_j = \frac{1}{\mu_j} \mathbf{X}' \mathbf{V} \mathbf{S}^{-1} \tilde{\mathbf{v}}_j, \quad (3.15)$$

are the eigenvectors of \mathbf{A} [89]. We have been therefore able to find both the eigenvalues and DMD modes of \mathbf{A} without having to construct the (potentially very large) \mathbf{A} explicitly. Each DMD mode has a single characteristic frequency of oscillation and growth/decay rate [99]. While discrete Fourier transform (DFT) based decompositions of the data will produce frequencies of a fixed magnitude, the growth/decay rate allows for modes to converge or diverge over time [94].

DMD normally requires data collected at twice the rate of any frequency of interest - in other words, it must obey the Nyquist-Shannon sampling theorem analogously to the DFT [81]. It is possible to overcome this restriction with compressed sensing techniques where measurements of the data are taken at random rather than at regular intervals [100]. Furthermore, while either an integer number of oscillatory periods must be supplied to a DFT or an additional windowing step must be used on the data to prevent spectral leakage, DMD can identify frequencies when only part of an oscillatory period is present [94].

If noise is present in the data then it may prove difficult to neatly separate frequencies containing dynamically important information and frequencies containing purely noise. Fortunately, the effects of noise on the accuracy of DMD have been well investigated. Duke *et al.* [101] investigated the effects of different noise types when applying DMD to synthetic wave forms and found that the most sensitive parameters are the signal-to-noise ratio and if the data contained sawtooth or square waveforms. Later, Pan *et al.* [102] focused on the effect of noise on identifying instabilities generated over time and found that noise can affect the identification of sub-structures with lower energetic dominance than the primary structure. When using regular DMD, computing the phase average of data sets will improve performance more than concatenating noisy data from multiple experiments [103]. A battery of modifications to DMD have also been proposed which aim to correct for noise issues [103–106]. Further analysis on noisy data in identifying the constitutive law parameters can be found in Section 5.6.

3.3 DMD with Control

For all of the data where we will be looking to use Koopman-based decomposition, the system will have an applied external force given by the rheometer deforming the fluid. DMD is designed for autonomous systems, and there are negative impacts to the system analysis if the effects of external control to the system are not taken into account [86]. The natural linear extension to DMD which accounts for external control is DMD with control, abbreviated to DMDc [107].

In addition to assuming a linear relationship between data \mathbf{X} and \mathbf{X}' , we assume that we also have l measurements of some control input at each time step that can similarly used to construct a matrix \mathbf{Y} ,

$$\mathbf{X}' = \begin{bmatrix} | & | & & | \\ \mathbf{x}_2 & \mathbf{x}_3 & \dots & \mathbf{x}_m \\ | & | & & | \end{bmatrix}, \quad \mathbf{X} = \begin{bmatrix} | & | & & | \\ \mathbf{x}_1 & \mathbf{x}_2 & \dots & \mathbf{x}_{m-1} \\ | & | & & | \end{bmatrix}, \quad \mathbf{Y} = \begin{bmatrix} | & | & & | \\ \mathbf{y}_1 & \mathbf{y}_2 & \dots & \mathbf{y}_{m-1} \\ | & | & & | \end{bmatrix}. \quad (3.16)$$

The new assumed relationship between the data snapshots is

$$\mathbf{X}' = \mathbf{A}\mathbf{X} + \mathbf{B}\mathbf{Y}. \quad (3.17)$$

where we now have an additional linear operator $\mathbf{B} \in \mathbb{R}^{n \times l}$. The two terms on the right-hand side can be combined to form larger matrices $\mathbf{G} = [\mathbf{A} \mathbf{B}] \in \mathbb{R}^{n \times n+l}$ and $\mathbf{\Phi} = [\mathbf{X}^T \mathbf{Y}^T]^T \in \mathbb{R}^{n+l \times m-1}$. The relationship between them is then

$$\mathbf{X}' = \mathbf{G}\mathbf{\Phi}. \quad (3.18)$$

Taking the SVD of $\mathbf{\Phi}$, $\mathbf{\Phi} = \mathbf{U}\mathbf{S}\mathbf{V}^T$, and truncating it to some number of modes $p \leq n + l$, we can either compute or approximate \mathbf{G} via

$$\mathbf{G} = \mathbf{X}'\mathbf{V}\mathbf{S}^{-1}\mathbf{U}^T. \quad (3.19)$$

It is now possible to directly retrieve approximations for \mathbf{A} and \mathbf{B} by computing Eq. 3.19 using just the first n rows of \mathbf{U} , defined as \mathbf{U}_1 or just the last l rows of \mathbf{U} , defined as \mathbf{U}_2 , respectively. However, as described in Section 3.2, the dimensions of these matrices are based on the number of spatial measurements taken per time step and may be prohibitively large. Reducing the dimensions of these matrices further will ideally also make the underlying dynamics more clear. In Section 3.2 we used the left singular vectors of the input data for this purpose, but we cannot do this here as the dimensions of the input and output space are not the same. Instead, a second SVD is performed on the output space data, $\mathbf{X}' = \hat{\mathbf{U}}\hat{\mathbf{S}}\hat{\mathbf{V}}^T$, with some truncation $r < p$. The new, reduced-order approximations for the coefficient matrices are

$$\mathbf{A} \approx \tilde{\mathbf{A}} = \hat{\mathbf{U}}^T \mathbf{X}'\mathbf{V}\mathbf{S}^{-1}\mathbf{U}_1^T \hat{\mathbf{U}} \in \mathbb{R}^{r \times r} \quad (3.20a)$$

$$\mathbf{B} \approx \tilde{\mathbf{B}} = \hat{\mathbf{U}}^T \mathbf{X}'\mathbf{V}\mathbf{S}^{-1}\mathbf{U}_2^T \in \mathbb{R}^{r \times l}. \quad (3.20b)$$

The eigendecomposition of \mathbf{A} can then be computed similarly to before,

$$\tilde{\mathbf{A}}\tilde{\mathbf{v}}_j = \mu_j\tilde{\mathbf{v}}_j \quad (3.21a)$$

$$\mathbf{v}_j = \frac{1}{\mu_j} \mathbf{X}'\mathbf{V}\mathbf{S}^{-1}\tilde{\mathbf{v}}_j, \quad (3.21b)$$

which can then be used to analyse the stability of the system. This is where the original description of the DMDc method concludes [107], but it is worth reiterating that the dimensions of the final approximations of the coefficient matrices are $r \times r$ for $\tilde{\mathbf{A}}$ and $r \times l$ for $\tilde{\mathbf{B}}$ - that is, the number of columns in $\tilde{\mathbf{B}}$ is still dependent on the spatial dimension of the measurement data. An additional SVD could be applied to \mathbf{Y} to remove this dependency, with the added

complication that the control data may then exist in a different subspace to the dynamics data. We will investigate this proposed additional step in later chapters.

3.4 Koopman decomposition

Both DMD and DMDC are meant to represent the data of linear dynamical systems and are often used as linear approximations to nonlinear systems. In fact, they both have roots in Koopman operator theory, initially introduced in 1931 for analysing Hamiltonian flows [13], which can alternatively be thought of as a generalisation of the eigenvalue/eigenvector decomposition to nonlinear systems [81]. We describe the Koopman decomposition method from this operator theoretic framework below.

We define a discrete, nonlinear dynamical system

$$\mathbf{x}_{t+1} = f(\mathbf{x}_t), \quad (3.22)$$

where $\mathbf{x}_k \in \mathcal{M}$, \mathcal{M} is a smooth manifold and $f : \mathcal{M} \rightarrow \mathcal{M}$. We also define a set of scalar-valued functions $\mathbf{g} : \mathcal{M} \rightarrow \mathbb{R}$ known as ‘observables’ [80]. The observables are functions applied to measurements from the state space of the system - for example, if \mathbf{x} were to describe the entire flow field during an experiment, \mathbf{g} could be polynomial functions of the velocity field, or the first normal stress difference, or radial basis functions applied to the same. The Koopman operator U is a linear operator that maps \mathbf{g} to a new function $U\mathbf{g}$ such that [108]

$$U\mathbf{g}(\mathbf{x}) = \mathbf{g}(f(\mathbf{x})). \quad (3.23)$$

Comparing Eqs. 3.22 and 3.23, we can see that U has described the evolution of the observables from one time point to the next, while the original function f did the same for \mathbf{x} . U is linear but the data itself is from a nonlinear dynamical system. The downside is that the initial

system existed on a finite-dimensional manifold \mathcal{M} , whereas our linear operator U is infinite-dimensional.

More formally, the Koopman operator, also known as the composition operator, is the left-adjoint to the Perron-Frobenius operator, which describes the evolution of densities [109]:

$$\langle Pf, g \rangle = \langle g, Ug \rangle, \quad (3.24)$$

with respect to the standard duality pairing $\langle \cdot, \cdot \rangle$, defined by $\langle f, g \rangle = \int_{\mathbb{X}} f(x)g(x)dx$, and where P is the Perron-Frobenius (push-forward) operator applied to the density f [110]. It has been shown how both operators can be treated within the same formalism, although this is beyond the scope of this thesis [82].

Since U is linear, we can compute its eigendecomposition

$$U\varphi_j(\mathbf{x}) = \lambda_j\varphi_j(\mathbf{x}), \quad j = 1, 2, \dots \infty. \quad (3.25)$$

Each of the observables \mathbf{g} can be expanded in terms of the eigenvalues and eigenvectors of U ,

$$\mathbf{g}(\mathbf{x}) = \sum_{j=1}^{\infty} \varphi_j \mathbf{v}_j, \quad (3.26)$$

where \mathbf{v}_j are the ‘Koopman modes’, or ‘dynamic modes’ [94] of the mapping f , provided that all of the observables lie in the span of φ_j . If this is the case, in other words Eq. 3.22 is conservative, then the Koopman modes can be computed using the standard inner product as

$$\mathbf{v}_j = \begin{bmatrix} \langle \varphi_j, g_1 \rangle \\ \langle \varphi_j, g_2 \rangle \\ \vdots \\ \langle \varphi_j, g_K \rangle \end{bmatrix} \quad (3.27)$$

where K is the total number of observables [82]. We may then write the observables as [20, 108]

$$U\mathbf{g}(\mathbf{x}) = \mathbf{g}(f(\mathbf{x})) = \sum_{j=1}^{\infty} \lambda_j \varphi_j(\mathbf{x}_k) \mathbf{v}_j. \quad (3.28)$$

This is the Koopman mode decomposition first introduced in 2005 [111], which describes an infinite-dimensional operator. A finite-dimensional representation of the Koopman operator is possible provided that U is restricted to an *invariant subspace*, in other words a subspace that is spanned by any set of the eigenfunctions of U [112, 113]. Using this technique, a nonlinear system identification problem in state space can be reframed as the identification of the linear Koopman operator in the space of the observables we have chosen [114].

If the underlying system is linear and the observable is restricted to the set of direct measurements of the system, $\mathbf{g}(\mathbf{x}) = \mathbf{x}$, then the $\varphi(\mathbf{x})$ are constant so can be incorporated with the Koopman modes and we may rewrite Eq. 3.22 as Eq. 3.10 [108]. The correspondence between DMD and the Koopman operator then becomes clear - the Koopman modes are the eigenvectors of \mathbf{A} . If the underlying equations are in fact nonlinear, then the observables generally will not span a Koopman-invariant subspace of the system, which means it may fail to pick up on nonlinear features of the system [115].

3.5 Koopman with inputs and control

DMD is able to compute, or at least approximate, the Koopman operator when the observables are constrained to linear functions of the state [108]. This can be too restrictive when trying to understand the dynamics of a nonlinear system and the Koopman decomposition may not be able to recreate the dynamics well. Recent work has looked at how the set of observable functions \mathbf{g} , sometimes referred to as a ‘dictionary’ when applied to data [116], can be augmented to include nonlinear observables also.

The extended DMD (or ‘eDMD’) [117] method is the nonlinear counterpart to DMD: the dictionary can now also contain nonlinear observables but is still restricted for use on autonomous

systems. Suggested choices for the observables include polynomials, Fourier modes, radial basis functions, and spectral elements. A subsequent paper from the same authors suggests a kernel trick [118] to reduce the computational cost of the SVD step on large dictionaries. Sparse regression techniques can also be employed to reduce the size of dictionary if some of the entries appear to be superfluous [119]. It is also possible to use stochastic gradient descent, a foundational technique from machine learning, to ‘learn’ the right dictionary [119], which also allows online updates to the dictionary for large and streaming data sets, or to ‘train’ the correct dictionary using an artificial neural network [120].

Analogous to how eDMD is a nonlinear extension to DMD, Koopman with Inputs and Control (KIC) is the nonlinear extension to DMDc [20]. A direct extension to eDMD for non-autonomous systems, eDMDc, does not allow for observables that are nonlinear in \mathbf{u} [121]. The KIC and EDMD methods are also both closely related to the variational approach of conformation dynamics (VAC) method [96] developed independently for analysing molecular dynamics.

For KIC, we define a Koopman operator on the observables $g(\mathbf{x}, \mathbf{u})$ rather than simply $g(\mathbf{x})$, but which still evolves only the state \mathbf{x} . The new Koopman operator will have eigenfunctions that depend on both \mathbf{x} and \mathbf{u} . For our scenario, we consider a discrete nonlinear dynamical system which depends on both the state \mathbf{x} and the inputs \mathbf{u} ,

$$\mathbf{x}_{t+1} = f(\mathbf{x}_t, \mathbf{u}_t) \tag{3.29}$$

where $\mathbf{x} \in \mathcal{M}$ as before, $\mathbf{u} \in \mathcal{N}$, and the set of observables \mathbf{g} are functions of both the state space and the input space, $\mathbf{g} : \mathcal{M} \times \mathcal{N} \rightarrow \mathbb{R}$. For the constitutive laws we are considering in this thesis, we know the control input \mathbf{u} exactly - it is the deformation applied by the rheometer. We therefore do not need to make predictions for \mathbf{u} or approximate its evolution over time as we do with \mathbf{x} , which somewhat simplifies the application of the KIC method. Similarly to Eq. 3.23, the KIC operator \mathcal{K} for our case can be defined as

$$\mathcal{K}\mathbf{g}(\mathbf{x}_t, \mathbf{u}_t) = \mathbf{g}(f(\mathbf{x}_t, \mathbf{u}_t), \mathbf{u}_{t+1}). \quad (3.30)$$

Here, the ‘ \mathbf{u}_{t+1} ’ signifies that the dynamics of \mathbf{u} are known and do not need to be predicted also - otherwise, we would need to utilise \mathbf{u}_t instead. The set of observables \mathbf{g} can be separated into functions just of \mathbf{x} , functions just of \mathbf{u} , and mixed functions. If only linear observables of the state and input are chosen and consequently there are no mixed functions, then KIC reduces to DMDC as described in Section 3.3.

The input space and output space of the system no longer have the same dimension - the right-hand side contains all of our observables, while our left-hand side only contains the measurements for which we want to understand the evolution. In contrast to Eq. 3.25 for the regular Koopman operator U , we can write the relationship between the input and output spaces of the KIC operator \mathcal{K} as

$$\mathcal{K}\varphi_j(\mathbf{x}, \mathbf{u}) = \lambda_j \phi_j(\mathbf{x}, \mathbf{u}), \quad j = 1, 2, \dots \infty. \quad (3.31)$$

Here, φ_j spans the full set of observables while ϕ_j only spans the observables that we wish to evolve [20]. The different input and output spaces allows for us to separate the effects of different observables on the evolution of the data, in the same way that DMDC allows for separation of the state space and the control space, but now with the ability to include nonlinear observables and mixed observables. The eDMDC method requires the input and output space to be the same [122], which causes issues on closing the system of equations if the dynamics are nonlinear [99, 123].

3.6 Choice of observables

Choosing a universally correct set of nonlinear observables for the Koopman mode decomposition is an open challenge. The correct dictionary will transform the data such that the

relationship between the input and output to the system can be represented by a linear operator. In practice, the set of observables is selected based on known information about the underlying system. It is also necessary to consider the complexity of the final model with respect to potential overfitting of the data, and taking into consideration the computational resources available for testing sets containing large numbers of observables.

An approach that is rapidly being developed for system identification while taking the issue of locating the correct observables into account is the Sparse Identification of Nonlinear Dynamics (SINDy) technique [124]. Given data regarding a state, \mathbf{X} and its time derivative $\dot{\mathbf{X}}$, SINDy finds the terms and coefficients of the underlying ODE for a given data set by solving

$$\dot{\mathbf{X}} = \Phi(\mathbf{X})\Xi \quad (3.32)$$

where $\Phi(\mathbf{X})$ is the library of candidate observables and Ξ is the corresponding vector of coefficients. A standard regression technique could then be applied to compute Ξ , but a library of K observables would require $2^K - 1$ regressions if every combination were to be tested. However, the key assumption behind this approach is that the underlying ODE contains only a few terms, causing Ξ to be sparse. Eq. 3.32 can therefore be solved using sparse regression techniques such as LASSO or the sequentially-thresholded least squares method to drastically improve the computational speed. When using a SINDy-type approach, it is necessary that the time derivative for the data, $\dot{\mathbf{X}}$, to be available, and if not it must be found using automatic differentiation techniques [125]. Placing the time derivative explicitly on the left-hand side of the equation additionally causes the input-output relationship between the two sides of the equation to be lost, which is necessary for Koopman analysis.

There has been a huge number of extensions to the original SINDy method, the most relevant for us being SINDyC, which incorporates control inputs in accordance with the DMDc extension to DMD [126]. Other notable modifications include incorporating uncertainty quantification [127], evaluating the results using information criteria [128, 129], detecting abrupt system changes [130], and extending the technique for identifying PDEs [131]. We certainly do

not rule out the potential for SINDy to be successfully employed for analysing rheological data in the future.

SINDy-type techniques overcome the issue of locating the correct observables by beginning with an oversized library of candidates, and then iteratively pruning any entries whose coefficients are smaller than a prescribed tolerance. The initial library however still needs to be chosen. In our case, by restricting ourselves to fluids represented under existing, well-researched frameworks of constitutive laws, we have a great deal of knowledge regarding the nonlinear observables we expect to be present in the underlying equation. By assuming that the constitutive law for the viscoelastic fluid in question exists within a larger framework of constitutive laws, we may use the set of all terms in the framework as our library of candidate observables.

We will use the GNMM framework initially introduced in Section 2.3 as the foundation for our library of observables. Assuming a time-dependent shear rate, the components of the tensors in the GNMM are

$$\underline{\dot{\gamma}} = \begin{bmatrix} 0 & 0 \\ \partial_y u_x & 0 \end{bmatrix} = \begin{bmatrix} 0 & 0 \\ \dot{\gamma} & 0 \end{bmatrix}, \quad \underline{\omega} = \begin{bmatrix} 0 & \dot{\gamma} \\ -\dot{\gamma} & 0 \end{bmatrix}, \quad \underline{\sigma} = \begin{bmatrix} \sigma_{xx} & \sigma_{xy} \\ \sigma_{xy} & \sigma_{yy} \end{bmatrix}. \quad (3.33)$$

The full GNMM equations written component-wise for the evolution of σ_{xx} , σ_{xy} , and σ_{yy} can be found in Appendix A. The most noteworthy points from writing Eq. 2.13 in this way are:

1. Every combination of $\dot{\gamma}$ and the components of $\underline{\sigma}$ up to cubic order are included, with the exception of $\dot{\gamma}\sigma_{xx}\sigma_{yy}$. There is also a time derivative of the strain rate, $\ddot{\gamma}$.
2. The terms found in the equation for σ_{xy} , and the terms found in the equation for σ_{xx} and σ_{yy} , form disjoint sets.

The terms present in each of the equations for the elements of $\underline{\sigma}$ are shown in Table 3.1. Using the GNMM framework as our set of observables thus produces a restricted library of 33 polynomial basis functions up to cubic order, with disjoint subsets of this library for the diagonal and off-diagonal components of the stress tensor. For example, when only the data

for σ_{xy} is available, Table 3.1 shows that 7 observables are required rather than 10, as none of the quadratic combinations of $\dot{\gamma}$ and σ_{xy} are found within the σ_{xy} equation.

	σ_{xx}	σ_{xy}	σ_{yy}	$\dot{\gamma}$
σ_{xx}	X	-	X	-
σ_{xy}	-	X	-	X
σ_{yy}	X	-	X	-

	σ_{xx}^2	σ_{xy}^2	σ_{yy}^2	$\dot{\gamma}^2$	$\sigma_{xx}\sigma_{xy}$	$\sigma_{xx}\sigma_{yy}$	$\sigma_{xy}\sigma_{yy}$	$\dot{\gamma}\sigma_{xx}$	$\dot{\gamma}\sigma_{xy}$	$\dot{\gamma}\sigma_{yy}$
σ_{xx}	X	X	X	X	-	X	-	-	X	-
σ_{xy}	-	-	-	-	X	-	X	X	-	X
σ_{yy}	X	X	X	X	-	X	-	-	X	-

	σ_{xx}^3	σ_{xy}^3	σ_{yy}^3	$\sigma_{xx}^2\sigma_{xy}$	$\sigma_{xx}^2\sigma_{yy}$	$\sigma_{xy}^2\sigma_{xx}$	$\sigma_{xy}^2\sigma_{yy}$	$\sigma_{yy}^2\sigma_{xx}$	$\sigma_{yy}^2\sigma_{xy}$	$\sigma_{xx}\sigma_{xy}\sigma_{yy}$
σ_{xx}	X	-	-	-	-	X	X	X	-	-
σ_{xy}	-	X	-	X	-	-	-	-	X	X
σ_{yy}	-	-	X	-	X	X	X	-	-	-

	$\dot{\gamma}^3$	$\dot{\gamma}^2\sigma_{xx}$	$\dot{\gamma}^2\sigma_{xy}$	$\dot{\gamma}^2\sigma_{yy}$	$\dot{\gamma}\sigma_{xx}^2$	$\dot{\gamma}\sigma_{xy}^2$	$\dot{\gamma}\sigma_{yy}^2$	$\dot{\gamma}\sigma_{xx}\sigma_{xy}$	$\dot{\gamma}\sigma_{xx}\sigma_{yy}$	$\dot{\gamma}\sigma_{xy}\sigma_{yy}$	$\ddot{\gamma}$
σ_{xx}	-	X	-	-	-	-	-	X	-	X	-
σ_{xy}	X	-	X	-	X	X	X	-	-	-	X
σ_{yy}	-	-	-	X	-	-	-	X	-	X	-

Table 3.1: Terms present (marked with ‘x’) and absent (marked with ‘-’) for each of the elements of $\underline{\underline{\sigma}}$ making up the GNMM.

3.7 The rheoKIC method

We will be applying the KIC method, using terms from the GNMM framework as our initial library of candidate observables, to the identification of constitutive laws for viscoelastic fluids.

For brevity, we name this combination of methods and application as ‘rheology using KIC’ or ‘rheoKIC’, but stress that it is not a new technique - it is a specific usage of the KIC method for understanding the constitutive laws of rheological data.

Below we lay out the steps for rheoKIC when the data comprises one measurement of the stress tensor at each time step i.e. there is no spatial variation:

1. *Data collection:* Collect data from one or more sources i.e. simulation or experimental data. Record time-resolved data at $m + 1$ time steps for the force input $\dot{\gamma}$ and elements of the stress tensor. The linearity of the stress response can be confirmed by checking the number of peaks in its frequency spectrum.
2. *Create data matrices:* Build an ‘output’ matrix Σ' , from all of the σ data except for the first entry. Build ‘input’ matrices Σ and $\dot{\Gamma}$ using all entries of the σ and $\dot{\gamma}$ data apart from the last entry. Re-scale each observable so that they have the same magnitude [132].
3. *Create library of observables:* Use the input matrices to compute Φ , a $K \times m$ library of the K candidate observables determined using the GNMM framework. If σ was shown to be linear, set $\Phi = [\sigma, \dot{\gamma}]$. We aim to find the vector of coefficients \mathbf{c} to solve

$$\Sigma' = \mathbf{c}\Phi. \quad (3.34)$$

4. *Compute the SVD of the observables:* Compute the SVD of the library of observables,

$$\Phi = \mathbf{U}\mathbf{S}\mathbf{V}^T \quad (3.35)$$

and check the rank of Φ via the entries in \mathbf{S} . If it is rank-deficient then more data will need to be supplied or the number of observables needs to be reduced. Use data from different experiments, or more instances of the same experiment with different experimental parameters, and check if this increases the rank of Φ . Ideally the data should probe the linear and nonlinear response of the fluid. Repeat this process until Φ is no longer rank-deficient.

5. *Compute observable coefficients:* Use the SVD to find \mathbf{c} :

$$c_k = \mathbf{\Sigma}' \mathbf{V}^T \mathbf{S}^{-1} \mathbf{u}_k \quad (3.36)$$

where c_k is the k^{th} entry of \mathbf{c} and \mathbf{u}_k is the k^{th} column of \mathbf{U} . If any of the coefficients are very small relative to the others, remove the corresponding observable from the library and rerun steps 4 and 5 with the updated library.

6. *Repeat across a range of experiments:* The steps above will typically be carried out on multiple data sets that form part of a parameter sweep - for example, data from a SAOS experiment where the frequency is swept over a range of values. A good indicator that the correct observable and associated coefficient has been found is if the value of the coefficient remains stable across the range of experiments.
7. *Construct the final constitutive law:* Once all observables and coefficients are determined, reconstruct the final equation. Any rescaling of the data should be reverted. The coefficients for all the observables except for σ should be divided by the time step size Δt , while the coefficient for σ (the characteristic relaxation time) is reverted via

$$\tilde{\lambda} = \frac{\Delta t}{1 - k_1}. \quad (3.37)$$

The details of these steps will be developed further across the subsequent chapters as we apply rheoKIC to increasingly challenging data sets. We will further generalise the rheoKIC method to account for data sets with multiple spatial measurements per snapshot in Chapter 7.

Chapter 4: Application to linear constitutive laws

We start by observing how rheoKIC performs on data from a simulation that employs a linear constitutive law, namely the linear Maxwell model. This model is appropriate when the magnitude of the applied force is small enough to not disturb the fluid’s microstructure such that the stress response is in the linear viscoelastic regime. It is beneficial to first check the validity of the rheoKIC method on a linear model as rheoKIC is an extension of the DMDc method that only considers linear observables. As such, when applying rheoKIC to linear data and only providing linear observables, the method reduces to DMDc and simplifies the analysis of the underlying system significantly.

4.1 The linear Maxwell model

One of the simplest viscoelastic constitutive laws is the linear Maxwell model [3]. The single-mode linear Maxwell model, first described in Chapter 2, is given by

$$\frac{\partial \underline{\underline{\sigma}}}{\partial t} = -\frac{1}{\lambda} \underline{\underline{\sigma}}(t) + G \dot{\underline{\underline{\gamma}}}(t), \quad (4.1)$$

where λ is the characteristic relaxation time of the fluid and G is the elastic modulus which dictates the stiffness of the material. Under simple shear with small deformations and no spatial dependence, the linear Maxwell model has the standard time derivative rather than a convected

derivative. The analytic solution for Eq. 4.1 is

$$\underline{\underline{\sigma}}(t) = G \int_{-\infty}^t e^{\frac{t'-t}{\lambda}} \underline{\underline{\dot{\gamma}}}(t') dt'. \quad (4.2)$$

We assume that a small-amplitude oscillatory shear is applied in the x -direction which results in a rate of strain given by

$$\underline{\underline{\dot{\gamma}}} = \begin{bmatrix} 0 & 0 \\ \dot{\gamma} & 0 \end{bmatrix}, \quad (4.3)$$

where

$$\dot{\gamma}(t) = \dot{\gamma}_0 \cos(\omega t) \quad (4.4)$$

and $\dot{\gamma}_0 = \gamma_0 \omega$. With the additional assumption that the fluid is initially at rest, $\underline{\underline{\sigma}}(t=0) = 0$, Eq. 4.1 has a closed-form solution for σ_{xy}

$$\sigma_{xy}(t) = -\frac{G\gamma_0(\omega\lambda)}{1 + (\omega\lambda)^2} e^{-\frac{t}{\lambda}} + \frac{G\gamma_0(\omega\lambda)^2}{1 + (\omega\lambda)^2} \sin(\omega t) + \frac{G\gamma_0(\omega\lambda)}{1 + (\omega\lambda)^2} \cos(\omega t), \quad (4.5)$$

while σ_{xx} and σ_{yy} have trivial solutions. The first term will decay at an exponential rate that is dependent on λ : the shorter the relaxation time, the faster the fluid will respond to the applied deformation and the exponential term will decay more quickly. We will begin to record σ from our oscillatory shear simulations after 10 periods have elapsed to ensure that no transient effects from starting the simulation remain within the data.

If the experiment is run until the first term in Eq. 4.5 can be neglected, it can be rewritten as (dropping subscripts)

$$\sigma(t) = \frac{G\gamma_0(\omega\lambda)^2}{1 + (\omega\lambda)^2} \sin(\omega t) + \frac{G\gamma_0(\omega\lambda)}{1 + (\omega\lambda)^2} \cos(\omega t) = G'(\omega)\gamma(t) + \frac{G''(\omega)}{\omega} \dot{\gamma}(t), \quad (4.6)$$

such that the equations for the material functions $G'(\omega)$ and $G''(\omega)$ are

$$G'(\omega) = \frac{G\gamma_0(\omega\lambda)^2}{1 + (\omega\lambda)^2}, \quad (4.7a)$$

$$G''(\omega) = \frac{G\gamma_0(\omega\lambda)}{1 + (\omega\lambda)^2}. \quad (4.7b)$$

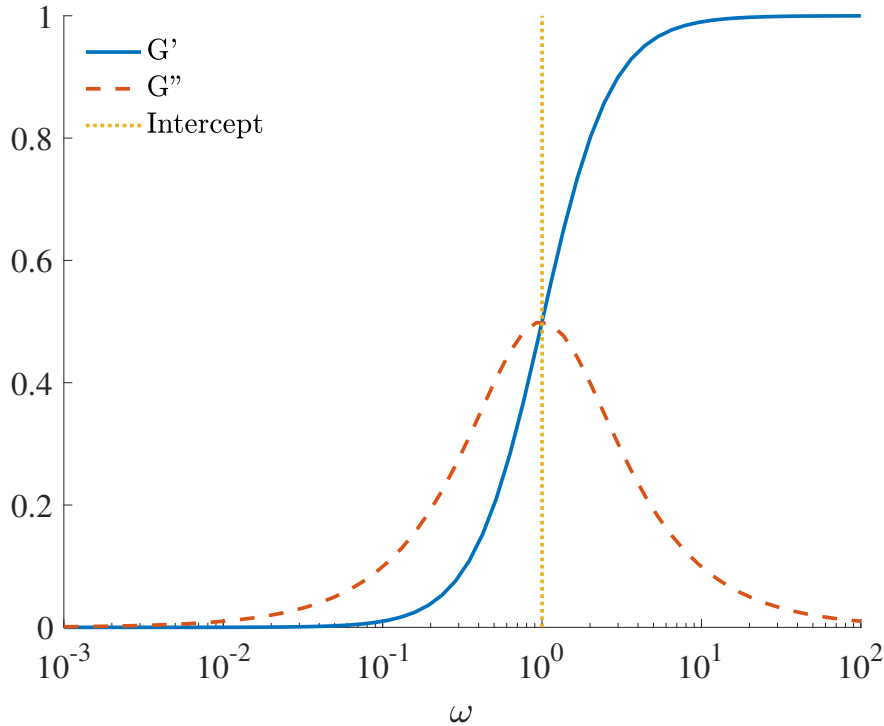


Figure 4.1: Representative data of the type typically produced by an oscillatory rheometer for a Maxwell fluid under small amplitude shear. $G = 1$ can be found as the value of G' for high frequencies, while $\lambda = 1$ can be found as the reciprocal of ω where G' and G'' coincide.

In a standard rheological test, $G'(\omega)$ and $G''(\omega)$ are computed by decomposing σ into sine and cosine signals and finding their respective coefficients. The values for G' and G'' are then plotted over a range of frequencies as exemplified in Fig. 4.1. The loss modulus G'' is small at high frequencies as there are no changes to the material's microstructure if the time scale of the oscillation frequency is significantly faster than the time scale of the fluid [58]. Approximations for the Maxwell equation coefficients can then be extracted from the material parameters: λ as the reciprocal of ω where G' and G'' intersect, and G as the asymptote of G' .

4.2 Errors from time derivative approximation

Using the first-order Euler approximation for the time derivative, Eq. 4.1 can be written in the form suitable for rheoKIC as

$$\sigma_{n+1} = \left(1 - \frac{\Delta t}{\lambda}\right) \sigma_n + \Delta t G \dot{\gamma}_n, \quad (4.8)$$

where the subscript n indicates that this is the data from the the n^{th} snapshot. The approximation for the time derivative will introduce an error of order $O(\Delta t)$. We can see the effects of the error on the results by comparing the coefficients of Eq. 4.8 with those found with the analytic solution to the Maxwell model. For snapshot $n + 1$, we have that

$$\begin{aligned} \sigma_{n+1} &= \frac{G\gamma_0(\omega\lambda)^2}{1 + (\omega\lambda)^2} \sin(\omega n + \omega\Delta t) + \frac{G\gamma_0\omega\lambda}{1 + (\omega\tau)^2} \cos(\omega n + \omega\Delta t) \\ &= \cos(\omega\Delta t) \sigma_n + \left[\frac{G\gamma_0(\omega\lambda)^2}{1 + (\omega\lambda)^2} \sin(\omega\Delta t) \right] \cos(\omega n) + \left[-\frac{G\gamma_0\lambda}{1 + (\omega\lambda)^2} \sin(\omega\Delta t) \right] \sin(\omega n). \end{aligned} \quad (4.9)$$

Rearranging Eq. 4.6 for $\sin(\omega n)$,

$$\sin(\omega n) = \frac{1 + (\omega\lambda)^2}{G\gamma_0(\omega\lambda)^2} \sigma_n - \frac{1}{\gamma_0\omega\lambda} \dot{\gamma}_n. \quad (4.10)$$

Substituting, we retrieve

$$\sigma_{n+1} = [\cos(\omega\Delta t) - \frac{1}{\omega\lambda} \sin(\omega\Delta t)] \sigma_n + \frac{G}{\omega} \sin(\omega\Delta t) \dot{\gamma}_n. \quad (4.11)$$

These are the exact values for the coefficients of σ and $\dot{\gamma}$ when we put the Maxwell model into a form suitable for applying rheoKIC. We can retrieve Eq. 4.8 by approximating $\sin(\omega\Delta t)$ and $\cos(\omega\Delta t)$ by their single-term Taylor expansions. By extending the Taylor expansion to one

more term, we can quantify the error between our equation for computing G and λ versus when the solution for σ is known explicitly:

$$\sigma_{n+1} = \left[1 - \frac{\Delta t}{\tau}\right] \sigma_n + G\Delta t \dot{\gamma}_n + (\omega\Delta t)^2 \left(\left[\frac{1}{6\lambda} \Delta t - \frac{1}{2} \right] \sigma_n - \frac{G\Delta t}{6} \dot{\gamma}_n \right) + O((\omega\Delta t)^4). \quad (4.12)$$

The effect of using approximations of different orders is shown in Fig. 4.2 where the number of time steps per oscillatory period with frequency $\omega = 1$ is varied between 10 and 10010, corresponding to time step sizes between $O(10^{-4})$ and $O(10^0)$.

As expected, larger time step sizes increase the amount of discrepancy between the analytic solution and the Taylor expansions. The most notable effect on the accuracy can be seen on the value of the σ observable coefficient shown in the top figure. For this observable, there is significant deviation for both Taylor approximations when $\Delta t > 10^{-2}$, corresponding to 512 time steps per period. Meanwhile, only the one-term Taylor approximation appears to deviate for time steps sizes as large as 10^{-1} in the case of the $\dot{\gamma}$ observable shown in the lower part of Fig. 4.2.

It is important to balance the number of measurements per period with the oscillatory frequency of the experiment. At high frequencies, measurements will need to be taken at small time intervals in order to see the dynamics of the stress response for each period, but using the same time interval at low frequencies could mean taking a large number of unnecessary measurements. Equally, while we are aware that rheoKIC will work best with the smallest time step size possible, our choice of time step size should also be feasibly achievable when using experimental data. We choose to limit ourselves to a maximum of 512 measurements per oscillatory period as a compromise between these arguments. This corresponds to $\Delta t = 0.0001 - 1.2272$ for the frequency range $\omega = 10^{-2} - 10^2$.

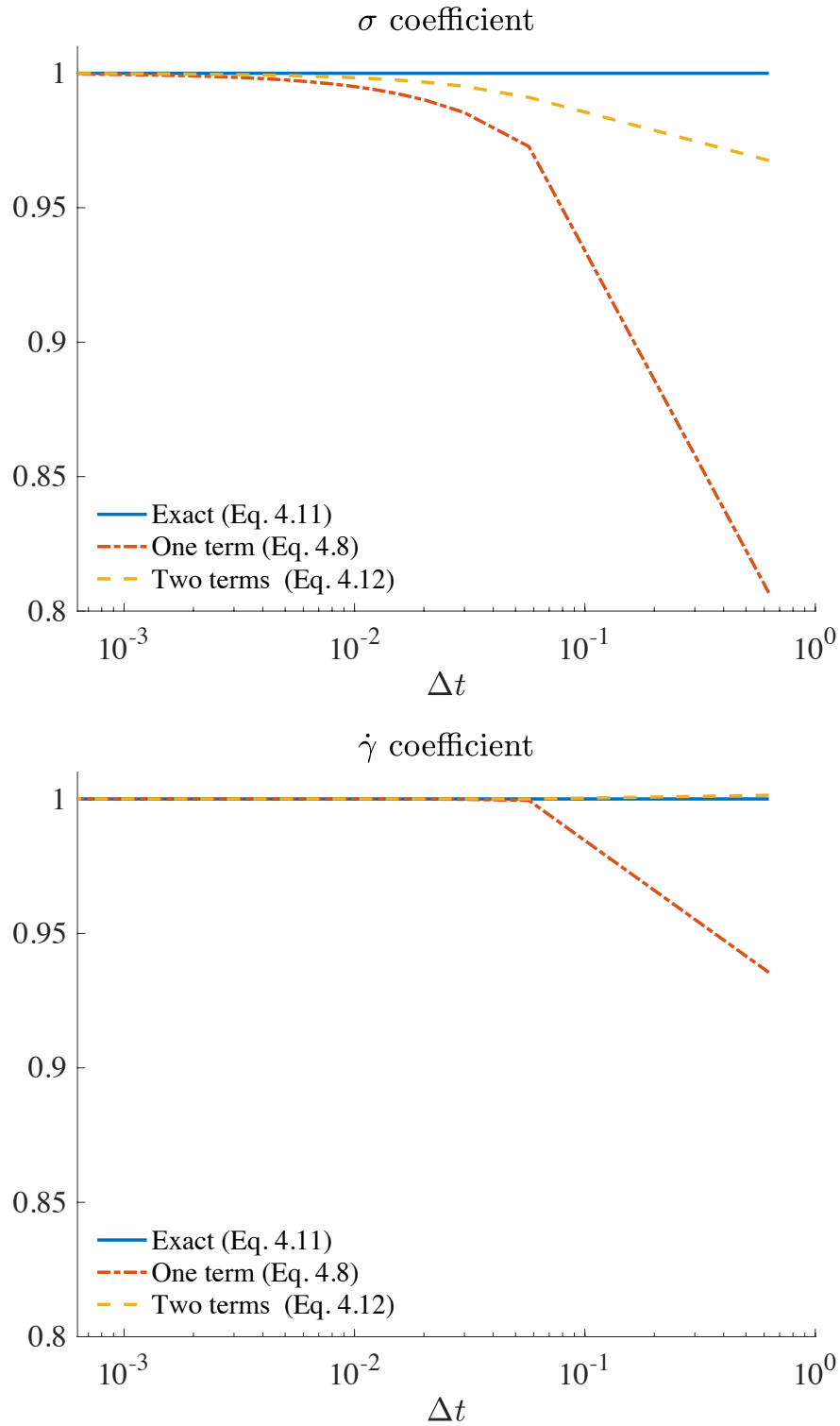


Figure 4.2: Values of the $\Phi = [\sigma, \dot{\gamma}]$ coefficients for the linear Maxwell model. (Solid line) Exact values using Eq. 4.11. (Dashed line) Taylor expansion with one term. (Dot-dashed line) Taylor expansion with two terms. Top: σ coefficient. Bottom: $\dot{\gamma}$ coefficient.

4.3 Reduction of rheoKIC to DMDc

Now that we understand the source of error from the time derivative approximation, we move onto an application of rheoKIC where we use only linear observables instead of the full set of candidate observables. If $\Phi = [\sigma, \dot{\gamma}]$, then not only do we have exactly the observables we need to identify the linear Maxwell model, but Φ also matches the conditions for DMDc as described in Section 3.3. The corresponding coefficients that we are trying to find are therefore

$$\sigma_{t+1} = \left(1 - \frac{\Delta t}{\lambda}\right)\sigma_t + \Delta t G \dot{\gamma}_t = k_1 \sigma_t + k_2 \dot{\gamma}_t. \quad (4.13)$$

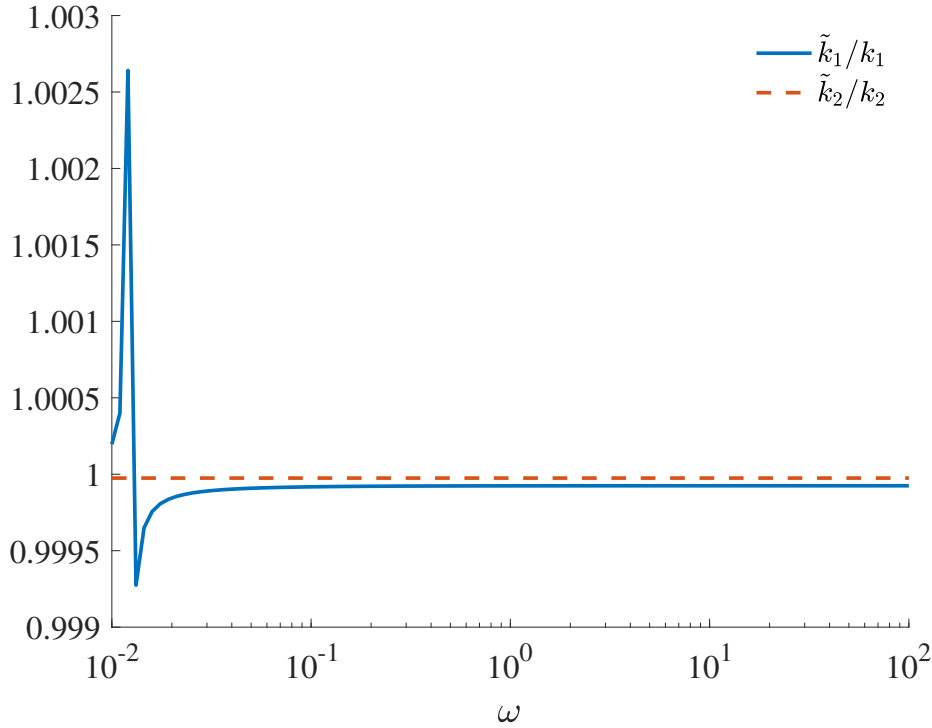


Figure 4.3: Predicted values for the coefficient multiplying each observable $\Phi = [\sigma, \dot{\gamma}]$, normalised k_1 and k_2 respectively. $G = \lambda = \dot{\gamma}_0 = 1$, data taken from one stationary period of data, 512 measurements taken per period.

We run a sweep of simulations where $\dot{\gamma}_0 = 1$ and $\omega = 10^{-2} - 10^2$. Data is recorded for one oscillatory period once the data is stationary. The simulation itself is run for 12800 time steps per period and subsequently down-sampled so that 512 measurements are recorded per period.

The predicted values of k_1 and k_2 , \tilde{k}_1 and \tilde{k}_2 , are shown in Fig. 4.3 where they have been normalised by their true values, k_1 and k_2 respectively.

The values of \tilde{k}_1 and \tilde{k}_2 are highly accurate, with some error at low ω for \tilde{k}_1 due to the larger time step size. However, the coefficients for the observables still have to be converted back to their parameters from the Maxwell model via

$$\tilde{\lambda} = \frac{\Delta t}{1 - k_1}, \quad \tilde{G} = \frac{k_2}{\Delta t}. \quad (4.14)$$

The values for $\tilde{\lambda}$ and \tilde{G} using these transformations are shown in Fig. 4.4. We can see that, while \tilde{k}_1 has high accuracy regardless of ω , $\tilde{\lambda}$ suffers due to the sensitivity of the transformation in Eq. 4.14. The accuracy before the transformation is meanwhile very stable regardless of the time step size.

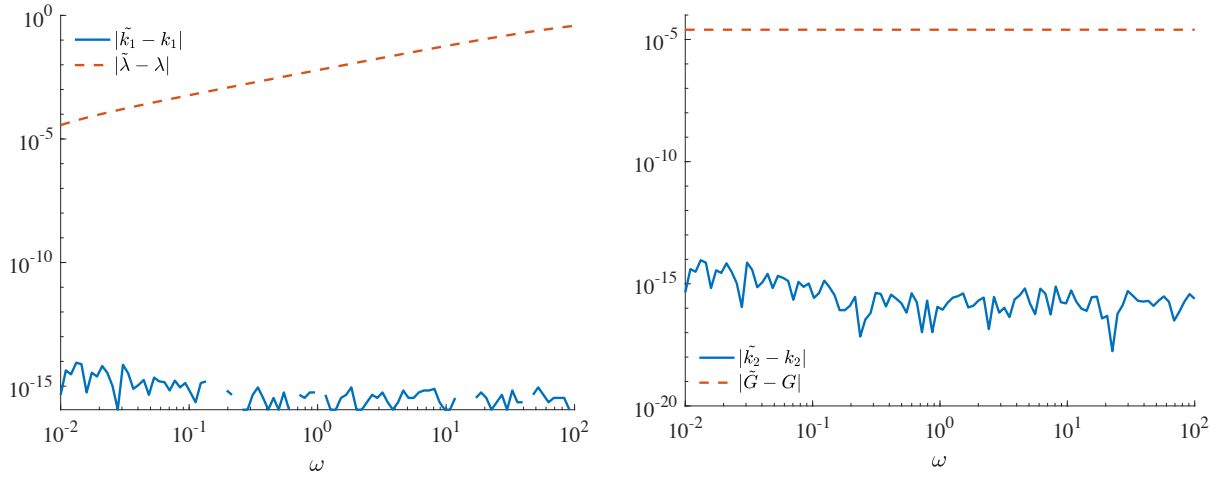


Figure 4.4: The difference between the predicted observable coefficients \tilde{k}_1 and their actual values, alongside the predictions for λ and G compared to their actual values, computed using Eq. 4.14.

Another important consideration concerning the data snapshots is the total simulation length. The results from applying DMDc do not change as we increase the number of oscillatory periods in the simulation. Furthermore, it is possible to retrieve good predictions of the coefficients even

when less than a full oscillatory data set is provided, while Fourier transform-based analysis of oscillatory data requires a full period of data in order to prevent spectral leakage [94]. This is interesting as it means we may be able to pick up features in a data set that are evolving over longer time scales than that of the data set itself, which a Fourier transform approach may miss. However, using shorter data sets of incomplete oscillatory periods may make the results more susceptible to the effects of measurement noise.

4.4 Inclusion of higher-order observables

It is not surprising that we were able to retrieve the linear observables somewhat easily if Φ only contains the linear observables that make up the equation. It should also be clear that only the linear observables are necessary in this regime from looking at the Fourier spectrum of the stress response. Be that as it may, can we show that only the σ and $\dot{\gamma}$ observables are required to reconstruct the constitutive law from data if higher order signals are provided? The full set of candidate observables from the GNMM model that do not include σ_{xx} and σ_{yy} is

$$\Phi = [\sigma, \dot{\gamma}, \sigma^3, \sigma^2\dot{\gamma}, \sigma\dot{\gamma}^2, \dot{\gamma}^3] \quad (4.15)$$

where the subscript for σ_{xy} has been dropped. The fact that the data is linear means that the $\ddot{\gamma}$ observable is automatically redundant. We have $K = 6$ candidate observables, of which we want to pick out only the two linear observables as necessary for modelling the provided simulation data. The full equation can be written as

$$\sigma_{n+1} = \begin{bmatrix} k_1 & k_2 \end{bmatrix} \begin{bmatrix} \sigma \\ \dot{\gamma} \end{bmatrix}_n + \begin{bmatrix} k_3 & k_4 & k_5 & k_6 \end{bmatrix} \begin{bmatrix} \sigma^3 \\ \sigma^2\dot{\gamma} \\ \sigma\dot{\gamma}^2 \\ \dot{\gamma}^3 \end{bmatrix}_n \quad (4.16)$$

where Δt has been absorbed into the k_i coefficients. With this in mind, rheoKIC aims to find the values k_i that minimises

$$\left| \sigma_{n+1} - \sum_{i=1}^K k_i \phi_i \right|_F \quad (4.17)$$

with respect to the Frobenius norm, where ϕ_i , $i = 1, \dots, K$ are the observables in Φ . Once the k_i are computed, all of the k_i aside from k_1 must be divided by Δt , while k_1 is transformed according to Eq. 4.14.

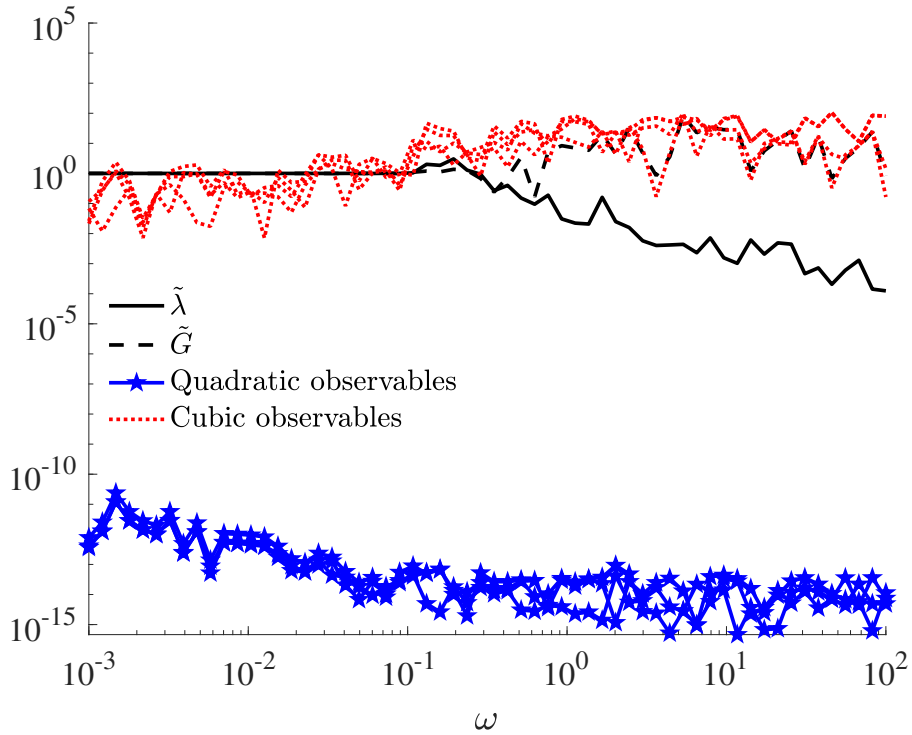


Figure 4.5: rheoKIC applied to data from the linear Maxwell model where $G = \lambda = \gamma_0 = 1$ and Φ is constructed according to Eq. 4.15.

In Fig. 4.5 we have used a Φ which contains every combination of σ_{xy} and $\dot{\gamma}$ up to cubic order to demonstrate that the GNMM equations have correctly determine that the quadratic combinations of σ_{xy} and $\dot{\gamma}$ not required. An evident result is that all of the coefficients for the quadratic observables are extremely small, clearly indicating that the underlying constitutive law does not contain quadratic terms. Even if we were not aware of the constraints from the GNMM equations and instead used a regular polynomial basis expansion to form Φ , we

can decide based on the output shown in Fig. 4.5 to rerun the method without supplying the quadratic observables, effectively forcing the coefficients for the quadratic observables to be zero. This is similar to how the SINDy method and its extensions [124, 126] uses a form of sequentially-thresholded least squares to narrow down the terms in the equation they wish to identify.

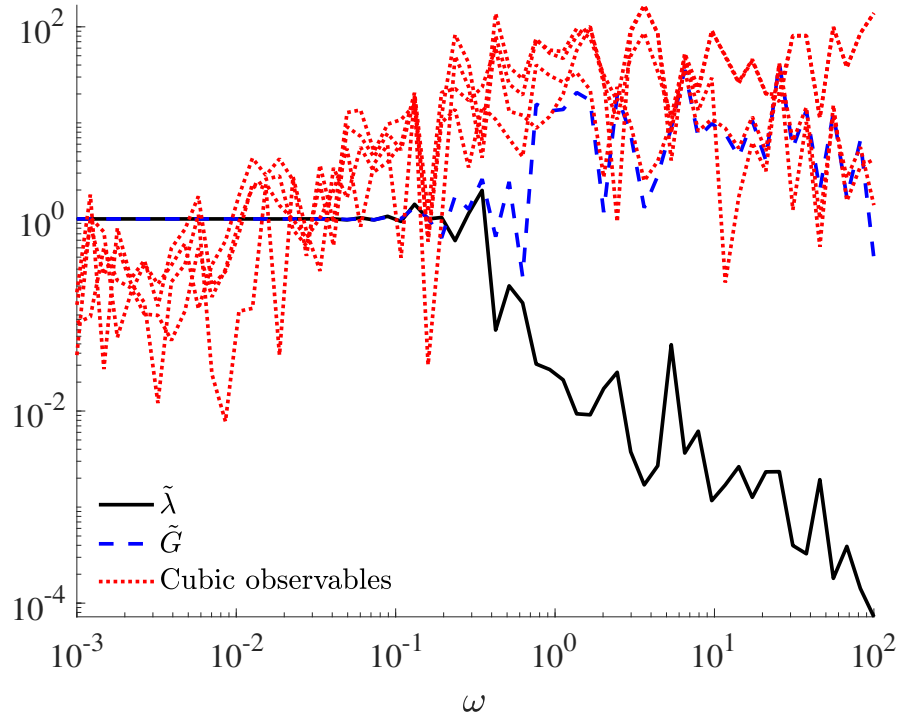


Figure 4.6: rheoKIC applied to data from the linear Maxwell model where $G = \lambda = \gamma_0 = 1$ and Φ contains linear and cubic observables only.

The results using the set of observables recognised in the GNMM equations is shown in Fig. 4.6. The rheoKIC method was applied in its most straightforward form: there was no truncation of the SVD of Φ and all of the candidate observables were supplied simultaneously. We identify constant values for the linear observables at frequencies $10^{-3} < \omega < 10^{-1}$, indicating both that these observables are required and that the coefficients have been identified correctly. On the other hand, at these frequencies the predicted coefficients for the cubic observables are noisy and are at a similar order of magnitude. At higher frequencies, rheoKIC is substituting σ with a linear combination of the cubic observables to reconstruct the output signal.

4.4.1 Cause of redundancy for the cubic observables

We can see whether the higher order observables are actually necessary by initially applying a Fourier transform to the σ measurements and checking the number of different frequencies that are visible. For this case, as expected, there is only a single frequency and the order of Φ can be reduced accordingly. Alternatively, we can check the reconstruction error using only the linear observables,

$$|\sigma_{n+1} - (k_1\sigma_n + k_2\dot{\gamma}_n)|, \quad (4.18)$$

with the reconstruction error using the full set of observables as defined in Eq. 4.17. This can be seen in Fig. 4.7. The reconstruction error is very small in both cases, across the entire range of ω , so it is reasonable to conclude that a constitutive law with only linear observables is sufficient to model the data.

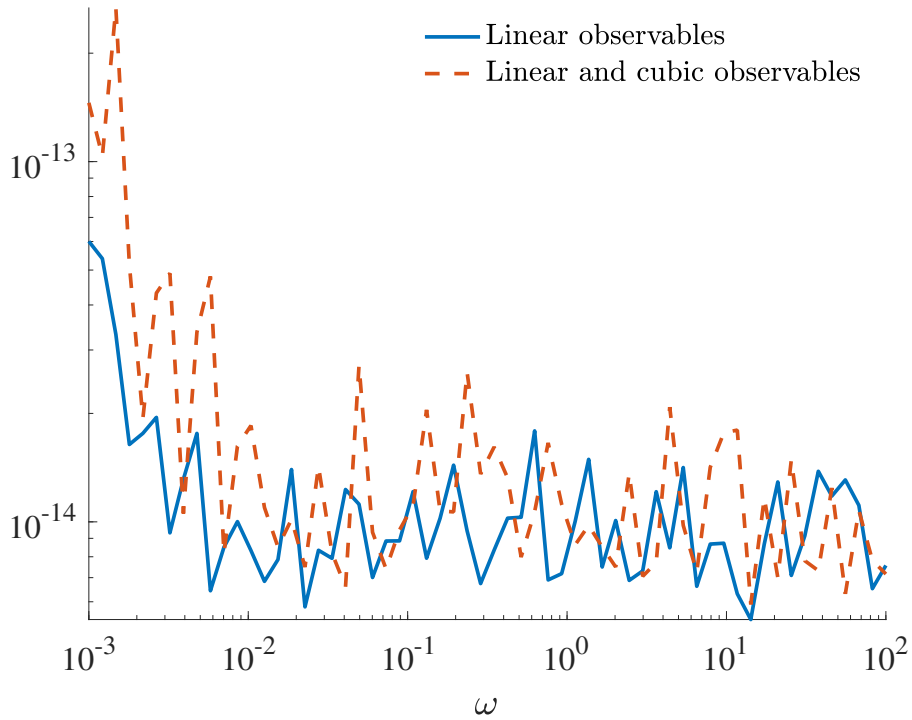


Figure 4.7: Reconstruction error for rheoKIC when the set of candidate observables contains only σ and $\dot{\gamma}$, and when all cubic order combinations of σ and $\dot{\gamma}$ are also provided.

Since we are looking for constant values of the coefficients independent of ω , it could be argued that this result indicates that the σ and $\dot{\gamma}$ are necessary while the others are not. However, we should also understand why the coefficients for the cubic observables seem to overwhelm those of the linear observables, in particular at high frequencies. We can understand more about this phenomenon by checking the rank of Φ : it is always equal to four, while there are six candidate observables in total. Truncating the SVD of Φ to four produces the predicted coefficients shown in Fig. 4.8. The values for all the predicted coefficients are significantly smoother and at frequencies $\omega < \lambda$ the cubic observables are clearly unnecessary to reconstruct the data. At high frequencies, the coefficients for the cubic observables are still large and interfere with the predictions for λ and G .

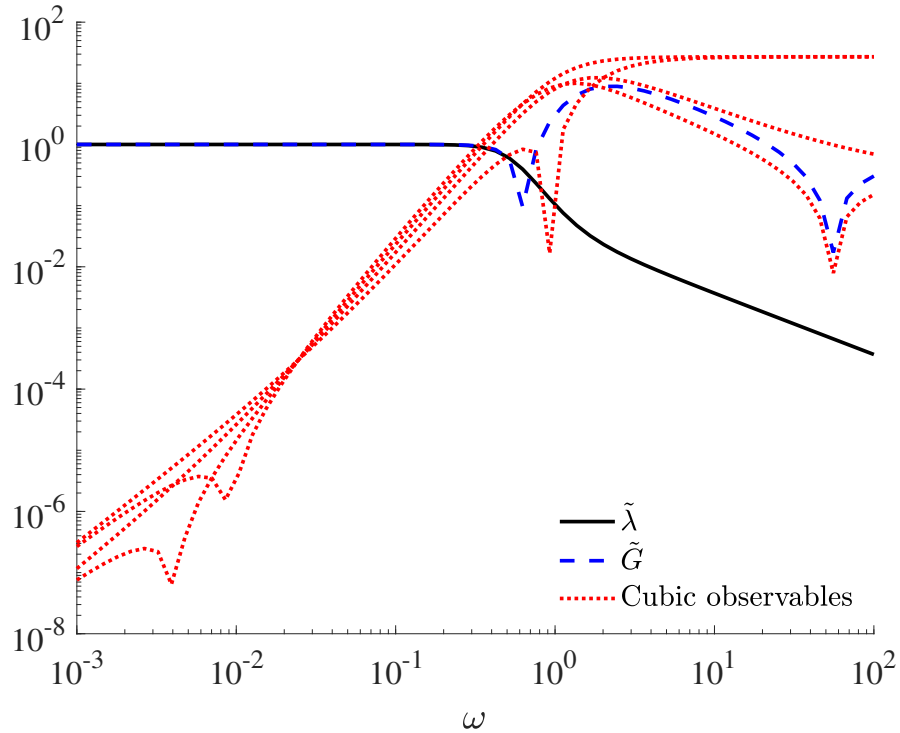


Figure 4.8: Data from the same scenario as in Fig. 4.6, but the SVD of Φ has been truncated to four.

We investigate this further by taking advantage of the fact that we know the analytic solutions for σ and $\dot{\gamma}$ exactly, shown in Eqs. 4.4 and 4.6 respectively. We rewrite each of the observables in terms of trigonometric basis functions:

$$\begin{bmatrix} \sigma \\ \dot{\gamma} \\ \sigma^3 \\ \sigma^2 \dot{\gamma} \\ \sigma \dot{\gamma}^2 \\ \dot{\gamma}^3 \end{bmatrix} = \begin{bmatrix} B \sin(\omega t) + A \cos(\omega t) \\ \dot{\gamma}_0 \cos(\omega t) \\ (B \sin(\omega t) + A \cos(\omega t))^3 \\ \dot{\gamma}_0 (B \sin(\omega t) + A \cos(\omega t))^2 \cos(\omega t) \\ \dot{\gamma}_0^2 (B \sin(\omega t) + A \cos(\omega t)) \cos(\omega t)^2 \\ \dot{\gamma}_0^3 \cos(\omega t)^3 \end{bmatrix}. \quad (4.19)$$

By expanding the powers of the trigonometric terms, we can see that this is a linear transformation of a Fourier basis expansion containing only odd terms,

$$\begin{bmatrix} \sigma \\ \dot{\gamma} \\ \sigma^3 \\ \sigma^2 \dot{\gamma} \\ \sigma \dot{\gamma}^2 \\ \dot{\gamma}^3 \end{bmatrix} = \begin{bmatrix} B & A & 0 & 0 \\ 0 & \dot{\gamma}_0 & 0 & 0 \\ \frac{3}{4}B(A^2 + B^2) & \frac{3}{4}A(A^2 + B^2) & \frac{1}{4}B(3A^2 - B^2) & \frac{1}{4}A(A^2 - 3B^2) \\ \frac{1}{2}AB\dot{\gamma}_0 & \frac{1}{4}(3A^2 + B^2)\dot{\gamma}_0 & \frac{1}{2}AB\dot{\gamma}_0 & \frac{1}{4}(A^2 - B^2)\dot{\gamma}_0 \\ \frac{1}{4}B\dot{\gamma}_0^2 & \frac{3}{4}A\dot{\gamma}_0^2 & \frac{1}{4}B\dot{\gamma}_0^2 & \frac{1}{4}A\dot{\gamma}_0^2 \\ 0 & \frac{3}{4}\dot{\gamma}_0^3 & 0 & \frac{1}{4}\dot{\gamma}_0^3 \end{bmatrix} \begin{bmatrix} \sin(\omega t) \\ \cos(\omega t) \\ \sin(3\omega t) \\ \cos(3\omega t) \end{bmatrix}. \quad (4.20)$$

If the quadratic order observables are still included, then the rank of Φ never rises above seven - the accompanying transformation is provided in Appendix B. Using only data from a SAOS experiment will subsequently always result in an under-determined system if higher order terms are used. We will need to find a way to increase the complexity of the data so that each of the observables in Φ is linearly independent to each other.

4.5 Increasing the data complexity

The issues with the cubic observables have arisen because Φ is rank-deficient for the given set of data and the linear Maxwell model. We will explore two different ways that the experimental data can be augmented so that Φ is full rank.

1. Combining data from different experiment types, namely stress relaxation and constant shear rate experiments.
2. Combining data from oscillatory experiments at different frequencies.

Other, more complex experiments described in Section 2.5.3 will be applied to data in subsequent chapters where the constitutive laws contain nonlinear terms.

4.5.1 Combined data sets from different experiments

We first look at how the rank of Φ can be augmented by using data from other commonly-used experiments that probe the linear viscoelastic regime: the stress relaxation experiment and the constant start rate, or shear start up, experiment.

As described in Chapter 4, the stress relaxation experiment involves shearing the fluid until the stress reaches a prescribed value, then removing the source of shear and observing the fluid as it returns to its quiescent state. Using the analytic solution for the Maxwell model, we know that the equations for our fluid in a stress relaxation experiment is

$$\dot{\gamma} = 0, \quad \sigma = \sigma_0 e^{-\frac{t}{\lambda}}, \quad \sigma(t = 0) = \sigma_0. \quad (4.21)$$

The shear rate is simply zero in this case. Any observables in Φ that involve $\dot{\gamma}$ will therefore also be zero, and the standard set of candidate observables reduces to

$$\Phi = [\sigma \ \sigma^3]. \quad (4.22)$$

From Eq. 4.21 we can also see that G cannot be approximated for this experiment. The approximation for λ , at least, is reasonable over a range of time step sizes, as shown in Fig. 4.9(left). The coefficient for the σ^3 observable is $O(10^{-10}) - O(10^{-15})$. At time step sizes $\lambda \approx 10\Delta t$, the distance between the measurements is too large to suitably resolve the exponential decay of the stress response.

For the constant shear rate protocol, the analytic solution to the Maxwell model is

$$\dot{\gamma} = \gamma_0, \quad \sigma = \lambda G \gamma_0 (1 - e^{-\frac{t}{\lambda}}). \quad (4.23)$$

The constant shear rate experiment is able to find an approximation for both λ and G , since the equation is in the form suitable for rheoKIC is

$$\sigma_{n+1} = \left(1 - \frac{\Delta t}{\lambda}\right) \sigma_n + \Delta t G \gamma_0. \quad (4.24)$$

None of the observables in Φ will be set to zero. However, the observables $\dot{\gamma}$ and $\dot{\gamma}^3$, and σ and $\sigma \dot{\gamma}^2$, will be scalar multiples of each other. The rheoKIC approach will not automatically choose one observable over another in these scenarios: instead, it will divide the coefficient associated to the signal equally amongst them. This fact is reflected in the rank of Φ , which is four. Since it is reasonable to assume that the lower order observables are more likely to be part of the underlying constitutive law than the higher order observables, we approach this

issue by keeping the lowest order duplicate of each signal, as follows:

$$\begin{bmatrix} \dot{\gamma} & \dot{\gamma}^3 \end{bmatrix} \longrightarrow \begin{bmatrix} \dot{\gamma} \end{bmatrix} \quad (4.25a)$$

$$\begin{bmatrix} \sigma & \sigma \dot{\gamma}^2 \end{bmatrix} \longrightarrow \begin{bmatrix} \sigma \end{bmatrix} \quad (4.25b)$$

$$\Phi = \begin{bmatrix} \sigma & \dot{\gamma} & \sigma^3 & \sigma^2 \dot{\gamma} & \sigma \dot{\gamma}^2 & \dot{\gamma}^3 \end{bmatrix} \longrightarrow \begin{bmatrix} \sigma & \dot{\gamma} & \sigma^3 & \sigma^2 \dot{\gamma} \end{bmatrix}. \quad (4.25c)$$

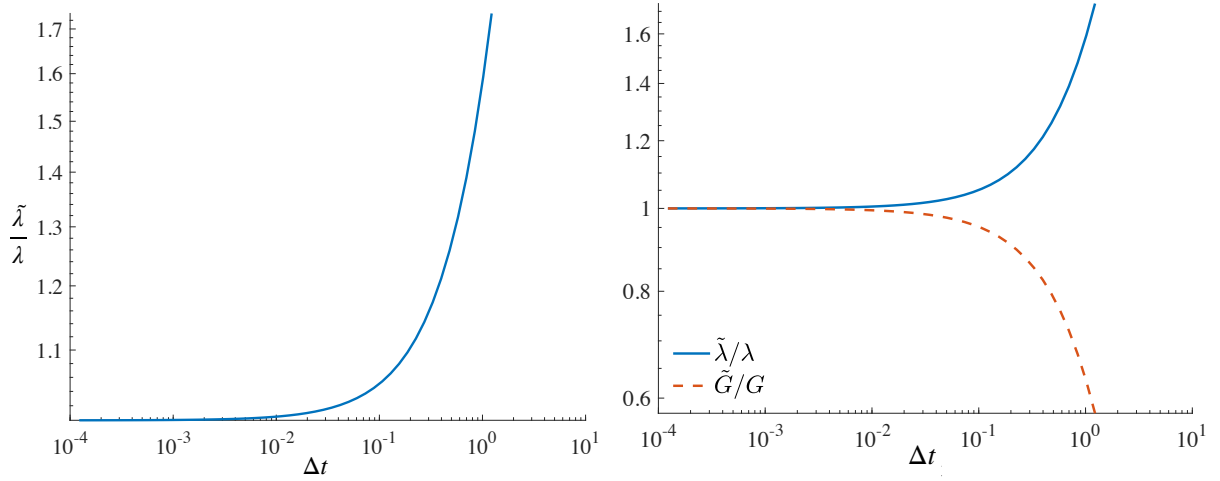


Figure 4.9: Normalised approximations for observable coefficients where the data set is computed to resemble (left) data from a stress relaxation experiment with $\Phi = [\sigma \ \sigma^3]$ and (right) data from a constant shear rate experiment with $\Phi = [\sigma \ \dot{\gamma} \ \sigma^3, \ \sigma^2 \dot{\gamma}]$.

The predictions for λ and G using just data from the constant shear rate experiment, with this reduced set of candidate observables, are shown in Fig. 4.9(right). Both approximations are good for low frequencies but deviate at higher frequencies and $\text{rank}(\Phi) = 4$ for each simulation. As in the stress relaxation data test, the coefficients for the cubic observables are $O(10^{-10}) - O(10^{-15})$.

Concatenating the data from both the stress relaxation experiment and the constant shear rate experiment maintains the same number of observables $K = 4$ and keeps Φ at full rank. The

approximations for λ and G are virtually identical to that when only the constant shear rate data is used.

We then check the effects of using concatenated data from all three types of simulation introduced in this chapter: for a given oscillatory frequency, we compute the data to resemble a SAOS experiment and then the corresponding stress relaxation and constant shear data with the same time step size. The resulting set of candidate observables when using this data set is full rank and no observables need to be discarded. The approximations for λ and G are shown in Fig. 4.10 (left), and alongside the approximated coefficients for the higher order coefficients in Fig. 4.10 (right).

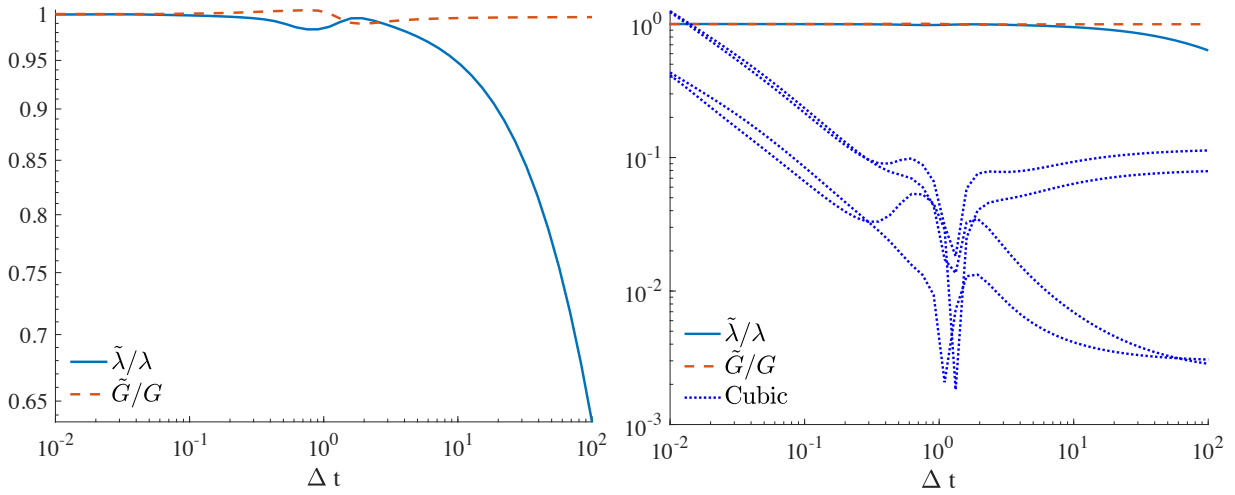


Figure 4.10: Normalised approximations for observable coefficients where, at each frequency, the data set consists of data from a stress relaxation simulation, a constant shear rate simulation, and a SAOS simulation. (Left) Normalised values of $\tilde{\lambda}$ and \tilde{G} only, corresponding to the linear observables. (Right) Coefficients for all the observables in rheoKIC.

We can see that both approximations are accurate across a wider range of frequencies than when data from any of the experiments was supplied individually. While all the coefficients are of a similar magnitude at the lowest frequencies, the coefficients for the higher order observables rapidly decay to significantly smaller values for the majority of the frequency spectrum. The approximations are similar in quality to when using SAOS data and only the linear observables were supplied, which required using existing knowledge about the linearity of the underlying

constitutive law - here, the full set of candidate observables was supplied and no assumptions about linearity of the data were required.

4.5.2 Combining multiple SAOS data sets

Instead of introducing further types of experimental data, we look at how we can exploit our oscillatory data set further to improve the accuracy of our model. We carry out 50 experiments at frequencies ω_i , $i = 1, \dots, 50$ distributed logarithmically between 10^{-2} and 10^2 , and concatenate the data for Φ according to

$$\sigma = \begin{bmatrix} \sigma_1^{\omega_1} & \sigma_2^{\omega_1} & \dots & \sigma_{n-1}^{\omega_1} & \sigma_1^{\omega_2} & \sigma_2^{\omega_2} & \dots & \sigma_{n-1}^{\omega_{50}} \end{bmatrix} \quad (4.26)$$

and

$$\dot{\gamma} = \begin{bmatrix} \dot{\gamma}_1^{\omega_1} & \dot{\gamma}_2^{\omega_1} & \dots & \dot{\gamma}_{n-1}^{\omega_1} & \dot{\gamma}_1^{\omega_2} & \dot{\gamma}_2^{\omega_2} & \dots & \dot{\gamma}_{n-1}^{\omega_{50}} \end{bmatrix} \quad (4.27)$$

The data we are trying to reconstruct is

$$\begin{bmatrix} \sigma_2^{\omega_1} & \sigma_3^{\omega_1} & \dots & \sigma_n^{\omega_1} & \sigma_2^{\omega_2} & \sigma_3^{\omega_2} & \dots & \sigma_n^{\omega_{50}} \end{bmatrix} \quad (4.28)$$

While the KIC method is capable of handling combined data sets that have different time step sizes [20], here for simplicity we have fixed the time step size so that the highest frequency contains 512 measurements per oscillatory period. Fig. 4.11 shows the approximations for λ and G , normalised by their true values, when using the data set from each experiment individually and when all the data sets are concatenated. In this case the full set of candidate observables is provided i.e. $K = 6$.

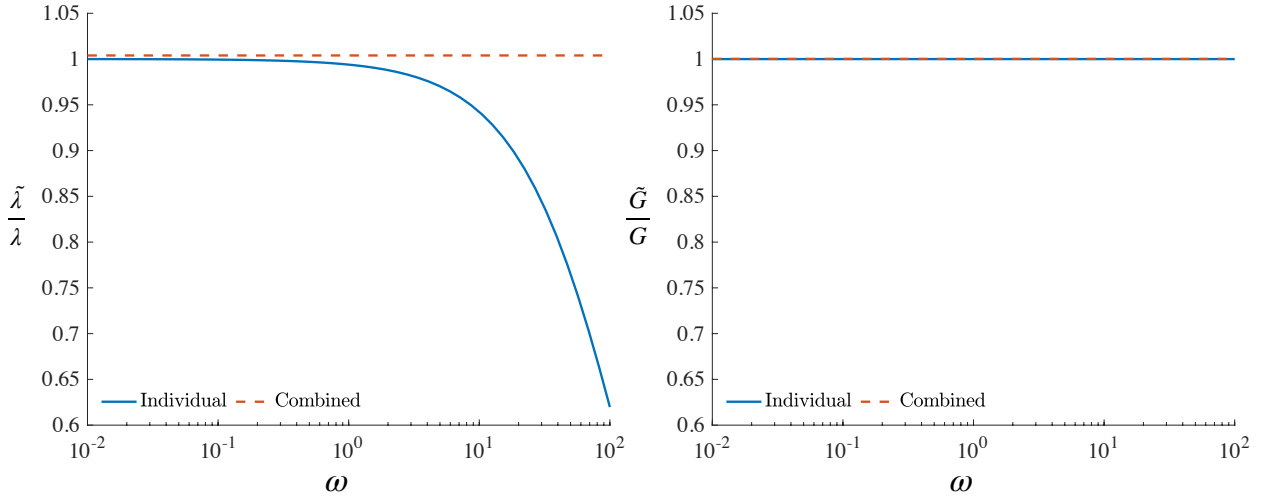


Figure 4.11: Approximations for λ (left) and G (right), normalised by their true values. The solid lines correspond to approximations where the provided data is only the data at that frequency, while the dashed lines correspond to approximations using data sets from all frequencies at once.

The data set of combined frequencies produces approximations for $\tilde{\lambda}$ and \tilde{G} with errors of 0.39% and 0.013%, respectively, and the combined data set of all the SAOS experiments, which would each be rank-deficient individually under this choice of Φ , is full rank. The coefficients for the higher order observables range from 10^{-2} to 10^{-9} in magnitude, and so can comfortably be regarded as unnecessary for the data reconstruction. Using a concatenated data set, representing frequencies spanning several orders of magnitude within a single data set, therefore produces the most accurate results when using rheoKIC out of all the more complex data sets that we have investigate here.

4.6 Conclusions

For this first chapter of results, we have applied rheoKIC to data from a constitutive law of a viscoelastic fluid, namely the linear Maxwell model, as a pathological example on which to build in subsequent chapters.

Before applying rheoKIC at all, we found that the first-order approximation for the time derivative required by rheoKIC introduces errors on the order of the time step size. It is therefore important to use data that is as well time-resolved as possible. A variation of DMD called ‘Higher order DMD’ [133, 134] has the potential to reduce this error by incorporating time lagged snapshots in the methodology such that more accurate approximations for the time derivative can be used instead, although we do not investigate this here. Additionally, the transformation from the observable coefficient for the stress signal to its actual value in the Maxwell model can also introduce error. Using data from lower oscillatory frequencies, or from a different type of experiment to oscillatory, can help to mitigate this issue.

Using a data from a linear constitutive law has allowed us to reduce rheoKIC, which uses a set of candidate observables that are linear and nonlinear in σ and $\dot{\gamma}$ and may contain superfluous entries, to DMDc, which uses only linear observables and no extra signals by definition. Applying DMDc to this linear data, as expected, returned better results than when superfluous observables were added.

Applying rheoKIC with the full set of GNMM observables correctly identifies the linear observables for low frequencies, but also identifies the cubic observables as relevant at high frequencies. The quadratic observables were shown to be unnecessary throughout, in agreement with the fact that these terms are absent in the GNMM equation for the off-diagonal element of the stress tensor. The set of candidate observables was observed to be rank-deficient when using a single data set from an oscillatory simulation. The cause of the degeneracy was found by looking at the analytic solution to the Maxwell model and noting that, in this case, the set of candidate observables for rheoKIC can be linearly transformed into the standard Fourier basis.

Finally, we investigated how the complexity of the observables could be increased so that none of the observables are degenerate. Using concatenated data sets of oscillatory data across a range of frequencies resulted in both high accuracy for the coefficients and a clear separation between the necessary and unnecessary observables. Using DMDc to produce excellent results was only possible because the model was known *a priori* to be linear; by using a combination of different data sources on the full set of GNMM observables, we were able to produce results

at a comparable level of accuracy without this knowledge.

Chapter 5: Application to weakly non-linear laws

As a next step in complexity for the types of constitutive laws we aim to identify, we add a term to the linear Maxwell model that is nonlinear in the shear rate and form the simple (or ‘scalar’) fluidity model (SFM) [70]

$$\frac{\partial \sigma}{\partial t} = G\dot{\gamma}(t) - \frac{1}{\lambda}g(\dot{\gamma}(t)^2)\sigma(t), \quad (5.1)$$

which is a simplified, non-spatial form of a model often used to describe soft glassy materials [10]. The elastic contribution to the stress evolution comes from the $G\dot{\gamma}(t)$ term, while the relaxation time is described by the nonlinear function of the shear rate. We choose a simple form for g by approximating it with a Taylor expansion:

$$g(\dot{\gamma}(t)^2) = g(0) + \beta\dot{\gamma}^2 + O(\dot{\gamma}^4). \quad (5.2)$$

We set $g(0) = 1$ as this value will only change the coefficient multiplying σ , which here is simply the relaxation rate of the fluid. The equation for the stress evolution then becomes

$$\frac{\partial \sigma}{\partial t} = G\dot{\gamma}(t) - \frac{1}{\lambda}\sigma(t) - \frac{\beta}{\lambda}\dot{\gamma}^2(t)\sigma(t). \quad (5.3)$$

The general solution to Eq. 5.3 with initial condition $\sigma(t = 0) = 0$ is given by

$$\sigma = e^{-\int P(t)dt} \left(\int \dot{\gamma}(t) e^{\int P(t)dt} dt - 1 \right). \quad (5.4)$$

In our case when the strain rate is oscillatory, $\dot{\gamma}(t) = \dot{\gamma}_0 \cos(\omega t)$, and we find that

$$\int P(t)dt = \frac{1}{\lambda} \left[\frac{\beta \dot{\gamma}_0^2}{4\omega} \sin(2\omega t) + \left(1 + \frac{\beta \dot{\gamma}_0^2}{2}\right)t \right]. \quad (5.5)$$

Eq. 5.3 is the linear Maxwell model from Chapter 4 with an extra term that is quadratic in $\dot{\gamma}$ and linear in σ . Fluids with larger magnitudes of β relative to the other coefficients will produce a stress response to the applied shear that deviates further from the Maxwell model. On the other hand, even for cases when β is relatively small, the magnitude of the shear rate will also effect the linearity of the stress response. The effect of the oscillation amplitude is demonstrated in Fig. 5.1 where $\lambda = G = 1$ and $\beta = 0.4$.

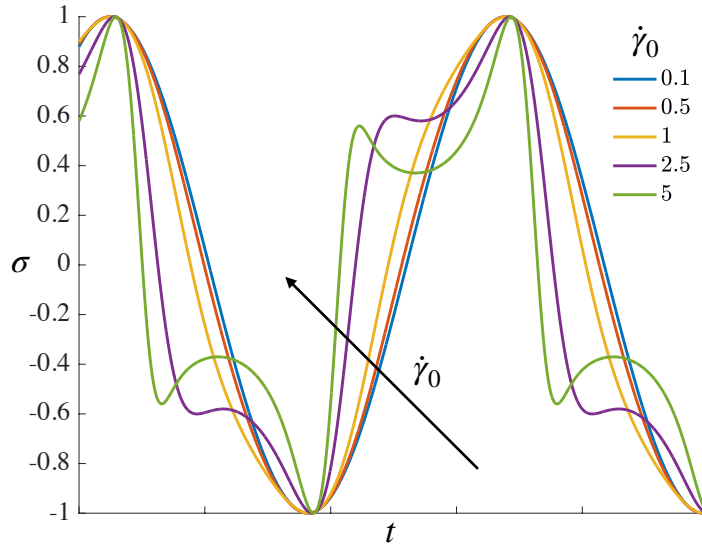


Figure 5.1: Stress response for a fluid governed by the SFM with fluid parameters $G = \lambda = 1$ and $\beta = 0.4$.

At values $\dot{\gamma}_0 > 1$, it is possible to see the stress response deviating from the Maxwell model purely by visual inspection. For $\dot{\gamma}_0 < 1$ it is unclear whether it is sufficient to model the stress

response with the linear Maxwell model or not. It would be reasonable to assume a linear response when $\dot{\gamma}_0 \ll 1$.

5.1 Linear/Maxwell regime

Discretising Eq. 5.3 and substituting the time derivative with its forward Euler approximation, the SFM can be rewritten in the form suitable for rheoKIC as

$$\sigma_{n+1} = \left(1 - \frac{\Delta t}{\lambda}\right)\sigma_n + \Delta t G \dot{\gamma}_n - \frac{\Delta t \beta}{\lambda} \dot{\gamma}_n^2 \sigma_n. \quad (5.6)$$

We will be aiming to identify that σ , $\dot{\gamma}$ and $\dot{\gamma}^2 \sigma$ are the observables that we need from Φ , using the same observables as in Eq. 4.15, and that their corresponding coefficients are

$$k_1 = 1 - \frac{\Delta t}{\lambda}, \quad k_2 = \Delta t G, \quad k_3 = -\frac{\Delta t \beta}{\lambda}. \quad (5.7)$$

Since any direct approximation for β will be dependent on our approximation of λ , we will focus instead on the accuracy of our approximation of k_3 as a whole. For small enough strain rate amplitudes, $|\dot{\gamma}_0|^2 = (\gamma_0 \omega)^2$, the $\dot{\gamma}^2 \sigma$ observable in the SFM will be negligibly small and we retrieve the equation for the linear Maxwell model.

To produce a data set within the linear viscoelastic regime, we carry out the same frequency sweep $\omega = 10^{-2} - 10^2$ as in the previous chapter while fixing $\gamma_0 = 10^{-5}$ to simulate a small amplitude oscillatory test. We compute the stress response from Eq. 5.1 with the `ode45` solver and use data after 100 periods have elapsed to ensure any initial transients have decayed.

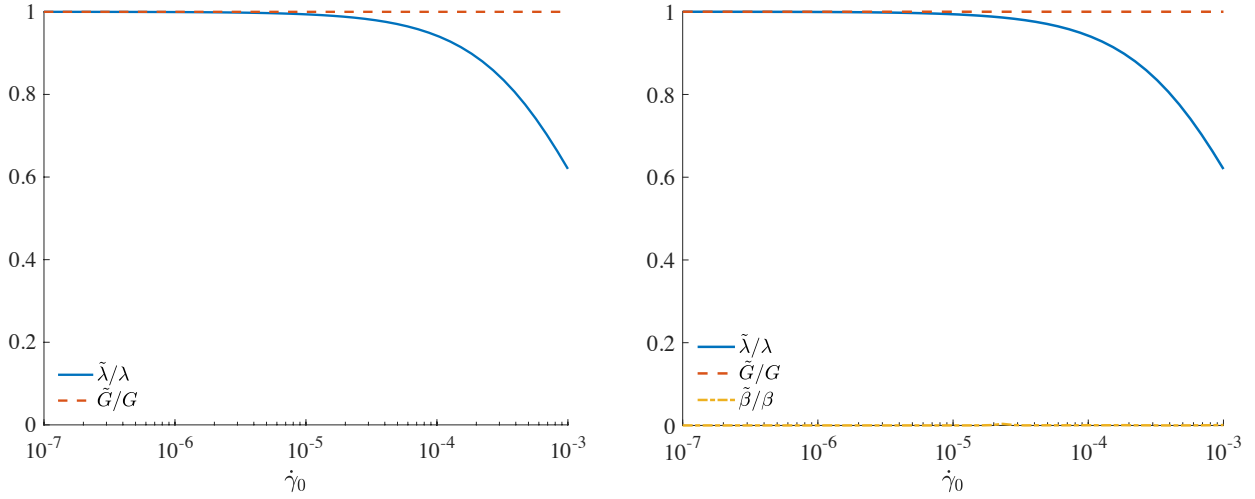


Figure 5.2: rheoKIC applied to SAOS data where $\gamma_0 = 10^{-5}$ and $\omega = 10^{-2} - 10^2$, such that $\dot{\gamma}_0 = 10^{-7} - 10^{-3}$. The supplied observables are (left) σ and $\dot{\gamma}$, and (right) σ , $\dot{\gamma}$, and $\dot{\gamma}^2\sigma$.

Fig. 5.2 shows the performance of rheoKIC on this data for the cases where we supply only the linear observables, $\Phi = [\sigma, \dot{\gamma}]$, and only the correct observables, $\Phi = [\sigma, \dot{\gamma}, \dot{\gamma}^2\sigma]$. Using only the linear observables produces the same approximations as in the linear Maxwell model from Chapter 4. When the extra nonlinear term from SFM is included, rheoKIC recognises that it is unnecessary for modelling the data and sets its coefficient to $O(10^{-4})$ across the full range of $\dot{\gamma}_0$.

We can confirm that the stress response is linear by checking that the Fourier transform of the data at each frequency has a single peak, confirming that only the linear observables are required. Alternatively, we can use the rank-deficiency of Φ before computing the coefficients as a metric for determining whether the stress response is linear. When observing the raw data from a simulation, we can see that the $\dot{\gamma}^2\sigma$ observable has such a small magnitude relative to the other observables that it appears to effectively be a vector of zeros causing $\text{rank}(\Phi) = 2$. However, we usually scale the signals for each observable to have the same magnitude before performing the SVD step,

$$\sigma \rightarrow \frac{\sigma}{|\sigma|}, \quad \dot{\gamma} \rightarrow \frac{\dot{\gamma}}{|\dot{\gamma}|}, \quad (5.8)$$

and then scale back afterwards while computing the constitutive law parameters from the k_i coefficients. Once Φ is rescaled we find that it is full rank and the impact from the $\dot{\gamma}^2\sigma$ signal appears to be as important as that of the other signals. It is therefore important to only apply this rank-deficiency metric on the raw entries of Φ in order to interpret the linearity of the data set correctly.

In Fig. 5.3, we fix ω and vary γ_0 to find where the $\dot{\gamma}^2\sigma$ term ‘kicks in’ and is considered necessary by rheoKIC for different frequencies. We find that γ_0 can be several orders of magnitude smaller than ω before the stress response falls within the linear regime, and that we require $\gamma_0 > 10^{-3}$ for all values of ω that we check.

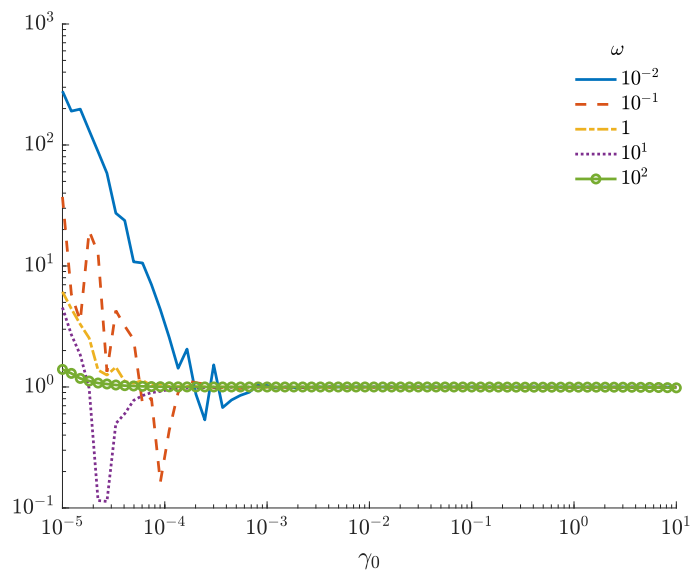


Figure 5.3: Re-scaled approximations for k_3 where ω has been fixed while $\gamma_0 = 10^{-5} - 10$. The supplied observables are $\Phi = [\sigma, \dot{\gamma}, \dot{\gamma}^2\sigma]$.

5.1.1 Frequency-sweep MAOS

We want to find a strain amplitude large enough to produce a stress response that no longer resembles that of the linear Maxwell model. The crux of the issue is that the importance of the extra term in the SFM equation is dependent on both γ_0 and ω , while we want the combination $\dot{\gamma}_0 = (\gamma_0\omega)^2$ to have a large enough value across an entire frequency sweep.

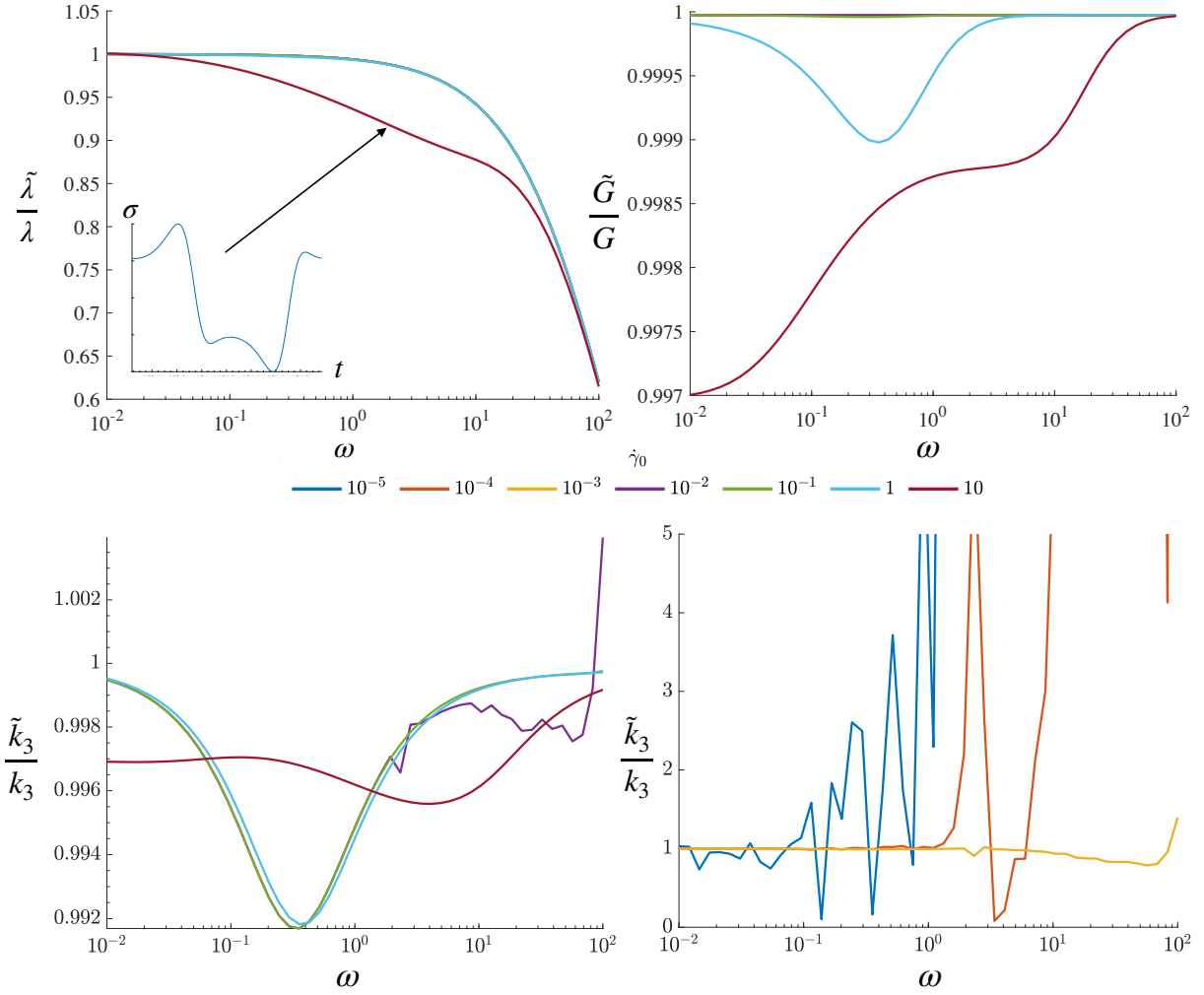


Figure 5.4: rheoKIC applied to ω -sweep MAOS data using $\Phi = [\sigma, \dot{\gamma}, \dot{\gamma}^2 \sigma]$. The legend in the top right describes the value of $\dot{\gamma}_0$ for all cases. Top left: Approximations for λ . Top right: Approximations for G . Bottom left: Approximations for β , $\dot{\gamma}_0 = 10^{-2} - 10$. Inset: σ for $\omega = 4$. Bottom right: Approximations for k_3 , $\dot{\gamma}_0 = 10^{-5} - 10^{-3}$.

The issue of finding this ‘sweet spot’ for medium amplitude oscillatory tests has already been investigated [135]: their proposed resolution is ‘frequency-sweep MAOS’, or ‘ ω -sweep MAOS’, whereby γ_0 is dependent on ω such that $\dot{\gamma}_0$ remains fixed across a frequency sweep at a value which produces the desired response. The original intention for ω -sweep MAOS was to ensure that the stress response always remained weakly nonlinear, since a fully nonlinear response requires a different form of analysis when using the FT-rheology approach. For our case, we use ω -sweep MAOS primarily to ensure that the stress response does not become linear at low frequencies, where our approximation for λ is the most accurate.

The results for ω -sweep MAOS with different choices of $\dot{\gamma}_0$ are shown in Fig. 5.4, where $\Phi = [\sigma, \dot{\gamma}, \dot{\gamma}^2\sigma]$. Our approximations for G only slightly deviate at the highest amplitudes. The approximations for λ are virtually independent of $\dot{\gamma}_0$ except for at the largest value $\dot{\gamma}_0 = 10$. The stress response deviates strongly from a sine curve at $\omega \approx \lambda$, as shown by the inset figure, which causes this reduction in accuracy. The stress response then appears to be more linear as ω is increased further and the oscillation frequency dominates significantly over the fluid's relaxation rate.

We find very good accuracy for \tilde{k}_3 when $\dot{\gamma}_0 \geq 10^{-2}$. When $\dot{\gamma}_0 \leq 10^{-3}$ we return to the linear regime and \tilde{k}_3 deviates considerably from the correct value. We can conclude that we will only be able to retrieve all the terms in the SFM model when the strain rate amplitude is high enough to produce a nonlinear stress response. Otherwise, rheoKIC cannot ‘see’ the relevance of the higher order term and the prediction will revert to the linear Maxwell model. Since the strain rate amplitude is dependent on both strain amplitude γ_0 and oscillation frequency ω , the stress response can span both the linear and nonlinear regimes during a frequency sweep if γ_0 is fixed. The ω -sweep MAOS approach, where $\dot{\gamma}_0 = \gamma_0\omega$ is fixed instead, resolves this issue.

5.2 GNMM observables

We initially chose to use a reduced set of candidate observables $\Phi = [\sigma, \dot{\gamma}, \dot{\gamma}^2\sigma]$ in order to focus on finding a range of values for the experimental parameters where the higher order term is well-represented. It is no surprise that rheoKIC is capable of retrieving good approximations for both the linear and nonlinear observables when only the correct observables are supplied. We intend for rheoKIC to be used when the terms in the constitutive law are unknown, and as such we now look at results where Φ is constructed according to Eq. 4.15, with the inclusion of $\ddot{\gamma}$ since we are looking at a nonlinear data set, so that now $K = 7$:

$$\Phi = [\sigma, \dot{\gamma}, \sigma^3, \sigma^2\dot{\gamma}, \sigma\dot{\gamma}^2, \dot{\gamma}^3, \ddot{\gamma}]. \quad (5.9)$$

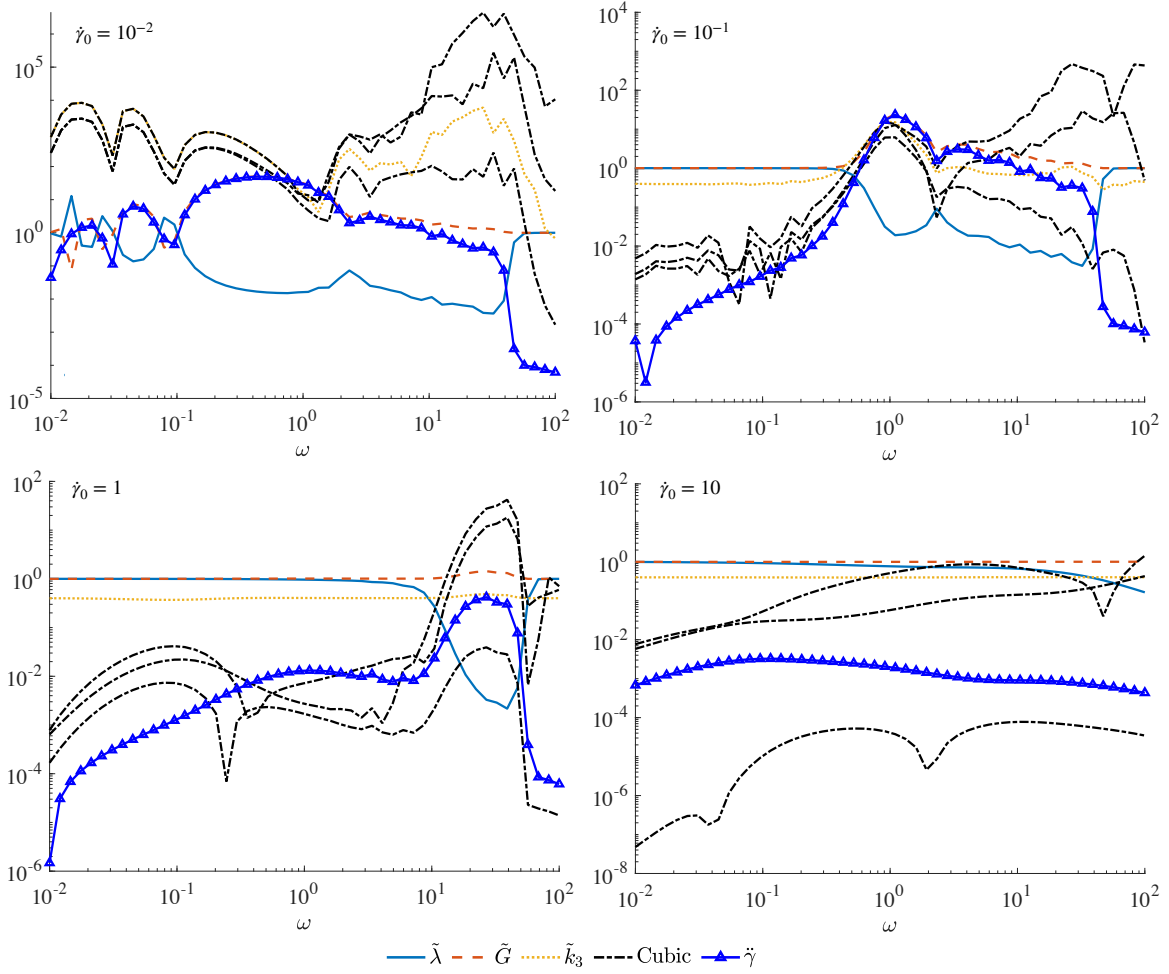


Figure 5.5: rheoKIC applied to ω -sweep MAOS data using the full set of observables, The value of $\dot{\gamma}_0$ is fixed for each sweep. In all cases $G = \omega = 1$ and $\beta = 0.4$.

Fig. 5.5 shows the approximations for each coefficient when applying ω -sweep MAOS and using this full set of candidate observables. Ideally, the three observables that are originally contained in the SFM equation should have coefficients with magnitudes large enough to separate them from the other observables, and these coefficients should remain consistent across a range of frequencies.

We were previously able to find a good approximation for k_3 using $\dot{\gamma}_0 = 10^{-2}$ when only the correct observables were provided. Now that Φ is aligned with what would be used in practice, it is no longer clear that the $\dot{\gamma}^2\sigma$ observable has different behaviour to the other nonlinear observables until $\dot{\gamma}_0 = 10^{-1}$. The coefficient for the $\dot{\gamma}^2\sigma$ observable becomes increasingly regular

across the range of ω as $\dot{\gamma}_0$ increases further. We find that Φ is full rank for all cases where $\dot{\gamma}_0 \geq 10^{-1}$. When $\dot{\gamma}_0 = 10^{-2}$, Φ is rank-deficient at both low and high frequencies. Using the QR decomposition of Φ , we find that the linearly dependent observables causing this rank deficiency are a combination of σ^3 , $\sigma^2\dot{\gamma}$, and $\dot{\gamma}^2\sigma$ which varies depending on the specific value of ω involved.

Throughout Fig. 5.5 there are intrusions by the cubic observables which should be discarded by the method onto the observables we wish to keep, particularly at the highest frequencies. We can see effect of this interference in Fig. 5.6 where we isolate the approximations for λ , G , and k_3 for the $\dot{\gamma}_0 = 1$ and $\dot{\gamma}_0 = 10$ cases. We can clearly see the impact at the highest frequencies, where a combination of signals from the other observables is being used to reconstruct the data instead using of the $\dot{\gamma}^2\sigma$ signal. Based on the results in Fig. 5.5 it is highly likely that a practitioner would consider some of the cubic signals necessary for reconstructing the constitutive law based on the magnitude of their coefficients. For example, in the $\dot{\gamma}_0 = 10$ case we might decide that the $\ddot{\gamma}$ observable and one of the cubic observables should be discarded. We will explore modifications to the methodology along this line of thought to prevent this intrusion from occurring.

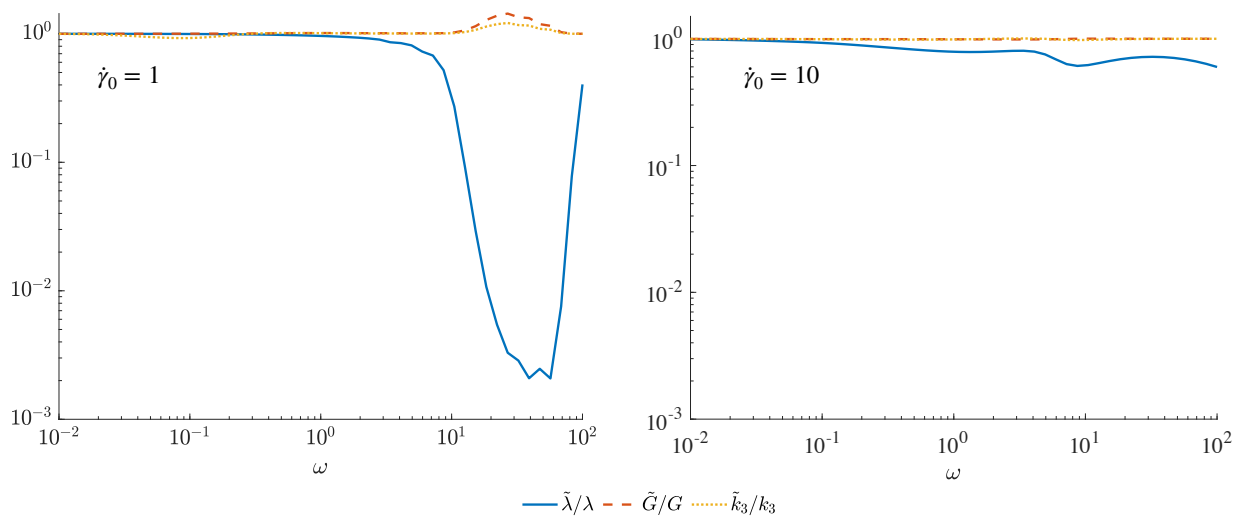


Figure 5.6: Approximations for SFM constitutive parameters when rheoKIC is applied to ω -sweep MAOS data using the full set of observables.

5.3 Combined data sets

As in the previous chapter, our first strategy for dealing with this issue is to employ combined data sets from across a full frequency sweep. We set the time step size so that there are 512 data points per period at the highest frequency, while using the same number of data points for each frequency, to ensure that there is no outsize influence from the lower frequency data sets. The approximations for each observable coefficient are shown in Table 5.1. We retrieve excellent approximations with less than 1% error for G independently of $\dot{\gamma}_0$, and similarly for λ when $\dot{\gamma}_0 < 10$. When $\dot{\gamma}_0 = 10^{-1}$ or higher, our approximations for k_3 have less than 1% error. The errors increase slightly for the largest shear rate amplitude value of $\dot{\gamma}_0 = 10$.

This approach fails to find good approximations for k_3 when $\dot{\gamma}_0 = 10^{-2}$ or 10^{-3} . We can see why this is the case by comparing the computed coefficient for the $\dot{\gamma}^2\sigma$ observable relative to the coefficients of the other higher order observables: when the accuracy for k_3 is high, it is at least two orders of magnitude larger than the others. Meanwhile, for the cases where a good approximation for k_3 is not found, the $\dot{\gamma}^2\sigma$ coefficient has the same or smaller order of magnitude as the other higher order observables. The method does not identify that this observable is necessary because the stress response is within the linear regime, and uses this signal to the same extent as the other unnecessary signals that have been provided. When $\dot{\gamma}_0 = 10$, the discrepancy between the coefficients is smaller but there is still an order of magnitude difference between them.

$\dot{\gamma}_0$	$\tilde{\lambda}$ (%)	\tilde{G} (%)	\tilde{k}_3 (%)	σ^3	$\sigma^2\dot{\gamma}$	$\dot{\gamma}^2\sigma$	$\dot{\gamma}^3$	$\ddot{\gamma}$
10^{-3}	0.999 (0.11)	1.000 (0.006)	13.6	35	45	13	1	10^{-5}
10^{-2}	0.999 (0.11)	1.000 (0.006)	32.9	0.35	0.45	0.53	0.01	10^{-5}
10^{-1}	0.999 (0.11)	1.000 (0.006)	0.4 (0.3)	10^{-3}	10^{-3}	0.4	10^{-5}	10^{-5}
1	1.0 (0.01)	1.000 (0.003)	0.40 (0.03)	10^{-5}	10^{-5}	0.4	10^{-5}	10^{-5}
10	1.01 (0.5)	1.001 (0.14)	0.39 (0.25)	0.07	0.01	0.4	10^{-5}	10^{-5}

Table 5.1: Approximated coefficients when concatenating the data sets used for ω -sweep MAOS. The ‘ 10^{-x} ’ entries indicate that the coefficients are of order $O(10^{-x})$ or smaller.

Each of the rows of results in Table 5.1 are within the same viscoelastic regime since $\dot{\gamma}_0$ is fixed for each concatenated data set. Alternatively, by fixing ω and concatenating data sets with different values of $\dot{\gamma}_0$, each data set can span both the linear and nonlinear viscoelastic regime. Table 5.2 shows the results of applying rheoKIC to five concatenated data sets with a fixed value for ω and $\dot{\gamma}_0 = [10^{-3}, 10^{-2}, 10^{-1}, 1, 10]$.

ω	$\tilde{\lambda}$ (%)	\tilde{G} (%)	\tilde{k}_3 (%)	σ^3	$\sigma^2\dot{\gamma}$	$\dot{\gamma}^2\sigma$	$\dot{\gamma}^3$	$\ddot{\gamma}$
10^{-2}	1.003 (0.25)	0.998 (0.29)	0.399 (0.29)	0.001	10^{-4}	0.398	10^{-7}	10^{-5}
10^{-1}	0.996 (0.39)	0.999 (0.13)	0.399 (0.27)	0.003	0.003	0.399	10^5	10^{-4}
1	0.98 (2.0)	0.994 (0.59)	0.403 (0.77)	0.060	0.065	0.403	10^{-4}	10^{-4}
10	0.823 (17.7)	0.996 (0.39)	0.413 (3.28)	2.678	0.229	0.413	10^{-4}	0.002
100	0.321 (67.9)	1.000 (0.011)	0.400 (0.215)	7.23	0.515	0.400	10^{-6}	10^{-4}

Table 5.2: Approximated coefficients when concatenating data sets with a fixed frequency and $\dot{\gamma}_0 = [10^{-3}, 10^{-2}, 10^{-1}, 1, 10]$.

At the lowest frequencies, we find the ideal combination of both excellent accuracy for the coefficients of the observables we need and relatively small coefficients for all the observables we should discard. As expected, the accuracy for $\tilde{\lambda}$ decreases at higher frequencies due to the errors from the Euler approximation. There is remarkably very little change in the accuracy as ω is increased for both \tilde{G} and \tilde{k}_3 . However, for $\omega = 10$ and $\omega = 100$ we see that the coefficients for σ^3 and $\sigma^2\dot{\gamma}$ are now large enough to not be discarded by the method. At these higher frequencies the σ observable is not used as accurately due to the Euler approximation, which is reflected in the reduced accuracy of $\tilde{\lambda}$, and causes the signals from the other observables to be used in its place.

Overall, we see that rheoKIC applied to these combined data sets will produce a good reconstruction of the data provided the right choice of experimental parameters is made. Fixing $\dot{\gamma}_0$ and varying ω produces excellent accuracy for the linear observables but varying levels of accuracy for the higher order observable. Fixing ω and varying $\dot{\gamma}_0$ produces good approximations for the higher order observable, but we find that the coefficients for the other observables start

to intrude at the highest frequencies. It is likely that a battery of tests as in the tables above would be required to determine the experimental parameters for the data sets to be combined. The increase in the number of data sets, and therefore the number of experiments/simulations to run, causes this approach to be expensive to carry out. Additionally, increasing the number of data sets leads to many questions during the data collection phase, including: the span of values for the experimental parameter that is varied; the values at which to produce a data set; and the number of data sets to supply in total. The answer to these questions are most likely data-specific and could lead to significant complications during analysis.

5.4 Sequential analysis

In this section and the following, we will look at ways to reduce the number of data sets and the number of choices that must be made when generating the data from that of the combined data set approach in Section 5.3. We first propose a *sequential* approach to the analysis, which was suggested in the original work presenting the GNMM framework [47] and is reminiscent of the step-wise selection technique more widely used in nonlinear system identification [136].

At this point it is clear we can identify the linear observables as necessary terms in the constitutive law across both the linear and nonlinear regimes. In fact, the terms σ , $\dot{\gamma}$, $\dot{\sigma}$, and $\ddot{\gamma}$ are common across all constitutive laws that lie within the GNMM framework [47]. We therefore know that all these terms must be identified when rheoKIC is applied to one of these data sets. We can enforce that non-zero coefficients for the linear observables are retrieved by first supplying data from within the linear viscoelastic regime and only the linear observables as candidates, which will also prevent the higher order observables reducing the accuracy of our predicted coefficients. The original suggestion was that all the linear terms are found together [47]; however, for the oscillatory strain rates that we use here, the $\ddot{\gamma}$ observable derived from this term will automatically be redundant in the linear regime and cause Φ to be rank-deficient, so we instead include it along with the higher order observables. Our steps for applying sequential rheoKIC are as follows:

1. Apply rheoKIC to data from within the linear viscoelastic regime while setting $\Phi = [\sigma, \dot{\gamma}]$.
2. Use the approximations for the coefficients to construct

$$\sigma_{n+1} = \left(1 - \frac{\Delta t}{\tilde{\lambda}}\right)\sigma_n + \Delta t \tilde{G} \dot{\gamma}_n. \quad (5.10)$$

3. Produce data from within the nonlinear viscoelastic regime and using $\omega \leq \frac{1}{\tilde{\lambda}}$
4. Subtract the right-hand side of Eq. 5.10 from data in the nonlinear viscoelastic regime,

$$\sigma_{2:T} - \left(1 - \frac{\Delta t}{\tilde{\lambda}}\right)\sigma_{1:T-1} - \Delta t \tilde{G} \dot{\gamma}_{1:T-1} = -\Delta t \frac{\beta}{\tilde{\lambda}} (\dot{\gamma}^2 \sigma)_{1:T-1}. \quad (5.11)$$

5. Apply rheoKIC to this data where Φ contains only the higher order observables.
6. Reconstruct the full constitutive law.

The importance of Step 3 is twofold. Firstly, we know that rheoKIC struggles the most at high frequencies due to the influence of the Euler approximation step, so a lower frequency will reduce numerical error. The second reason is illustrated in Fig. 5.7: when $\omega \leq 1/\lambda$, the stress response can be fully developed over one oscillatory period and it can be observed as highly nonlinear from looking at its power spectrum. Meanwhile, when $\omega > 1/\lambda$, the stress response is cut short by the rapid change in direction of the applied force on the fluid, and the power spectrum of the stress response indicates that it is only weakly nonlinear. By finding an approximation for λ and setting $\omega \leq 1/\tilde{\lambda}$, we can ensure that rheoKIC ‘sees’ the full dynamics of the fluid in the nonlinear regime.

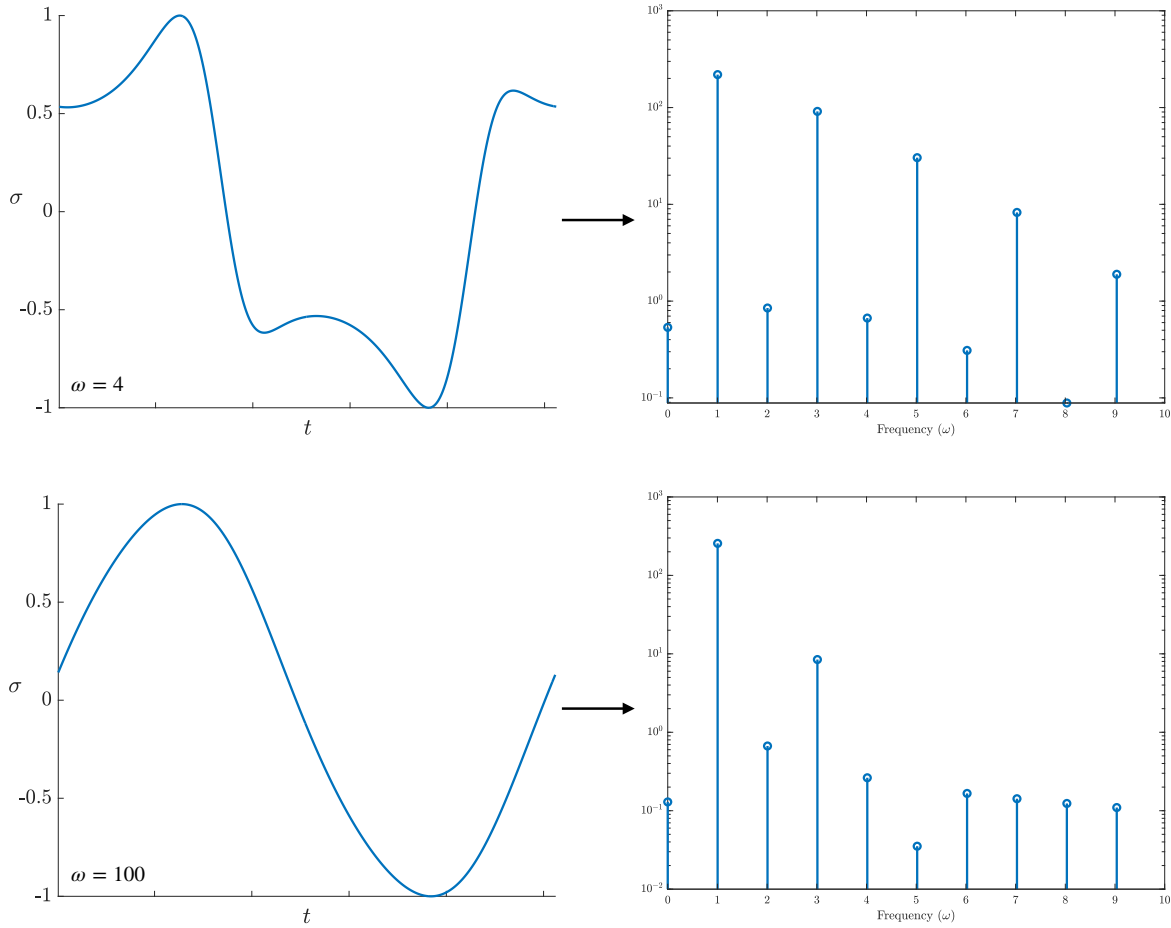


Figure 5.7: Stress response when $\dot{\gamma}_0 = 10$ and (top row) $\omega = 4$ and (bottom row) $\omega = 100$, and their corresponding power spectra.

Before proceeding, it is important to mention very recent work on the effect of fitting data sequentially rather than the standard, simultaneous approach when finding the parameters for a viscoelastic model [137]. By fitting the data sequentially, any cross-correlations between different parameter values are ignored, which can result in falsely high levels of certainty in the parameters that are retrieved. A key difference between our approach and these findings is that they are searching for the material functions $G'(\omega)$ and $G''(\omega)$ as well as their counterparts in the weakly nonlinear regime, whereas we are directly seeking the parameters in the constitutive equation across both the linear and nonlinear regimes. Nevertheless, with this warning in mind we will check our coefficient approximations from the sequential and simultaneous approaches throughout to ensure that they are consistent.

Using data from the linear regime, we set $\dot{\gamma}_0 = 10^{-3}$ and choose the lowest value of ω from

the range that we look at, which for our case is $\omega = 10^{-2}$. This ensures to the best of our abilities that we can observe the full relaxation time of the fluid. Under these values for the experimental parameters, we find $\tilde{\lambda}$ and \tilde{G} with 0.004% and 0.003% error, respectively.

Next, we need to choose values for ω and $\dot{\gamma}_0$ to produce data from within the nonlinear viscoelastic regime, and then apply rheoKIC using data described by Eq. 5.11 and where Φ contains the five higher order observables. Based on the results from the linear regime, we know the ranges for these parameters are $\omega = 10^{-2} - \tilde{\lambda}$ and $\dot{\gamma}_0 > 10^{-3}$. Table 5.3 shows the results for this step using $\omega = [10^{-2}, 10^{-1}, 1/\tilde{\lambda}]$ and $\dot{\gamma}_0 = [1, 10]$.

ω	$\dot{\gamma}$	σ^3	$\sigma^2\dot{\gamma}$	$\dot{\gamma}^2\sigma$	$\dot{\gamma}^3$	$\ddot{\gamma}$
10^{-2}	1	6.98	22.40	23.47	8.45	10^{-8}
10^{-2}	10	56.2	16.70	16.58	54.6	10^{-5}
10^{-1}	1	2.42	1.45	3.83	3.3	10^{-4}
10^{-1}	10	0.44	1.05	1.24	0.22	10^{-3}
$1/\tilde{\lambda}$	1	0.02	0.04	0.36	0.01	10^{-3}
$1/\tilde{\lambda}$	10	0.39	0.07	0.41	10^{-5}	10^{-3}

Table 5.3: Approximated coefficients for the higher order observables when applying sequential rheoKIC.

We would like the coefficient for the $\dot{\gamma}^2\sigma$ to be significantly larger than all the other higher order observables. For the oscillatory frequency, from Table 5.3 it is clear that the second stage of the sequential method should use $\omega = 1/\tilde{\lambda}$ to produce the best outcome. The situation is less clear when it comes to choosing an ideal value for $\dot{\gamma}_0$. Smaller values of $\dot{\gamma}_0$ increases the influence of the higher order parameters, indicating that in general the data must be highly nonlinear for the correct observable to be recognised, although there appears to be a limit to this assumption as using $\dot{\gamma}_0 = 10$ produces less satisfactory results than when using $\dot{\gamma}_0 = 1$: we find k_3 with the smallest amount of error (1.2%), but we also find that the coefficient for the σ^3 observable is of a similar magnitude.

Since we have previously shown how combining multiple data sets strengthens results, we use

this idea again and combine the $\dot{\gamma}_0 = 1$ and $\dot{\gamma}_0 = 10$ data sets while $\omega = 1/\tilde{\lambda}$ to improve on our results. This is shown in Table 5.4.

	Final equation
Correct	$\dot{\sigma} = -1.0\sigma + 1.0\dot{\gamma} - 0.4\dot{\gamma}^2\sigma$
Reconstructed	$\dot{\sigma} = -1.0\sigma + 1.0\dot{\gamma} - 0.405\dot{\gamma}^2\sigma - 0.1279\sigma^3 + 0.0491\sigma^2\dot{\gamma} + 0.000\dot{\gamma}^3 - 0.001\ddot{\gamma}.$

Table 5.4: Final reconstructed constitutive law when applying rheoKIC using the sequential approach and two data sets $\omega = 1/\tilde{\lambda}$, $\dot{\gamma}_0 = 1, 10$.

The approximation for the $\dot{\gamma}^2\sigma$ observable using this combined data set is better than the approximations when using the $\dot{\gamma}_0 = 1$ and $\dot{\gamma}_0 = 10$ data sets individually. The observables $\ddot{\gamma}$ and $\dot{\gamma}^3$ have small enough coefficients to be removed from the reconstruction with minimal disruption, while the coefficient for the σ^3 observable is smaller than in the $\dot{\gamma}_0 = 10$ case but is still not small enough to reasonably be discarded.

5.5 MAPS data

We need to find a method which consistently ensures that only the correct observables are identified. To this end, we look at how data from different experimental protocols can improve our results. In comparison to Section 4.5, which focused on alternative experiments to probe the linear response of the fluid, we now require data that will probe the fluid's nonlinear response to differentiate the signals from the higher order observables.

In Section 5.3 we were successful in identifying the correct terms and their coefficients when concatenating multiple data sets at a different frequencies. The medium amplitude parallel superposition (MAPS) [70] technique instead applies three oscillatory shear tests in concert, as first described in Section 2.5.3. The MAPS protocol used on the SFM results in

$$\begin{aligned}
& \frac{\partial \sigma}{\partial t} = -\frac{1}{\lambda} \sigma + G \dot{\gamma}_{\text{MAPS}} - \frac{\beta}{\lambda} \sigma \dot{\gamma}_{\text{MAPS}}^2 \\
& = -\frac{1}{\lambda} \sigma + G \left[\gamma_0 \omega_0 \sum_{j=1}^3 n_j \cos(n_j \omega_0 t + \alpha_j) \right] - \frac{\beta}{\lambda} \sigma \left[\gamma_0 \omega_0 \sum_{j=1}^3 n_j \cos(n_j \omega_0 t + \alpha_j) \right]^2.
\end{aligned} \tag{5.12}$$

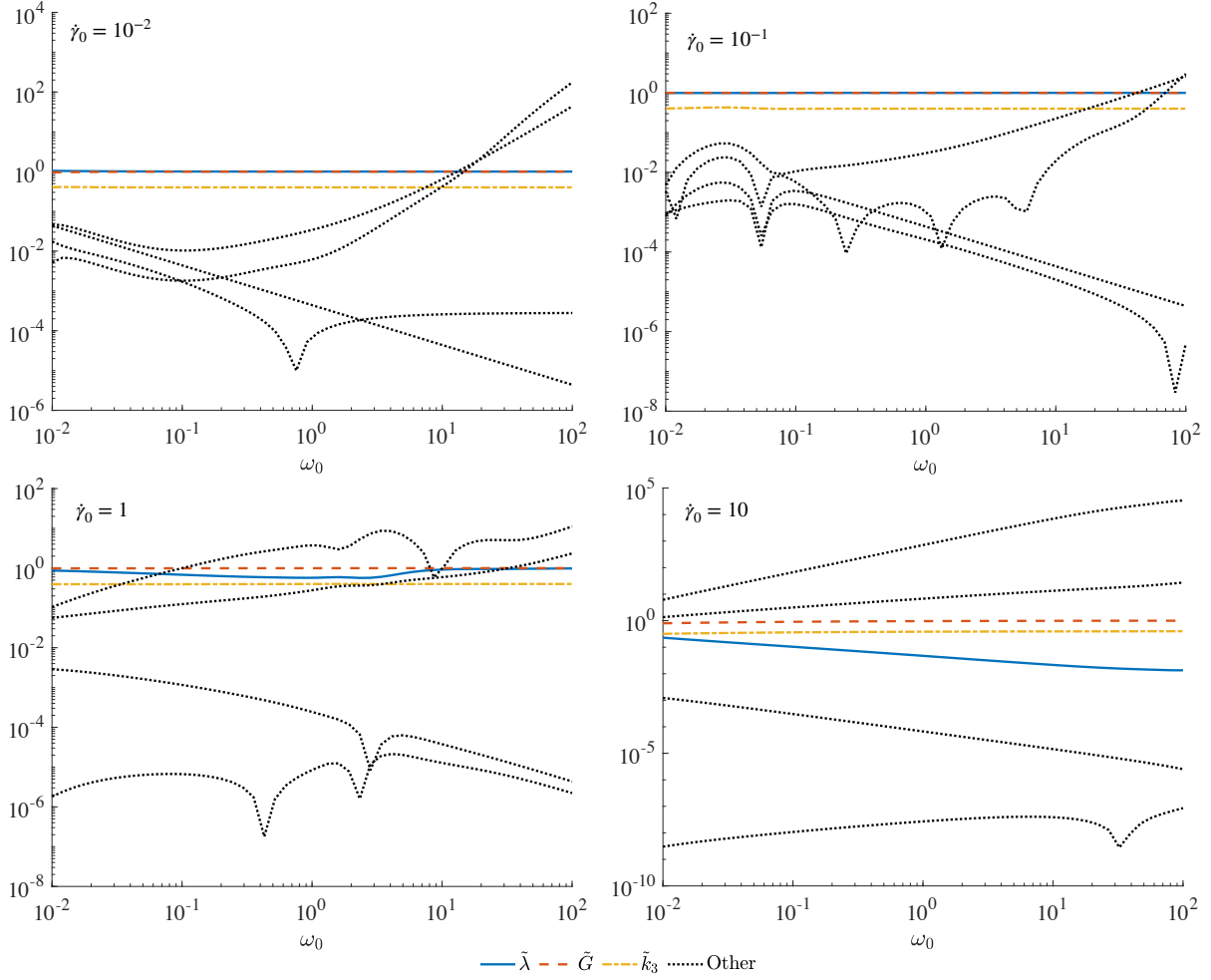


Figure 5.8: RheoKIC applied to MAPS data where $[\omega_1, \omega_2, \omega_3] = [1, 4, 16]\omega_0$.

The three frequencies ω_j are written in terms of a fundamental frequency ω_0 , $[\omega_1, \omega_2, \omega_3] = [n_1, n_2, n_3]\omega_0$. We focus on simulations where there are no phase shifts, $\alpha_j = 0$, and use two sets of frequency triplets which have been proven to probe the higher order frequencies of the data without interfering with each other, $[\omega_1, \omega_2, \omega_3] = [1, 4, 16]\omega_0$ and $[5, 6, 9]\omega_0$ [71]. This leaves us with two remaining experimental parameters, ω_0 and γ_0 , to analyse. As in the ω -

sweep MAOS cases, we vary γ_0 based on ω so that $\dot{\gamma}_0$ is fixed. The simulation is run for 100 of periods of the fastest frequency ω_3 , and then snapshots are recorded for one period of the slowest frequency ω_1 . The time step size has been chosen so that there are 512 measurements for ω_3 .

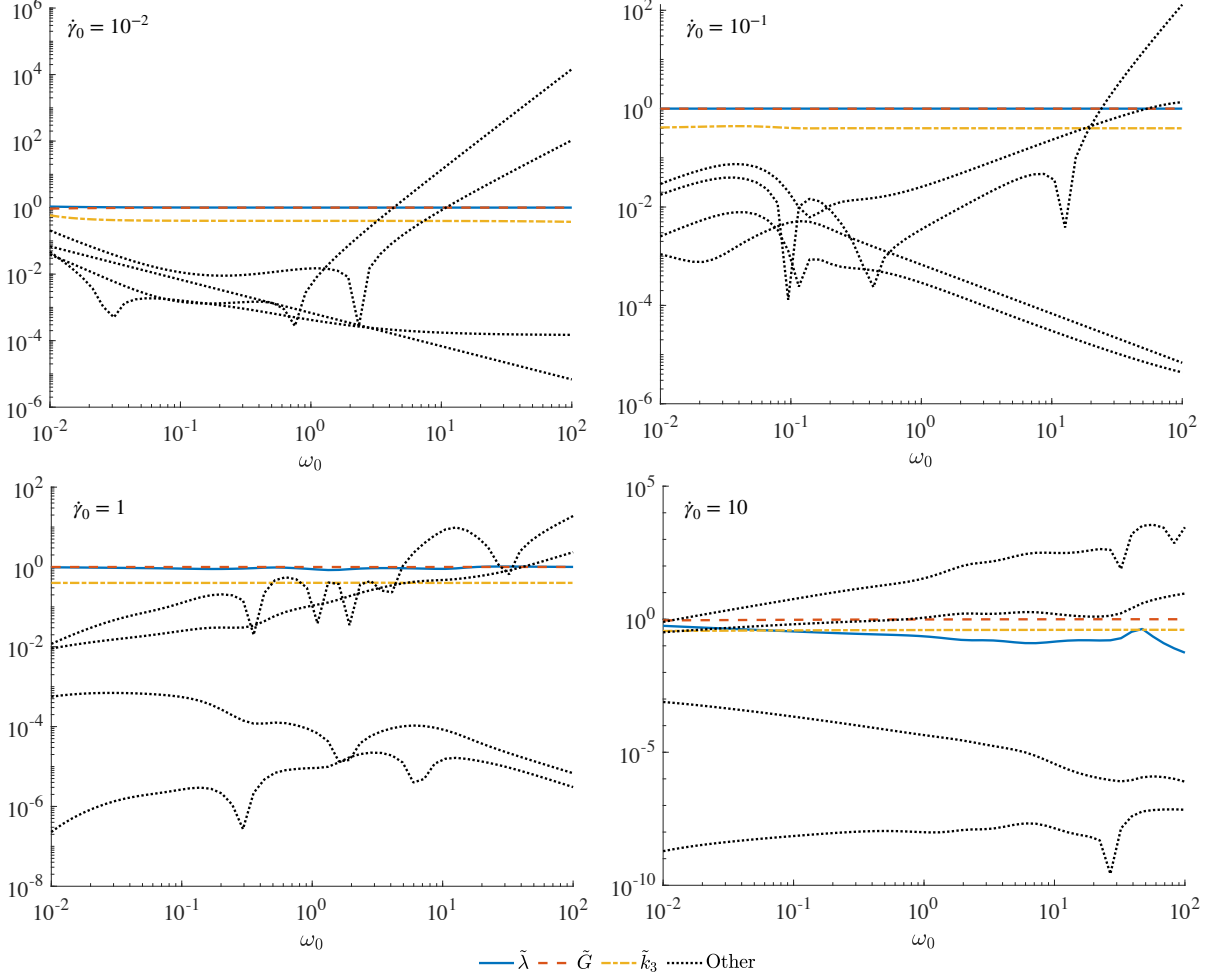


Figure 5.9: RheoKIC applied to MAPS data where $[\omega_1, \omega_2, \omega_3] = [5, 6, 9]\omega_0$.

The results are shown in Fig. 5.8 for the case where $[\omega_1, \omega_2, \omega_3] = [1, 4, 16]\omega_0$ and Fig. 5.9 for the case where $[\omega_1, \omega_2, \omega_3] = [5, 6, 9]\omega_0$. For both triplets we find that the smaller strain rate amplitudes $\dot{\gamma}_0 = 10^{-2}$ and $\dot{\gamma}_0 = 10^{-1}$ produce the longest range of values for ω_0 where $\tilde{\lambda}$ and \tilde{G} are stable and also where \tilde{k}_3 is the most distinguishable coefficient from the higher order observables. As before, rheoKIC does not consider the $\dot{\gamma}^2\sigma$ observable necessary when setting $\dot{\gamma}_0 \leq 10^{-3}$. In general we find that the $[1, 4, 16]\omega_0$ frequency triplet produces marginally

better results than the $[5, 6, 9]$ triplet. In both cases, Φ has full rank when $\dot{\gamma}_0 \geq 10^{-1}$, while $\text{rank}(\Phi) = 6$ for $\omega > 30$ when $\dot{\gamma} = 10^{-2}$, .

Fig. 5.10 shows the approximations for exclusively the terms in the SFM constitutive law parameters when $\dot{\gamma} = 10^{-1}$. In contrast to Fig. 5.6, we retrieve good approximations for all parameters despite the inclusion of the full set of GNMM observables, and the largest deviations are found at the low frequencies rather than at the high frequencies. The \tilde{k}_3 value is most influenced by the presence of the other observables.

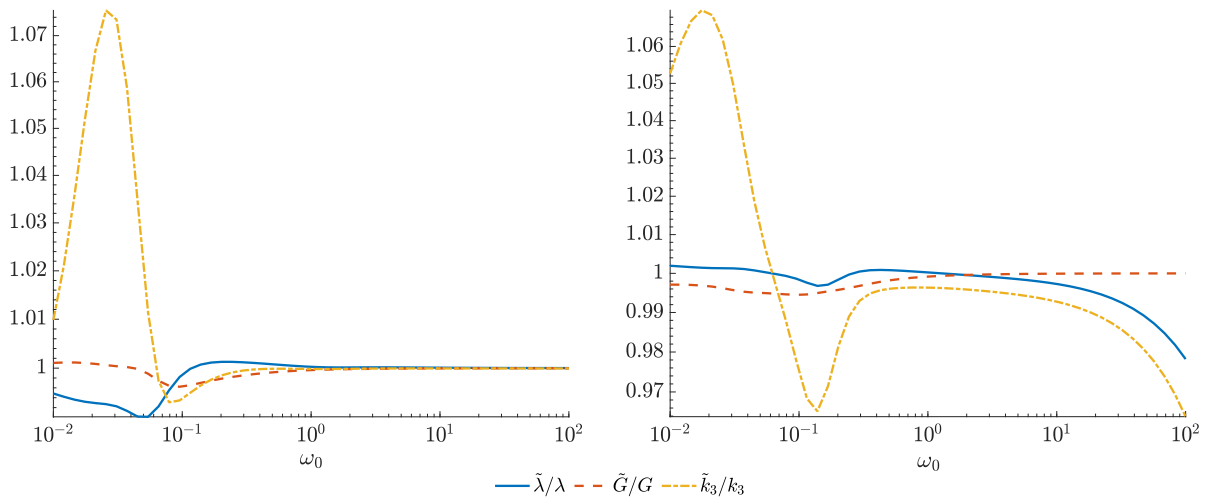


Figure 5.10: Approximations for the SFM constitutive law parameters applied to MAPS data where (left) $[\omega_1, \omega_2, \omega_3] = [1, 4, 16]\omega_0$ and (right) $[\omega_1, \omega_2, \omega_3] = [5, 6, 9]\omega_0$. The full set of 7 GNMM observables has been provided in both cases.

In Section 5.4, through judicious choice of the experimental parameters we were able to isolate the correct observables and find good approximations for their parameters with just two data sets, although unfortunately with the inclusion of one extra higher order observable which could not be discarded. The MAPS experimental protocol was originally designed to speed up material identification by producing the same results as when carrying out a full frequency sweep of experiments within just one experiment. Since we have no ability to narrow down the choice of values for the experimental parameters between data sets as we did in the sequential method, we need the separation of the correct observables from the higher order observables to

be robust across a wide range of ω and $\dot{\gamma}_0$.

We can compare the robustness of MAPS data to that of other experimental protocols by looking at the coefficients before the final rescaling step,

$$C = \mathbf{X}'\mathbf{V}\mathbf{S}^{-1}\mathbf{U}^T, \quad (5.13)$$

where \mathbf{X}' is the data for σ from the second snapshot onward, and the other matrices come from the SVD of Φ . If it is possible to reliably separate the correct observables from the unnecessary observables at this stage, then the unnecessary observables could be removed as in the sequential method described earlier but without having to run multiple experiments.

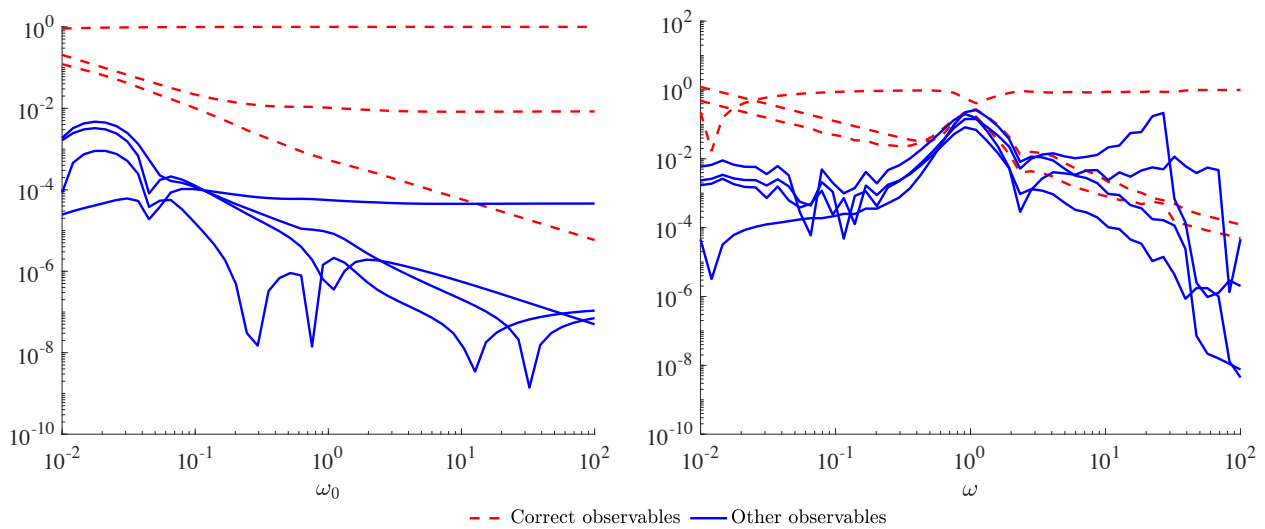


Figure 5.11: Values for the coefficients C described in Eq. 5.13 using data from (left) MAPS data where $[\omega_1, \omega_2, \omega_3] = [1, 6, 14]\omega_0$ and (right) ω -sweep MAOS data. In both cases, $\dot{\gamma}_0 = 10^{-1}$ and the full set of 10 GNMM observables has been provided.

In Fig. 5.11 we compare the coefficients produced by MAPS with those produced by a ω -sweep MAOS simulation, both carried out when $\dot{\gamma}_0 = 10^{-1}$. All MAPS data sets apart from those at the very highest values of ω show a clear separation between the correct observables and the others. Meanwhile, for the ω -sweep MAOS case, the correct observables are significantly closer in magnitude to the observables which should be discarded and there is considerable

interference at high frequencies. With this in mind, we propose the following steps for including a ‘thresholding’ step when using MAPS data:

1. Use the MAPS protocol setting a low value of ω_0 . The choice for $\dot{\gamma}_0$ needs to be just high enough such that Φ is full rank.
2. Compute the SVD of Φ containing the full set of GNMM observables constructed from the MAPS data.
3. Determine which observables are necessary from observing the magnitude of the coefficients computed with Eq. 5.13.
4. Create a new, reduced Φ containing only the necessary observables and proceed with the rest of the steps of rheoKIC.

This process is slightly different from the sequential rheoKIC steps described earlier in that here we are using a single, nonlinear data set, and choosing the entries in Φ based on the coefficients from the pseudo inverse step. The threshold for the coefficient size must be determined on a case-by-case basis by considering the entries in C . The constitutive laws produced from this protocol using $\omega_0 = 10^{-2}$ are presented in Table 5.5.

$\dot{\gamma}_0$	Final equation
Correct	$\dot{\sigma} = -1.0\sigma + 1.0\dot{\gamma} - 0.4\dot{\gamma}^2\sigma$
10^{-3}	$\dot{\sigma} = -0.999\sigma + 1.0\dot{\gamma}$
10^{-2}	$\dot{\sigma} = -0.999\sigma + 0.999\dot{\gamma} - 0.389\dot{\gamma}^2\sigma$
10^{-1}	$\dot{\sigma} = -0.998\sigma + 0.999\dot{\gamma} - 0.398\dot{\gamma}^2\sigma$
1	$\dot{\sigma} = -0.975\sigma + 0.997\dot{\gamma} - 0.399\dot{\gamma}^2\sigma$
10	$\dot{\sigma} = -0.649\sigma + 0.92\dot{\gamma} - 0.368\dot{\gamma}^2\sigma$

Table 5.5: Reconstructed constitutive laws when applying rheoKIC to a single MAPS data set, then reducing the set of candidate observables based on the coefficients from the pseudo inverse step. $\lambda = G = 1$, $\beta = 0.4$, $[\omega_1, \omega_2, \omega_3] = [1, 4, 16]10^{-2}$ in all cases.

As before, at very low strain rate amplitudes we retrieve the linear Maxwell model and the $\dot{\gamma}^2\sigma$ observable is discarded. The correct three observables are successfully selected for all other choices of $\dot{\gamma}_0$. We find excellent accuracy to within a fraction a percentage of error for most of the coefficients, with decay in the accuracy for the σ observable at $\dot{\gamma}_0 = 10$. With these results in mind, we can say that the MAPS protocol allows for a constitutive law containing higher order terms to be reconstructed using a single data set - however, there is only a window of strain rate amplitudes where it is successful, and the identification of this window may require more measurements to be taken.

Returning to the sequential approach from Section 5.4, applying this thresholding technique reduces Φ in the second stage of the method to $\Phi = [\sigma^3, \dot{\gamma}^2\sigma]$. The final reconstructed constitutive law is

$$\dot{\sigma} = -1.0\sigma + 1.0\dot{\gamma} - 0.400\dot{\gamma}^2\sigma - 0.0692\sigma^3. \quad (5.14)$$

The approximation for k_3 is found with just a 0.03% error. The σ^3 observable is smaller by around one order of magnitude than the $\dot{\gamma}^2\sigma$ observable and so it is possible that a practitioner would remove it during thresholding, but ideally we would like the difference between the magnitudes to be larger than this for it to be more definitive. Using a combination of sequential analysis, combined data sets, and thresholding, we therefore appear to achieve successful results when using oscillatory data only. This approach required several more data sets and decisions to be made by the practitioner in comparison to the MAPS approach, but the fact that we achieve very high accuracy for the coefficients we do correctly identify makes it worthy of exploring further.

5.6 Effect of noise on rheoKIC

Before moving onto more complex constitutive laws, it is important that we address the potential issue of noisy data when applying rheoKIC. It has been found [101] that one of the most

sensitive parameters when using DMD is the signal-to-noise (SNR) ratio: the ratio between the strength of the ‘true’ signal we wish to record and the strength of the background noise [138]. Fortunately, advances in rheometer technology and sensor hardware have meant that noise in the output signal is kept small, with reported values of the true signal being up to four orders of magnitude higher than noise during LAOS experiments [138]. Be that as it may, it is necessary that we understand any impact noise produces on the results when applying rheoKIC. We will also provide various solutions for how noisy signals should be treated during its application.

We will consider two main sources of noise:

1. Error during the applied deformation $\dot{\gamma}(t) \rightarrow \dot{\gamma}(t) + \tilde{\dot{\gamma}}(t)$.
2. Error during the measurement of the stress response $\sigma(t) \rightarrow \sigma(t) + \tilde{\sigma}(t)$.

Alternative sources of error include uncertainties from the geometry of the rheological setup [30] as well as rheometer calibration errors [50], but we consider these beyond the scope of this thesis. We will additionally consider only the impact of Gaussian noise with zero mean, and entrust that structural errors such as measurement drift are identified and corrected for during the experimental process.

We first look at the results from rheoKIC where we apply different levels of noise to vary the SNR of the resulting signal and where no measures have been taken to remove it. For each of the data sets used to produce the coefficient approximations, additional noise has first been applied to $\dot{\gamma}$, which is then used to compute σ , and finally additional noise with the same SNR is added to σ , incorporating both types of error listed above. The Matlab function `awgn` is used in both cases, which applies white Gaussian noise to the signal in order to achieve the specified SNR.

Fig. 5.12(left) shows the coefficient approximations when applying the protocol we developed in Section 5.4 to oscillatory data, while Fig. 5.12(right) shows the coefficient approximations using a data set from a MAPS simulation. For the oscillatory data case, we find there is no impact on the accuracy of our results once $\text{SNR} > 200$, while the results from the MAPS data are not affected until the $\text{SNR} < 100$.

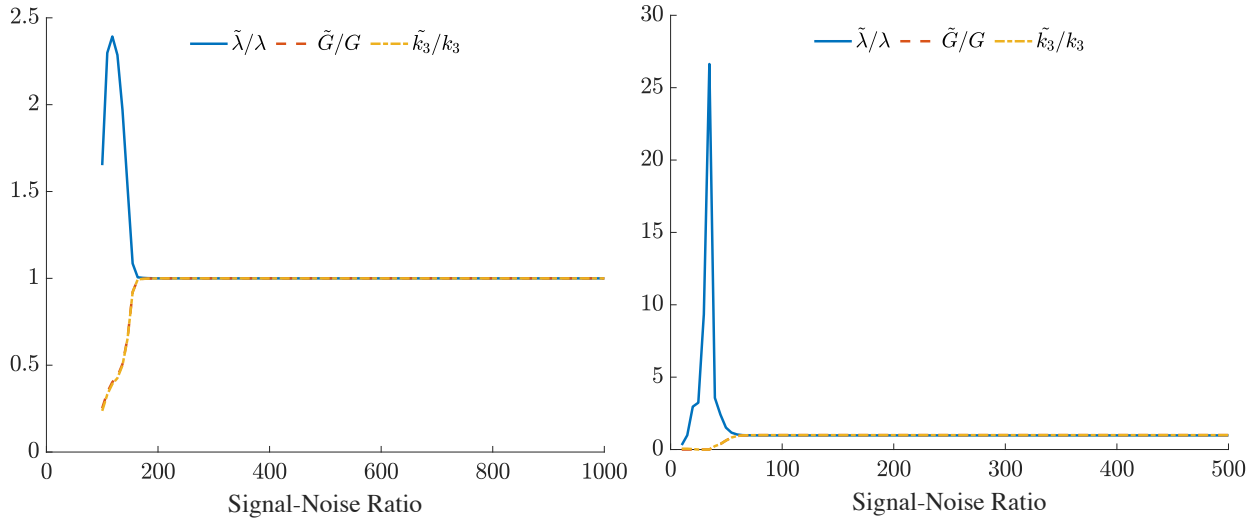


Figure 5.12: Approximated coefficients (normalised) as Gaussian white noise is added to both $\dot{\gamma}$ and σ to produce data with different SNR values. (Left) Oscillatory data analysed with the method developed in Section 5.4. (Right) MAPS data with thresholding applied during analysis.

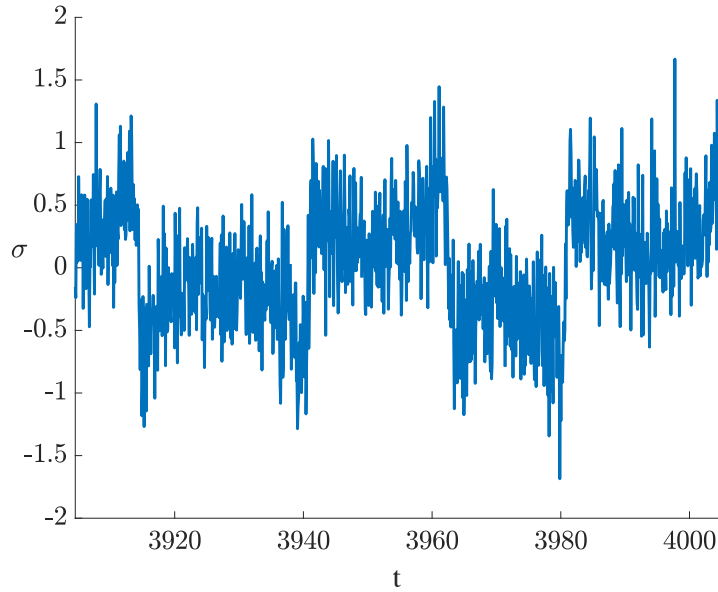


Figure 5.13: MAPS data where $\omega = 0.01$, $\dot{\gamma}_0 = 1$, $[\omega_1, \omega_2, \omega_3] = [1, 4, 16]$, and with a SNR of 50.

Since we will be considering spatial measurements in Chapter 7, which potentially will incur much greater levels of noise than that expected from a standard rheometer, we will also focus on data with a low SNR. An example of σ from a MAPS data set where white noise has been

applied to both $\dot{\gamma}$ and σ with a SNR of 50 is shown in Fig. 5.13. The reconstructed constitutive law using this data is

$$\dot{\sigma} = -1.452\sigma + 0.659\dot{\gamma} - 0.263\dot{\gamma}^2\sigma. \quad (5.15)$$

Remarkably, the correct observables have still successfully been isolated despite the level of noise, although the coefficients themselves are not very accurate. We have multiple options for pre-processing this data at our disposal to remove the noise and potentially improve upon this result.

A straight-forward way to remove noise from data is to apply a low-pass filter, which removes higher frequencies from data, or a low-pass filter which removes the lower frequencies [104]. In either case we must choose an attenuation point at which these frequencies are reduced to zero in the data set. We can use our knowledge of the construction of the MAPS signal to determine the attenuation point of a low-pass filter: from the process of intermodulation [139], and taking into account the fact that we are only considering constitutive laws with terms up to cubic order, we know that the triplet of frequencies used to produce this data will only appear at frequencies up to 48ω [70]. We can therefore use 48ω as the start of our low-pass filter and be confident that we are not removing essential features from the data. The reconstructed constitutive law after applying a low-pass filter with this attenuation point becomes

$$\dot{\sigma} = -1.187\sigma + 0.813\dot{\gamma} - 0.325\dot{\gamma}^2\sigma. \quad (5.16)$$

This is a very straightforward method which relies exclusively on known features of the applied input signal, but all of the approximated coefficients are now significantly more accurate. There are many ways in which the method of removing noise could be improved upon, including averaging over multiple data sets [103] and applying more complicated filters such as rolling average filters [140]. There are also multiple modifications to DMD-type methods to account for data noise, of which we listed several in Section 3. However, this exploration has served to

confirm that rheoKIC can comfortably handle the levels of noise that one might expect to see within standard rheological data without requiring modification.

5.7 Conclusions

In this chapter we have demonstrated that rheoKIC can be readily extended to the identification of a constitutive law containing a nonlinear term. The SFM constitutive law reduces to the linear Maxwell model when the amplitude of the strain rate, $\dot{\gamma}_0$, is small. We can observe this transition to nonlinearity the classical way, by looking at the frequency spectrum of σ , or alternatively by checking whether Φ is under-determined.

Since the nonlinear term in the model depends quadratically on $\dot{\gamma}_0 = \gamma_0\omega$, it is difficult to perform a sweep across multiple frequencies while staying within the weakly nonlinear regime. Using the ω -sweep MAOS technique ensures that viscoelastic regime remains the same across all frequencies.

We investigated several modifications to the rheoKIC method and the data sets themselves to improve our results. Combining data sets across frequencies and across strain rate amplitudes produces good results, but this approach required multiple experiments and the outcome is highly dependent on the practitioner's decisions regarding which data sets to use. Applying rheoKIC sequentially to a SAOS and then a LAOS data set allows us to find the linear observables robustly and with excellent accuracy. Using a single nonlinear data set for the second stage of rheoKIC approximated the coefficient for the correct higher order observable we know we need to good accuracy, but the other higher order observables are predicted to have coefficients with a similar order of magnitude which makes them difficult to discard. Using both of these methods in concert - a linear data set first, followed by a combined data set from two nonlinear simulations - allows us to discard the majority of the spurious higher order observables from our final equation.

With a data set inspired by the MAPS experimental protocol, rheoKIC consistently identifies which observables are necessary over a wide choice of values for the experimental parameters.

We can then discard observables with small coefficients by using a thresholding technique and rerun rheoKIC using the reduced set of candidate observables on the same data set to improve our model accuracy. The reconstructed equation for the SFM constitutive law requires analysis upon only one data set, retrieves exactly the correct observables, and returns predictions for the coefficients with only fractions of percentage points in error.

Finally, we investigated the performance of rheoKIC on oscillatory and MAPS data with varying levels of Gaussian noise. We found that both data sets performed well for signal-to-noise ratios as low as 100 : 1. A simple low-pass filter was shown to significantly improve results when using data with higher levels of noise, and the attenuation point of the filter can be determined based on our knowledge of the applied shear rate. We also identified multiple avenues that could be pursued both within signal pre-processing and throughout the method to improve these results further.

Chapter 6: Applications to systems of nonlinear equations

The previous chapters have focused exclusively on constitutive laws where the only non-trivial equation for the stress evolution is a function of $\dot{\gamma}$ and σ_{xy} exclusively. We now move onto considering a more complex constitutive law which is expressed by a system of evolution equations that includes multiple elements of the stress tensor.

The constitutive law we have chosen to analyse is the non-stretching Rolie-Poly model, which we will refer to as the ‘nRP’ model throughout. The origins of the nRP model lie in the GLaMM constitutive law [141], a detailed model for linear, entangled polymer chains that incorporates relaxation from multiple sources: chain stretching, convective constraint release, contour length fluctuations, and chain diffusion. While highly sophisticated, it is computationally expensive and requires detailed information concerning the molecular structure of the suspension. A course-grained version of the GLaMM model is the ‘ROuse LInear Entangled POLYmers’ (Rolie-Poly) model [142] where the fluctuations of contour length are not considered. A final assumption of fast chain stretch relaxation reduces this to the nRP model.

We firstly assume that the total stress $\underline{\underline{\Sigma}}$ can be decomposed into a combination of a viscoelastic component $\underline{\underline{\sigma}}$ and a Newtonian component with viscosity η ,

$$\underline{\underline{\Sigma}} = \underline{\underline{\sigma}} + 2\eta\underline{\underline{e}} - p\underline{\underline{I}} \quad (6.1)$$

where $\underline{\underline{e}} = \frac{1}{2}(\nabla\underline{u} + (\nabla\underline{u})^T)$ is the symmetric rate of strain tensor and p is the isotropic pressure.

We continue to assume that the fluid is incompressible

$$\nabla \cdot \underline{u} = 0 \quad (6.2)$$

and also divergence-free

$$\nabla \cdot \underline{\underline{\Sigma}} = 0 \quad (6.3)$$

which determines p in Eq. 6.1. Writing the viscoelastic stress $\underline{\underline{\sigma}}$ in terms of a conformation tensor $\underline{\underline{W}}$,

$$\underline{\underline{\sigma}} = G(\underline{\underline{W}} - \underline{\underline{I}}), \quad (6.4)$$

ensures that the isotropic stress is zero when no external force is being applied. Under this type of flow, the evolution of $\underline{\underline{W}}$ governed by the nRP equations is [49]

$$\frac{\partial W_{xy}}{\partial t} = \dot{\gamma} \left[W_{yy} - \frac{2}{3}(1 + \beta)W_{xy}^2 \right] - \frac{1}{\lambda}W_{xy}, \quad (6.5a)$$

$$\frac{\partial W_{yy}}{\partial t} = \frac{2}{3}\dot{\gamma} \left[\beta W_{xy} - (1 + \beta)W_{xy}W_{yy} \right] - \frac{1}{\lambda}(W_{yy} - 1). \quad (6.5b)$$

The equation for \dot{W}_{xx} can be decoupled and solved trivially [142]. With initial conditions

$$W_{xy}(t = 0) = 0, \quad (6.6a)$$

$$W_{yy}(t = 0) = 1, \quad (6.6b)$$

we update W_{xy} and W_{yy} according to Eq. 6.5, then compute the elements of σ and Σ according

to Eq. 6.4 and Eq. 6.1 respectively. We use 12800 time steps per oscillatory period for accuracy, and then down-sample so that 512 data points per period are used for analysis.

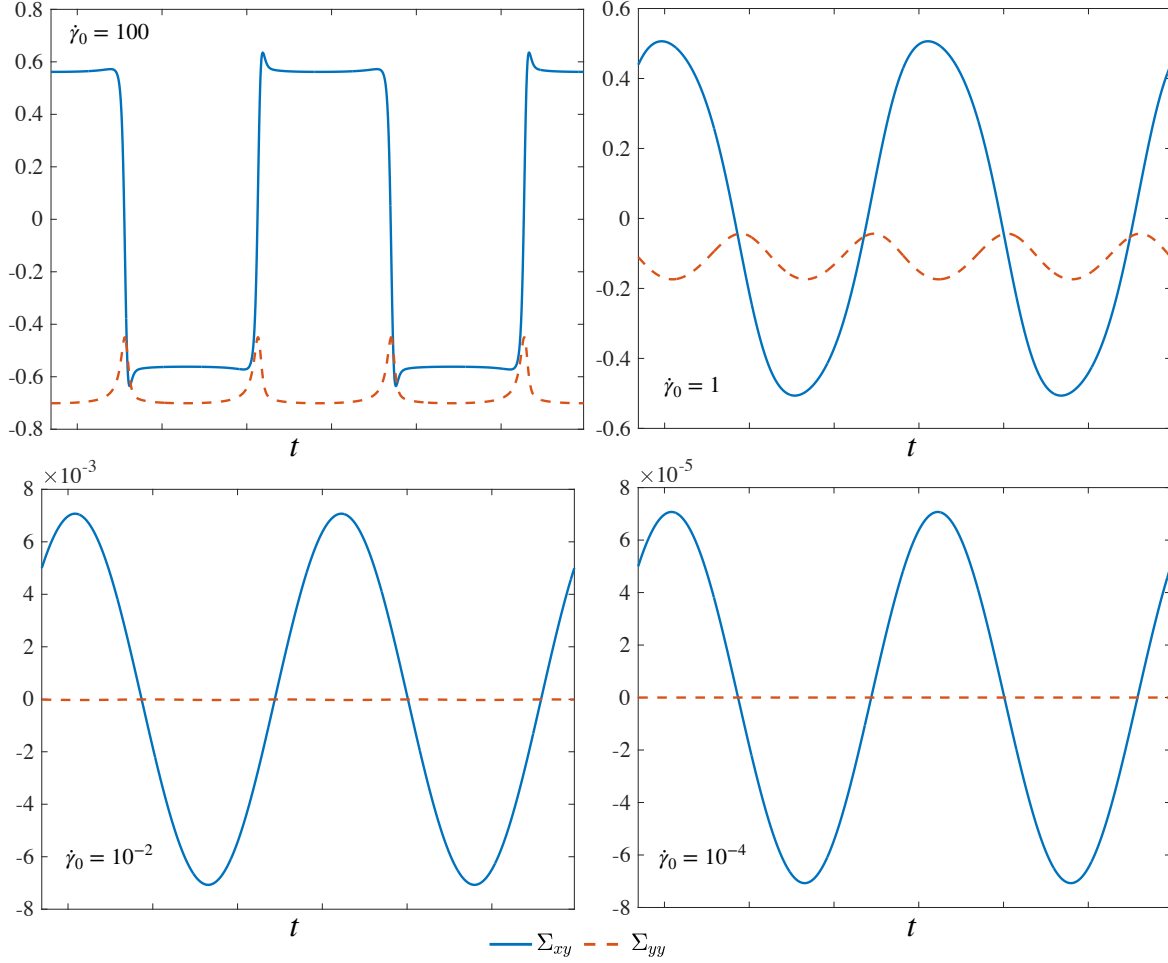


Figure 6.1: Examples of Σ_{xy} and Σ_{yy} from the nRP model after 20 oscillatory periods have elapsed, for different values of $\dot{\gamma}_0$. In all cases $G = \lambda = \omega = 1$, $\beta = 0.4$, $\eta = 10^{-5}$.

Examples of the stress response for different values of $\dot{\gamma}_0 = \gamma_0 \omega$ are shown in Fig. 6.1. We find that the magnitude of σ_{yy} is always smaller than that of σ_{xy} . When $\dot{\gamma}_0$ is very small, for example when $\dot{\gamma}_0 = 10^{-4}$ as in the bottom right of Fig. 6.1, $\sigma_{yy} \approx 0$ to order $O(10^{-9})$ while σ_{xy} is of order $O(10^{-5})$. For this reason, it is important to check whether Φ is rank-deficient at low strain rate amplitudes similarly to how the $\dot{\gamma}^2 \sigma$ term degenerated at small amplitudes when analysing the SFM data in Chapter 5.

While Eq. 6.5 is the standard set of equations when referring to the nRP model, we cannot measure $\underline{\underline{W}}$ directly - we can only record the total stress response of the fluid $\underline{\underline{\Sigma}}$. Using Eqs. 6.1-

6.5, we write the nRP evolution equations in terms of $\underline{\underline{\Sigma}}$ as

$$\dot{\Sigma}_{xy} - \eta\ddot{\gamma} = -\frac{1}{\lambda}\Sigma_{xy} + (G + \frac{\eta}{\lambda})\dot{\gamma} + \dot{\gamma}\Sigma_{yy} - \frac{2}{3G}(1 + \beta)\dot{\gamma}\Sigma_{xy}^2 + \frac{4\eta}{3G}(1 + \beta)\dot{\gamma}^2\Sigma_{xy} - \frac{2\eta^2}{3G}(1 + \beta)\dot{\gamma}^3 \quad (6.7a)$$

$$\dot{\Sigma}_{yy} = -\frac{1}{\lambda}\Sigma_{yy} - \frac{2}{3}\dot{\gamma}\Sigma_{xy} + \frac{2\eta}{3}\dot{\gamma}^2 - \frac{2}{3G}(1 + \beta)\dot{\gamma}\Sigma_{xy}\Sigma_{yy} + \frac{2\eta}{3G}(1 + \beta)\dot{\gamma}^2\Sigma_{yy}. \quad (6.7b)$$

We need to determine the observables to include in Φ . Since we now have a system of two equations to reconstruct, the terms involving Σ_{yy} must also be included. Based on the terms in the GNMM laid out in Section 3.6, the sets of candidate observables for the elements of the stress tensor being evolved become

$$\Phi_{xy} = [\Sigma_{xy}, \dot{\gamma}, \Sigma_{xy}\Sigma_{yy}, \dot{\gamma}\Sigma_{yy}, \Sigma_{xy}^3, \Sigma_{xy}\Sigma_{yy}^2, \dot{\gamma}^3, \dot{\gamma}^2\Sigma_{xy}, \dot{\gamma}\Sigma_{xy}^2, \dot{\gamma}\Sigma_{yy}^2, \ddot{\gamma}], \quad (6.8a)$$

$$\Phi_{yy} = [\Sigma_{yy}, \Sigma_{xy}^2, \Sigma_{yy}^2, \dot{\gamma}^2, \dot{\gamma}\Sigma_{xy}, \Sigma_{yy}^3, \Sigma_{xy}^2\Sigma_{yy}, \dot{\gamma}^2\Sigma_{yy}, \dot{\gamma}\Sigma_{xy}\Sigma_{yy}]. \quad (6.8b)$$

We find that for the off-diagonal element of the stress tensor there are four more observables in comparison to the previous chapters so that in total $K_{xy} = 11$. We also see that quadratic order terms, which in Chapter 4 we demonstrated were not needed in Φ_{xy} , all are present in Φ_{yy} . There are $K_{yy} = 9$ observables in total which may represent the evolution of Φ_{yy} .

6.1 Initial analysis

Eq. 6.7 can be rewritten in a form suitable for rheoKIC as

$$\begin{aligned}
\begin{bmatrix} \Sigma_{xy} \\ \Sigma_{yy} \end{bmatrix}_{n+1} &= \begin{bmatrix} 1 - \frac{\Delta t}{\lambda} & 0 & \Delta t(G + \frac{\eta}{\lambda}) \\ 0 & 1 - \frac{\Delta t}{\lambda} & 0 \end{bmatrix} \begin{bmatrix} \Sigma_{xy} \\ \Sigma_{yy} \\ \dot{\gamma} \end{bmatrix}_n \\
&+ \Delta t \begin{bmatrix} 1 & -\frac{2}{3G}(1 + \beta) & 0 & 0 \\ 0 & 0 & -\frac{2}{3} & -\frac{2}{3G}(1 + \beta) \end{bmatrix} \begin{bmatrix} \dot{\gamma} \Sigma_{yy} \\ \dot{\gamma} \Sigma_{xy}^2 \\ \dot{\gamma} \Sigma_{xy} \\ \dot{\gamma} \Sigma_{xy} \Sigma_{yy} \end{bmatrix}_n \\
&+ \Delta t \eta \begin{bmatrix} 1 & \frac{4}{3G}(1 + \beta) & 0 & 0 \\ 0 & 0 & \frac{2}{3} & -\frac{2}{3G}(1 + \beta) \end{bmatrix} \begin{bmatrix} \ddot{\gamma} \\ \Sigma_{xy} \dot{\gamma}^2 \\ \dot{\gamma}^2 \\ \Sigma_{yy} \dot{\gamma}^2 \end{bmatrix}_n \\
&+ \Delta t \eta^2 \begin{bmatrix} -\frac{2}{3G}(1 + \beta) \\ 0 \end{bmatrix} \dot{\gamma}_n^3.
\end{aligned} \tag{6.9}$$

The terms have been separated as much as possible by their order with respect to η , the reason for which we will explain in Sec. 6.1.1. Fig. 6.2 shows the results from applying rheoKIC to nRP data with different values of $\dot{\gamma}_0$ and using Φ_{xy} and Φ_{yy} from Eq. 6.8. All signals have been rescaled to unit magnitude before the pseudoinverse is applied to ensure that no rank deficiency is caused by the relative magnitudes of the signals being large. The scaling is then reverted back when the signal coefficients are approximated. As usual, we find that the correct observables are more easily distinguishable from the other observables as $\dot{\gamma}_0$ is increased. The predicted coefficients for the correct observables are not stable across the full range of frequencies. Furthermore, several of the other observables have coefficients of a similar or higher magnitude and so would not be discarded using the thresholded type approach in the previous chapter.

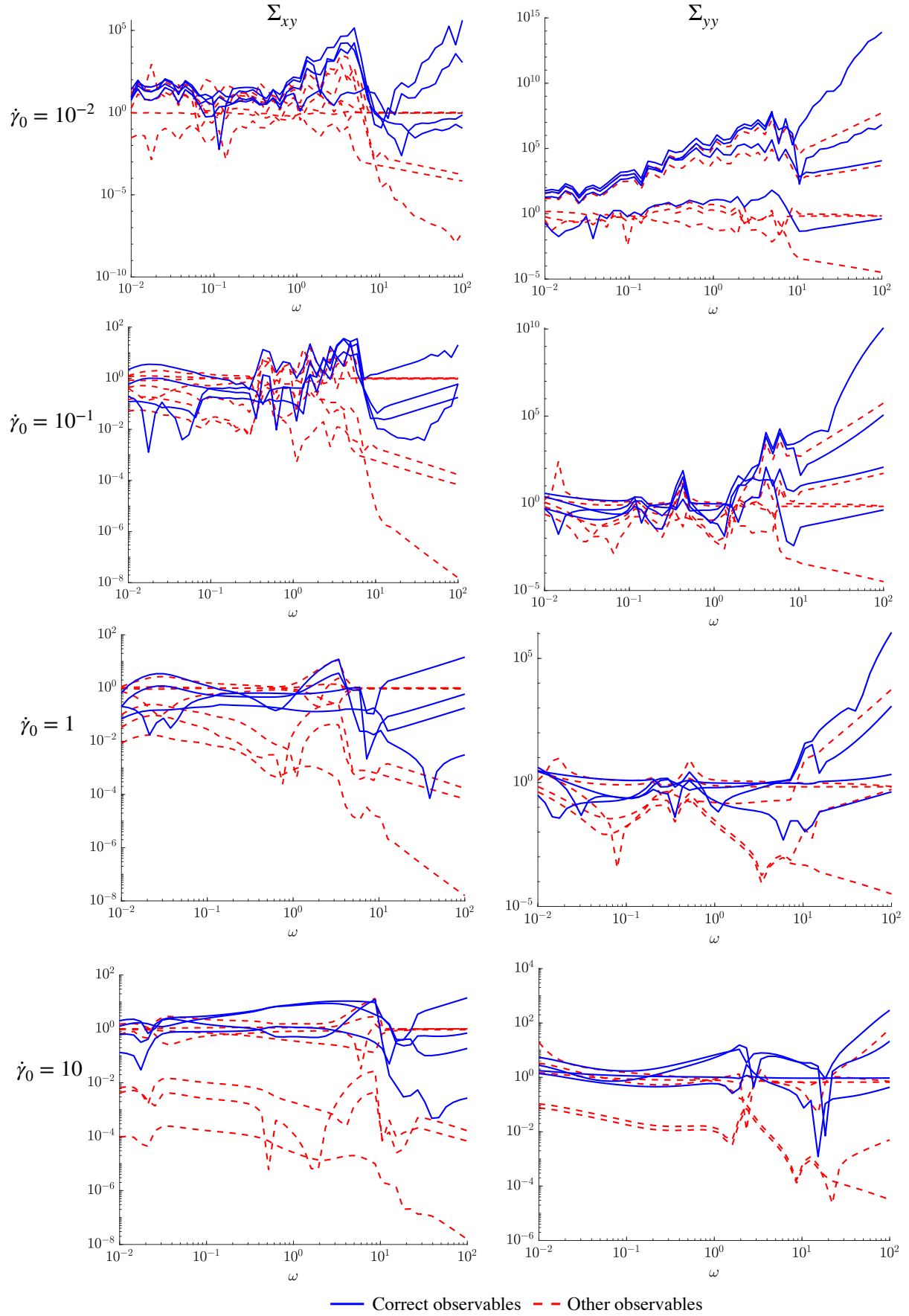


Figure 6.2: Predicted coefficients for observables using Φ_{xy} and Φ_{yy} from Eq. 6.8 and data from the nRP model where $G = \lambda = 1$, $\beta = 0.4$, $\eta = 10^{-5}$.

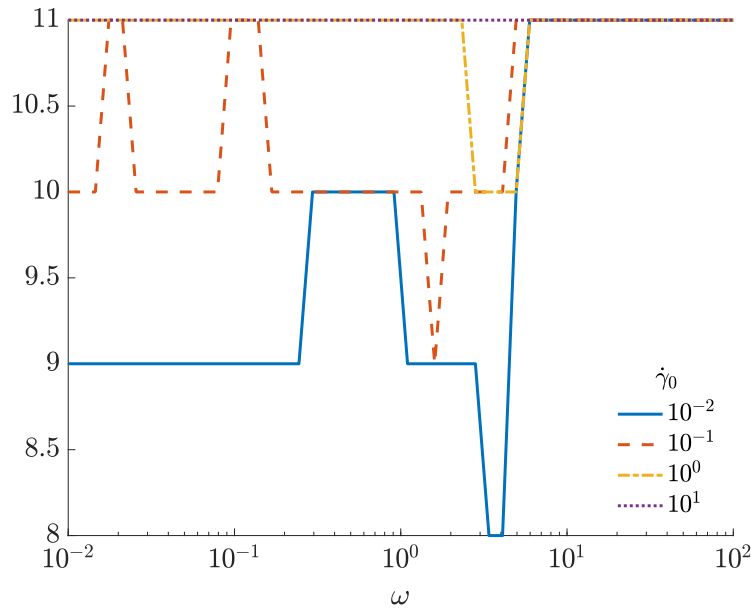


Figure 6.3: The rank of Φ_{xy} where $K_{xy} = 11$ and data comes from the nRP model, for different strain rate magnitudes $\dot{\gamma}_0$.

In Fig. 6.3 we show the rank of Φ_{xy} for the different choices of $\dot{\gamma}_0$. The set of observables is rank deficient for the majority of ω when $\dot{\gamma}_0 = 10^{-2}$ and $\dot{\gamma}_0 = 10^{-1}$, then becomes full rank for roughly when $\omega > 5$. When $\dot{\gamma}_0 = 10$, Φ_{xy} is primarily full rank and sometimes rank 10 or lower, which we can find is due to either the $\Sigma_{yy}^2 \Sigma_{xy}$ or $\dot{\gamma} \Sigma_{yy}^2$ observable being degenerate. Φ_{yy} is always full rank regardless of $\dot{\gamma}_0$, bearing in mind that $K_{yy} = 9$.

6.1.1 Effect of the viscosity term

In Eq. 6.8 we separated the terms as much as possible by the order of the solvent viscosity, η . The solvent viscosity is typically of order $O(10^{-4})$ or smaller [143] for fluids that can be modelled appropriately with the nRP equations, while the coefficients G , λ , and β for the types of fluids we are looking at are often $O(1)$ (and in fact $0 \leq \beta \leq 1$ by construction) [142]¹. It therefore may not be reasonable to expect rheoKIC to be able to pick out the terms multiplied by η or η^2 when their relative magnitudes are so much smaller, especially when the full set of GNMM observables is being used or when the data is corrupted with some level of measurement

¹In theory, it may be possible to enforce that any approximation for β lies within this range by including an additional constraint during the pseudo inverse step, although this lies beyond the scope of the thesis [136].

noise.

While $\eta = 10^{-5}$ for the fluid we are looking at, as is recommended in the literature [49], we can vary its value in our simulations to see how its magnitude relative to the other fluid parameters affects our predictions. Fig. 6.4 shows the predicted and actual coefficient values for an experiment where $\omega = \dot{\gamma}_0 = 1$ but η is varied.

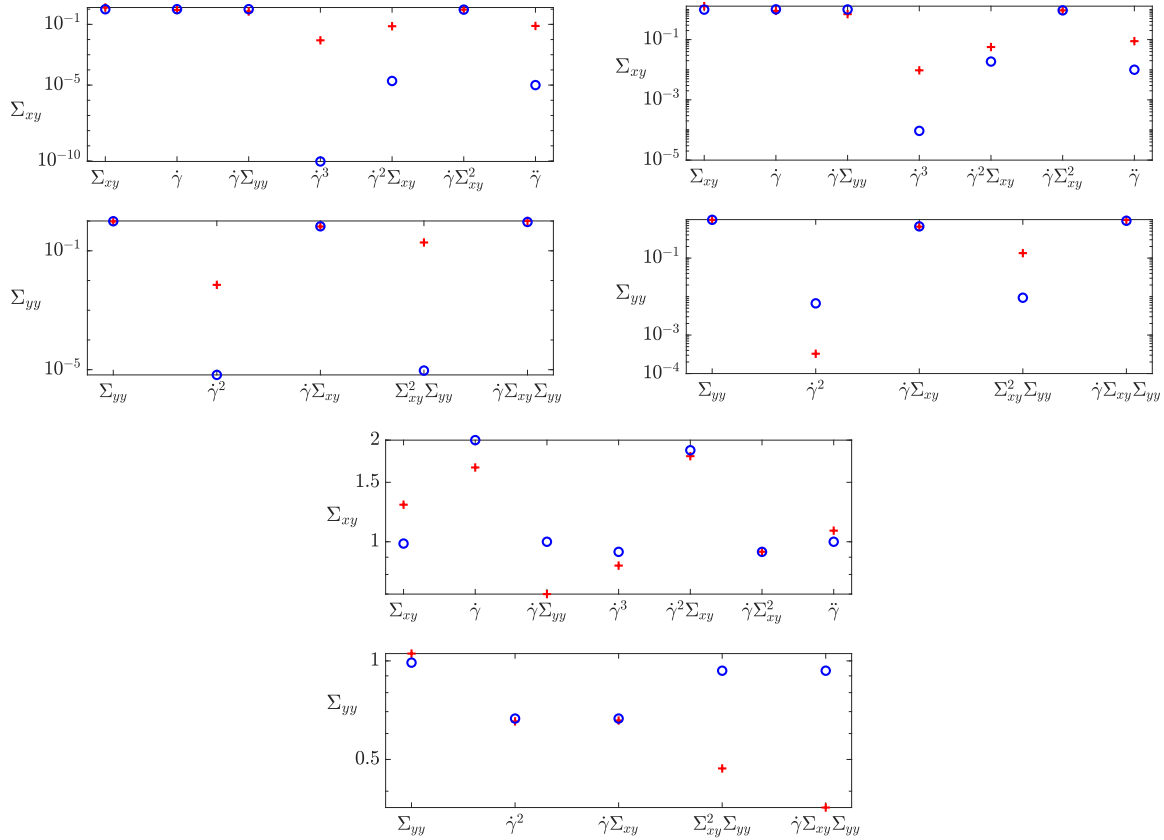


Figure 6.4: Predicted (red crosses) versus correct (blue circles) coefficients for observables where (top left) $\eta = 10^{-5}$, (top right) $\eta = 10^{-2}$, and (bottom) $\eta = 1$. In all cases $\omega = \dot{\gamma}_0 = 1$. The exact observables have been supplied for clarity.

Using a physically realistic value for η , $\eta = 10^{-5}$, means that the coefficients for the terms multiplied by η and η^2 cannot be identified correctly. The discrepancy between the η and η^2 coefficients and the predicted coefficients has decreased for $\eta = 10^{-2}$, while for $\eta = 1$ we retrieve a similar level of approximation for all coefficients including the one multiplied by η^2 . However, this type of test is not feasible in reality: changing the value of η means the fluid under observation is also being changed. We see two possible avenues for resolving this issue:

1. We assume that the dynamic viscosity for the solvent is well-characterised and can be subtracted from the calculations according to Eq. 6.1;
2. In the cases where the solvent viscosity of the solvent is so small as to be negligible for modelling the fluid, the terms with a magnitude of $O(\eta)$ or smaller have negligible impact on the constitutive law and can be discarded with little effect on the reconstruction error.

Either avenue results in dismissing the $O(\eta)$ and $O(\eta^2)$ terms from the equation as unnecessary during the rheoKIC process. The nRP equations without these terms involving η are then

$$\dot{\Sigma}_{xy} = -\frac{1}{\lambda}\Sigma_{xy} + G\dot{\gamma} + \dot{\gamma}\Sigma_{yy} - \frac{2}{3G}(1 + \beta)\dot{\gamma}\Sigma_{xy}^2 \quad (6.10a)$$

$$\dot{\Sigma}_{yy} = -\frac{1}{\lambda}\Sigma_{yy} - \frac{2}{3}\dot{\gamma}\Sigma_{xy} - \frac{2}{3G}(1 + \beta)\dot{\gamma}\Sigma_{xy}\Sigma_{yy}. \quad (6.10b)$$

6.2 Combined data sets

Even when we no longer consider terms involving η , there are still many observables which are unnecessary for reconstructing the constitutive law that have large coefficients - in other words, there are ‘false positive’ terms which we must somehow remove. The values of the coefficients are also not consistent over a range of oscillatory frequencies. As before, we approach the problem by first creating data sets at a fixed value of $\dot{\gamma}_0$ but different choices of ω , and concatenate the data sets before using them in rheoKIC to see if this improves our approximations. We also look at applying rheoKIC to data from the converse scenario, where ω is fixed and we use concatenated data where $\dot{\gamma} = [10^{-2}, 10^{-1}, 1, 10]$. The results are shown in Fig. 6.5 and Fig. 6.6, respectively.

Firstly, for the combined ω data set shown in Fig. 6.5, we see that we accurately locate the coefficients for the linear and quadratic coefficients for all values of $\dot{\gamma}_0$, but we only find the coefficient for the cubic observable $\dot{\gamma}\Sigma_{xy}\Sigma_{yy}$ when $\dot{\gamma}_0 \geq 1$. In all cases we find that there are many false positives, and increasing $\dot{\gamma}_0$ causes the magnitudes of their coefficients to decrease

until they are of a similar magnitude to the correct observables coefficients. Choosing even higher values of $\dot{\gamma}_0$ causes the accuracy of the coefficients for the correct observables to degrade.

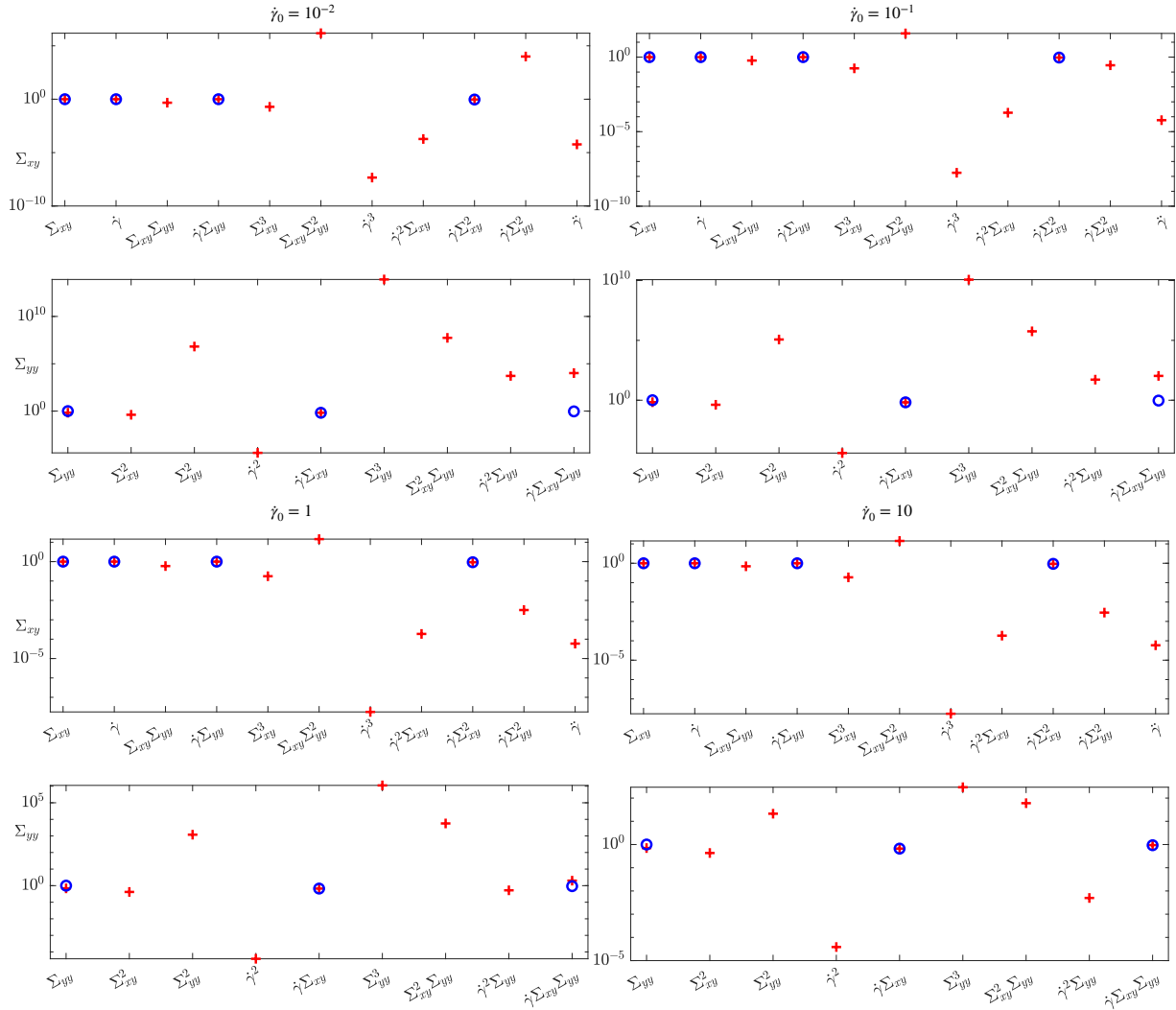


Figure 6.5: Predicted (red crosses) versus correct (blue circles) coefficients for observables where the data has been concatenated from simulations where $\dot{\gamma}_0$ is fixed and ω is varied.

When we combine data from multiple amplitudes at a fixed frequency, shown in Fig. 6.6, the issue of failing to find the cubic observable coefficient in some cases does not occur - this is because each data set contains a combination of linear, weakly nonlinear, and fully nonlinear data, causing the higher order dynamics to be visible. Instead, we find that in general the accuracy of the predicted coefficients improves as the chosen value for ω is increased, while the issue of false positives is still prevalent.

For both choices of combined data sets from multiple oscillatory experiments, we still find that

the coefficients for some of the higher order observables are so large as to be considered ‘necessary’ for reconstructing the constitutive law, despite Φ being full rank. We can see the impact of these extra observables by comparing the normed difference between a data reconstruction using the predicted coefficients for the correct observables only, and a reconstruction using the predicted coefficients for all the observables. The total improvement in the data reconstruction when using these extra observables is $O(10^{-4})$. The unnecessary observables are therefore being used for marginal gains in increasing the reconstruction accuracy, which is a key indicator that the signals are overfitting to the data.

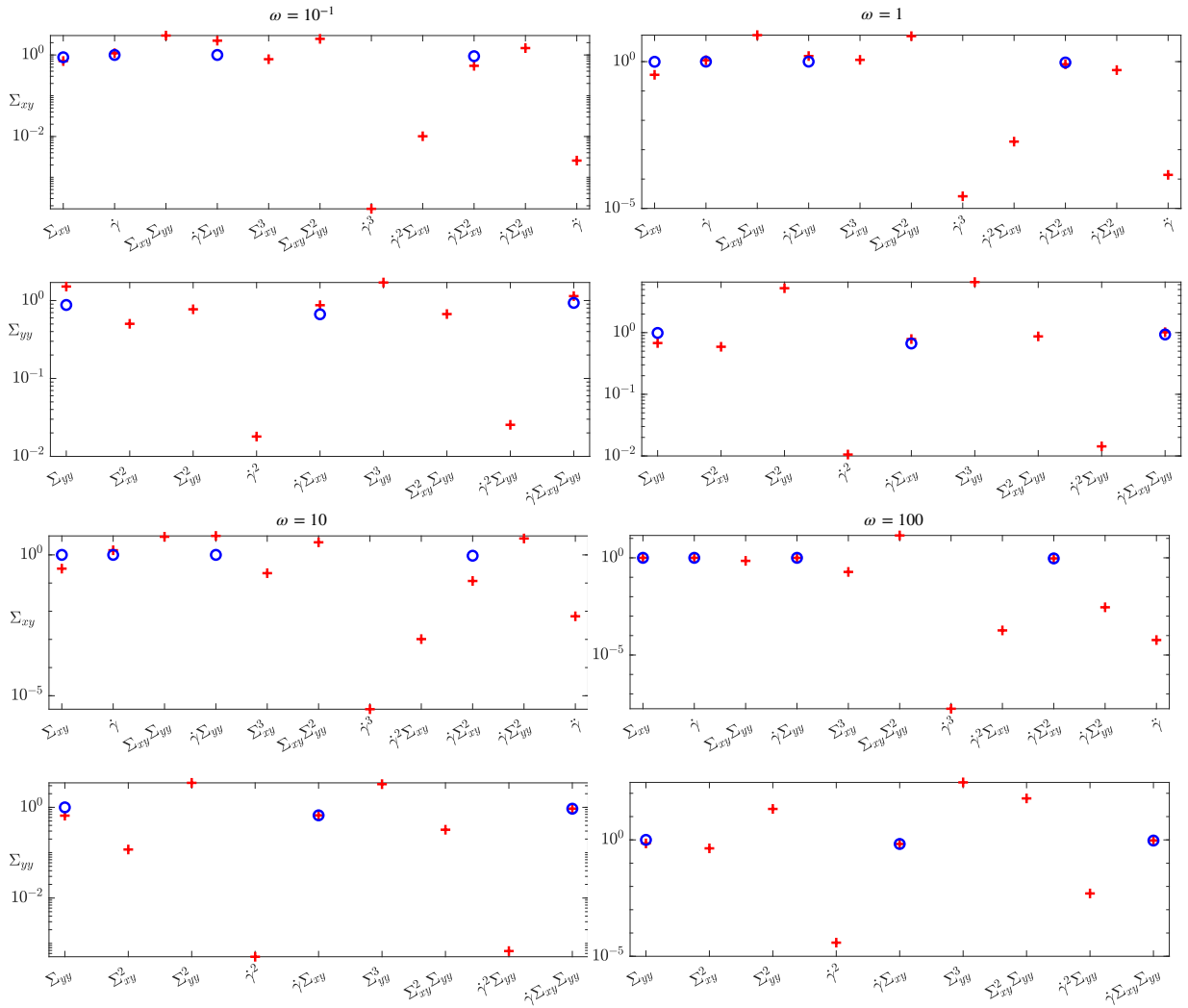


Figure 6.6: Predicted (red crosses) versus correct (blue circles) coefficients for observables where the data has been concatenated from simulations where ω is fixed and $\dot{\gamma} = [10^{-2}, 10^{-1}, 1, 10]$.

6.3 Sequential analysis

Instead of supplying all the candidate observables simultaneously, we try the same procedure as in Sec. 5.4 and apply sequential analysis to the standard oscillatory data: compute a low frequency, small amplitude data set to find the parameters for the linear terms, then find the higher order observables and their coefficients with a nonlinear data set. At small amplitudes, Eqs. 6.7 reduce to

$$\dot{\Sigma}_{xy} = -\frac{1}{\lambda}\Sigma_{xy} + (G + \frac{\eta}{\lambda})\dot{\gamma} \quad (6.11a)$$

$$\dot{\Sigma}_{yy} = -\frac{1}{\lambda}\Sigma_{yy}. \quad (6.11b)$$

Notably, the equation for Σ_{yy} can be solved using the initial condition $\Sigma_{yy}(t=0) = 1$ to find

$$\Sigma_{yy} = e^{-\frac{t}{\lambda}}. \quad (6.12)$$

Since we are considering data at longer time scales $t \gg 0$, Eq. 6.12 reduces to zero and the evolution for Σ_{yy} becomes trivial. We subsequently retrieve the linear Maxwell model

$$\Sigma_{xy}^{n+1} = \left(1 - \frac{\Delta t}{\lambda}\right)\Sigma_{xy}^n + G\dot{\gamma}^n \quad (6.13)$$

for the nRP equations at small strain rate amplitudes, to which we apply rheoKIC. Setting $\Phi = [\Sigma_{xy}, \dot{\gamma}]$, and the experimental parameters as $\omega = 10^{-2}$ and $\dot{\gamma} = 10^{-2}$, we find the coefficients for Σ_{xy} and $\dot{\gamma}$ with errors of 0.0015% and 0.02% respectively.

After computing $\tilde{\lambda}$ and \tilde{G} as in Eq. 4.14, we subtract the linear terms from the higher order data via

$$\Sigma'_{xy} \rightarrow \Sigma'_{xy} - \left(1 - \frac{\Delta t}{\tilde{\lambda}}\right) \Sigma_{xy} - \Delta t \tilde{G} \dot{\gamma} \quad (6.14a)$$

$$\Sigma'_{yy} \rightarrow \Sigma'_{yy} - \left(1 - \frac{\Delta t}{\tilde{\lambda}}\right) \Sigma_{yy} \quad (6.14b)$$

,

where the presence of an apostrophe indicates the data matrices of snapshots $2, \dots, T$ and the absence indicates the data matrices of snapshots $1, \dots, T - 1$. The equations we intend to reconstruct using rheoKIC once the linear terms have been successfully removed are the nRP equations containing only the higher order terms,

$$\Sigma'_{xy} = \dot{\gamma} \Sigma_{yy} - \frac{2}{3G} (1 + \beta) \dot{\gamma} \Sigma_{xy}^2 \quad (6.15a)$$

$$\Sigma'_{yy} = -\frac{2}{3} \dot{\gamma} \Sigma_{xy} - \frac{2}{3G} (1 + \beta) \dot{\gamma} \Sigma_{xy} \Sigma_{yy}. \quad (6.15b)$$

Fig. 6.7 shows the predicted values for the quadratic and cubic observables once a second simulation is carried out using $\omega = \frac{1}{\tilde{\lambda}}$ and $\dot{\gamma}_0 = 1$, as the results in the previous chapter have shown these are suitable choices for the second round of the sequential method. The sets of candidate observables are full rank ($\Phi_{xy} = 9$ and $\Phi_{yy} = 8$) for the second pass of the method. We see that we have good accuracy for the Σ_{yy} coefficients, while the Σ_{xy} coefficients are slightly less accurate. This is due to the influence of spurious higher order observables rather than an issue with the sequential method itself: if only the correct observables $\dot{\gamma} \Sigma_{yy}$ and $\dot{\gamma} \Sigma_{xy}^2$ are provided, we retrieve all coefficients with excellent accuracy.

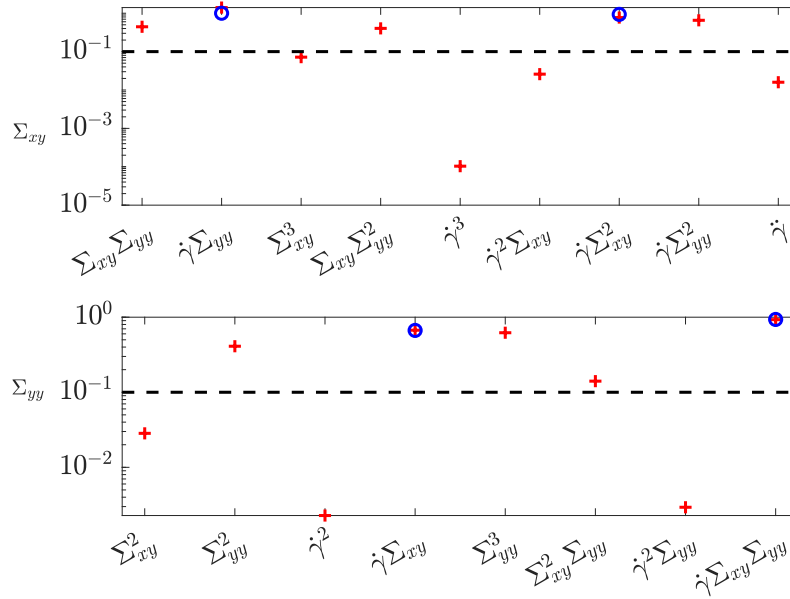


Figure 6.7: Predicted (red crosses) versus correct (blue circles) coefficients when applying sequential rheoKIC to data representing an nRP fluid. The black dashed line is located at 10^{-1} .

We can also see in Fig. 6.7 that there is a separation in the magnitudes of the observable coefficients, indicated by a dashed black line at 10^{-1} . In Chapter 4, we looked at removing the quadratic observables due to their small coefficients and rerunning the analysis on the subsequent reduced Φ . Here, we may need to choose different thresholds for each stress evolution equation based on the relative magnitudes of the coefficients. Using 10^{-1} as our threshold as a first pass, we reduce the number of observables to 5 for both Σ_{xy} and Σ_{yy} , although the actual terms themselves are different in each equation.

The results of re-applying the second stage of rheoKIC to only the observables above the threshold are shown in Fig. 6.8. For Σ_{yy} we have lost accuracy in predicting the coefficient for $\dot{\gamma}\Sigma_{xy}\Sigma_{yy}$ and all of the coefficients are of a very similar size, ranging between 0.6 and 1. It is unlikely that someone would reduce Φ_{yy} further based on these results. For Σ_{xy} , we can see that the next logical step would be to discard the $\Sigma_{xy}\Sigma_{yy}$ and $\dot{\gamma}\Sigma_{yy}^2$ observables. The consequences of iterating the thresholding step using the threshold shown in Fig. 6.8 are laid out in Fig. 6.9. We eventually identify the correct observables and predict their coefficients to within 2% error.

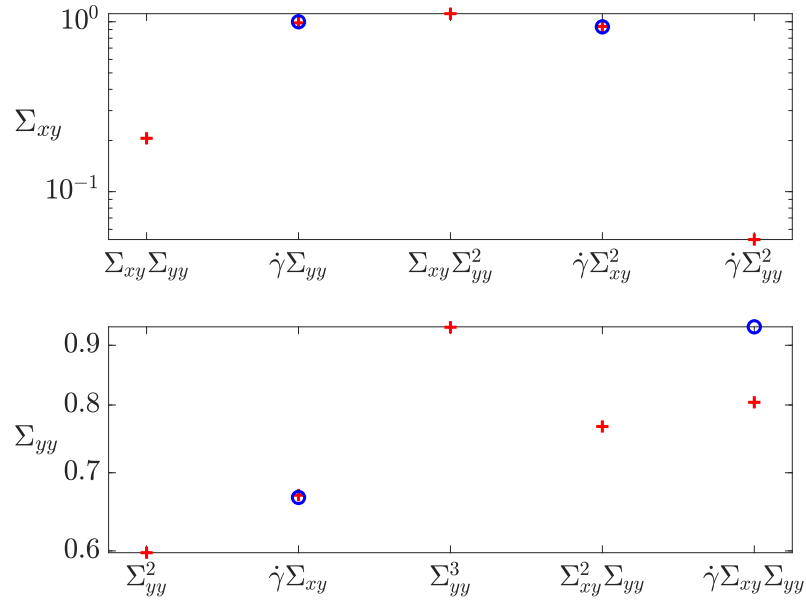


Figure 6.8: Predicted (red crosses) versus correct (blue circles) coefficients when the second step of sequential has been applied using only the observables with coefficients above the black dashed line in Fig 6.7.

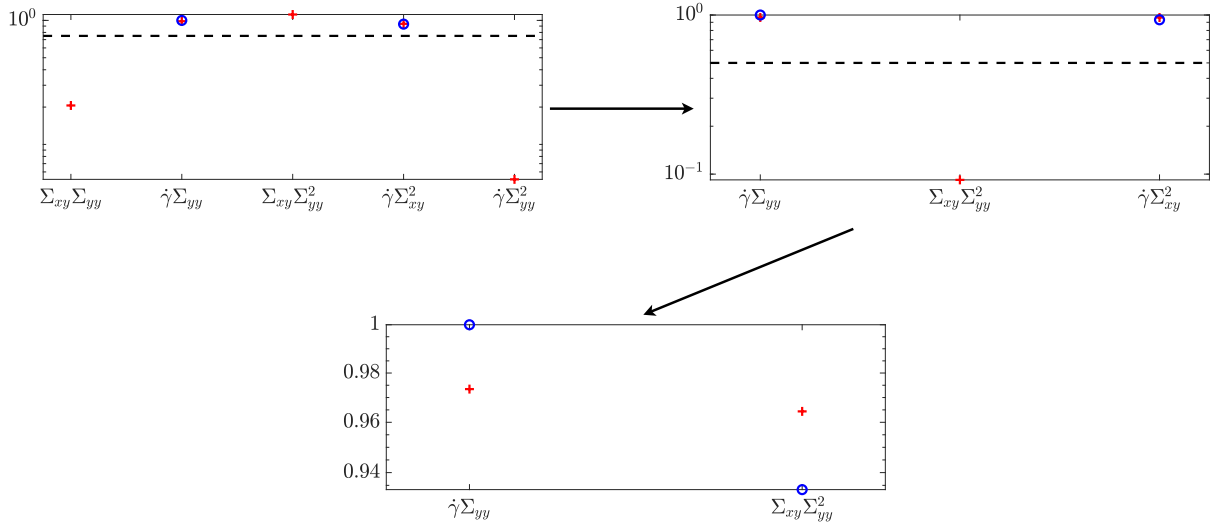


Figure 6.9: Predicted (red crosses) versus correct (blue circles) coefficients from an application of rheoKIC where the results in the top row are as in Fig. 6.8, then rheoKIC is iteratively applied while the candidate observables for Σ_{xy} are removed based on the thresholds shown by the dashed lines.

The reconstructions for both equations from Fig. 6.8 and Fig. 6.9 are laid out in Table 6.1. The accuracy for the linear terms in both equations is very good due to the initial linear step. While

we have managed to reconstruct the equation for Σ_{xy} very well, we have significant errors in both the observables and their coefficients for Σ_{yy} . It is also possible that, given a data set with different values for the experimental or fluid parameters, the accuracy of the final result might be entirely different. It is clear that iteratively removing observables based on their coefficients is not going to be universally successful here, despite it being essentially an analogue version of the sequentially-thresholded least squares method used in SINDy and its extensions [124].

$\dot{\Sigma}_{xy}$	
Correct	$-1.000\Sigma_{xy} + 1.000\dot{\gamma} + 1.000\dot{\gamma}\Sigma_{yy} - 0.933\dot{\gamma}\Sigma_{xy}^2$
Predicted	$-1.000\Sigma_{xy} + 1.000\dot{\gamma} + 0.973\dot{\gamma}\Sigma_{yy} - 0.964\dot{\gamma}\Sigma_{xy}^2$
$\dot{\Sigma}_{yy}$	
Correct	$-1.000\Sigma_{yy} - 0.667\dot{\gamma}\Sigma_{xy} - 0.933\dot{\gamma}\Sigma_{xy}\Sigma_{yy}$
Predicted	$-1.000\Sigma_{yy} - 0.669\dot{\gamma}\Sigma_{xy} - 0.804\dot{\gamma}\Sigma_{xy}\Sigma_{yy} - 0.598\Sigma_{yy}^2 + 0.933\Sigma_{yy}^3 - 0.767\Sigma_{xy}^2\Sigma_{yy}$

Table 6.1: Final reconstructed equations for $\dot{\Sigma}_{xy}$ and $\dot{\Sigma}_{yy}$ when applying rheoKIC sequentially, then reducing the set of candidate observables based on the coefficients from the pseudo inverse step. $\lambda = G = 1$, $\beta = 0.4$.

6.3.1 Combined data sets with sequential and thresholded analysis

In the previous chapter, we tested a combination of the three tools we have developed for robustly identifying the constitutive equations: using combined data sets to improve the ability to locate the correct higher order observables; extracting approximations for the linear observables first with high accuracy by applying rheoKIC sequentially; and applying a SINDy-inspired ‘thresholded’ technique to remove from consideration any observables whose coefficients are relatively small compared to the others. We now have significantly more quadratic and cubic observables that need to be removed and the combinations of these tools requires further investigation.

Based on the results we have been building up over this chapter and those preceding it, we propose the following steps for reconstructing the constitutive law using oscillatory data:

1. Produce a data set within the linear viscoelastic regime and with low ω .
2. Use this data set to extract the approximated coefficients \tilde{G} and $\tilde{\lambda}$ for the linear observables that must be present in the constitutive law.
3. Produce multiple data sets where $\omega = 1/\tilde{\lambda}$ and $\dot{\gamma}_0$ is high enough to induce a nonlinear stress response and concatenate them.
4. Use Eq. 6.14 on this data to remove the impact of the linear observables.
5. Apply rheoKIC to this data to retrieve first approximations to the coefficients for the higher order observables.
6. If any coefficients are significantly smaller than the others, use the thresholding technique to remove the corresponding observables from those under consideration and rerun rheoKIC on the data set with the reduced Φ .

Within Step 6, we use the ‘rule of thumb’ that a distinction can be drawn between groups of observables to keep and observables to discard if there is a gap larger than an order of magnitude in size between them. The value of the threshold may therefore vary between each iteration as the coefficient predictions are updated rather than a fixed threshold being used for an entire data set. Other metrics to determine the threshold location include the Akaike information criterion and the Bayesian information criterion, which would be particularly well-suited to cases where there are many more candidate observables than the number proposed here [128].

The results of this approach are shown in Fig. 6.10 where for Step 2 we used two data sets with strain rate amplitudes $\dot{\gamma}_0 = 1$ and $\dot{\gamma}_0 = 10$.

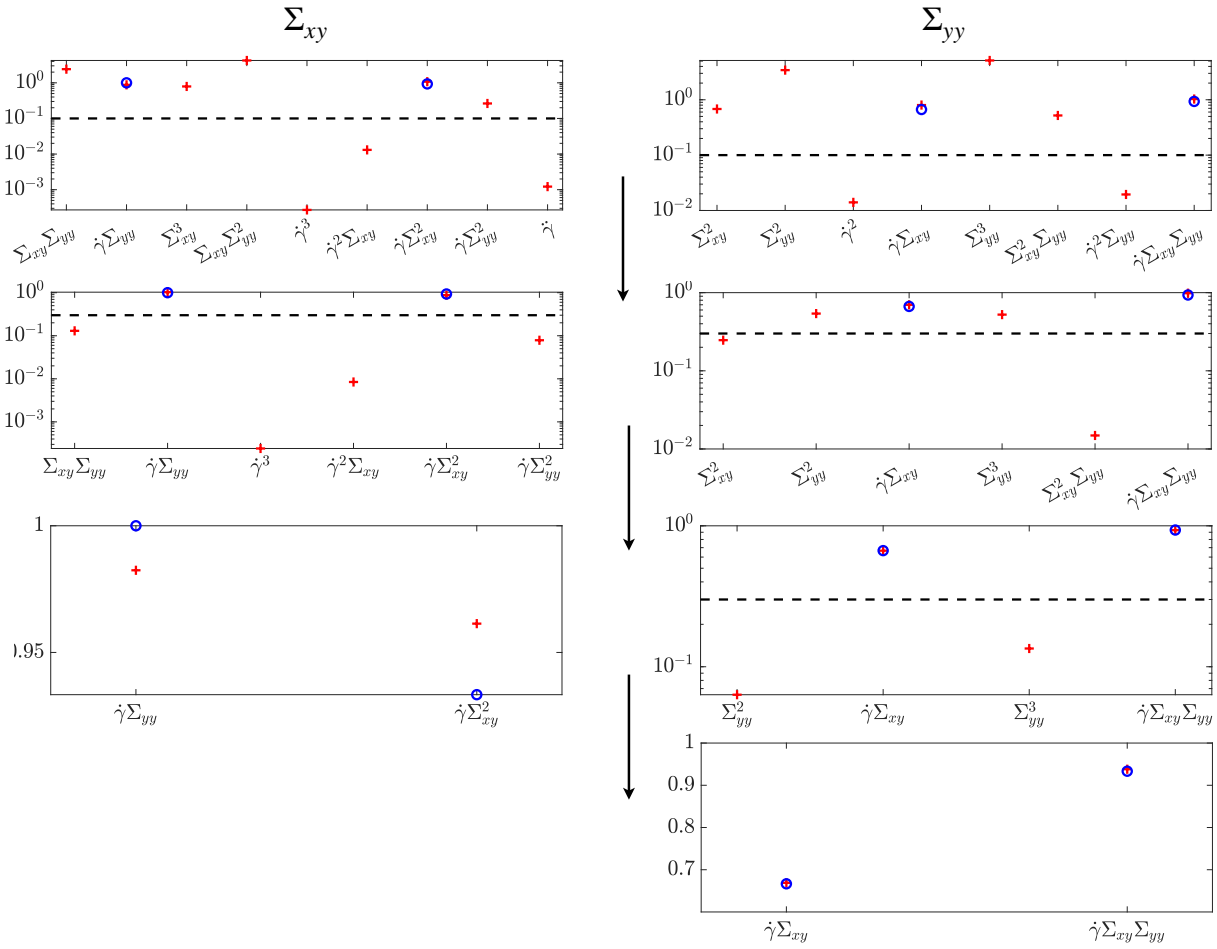


Figure 6.10: Predicted (red crosses) versus correct (blue circles) coefficients from an application of rheoKIC using a combination of concatenated data sets, the sequential method, and thresholding.

The reconstructed nRP equations are shown in Table. 6.2. The correct observables have been isolated. Most coefficients have been predicted with less than 1% error, and the maximum error is 3% for the $\dot{\gamma}\Sigma_{xy}^2$ observable.

$\dot{\Sigma}_{xy}$	
Correct	$-1.000\Sigma_{xy} + 1.000\dot{\gamma} + 1.000\dot{\gamma}\Sigma_{yy} - 0.933\dot{\gamma}\Sigma_{xy}^2$
Predicted	$-1.000\Sigma_{xy} + 1.000\dot{\gamma} + 0.982\dot{\gamma}\Sigma_{yy} - 0.961\dot{\gamma}\Sigma_{xy}^2$
$\dot{\Sigma}_{yy}$	
Correct	$-1.000\Sigma_{yy} - 0.667\dot{\gamma}\Sigma_{xy} - 0.933\dot{\gamma}\Sigma_{xy}\Sigma_{yy}$
Predicted	$-1.000\Sigma_{yy} - 0.669\dot{\gamma}\Sigma_{xy} - 0.938\dot{\gamma}\Sigma_{xy}\Sigma_{yy}$

Table 6.2: Final reconstructed equations from the last thresholding step in Fig. 6.10.

These results were found using data from three oscillatory data sets, one in the linear viscoelastic regime for the first sequential step and two from the nonlinear viscoelastic regime to find the higher order terms. The steps outlined above have narrowed down the decisions to be made somewhat, but it is worth bearing in mind that there are still many moving parts to consider when combining all of the techniques we have developed to correctly identify a fluid's constitutive law. Nevertheless, this is a drastic improvement in results in comparison to those at the beginning of the chapter.

6.4 MAPS data

Finally, we investigate whether rheoKIC applied to this highly nonlinear system of constitutive equations can be streamlined by using data that is inherently more complex. As described in Chapter 5, we replicate data from the MAPS protocol by setting the strain rate according to

$$\dot{\gamma}(t) = \gamma_0 \omega_0 \sum_{j=1}^3 n_j \cos(n_j \omega_0 t + \alpha_j), \quad (6.16)$$

and choosing $\alpha_j = 0 \ \forall j$, $\omega_0 = 1$ and $n_j = [5, 6, 9]$. As in the previous chapter, the time step size is set such that there are 512 measurements for the fastest frequency, while we take measurements for the length for the slowest frequency to ensure that all the frequencies can be

fully observed. We use data after 20 periods have elapsed to ensure that the data is stationary.

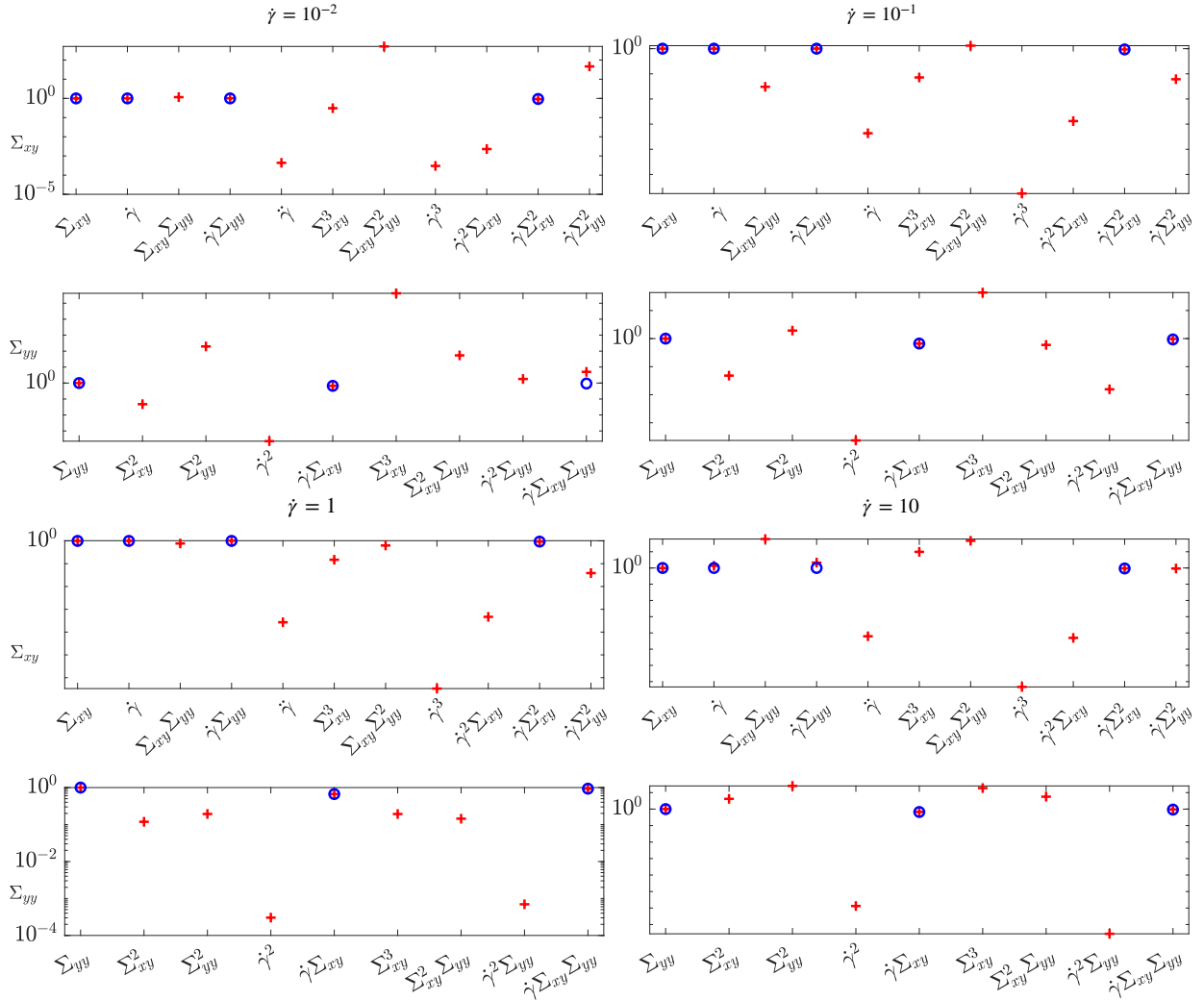


Figure 6.11: Predicted (red crosses) versus correct (blue circles) coefficients from an application of rheoKIC on MAPS data where $n_j = [5, 6, 9]$.

Fig. 6.11 shows the results for different values of $\dot{\gamma}_0$. In contrast to the previous sections, we do not employ data from a small amplitude simulation to find the linear terms and instead use data from only one simulation to find the terms at every order. As expected, the smallest values of $\dot{\gamma}_0$ produces less accurate predictions for the higher order observables as they are less well represented in the data. The coefficients are all identified well when $\dot{\gamma}_0 \geq 1$. Some of the higher order observables, such as $\ddot{\gamma}$ for the Σ_{xy} case and $\dot{\gamma}^2$ for the Σ_{yy} case, can be easily seen as unnecessary for reconstructing the data, while others cannot be separated from the observables we know that we need.

We focus on the data set from the $\dot{\gamma}_0 = 1$ MAPS simulation since it is suitably nonlinear to find all the observables. We iteratively apply rheoKIC while removing observables from Φ_{xy} and Φ_{yy} with much smaller coefficients relative to others in the set. The results are shown in Fig. 6.12.

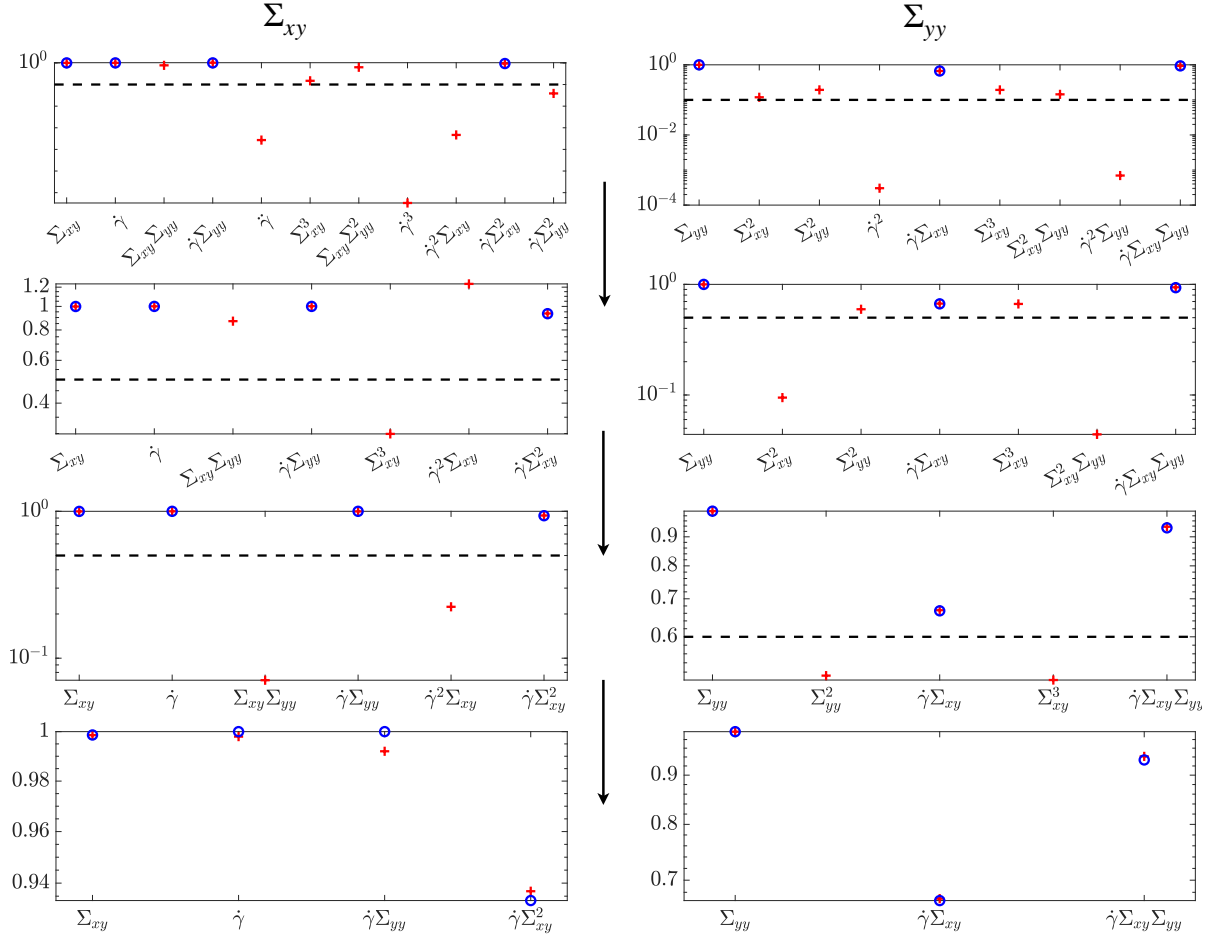


Figure 6.12: Predicted (red crosses) versus correct (blue circles) coefficients from an application of rheoKIC where the results in the top row are as in Fig. 6.11 for $\dot{\gamma}_0 = 1$, then rheoKIC is iteratively applied with reduced numbers of observables.

We see that for both the Σ_{yy} and Σ_{xy} cases, we require three rounds of thresholding for all incorrect observables to be discarded. At each iteration there is always a clear separation of the coefficients into two groups based on their sizes, causing a straightforward decision for where the threshold should be located. The corresponding reconstructed constitutive laws for the final round of thresholding are shown in Table 6.3, with all coefficients having $< 1\%$ error.

$\dot{\Sigma}_{xy}$	
Correct	$-1.000\Sigma_{xy} + 1.000\dot{\gamma} + 1.000\dot{\gamma}\Sigma_{yy} - 0.933\dot{\gamma}\Sigma_{xy}^2$
Predicted	$-0.999\Sigma_{xy} + 0.998\dot{\gamma} + 0.992\dot{\gamma}\Sigma_{yy} - 0.937\dot{\gamma}\Sigma_{xy}^2$
$\dot{\Sigma}_{yy}$	
Correct	$-1.000\Sigma_{yy} - 0.667\dot{\gamma}\Sigma_{xy} - 0.933\dot{\gamma}\Sigma_{xy}\Sigma_{yy}$
Predicted	$-0.999\Sigma_{yy} - 0.670\dot{\gamma}\Sigma_{xy} - 0.941\dot{\gamma}\Sigma_{xy}\Sigma_{yy}$

Table 6.3: Final reconstructed equations for $\dot{\Sigma}_{xy}$ and $\dot{\Sigma}_{yy}$ when applying rheoKIC to a single MAPS data set, then reducing the set of candidate observables based on the coefficients from the pseudo inverse step. $\lambda = G = 1$, $\beta = 0.4$, $[\omega_1, \omega_2, \omega_3] = [5, 6, 9]$.

6.5 Conclusions

Increasing the complexity of our target constitutive law with respect to both the number of equations and the number of higher order terms naturally causes our approach for reconstructing the law to increase in complexity. The number of terms that could possibly be included in the equations increases to twenty in total, and as such there is a higher possibility that we may overfit our solution to the data available.

We first found that terms involving the solvent viscosity had coefficients multiple orders of magnitude smaller than those of the other terms, meaning that, without incredibly well time-resolved data, it would be virtually impossible to separate these signals from the noise of other candidate terms which should be discarded. Assuming that the viscosity is already known or so small as to be negligible on the impact of the constitutive equations, we started the analysis by applying a ‘naive’ approach where all possible candidate observables were supplied simultaneously. As expected, the increase in the number of candidate observables caused multiple false positives to be present.

From here, we followed the same template as in Chapter 5 to explore various methods to break down the set of observables to more effectively isolate the subset of correct observables we

knew we wanted and to prevent overfitting. Combining data sets produced accurate predictions for the coefficients of the correct observables but still erroneously indicated that some of the unnecessary observables should be included. We showed how using data from the linear viscoelastic regime reduced the nRP equations to the linear Maxwell model, where we can produce excellent accuracy for the linear coefficient terms as rheoKIC can be reduced to DMDc. Using the ‘sequential’ approach to then extract the higher order term produced good accuracy for the coefficient we hoped to find, but we were unable to remove the observables we needed to discard. The ‘thresholded’ approach, informed by the sequentially-thresholded least-squares method used within SINDy-type methods [124], successfully isolated the correct observables in some cases, but there were other cases where the incorrect observables were saved and correct observables were discarded. Using a combination of all three techniques - combined data sets, sequential analysis, and thresholding - required three data sets in total and allowed us to find exactly the correct observables and the coefficients to 2% error.

Finally, we compared these results to those using data emulating that from a MAPS experiment. By choosing a data set with strain rate amplitude high enough to for the data to definitely exist in the nonlinear viscoelastic regime, but not so high that the predictions for the linear observables did not degrade, we were able to reconstruct the exact terms from the constitutive law with $< 1\%$ error.

Chapter 7: Incorporating spatial inhomogeneity

When carrying out a rheometry experiment, an equation for the input strain or strain rate is inputted to the rheometer and the raw data of the stress response is recorded. Built-in software from the rheometer manufacturers can be used to instantly convert this raw data to produce common measurements such as the dynamic viscosity of the data, or the storage and loss moduli if the experiment is within the linear viscoelastic regime [55]. An important assumption made implicitly throughout this form of analysis is that the deformation is *affine*: there is no spatial variation in the strain rate. This assumption, along with the fluid being translationally or rotationally invariant, means that a measurement at the wall of the rheometer at each time step is sufficient to characterise the stress response of the fluid, and this is what is used during traditional rheology. In this chapter, we will explore how rheoKIC is able to incorporate non-affine data and its subsequent effects on the constitutive law of the fluid. We will investigate this by using data from simulations that exhibit shear banding behaviour. We will compare how rheoKIC performs using data just from the rheometer wall, as we have assumed to be the case in the previous chapters, and then data from each spatial region with different dynamics. Lastly, we show how rheoKIC represents data with spatially varying dynamics in the observable coefficients that it produces.

Advances in rheometry have allowed for the expansion of measurements to two and even three dimensions. Particle image velocimetry (PIV) [144] and particle tracking velocimetry (PTV) [145] techniques involve adding tracer particles to the fluid and tracking either their

movement or displacement during the experiment with high-frequency cameras [146], from which the trajectories of the particles are interpolated to recreate the dynamics for the entire fluid. Care must be taken during this process that the number of particles isn't enough to alter the fluid's microstructure, and the particles must be visible to the type of camera used to take the images. Alternative, less intrusive techniques include ultrasound imaging [147], magnetic resonance imaging (MRI), and nuclear magnetic resonance (NMR) imaging [148].

The ability for an experiment to be visualised in multiple dimensions has confirmed the existence of a phenomenon known as 'shear banding' [149]; a spatial localisation of the fluid's deformation under a critically high applied stress or strain rate whereby multiple (usually assumed to be two, although three or more have also been observed [150]) regions of the fluid exhibit different apparent viscosities, as illustrated in Fig. 7.1. The region l determines the width of the interface between the two larger banding regions where diffusion may occur, and prevents discontinuities of the spatial gradient where the bands coincide [151, 152].

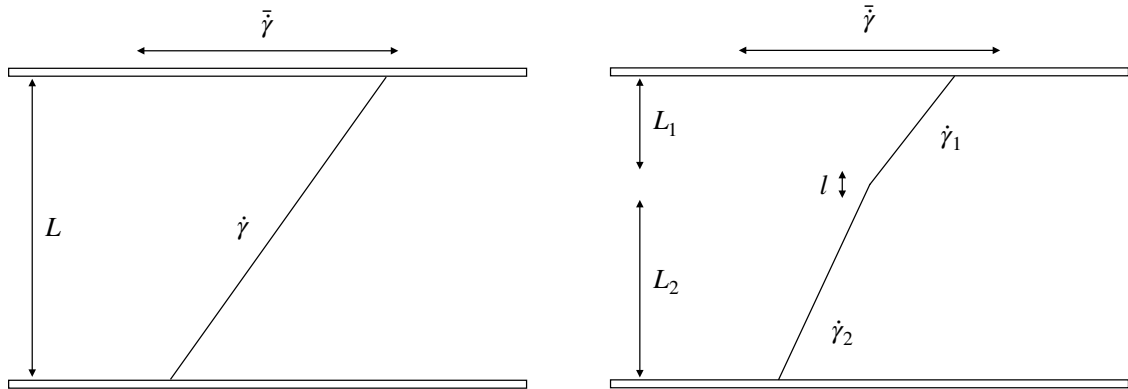


Figure 7.1: Illustration of the shear banding phenomenon in an oscillatory cell. (left) Homogeneous flow. (right) shear banding has separated the fluid's strain local rate into two regions in the gapwise direction.

The applied strain rate is typically described as being decomposed according to the 'lever rule'

$$\bar{\dot{\gamma}} = f\dot{\gamma}_1 + (1 - f)\dot{\gamma}_2, \quad (7.1)$$

where f is the volume fraction occupied by the upper band [148] and $\dot{\gamma}_1$ and $\dot{\gamma}_2$ are the local shear rates for the upper and lower bands, respectively.

Shear banding can occur as gradient banding, the type presented here where the regions lie along the direction of the flow gradient, and also as vorticity banding, where the regions lie in the vorticity direction (facing out of the page in Fig. 7.1). Both types may appear only transiently during the initial start-up of the flow [153] or as steady-state banding that persists once the initial effects of start-up have decayed. We focus exclusively on the gradient banding, assuming that the fluid is invariant in the vorticity direction, and on steady-state banding for stationary data.

Shear banding was first discovered in the study of metals [154] and soils [155], then was later found to exist in wide range of complex fluids, encompassing foams [156], entangled DNA solutions [157], and polymer solutions [9]. We will be focusing on shear banding behaviour in wormlike micellar solutions [158]. These are fluids containing surfactant molecules at high enough concentrations that they aggregate to form semi-flexible, rod-like chains, which are then capable of breaking, entangling, and recombining under shear [159]. If the applied shear rate is high enough, shear banding occurs due to a region near the moving wall containing micelles that are short and/or aligned with the wall having a higher shear rate [11], while the rest of the fluid containing the unbroken and unaligned micelles moves at a slower rate [160, 161].

It is possible to observe theoretically when shear banding would take place by examining the stress response under a given constitutive law against the applied strain rate - its ‘flow curve’ or ‘constitutive curve’ - and noting a region where the stress is nonmonotonic, an illustration of which is shown in Fig. 7.2. This region is found due to enforcing homogeneity of the shear rate in simulations and is not seen with experimental data; instead, a region of flat or gradually increasing stress can be observed [149]. The range of values $\dot{\gamma}_1 < \dot{\gamma} < \dot{\gamma}_2$ over which the stress response is nonmonotonic is known as the ‘stress plateau’ and indicates where the fluid has become unstable and is no longer spatially homogeneous [162]. For the case of wormlike micellar solutions, the width of the high shear rate region then increases linearly with the shear rate past $\dot{\gamma}_1$ [163]. Spatial homogeneity is restored once $\dot{\gamma} > \dot{\gamma}_2$ as the behaviour of the high

shear rate band has expanded to fill the entire gap.

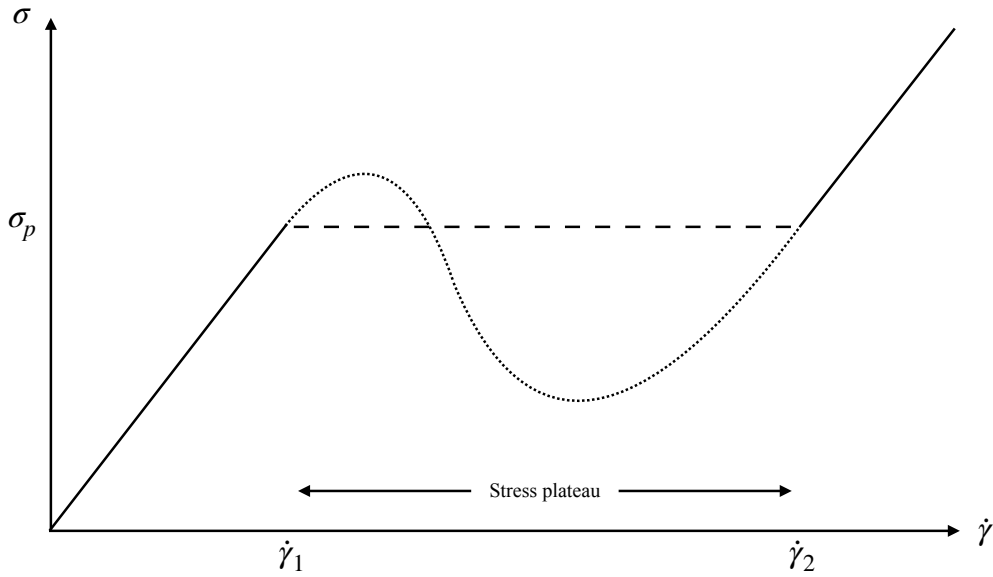


Figure 7.2: Example flow curve for a constitutive law demonstrating shear banding. The dotted line illustrates the theoretical stress response produced by constitutive law with constrained spatial homogeneity, while the dashed line illustrates the type of stress response recorded from experiments.

Pushing the strain rate further past $\dot{\gamma}_2$ leads to the appearance of Taylor vortices at the interface between the bands and eventually lead to ‘elasto-inertial turbulence’, a form of turbulent fluid behaviour that can exist even within the Stokes regime due to the presence of nonlinearities in the fluid’s stress-strain relationship [164–167]. While this domain is beyond the scope of the thesis, applications of rheoKIC to data from this regime would be a highly interesting topic for future investigation.

7.1 Inducing shear banding

We follow the procedure given by Carter *et al.* [49, 168] for establishing the nRP equations in the Stokes regime in a form that allows for shear banding to occur. Among other results, this paper presented the parameter space for large amplitude oscillatory shear simulations of the Rolie-Poly model where shear banding behaviour can be observed, and analysed the causes of its onset. In this chapter we will continue to use the non-stretching Rolie-Poly (nRP) model

first described in Chapter 6 for our analysis. The nRP model is widely used for the modelling of both polymeric and wormlike micellar solutions, of which both have been shown capable of producing shear banding [150, 151, 165].

We envision the fluid in two dimensions only, existing between plates parallel plates that can be considered infinitely long separated by a distance L , as shown in Fig. 7.3. We assume the top plate is being moved under an oscillatory strain scenario with velocity $\underline{u} = (\bar{\dot{\gamma}}(t)L, 0, 0)$, where $\bar{\dot{\gamma}}(t) = \dot{\gamma}_0 \cos(\omega t)$, and that the system is invariant in the flow and vorticity directions. We use the over-bar to indicate the mean across the channel.

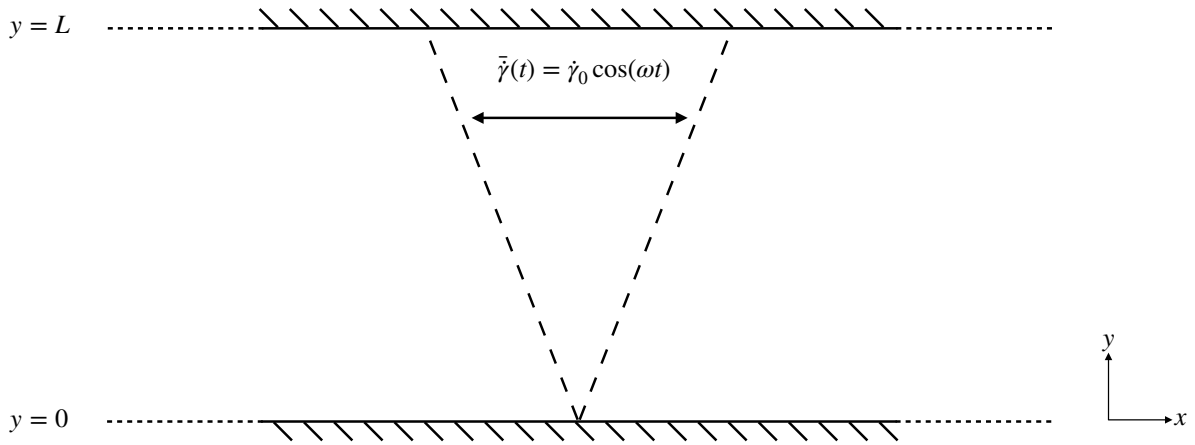


Figure 7.3: Illustration of an oscillatory shear experimental protocol in two dimensions where the fluid response (dashed line) is assumed to be spatially homogeneous.

The equations for the nRP model must be modified slightly to allow for changes in the local strain rate:

$$\underline{\underline{\Sigma}} = \underline{\underline{\sigma}} + 2\eta\underline{\underline{e}} - p\underline{\underline{I}}, \quad (7.2a)$$

$$\underline{\underline{\sigma}} = G(\underline{\underline{W}} - \underline{\underline{I}}), \quad (7.2b)$$

$$\frac{\partial W_{xy}}{\partial t} = \bar{\dot{\gamma}} \left[W_{yy} - \frac{2}{3}(1 + \beta)W_{xy}^2 \right] - \frac{1}{\lambda}W_{xy} + D \frac{\partial^2 W_{xy}}{\partial y^2}, \quad (7.2c)$$

$$\frac{\partial W_{yy}}{\partial t} = \frac{2}{3}\bar{\dot{\gamma}} \left[\beta W_{xy} - (1 + \beta)W_{xy}W_{yy} \right] - \frac{1}{\lambda}(W_{yy} - 1) + D \frac{\partial^2 W_{yy}}{\partial y^2}. \quad (7.2d)$$

The additional final terms in Eqs. 7.2c-d are stress diffusion terms [169] that allows for variation in the shear rate, and thus the fluid velocity, across the width of the channel. Setting our interface region to have width $l = 2 \cdot 10^{-2}L = \sqrt{D\lambda}$, we find a non-zero value for the diffusion constant of $D = (l\lambda)^2 = 0.0004$ that is necessary to model the strongly inhomogeneous flow between the banded regions [170].

An assumption that the field is incompressible determines the pressure field in Eq. 7.2a. We assume that there is no slip and no permeation for the fluid velocity to enforce the boundary conditions at the systems' walls, and that there is also zero spatial gradient of the conformation tensor

$$\frac{\partial W_{xy}}{\partial y} = \frac{\partial W_{yy}}{\partial y} = 0. \quad (7.3)$$

When simulating the stress response for the nRP model, the assumption that we are in the Stokes regime produces a divergence-free condition on the stress,

$$\nabla \cdot \underline{\underline{\Sigma}} = 0. \quad (7.4)$$

This means there will be no spatial variation of Σ_{xy} overall in the fluid. However, allowing spatial variations within each of the components of Σ_{xy} , σ_{xy} and $\dot{\gamma}$, is necessary for shear banding to be possible. Taking the spatial gradient of Eq. 7.2a and rearranging, we have that

$$\frac{\partial \Sigma_{xy}}{\partial y} = G \frac{\partial W_{xy}}{\partial y} + \eta \frac{\partial \dot{\gamma}}{\partial y} = 0 \longrightarrow GW_{xy} + \eta \dot{\gamma} = K(t) \quad (7.5)$$

for the off-diagonal term, where $K(t)$ allows for the initial conditions to be enforced. Integrating over the width of the gap L ,

$$\frac{G}{L} \int_0^L W_{xy} dy + \frac{\eta}{L} \int_0^L \dot{\gamma} dy = G\bar{W}_{xy}(t) + \eta\bar{\dot{\gamma}}(t) = K(t) \quad (7.6)$$

and, using Eq. 7.5 (since the initial conditions hold across both equations),

$$GW_{xy}(y, t) + \eta\dot{\gamma}(y, t) = G\bar{W}_{xy}(t) + \eta\bar{\dot{\gamma}}(t). \quad (7.7)$$

We use the over-bar on W_{xy} to separate the average response across the rheometer gap from the inhomogeneous response. This leads to our final equation for the local shear rate

$$\dot{\gamma}(y, t) = \bar{\dot{\gamma}}(t) + \frac{G}{\eta}[\bar{W}_{xy}(t) - W_{xy}(y, t)]. \quad (7.8)$$

Grouping the spatial and non-spatial terms together, Eq. 7.2(c-d) can be written as

$$\partial_t W_{xy} = R_{xy}(W_{xy}, W_{yy}, \bar{\dot{\gamma}}) + D\partial_y^2 W_{xy}, \quad (7.9a)$$

$$\partial_t W_{yy} = R_{yy}(W_{xy}, W_{yy}, \bar{\dot{\gamma}}) + D\partial_y^2 W_{yy}. \quad (7.9b)$$

We discretise L into J grid points spaced Δy apart, $j = 0, \Delta y, \dots, L$, and simplify the notation such that $W(y = j, t) = W_j^t$. To discretise the transport equation, the nonlinear term is discretised in time using the forward Euler method, while the linear diffusive term is treated by combining the the trapezoidal rule for the time discretisation with a second-order central differencing for the spatial discretisation (the Crank-Nicholson method) [171]. Each of the equations for \underline{W} can then be approximated as

$$(1 + 2\alpha)W_j^{t+1} - \alpha(W_{j+1}^{t+1} + W_{j-1}^{t+1}) = (1 - 2\alpha)W_j^t + \alpha(W_{j+1}^t + W_{j-1}^t) + \Delta t R_j^t. \quad (7.10)$$

where $\alpha = \frac{D\Delta t}{2(\Delta y)^2}$. Note that this causes Eq. 7.10 to reduce to the Euler approximation for the time derivative when $D = 0$. Eq. 7.10 can be written in matrix form as

$$W^{t+1} = [I - \alpha C_N]^{-1} \{ [I + \alpha C_N] W^t + \Delta t R^t \}, \quad (7.11)$$

where

$$C_N = \begin{bmatrix} -2 & 2 & 0 & 0 & & \dots & 0 \\ 1 & -2 & 1 & 0 & 0 & \dots & 0 \\ & & & \ddots & \ddots & \ddots & \\ & & & & 1 & -2 & 1 \\ 0 & & 0 & 0 & 2 & -2 & \end{bmatrix} \in \mathbb{R}^{J \times J}. \quad (7.12)$$

The different off-diagonal terms on the first and last rows stem from the divergence-free boundary conditions on the plates [168, 171] described in Eq. 7.3, which enforce the values of the phantom points at $j = 0$ and $j = J + 1$ to be equal to the values at $j = 2$ and $j = J - 1$.

We apply an initial spatial heterogeneity to the system at $t = 0$ in a way that mimics the curvature of a Taylor-Couette cell rheometer [49] to introduce an instability to the system,

$$\Sigma_{xy}(y, t = 0) \rightarrow \Sigma_{xy}(y, t = 0)(1 + qh(y)). \quad (7.13)$$

where $h(y) = \cos(\frac{\pi}{L}y)$ and $q = 10^{-4}$. The total stress is then

$$\begin{bmatrix} \Sigma_{xy} \\ \Sigma_{yy} \end{bmatrix} = G \begin{bmatrix} W_{xy} \\ W_{yy} - 1 \end{bmatrix} + \eta \begin{bmatrix} \dot{\gamma} \\ 0 \end{bmatrix} \quad (7.14)$$

such that initially

$$\begin{bmatrix} \Sigma_{xy} \\ \Sigma_{yy} \end{bmatrix}_{t=0} = \eta \begin{bmatrix} \dot{\gamma}_0 \\ 0 \end{bmatrix} (1 + qh(y)). \quad (7.15)$$

The initial values for the conformation tensor can then be found by substituting the initial values for Σ ,

$$\begin{bmatrix} W_{xy} \\ W_{yy} \end{bmatrix}_{t=0} = \frac{1}{G} \begin{bmatrix} \Sigma_{xy} \\ \Sigma_{yy} \end{bmatrix}_{t=0} - \frac{\eta}{G} \begin{bmatrix} \bar{\dot{\gamma}} \\ 0 \end{bmatrix}_{t=0} + \begin{bmatrix} 0 \\ 1 \end{bmatrix} = \begin{bmatrix} \frac{\eta}{G} \dot{\gamma}_0 qh(y) \\ 1 \end{bmatrix}. \quad (7.16)$$

Once the next values for W_{xy} and W_{yy} are found with Eq. 7.10, the total stress is updated according to Eq. 7.2(a-b)

$$\Sigma_{xy} = GW_{xy} + \eta \bar{\dot{\gamma}}, \quad (7.17a)$$

$$\Sigma_{yy} = G(W_{yy} - 1). \quad (7.17b)$$

Finally, the local force balance is updated according to Eq. 7.8 and the velocity field at each time step is found by numerically integrating $\dot{\gamma}$ across the width of the gap while enforcing the boundary conditions for the velocity at the rheometer walls. It is important to note that the no-slip condition for \underline{u} is a fundamental assumption throughout these calculations. There has been significant discussions regarding the effect of wall slip on shear banding and whether it is an origin for shear banding in itself [172]. The presence of wall slip can appear to affect the validity of the lever rule presented in Eq. 7.1 [173], and has been shown to alter the values for $\dot{\gamma}$ at which the high shear rate band appears [174]. Care would therefore need to be taken when directly comparing this simulation data to experimental data when wall slip may be occurring.

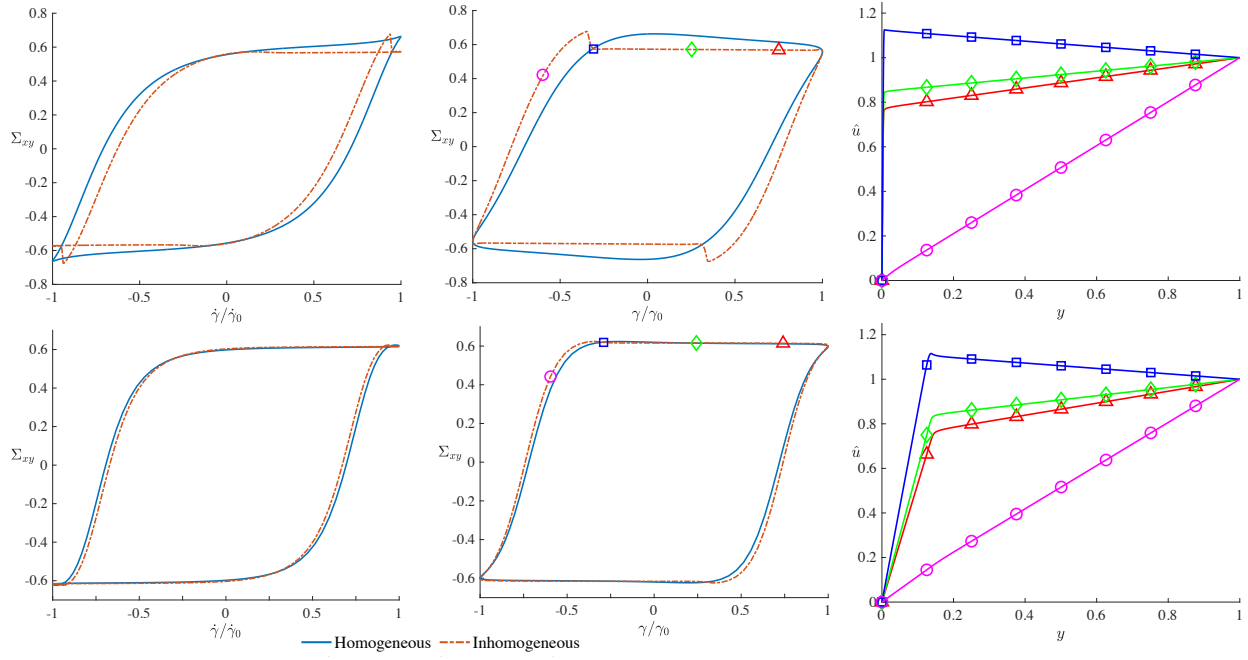


Figure 7.4: (l-r) Stress vs. strain rate, stress vs. strain, and velocity profiles for the nRP model in both the spatially homogeneous and inhomogeneous cases. Top row: $\beta = 0.4$, $\gamma_0 = 1$, $\omega = 10^{0.5}$. Bottom row: $\beta = 1$, $\omega = 1$, $\gamma_0 = 0.1 \cdot 10^{0.75}$. $J = 512$ when $\beta = 0.4$ and $J = 1024$ when $\beta = 1$. The symbols in the stress vs. strain curves correspond to the points in time where the velocity profiles have been plotted.

Fig. 7.4 shows the comparison between the stress-strain and stress-strain rate curves for the nRP model with and without spatial heterogeneity once 20 periods have elapsed, validating that our simulation matches that originally presented by Carter *et al* [49]. We also confirm that the spatially homogeneous results align with those presented in Chapter 6 by finding that the difference between the data sets is $O(10^{-12})$.

In the following, we will present results using data sets simulating two different fluids by altering the value of the fluid parameter β to show how this causes structural changes in the shear banding behaviour. This is exemplified in the velocity profiles also shown in Fig. 7.4: while the difference between the stress-strain curves is much more pronounced when $\beta = 0.4$, the high shear rate region only spans a very thin slice ($< 1\%$) of the rheometer gap. Meanwhile, a more modest difference between the stress-strain and stress-strain rate curves for the $\beta = 1$ case results in a high shear rate region of approximately $f = 0.15$.

7.2 Methodology for interpreting spatial data

One reason for applying techniques related to Koopman operator theory to data recorded from shear banding scenarios is that they are built for dealing with large and multi-dimensional data sets. The methodology presented in Chapter 3 can therefore be generalised to cases where $J > 1$ and there are multiple measurements of the stress response in each snapshot. We assume here that J is the same for each observable, but in theory rheoKIC is capable of dealing with different numbers of measurement points provided that the number and location of those points remains consistent across the data set [81]. The measurements from each snapshot are stacked to form vectors so that the total recorded data is a $J \times T$ matrix. We claim that the relationship between the input candidate observables data and the output value for the elements of the stress tensor can be written in matrix form as

$$\boldsymbol{\Sigma}' = \mathbf{C}\boldsymbol{\Phi}, \quad (7.18)$$

where $\boldsymbol{\Sigma}' = \Sigma'_{xy}$ or $\Sigma'_{yy} \in \mathbb{R}^{J \times T-1}$, $\mathbf{C} \in \mathbb{R}^{J \times KJ}$, $\boldsymbol{\Phi} \in \mathbb{R}^{KJ \times T-1}$, and K is the number of candidate observables. We assume that Σ_{xy} and Σ_{yy} are being treated separately using disjoint sets of observables as in the previous chapters. We may take the SVD of $\boldsymbol{\Phi}$ and truncate it to $p \leq KJ$ modes,

$$\boldsymbol{\Phi} \approx \tilde{\mathbf{U}}\tilde{\mathbf{S}}\tilde{\mathbf{V}}^T, \quad (7.19)$$

$\tilde{\mathbf{U}} \in \mathbb{R}^{KJ \times p}$, $\tilde{\mathbf{S}} \in \mathbb{R}^{p \times p}$, and $\tilde{\mathbf{V}}^T \in \mathbb{R}^{p \times T-1}$. Using this SVD directly to apply the (potentially truncated) pseudoinverse would give

$$\mathbf{C} \approx \tilde{\mathbf{C}} = \boldsymbol{\Sigma}'\tilde{\mathbf{V}}\tilde{\mathbf{S}}^{-1}\tilde{\mathbf{U}}^T \in \mathbb{R}^{J \times KJ}, \quad (7.20)$$

a rank p approximation for \mathbf{C} . At this point $\tilde{\mathbf{C}}$ is difficult to compare with the scalar coefficients

in the original constitutive law, as the size of both dimensions of $\tilde{\mathbf{C}}$ depend on the number of data points at each time step J . We would ideally like our predicted coefficients to be independent of the number of measurements we have available. Firstly, we can follow the same route as in the DMDc method [107] and reduce the output space by computing the SVD of Σ' and truncating to r modes, $\Sigma' \approx \hat{\mathbf{U}}\hat{\mathbf{S}}\hat{\mathbf{V}}^T$ where $r \leq J$ and $r < p$. The reduced-order approximation of \mathbf{C} is then

$$\hat{\mathbf{C}} = \hat{\mathbf{U}}^T \tilde{\mathbf{C}} = \hat{\mathbf{U}}^T \Sigma' \tilde{\mathbf{V}} \tilde{\mathbf{S}}^{-1} \tilde{\mathbf{U}}^T \in \mathbb{R}^{r \times KJ}. \quad (7.21)$$

The updated version of Eq. 7.18 taking this projection into account is

$$\hat{\mathbf{U}}^T \Sigma' = \hat{\Sigma}' = \hat{\mathbf{C}} \Phi \in \mathbb{R}^{r \times T-1}. \quad (7.22)$$

The number of rows in $\hat{\mathbf{C}}$ now depends on the number of spatial modes in $\hat{\Sigma}'$, while there are J columns in $\hat{\mathbf{C}}$ for each of the K candidate observables,

$$\hat{\mathbf{C}} = \left[\begin{array}{c|c|c|c|c|c|c|c|c|c|c|c|c|c|c} | & | & \dots & | & | & | & \dots & | & \dots & | & | & | & \dots & | \\ \hline \hat{c}_{1,1} & \hat{c}_{1,2} & \dots & \hat{c}_{1,J} & \hat{c}_{2,1} & \hat{c}_{2,2} & \dots & \hat{c}_{2,J} & \dots & \hat{c}_{K,1} & \hat{c}_{K,2} & \dots & \hat{c}_{K,J} \\ \hline | & | & \dots & | & | & | & \dots & | & \dots & | & | & | & \dots & | \end{array} \right] \in \mathbb{R}^{r \times KJ}. \quad (7.23)$$

To remove the dependence on the number of measurements J from the number of columns in $\hat{\mathbf{C}}_k$, we project each of the candidate observables ϕ_k onto their own truncated left-singular vectors $\check{\mathbf{U}}_k$,

$$\check{\phi}_k = \check{\mathbf{U}}_k^T \phi_k \in \mathbb{R}^{J \times q_k} \quad (7.24)$$

where q_k is the number of spatial modes in the k^{th} observable. Eq. 7.22 can be updated to include the projections of the input data as

$$\hat{\Sigma}' = \sum_{k=1}^K \check{\mathbf{C}}_k \check{\mathbf{U}}_k^T \phi_k. \quad (7.25)$$

We are required to use a summation in contrast to Eq. 7.18 and Eq. 7.22 because the truncated SVD of the entire set of observables Φ is not necessarily equal to a matrix formed by concatenating the truncated SVDs from each individual observable ϕ_k . From the properties of the SVD,

$$\hat{\Sigma}' = \sum_{k=1}^K \check{\mathbf{C}}_k \check{\mathbf{U}}_k^T \phi_k \quad (7.26a)$$

$$\approx \sum_{k=1}^K \hat{\mathbf{C}}_k \check{\mathbf{U}}_k \check{\mathbf{U}}_k^T \phi_k \quad (7.26b)$$

$$\approx \sum_{k=1}^K \hat{\mathbf{C}}_k \check{\mathbf{U}}_k \check{\mathbf{U}}_k^T \check{\mathbf{U}}_k \check{\mathbf{S}}_k \check{\mathbf{V}}_k^T \quad (7.26c)$$

$$= \sum_{k=1}^K \hat{\mathbf{C}}_k \check{\mathbf{U}}_k \check{\mathbf{S}}_k \check{\mathbf{V}}_k^T \quad (7.26d)$$

$$= \sum_{k=1}^K \hat{\mathbf{C}}_k \check{\mathbf{U}}_k \check{\phi}_k. \quad (7.26e)$$

At this point, it is possible to effectively enforce that the observable coefficients are scalar by solving Eq. 7.26 as a matrix-vector problem for a vector $\hat{\underline{c}}_k$. The resulting generalised coefficient for each observable k may be computed via

$$\hat{\underline{c}}_k = \begin{bmatrix} \hat{\mathbf{U}}_1^T \Sigma' (\hat{\mathbf{U}}_1^T \check{\mathbf{U}}_{1:q_k} \check{\mathbf{U}}_{1:q_k}^T \phi_k)^\dagger \\ \vdots \\ \hat{\mathbf{U}}_r^T \Sigma' (\hat{\mathbf{U}}_r^T \check{\mathbf{U}}_{1:q_k} \check{\mathbf{U}}_{1:q_k}^T \phi_k)^\dagger \end{bmatrix} \in \mathbb{R}^{r \times 1}, \quad (7.27)$$

where the † symbol denotes the Moore-Penrose pseudoinverse. After reversing any rescaling carried out on the data, we are left with a generalised, one-dimensional coefficient approximation for each observable.

We will show in Sec. 7.4 that the entries of these coefficients align remarkably well with the coefficients from the underlying, homogeneous equation while only using the first singular mode from the spatial measurements of the output data. We believe that this could be a useful approach for extracting an underlying affine constitutive law from a data set where there are multiple spatial measurements per time step available.

While the outputs of the approach above appear to be successful, we would additionally like to see if it is possible for both dimensions of our generalised coefficients to be dependent on the amount of spatial detail in the data. We do this by including the instance of $\check{\mathbf{U}}_k$ in Eq. 7.26 within our definition of $\check{\check{\mathbf{C}}}_k$:

$$\check{\check{\mathbf{C}}}_k = \hat{\mathbf{C}}_k \check{\mathbf{U}}_k = \hat{\mathbf{U}}^T \check{\mathbf{C}}_k \check{\mathbf{U}}_k = \hat{\mathbf{U}}^T \boldsymbol{\Sigma}' \tilde{\mathbf{V}} \tilde{\mathbf{S}}^{-1} \tilde{\mathbf{U}}_k^T \check{\mathbf{U}}_k \in \mathbb{R}^{r \times q_k} \quad (7.28)$$

where $\tilde{\mathbf{U}}_k^T$ only contains the columns of $\tilde{\mathbf{U}}^T$ related to the k^{th} observable. Care must be taken to ensure that the operations are performed in an order such that the dimensions of the matrices in Eq. 7.28 are still aligned. The generalised coefficient for an observable with q_k spatial modes, being used to reconstruct output data $\boldsymbol{\Sigma}'$ with r spatial modes, will then have the form

$$\check{\check{\mathbf{C}}}_k = \begin{bmatrix} \hat{\mathbf{U}}_1^T \boldsymbol{\Sigma}' \tilde{\mathbf{V}} \tilde{\mathbf{S}}^{-1} \tilde{\mathbf{U}}_k^T \check{\mathbf{U}}_1 & \hat{\mathbf{U}}_1^T \boldsymbol{\Sigma}' \tilde{\mathbf{V}} \tilde{\mathbf{S}}^{-1} \tilde{\mathbf{U}}_k^T \check{\mathbf{U}}_2 & \dots & \hat{\mathbf{U}}_1^T \boldsymbol{\Sigma}' \tilde{\mathbf{V}} \tilde{\mathbf{S}}^{-1} \tilde{\mathbf{U}}_k^T \check{\mathbf{U}}_{q_k} \\ \hat{\mathbf{U}}_2^T \boldsymbol{\Sigma}' \tilde{\mathbf{V}} \tilde{\mathbf{S}}^{-1} \tilde{\mathbf{U}}_k^T \check{\mathbf{U}}_1 & \hat{\mathbf{U}}_2^T \boldsymbol{\Sigma}' \tilde{\mathbf{V}} \tilde{\mathbf{S}}^{-1} \tilde{\mathbf{U}}_k^T \check{\mathbf{U}}_2 & \dots & \hat{\mathbf{U}}_2^T \boldsymbol{\Sigma}' \tilde{\mathbf{V}} \tilde{\mathbf{S}}^{-1} \tilde{\mathbf{U}}_k^T \check{\mathbf{U}}_{q_k} \\ \vdots & \vdots & \dots & \vdots \\ \hat{\mathbf{U}}_r^T \boldsymbol{\Sigma}' \tilde{\mathbf{V}} \tilde{\mathbf{S}}^{-1} \tilde{\mathbf{U}}_k^T \check{\mathbf{U}}_1 & \hat{\mathbf{U}}_r^T \boldsymbol{\Sigma}' \tilde{\mathbf{V}} \tilde{\mathbf{S}}^{-1} \tilde{\mathbf{U}}_k^T \check{\mathbf{U}}_2 & \dots & \hat{\mathbf{U}}_r^T \boldsymbol{\Sigma}' \tilde{\mathbf{V}} \tilde{\mathbf{S}}^{-1} \tilde{\mathbf{U}}_k^T \check{\mathbf{U}}_{q_k} \end{bmatrix} \in \mathbb{R}^{r \times q_k}. \quad (7.29)$$

If the output data and the observable can be represented with a single spatial mode, then $r = q_k = 1$ and the approximated coefficients will be scalars. If the data is spatially homogeneous, then this coefficient can be converted back to the original parameters in the constitutive law identically to how we have done in previous chapters.

Spatial inhomogeneity is reflected in the dimensions and entries of $\check{\check{\mathbf{C}}}_k$ for each observable.

Equally, if the k^{th} candidate observable is not required then the entries in $\check{\check{\mathbf{C}}}_k$ will be very small and should indicate that the observable can be removed during the thresholding process. On the other hand, their construction means that they are significantly more complex to interpret relative to the one-dimensional coefficients \hat{c}_k described in Eq. 7.27.

7.2.1 Interpreting the generalised coefficients

Returning to the theory behind the KIC method [20] originally described in Chapter 3, we are seeking to represent the output data as a linear combination of the observables ϕ_k

$$\Sigma(t + \Delta t, y) = \sum_k \mathcal{L}_k[\phi_k(t, y')](y) \quad (7.30)$$

where \mathcal{L}_k are the spatial linear operators corresponding to each observable. We write each of the observables in terms of an orthonormal expansion

$$\phi_k(t, y) = \sum_{q_k} \varphi_{q_k}^k(t) a_{q_k}^k(y) \quad (7.31)$$

which separates the data into the product of spatially-dependent functions $a_{q_k}^k(y)$ and time-dependent functions $\varphi_{q_k}^k(t)$. The output of the system can similarly be written in its own orthonormal basis

$$\Sigma(t + \Delta t, y) = \sum_n \sigma_n(t + \Delta t) b_n(y). \quad (7.32)$$

We wish to rewrite Eq. 7.30 in terms of the time-dependent functions $\sigma_n(t + \Delta t)$ defined in Eq. 7.32, as this will restrict all possible spatial dependencies to within the function evolving

the observables. Using the fact that the $b_n(y)$ are orthonormal,

$$\sigma_n(t + \Delta t) = \langle b_n(y), \Sigma(t + \Delta t, y) \rangle \quad (7.33a)$$

$$\rightarrow \sigma_n(t + \Delta t) = \langle b_n(y), \sum_k \mathcal{L}_k[\phi_k(t, y)] \rangle, \quad (7.33b)$$

where $\langle f, g \rangle = \int_0^L f(y)g(y)dy$ is the standard vector inner product and we assume that the functions are continuous and square-integrable within $[0, L]$. Substituting using Eq. 7.31 and rearranging,

$$\sigma_n(t + \Delta t) = \sum_k \sum_{q_k} \varphi_{q_k}^k(t) \langle b_n(y), \mathcal{L}_k[a_{q_k}^k(y')](y) \rangle. \quad (7.34)$$

Since the $\varphi_{q_k}^k(t)$ represent purely the temporal aspect for each of the observables, Eq. 7.34 is a summation over the observables, where the spatial linear operator has been applied to its spatial modes, and then these results have been projected onto the n^{th} spatial mode of the output data - in other words, it is the continuous form for the generalised coefficients described in Eq. 7.25 and Eq. 7.29 where the spatial linear operator \mathcal{L}_k is represented by $\tilde{\mathbf{C}}_k$.

Meanwhile, the underlying constitutive equations for the cases we are looking at take the general form

$$\frac{\partial \Sigma(t, y)}{\partial t} = -\frac{1}{\lambda} \Sigma(t, y) + D \frac{\partial^2 \Sigma(t, y)}{\partial y^2} + \sum_k \alpha_k \phi_k(t, y) \quad (7.35)$$

for both $\Sigma = \Sigma_{xy}$ and $\Sigma = \Sigma_{yy}$, where α_k are the (scalar) material coefficients in the constitutive law. Replacing each of the terms with their respective spatiotemporal decompositions,

$$\sum_n \frac{\partial \sigma_n(t + \Delta t)}{\partial t} b_n(y) = -\frac{1}{\lambda} \sum_n \sigma_n(t) b_n(y) + \sum_n D \sigma_n(t) \frac{\partial^2 b_n(y)}{\partial y^2} + \sum_k \alpha_k \sum_{q_k} \varphi_{q_k}^k(t) a_{q_k}^k(y). \quad (7.36)$$

Taking the inner product with $b_n(y)$,

$$\sum_n \frac{\partial \sigma_n(t + \Delta t)}{\partial t} = \sum_n \left[-\frac{1}{\lambda} + D \left\langle \frac{\partial^2 b_n(y)}{\partial y^2}, b_n(y) \right\rangle \right] \sigma_n(t) + \sum_k \alpha_k \sum_{q_k} \varphi_{q_k}^k(t) \sum_n \langle a_{q_k}^k(y), b_n(y) \rangle. \quad (7.37)$$

For the first term in Eq. 7.37, we compute the inner product using integration by parts and use the fact that the flow is divergence-free at the domain boundaries to find

$$\left\langle \frac{\partial^2 b}{\partial y^2}, b(y) \right\rangle = - \int_0^L \left| \frac{\partial b}{\partial y} \right|^2 dy. \quad (7.38)$$

This is the magnitude of the spatial gradient across the rheometer and can be computed numerically using the data we have available, allowing us to directly extract our predicted coefficient for Σ_{xy} and Σ_{yy} from the first term in Eq. 7.37. Substituting Eq. 7.38 into Eq. 7.37, we retrieve

$$\sum_n \frac{\partial \sigma_n(t + \Delta t)}{\partial t} = \left[-\frac{1}{\lambda} - D \int_0^L \left| \frac{\partial b}{\partial y} \right|^2 dy \right] \sum_n \sigma_n(t) + \sum_k \alpha_k \sum_{q_k} \varphi_{q_k}^k(t) \sum_n \langle a_{q_k}^k(y), b_n(y) \rangle. \quad (7.39)$$

The resulting linear operator for the Σ data will be the identity matrix, scaled by $-\frac{1}{\lambda}$ and minus the magnitude of the spatial gradient. The remaining terms in the equation can be written as

$$\sum_k \alpha_k \sum_{q_k} \varphi_{q_k}^k(t) \sum_n \langle a_{q_k}^k(y), b_n(y) \rangle \quad (7.40a)$$

$$= \alpha_1 \sum_{q_1} \varphi_{q_1}^1(t) \sum_n \langle a_{q_1}^1(y), b_n(y) \rangle + \cdots + \alpha_K \sum_{q_K} \varphi_{q_K}^K(t) \sum_n \langle a_{q_K}^K(y), b_n(y) \rangle. \quad (7.40b)$$

These terms describe the dynamics for all of the observables which are not directly evolved by the equation, where the input space and output space for the data are no longer the same. Writing the equations in this form does not take into account that some of the ϕ_k terms are constructed using Σ_{xy} and Σ_{yy} , which means that they are also being evolved by the equation. On the other hand, it allows us to write a discrete approximation for \mathcal{L} which separates α_k from the inner product operations.

We will no longer be left with the identity matrix when we are computing the inner product between the spatial modes $a_{q_k}^k(y)$ and $b_n(y)$. However, since they both have unit length by construction, their inner product can be thought of as a measurement of the correlation between the spatial modes of the input data and the output data. From the properties of the SVD, the $a_{q_k}^k(y)$ have a hierarchy: the first entry is related to the rank-one approximation of its observable and will contribute the most to the reconstruction of the left-hand side of Eq. 7.40, followed by the second entry related to the rank-two approximation, and so on.

Comparing Eq. 7.40 and Eq. 7.34, we see that the assumption underlying this method is that, for the n^{th} spatial mode of the output data,

$$\sum_k \sum_{q_k} \varphi_{q_k}^k(t) \langle b_n(y), \mathcal{L}_k[a_{q_k}^k(y')](y) \rangle \approx \sum_k \alpha_k \sum_{q_k} \varphi_{q_k}^k(t) \langle b_n(y), a_{q_k}^k(y) \rangle. \quad (7.41)$$

In other words, we are attempting to write the linear operator acting on the spatial modes of each observable as a matrix of ones scaled by the corresponding coefficient from the spatially homogeneous underlying equations. The generalised coefficient vector \hat{c}_k described in Eq. 7.27 enforces this structure for the linear operator given in Eq. 7.41, which allows us to extract the α_k from the inner product operations.

Meanwhile, for the generalised coefficient $\check{\tilde{\mathbf{C}}}_k$ described in Eq. 7.29, each entry instead contains the $J \times J$ matrix $\mathbf{\Sigma}' \tilde{\mathbf{V}} \tilde{\mathbf{S}}^{-1} \tilde{\mathbf{U}}_k^T = \check{\tilde{\mathbf{C}}}_k$. This acts as the linear operator on the retained spatial modes of the observable, and cannot be extracted from the inner product. From Eq. 7.18 we can see that, while $\check{\tilde{\mathbf{C}}}_k$ will contain α_k , it will also contain information regarding the spatiotemporal evolution of the entire data set. In fact, as described in Chapter 3, this is the section of the approximated Koopman operator describing the nonlinear dynamics of the system with respect to the k^{th} observable. The generalised coefficients $\check{\tilde{\mathbf{C}}}_k$, while more difficult to relate back to the underlying material coefficients α_k , pave the way for future Koopman-type investigations on the temporal evolution of the data.

7.2.2 Determining the number of modes to keep

An important decision to make at this juncture is how to determine the truncation point for the spatial projections at a value which balances the accuracy and complexity of the resulting model. We would like to accurately reflect the spatial inhomogeneity incurred when shear banding is present, but choosing to retain all the information about every observable results in a $J \times J$ matrix for each coefficient. These matrices would be likely ill-conditioned if J is large since we are only expecting at most two distinct regions for the dynamics of the fluid, and larger matrices will be more difficult to compare with the scalar coefficients produced during standard analysis when assuming spatial homogeneity. Using the Eckart-Young-Mirsky theorem [83] first described in Chapter 3, we know that a truncation of the SVD to r will produce the best possible rank r approximation of the data (with respect to the Frobenius norm). We can determine how many modes to keep by computing

$$\min_{r \leq R} \frac{\sum_{i=1}^r s_i}{\sum_{i=1}^R s_i} \geq e, \quad (7.42)$$

where R is the rank of the data set, s_i is its i^{th} singular value, and $0 < e \leq 1$ is a value determined by the user. If we were applying this to a velocity vector, then e could be considered as the amount of kinetic energy that we choose to retain when approximating the data.

7.3 Effects of shear banding on rheoKIC

We will be considering data representing two different fluids, which require different experimental parameters to produce shear banding behaviour:

1. $G = \lambda = 1, \beta = 0.4, \omega = \sqrt{10}, \dot{\gamma}_0 = 10.$
2. $G = \lambda = 1, \beta = 1, \omega = 10, \dot{\gamma}_0 = 10^{1.75}.$

To begin with we consider the following scenario: we have data from a fluid showing shear banding behaviour, but we continue to characterise the fluid's entire stress response from a single data point at the rheometer wall opposite to that of the imposed shear. The coefficients for the output will therefore always be scalar, regardless of the number of spatial modes actually required to represent the data.

For the data used to construct the shear rate observable applying exogenous input to the system, we can maintain the typical assumption of an affine deformation and use the imposed shear $\bar{\dot{\gamma}}$, or we can use the local shear rate $\dot{\gamma}$ at the same wall as where we collect the stress response data. We will compare the output from rheoKIC using these different choices of data below.

As described in the previous chapters, when carrying out rheoKIC we first use data from a low frequency, small strain rate amplitude simulation which will be spatially homogeneous to pick out the coefficients for the linear terms, then run frequency sweeps at higher strain rate amplitudes to find approximations for the higher order observables. We use the parameter space diagrams from Carter *et al.* as a guide [49] to choose $\dot{\gamma}_0$ such that there are both spatially homogeneous and inhomogeneous data sets as ω is varied. In agreement with their results, both fluids demonstrate shear banding behaviour when $\omega = \{10^{0.5}, 10\}$ and are spatially homogeneous when $\omega = \{10^{1.5}, 100\}.$

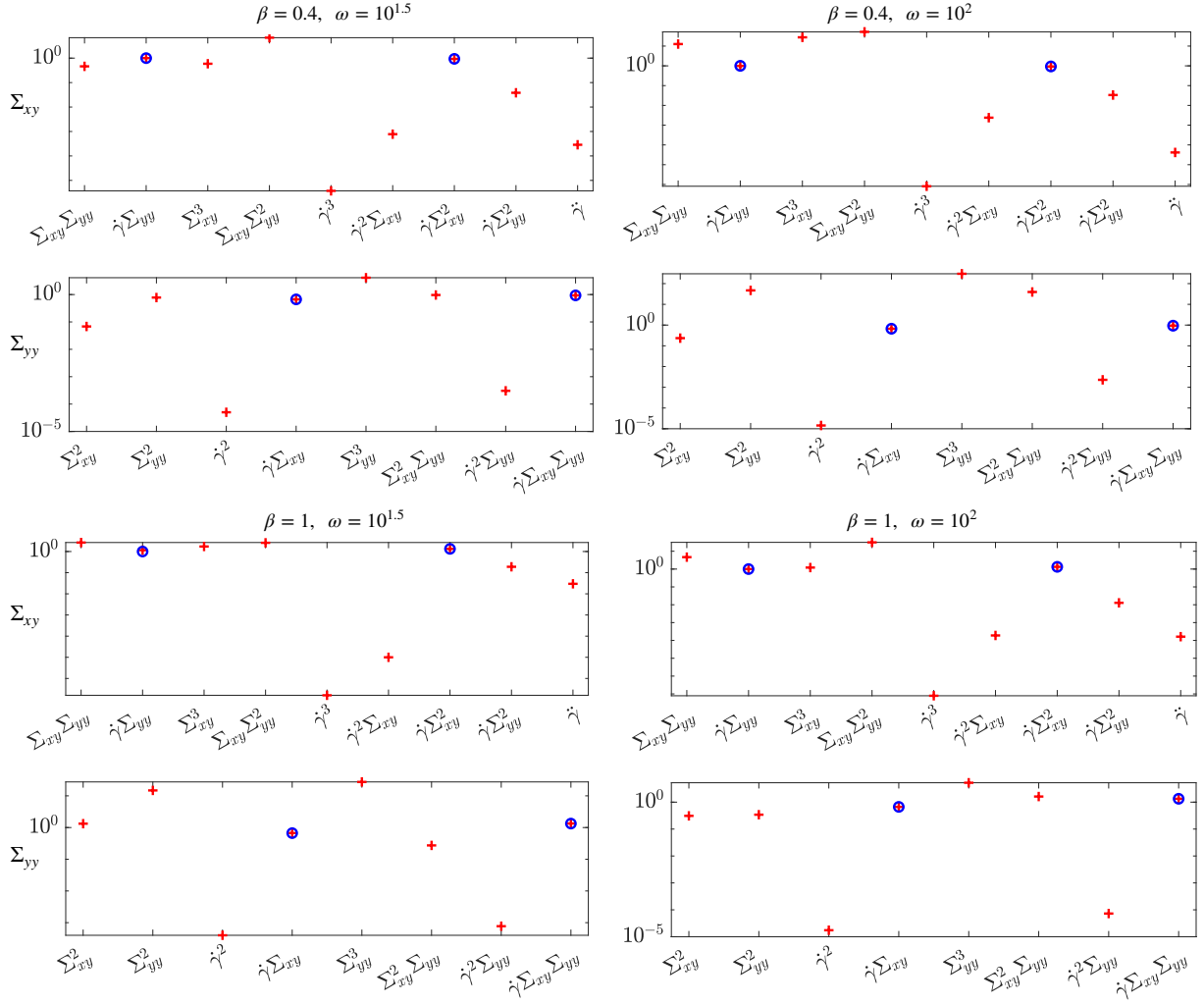


Figure 7.5: Predicted higher order coefficients (red crosses) in comparison to the coefficients from the homogeneous nRP equations (blue circles) when $\omega = \{10^{0.5}, 10\}$, the fluid is spatially homogeneous, and stress data is only recorded at the rheometer wall. The results are the same whether we use the imposed strain rate $\bar{\dot{\gamma}}$ or the local strain rate to construct the $\dot{\gamma}$ observable.

For the spatially homogeneous cases $\omega = \{10^{1.5}, 100\}$, as expected our results are virtually identical when using either source of shear rate since the value of $\dot{\gamma}$ is spatially independent. We show these results for both fluids in Fig. 7.5. We find good approximations of the coefficients for the observables we know we need, and at least some of the other observables have predicted coefficients with significantly smaller magnitudes, making them ideal for the thresholding process.

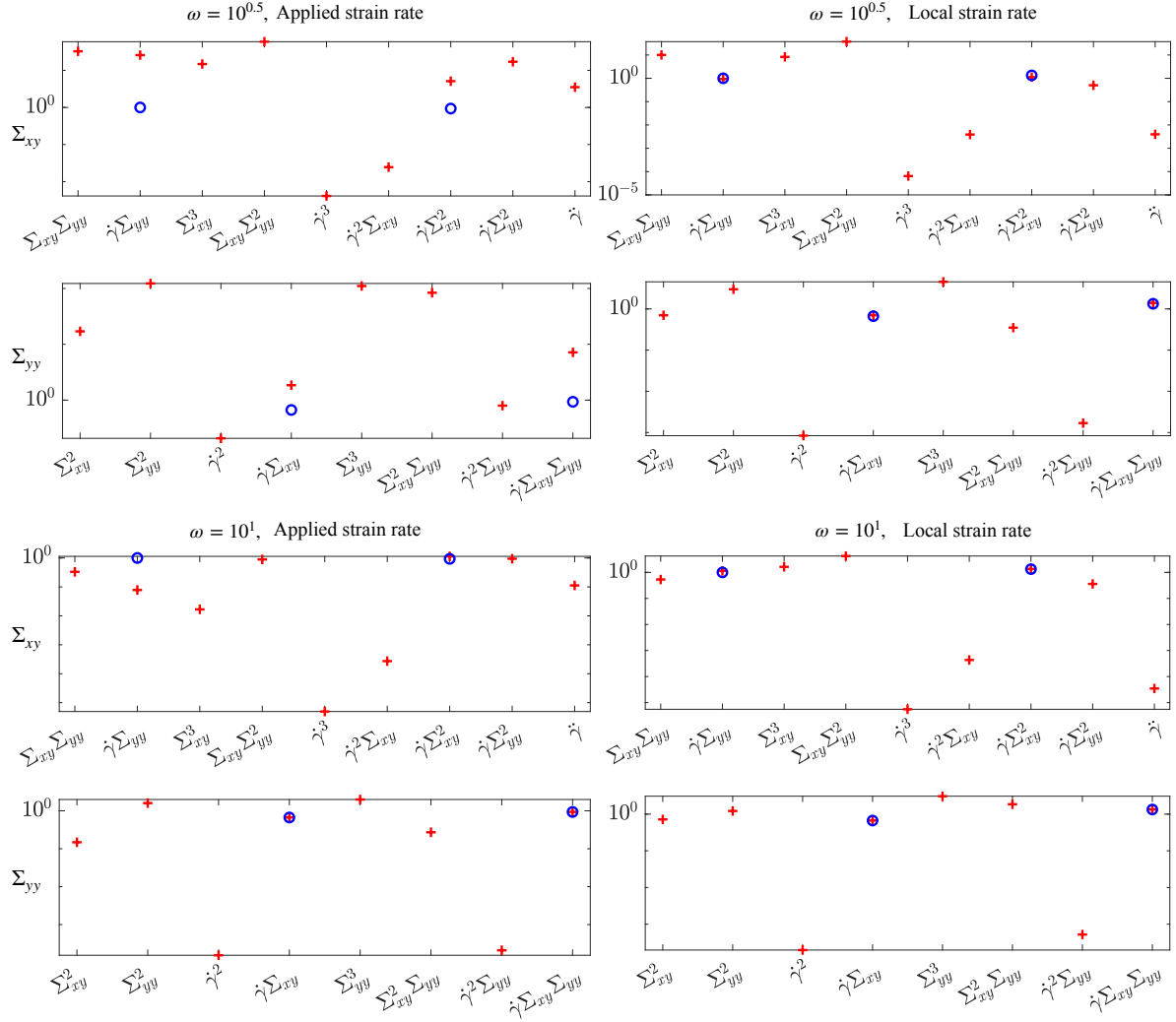


Figure 7.6: Predicted higher order coefficients (red crosses) and coefficients from the homogeneous nRP equations (blue circles) for the $\beta = 0.4$ fluid when $\dot{\gamma}_0 = 10$ and $\omega = [10^{0.5}, 10]$. We show the results when using the applied strain rate $\bar{\dot{\gamma}}$ (left) and the local strain rate $\dot{\gamma}$ for the shear rate observable.

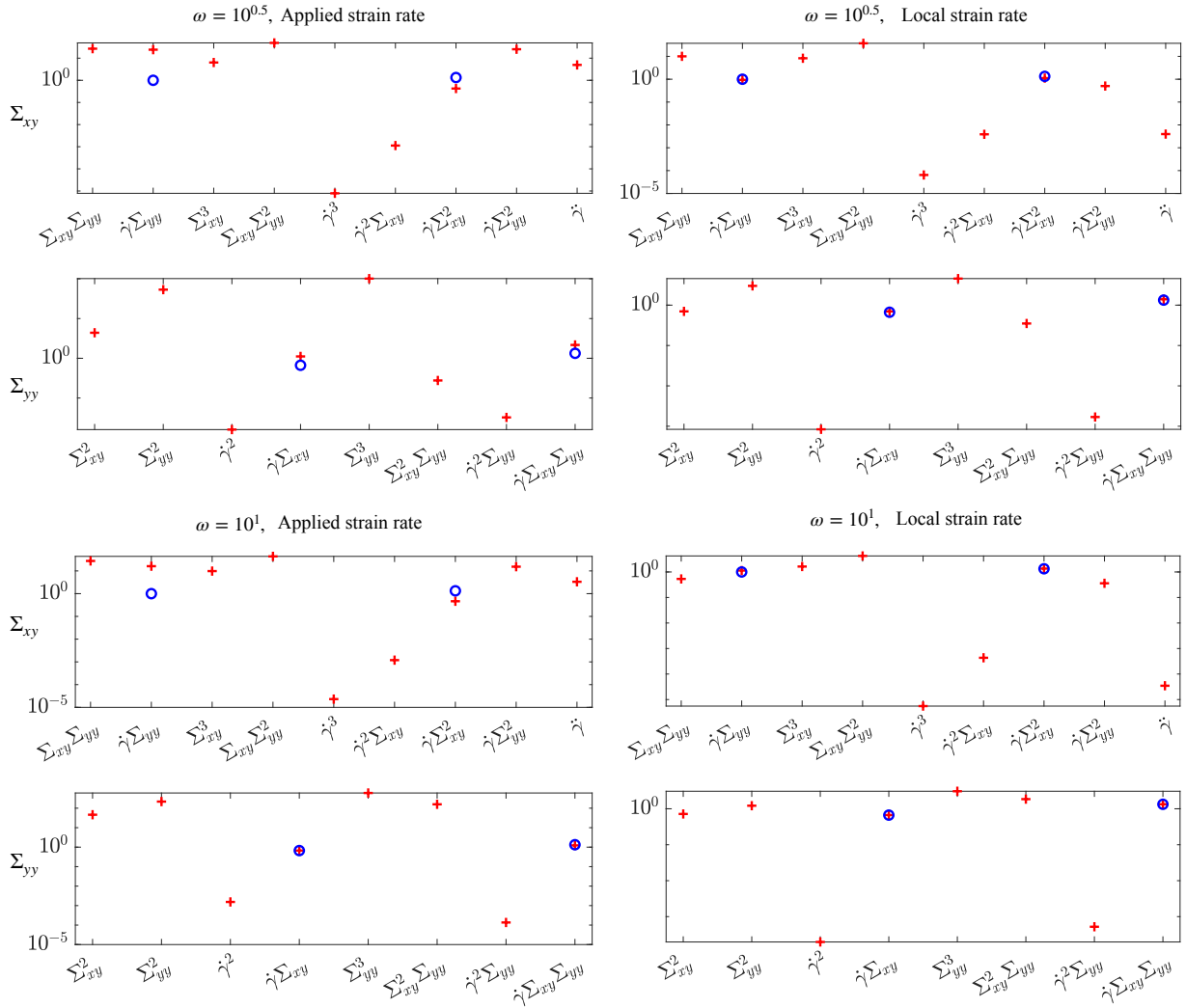


Figure 7.7: Predicted higher order coefficients (red crosses) and coefficients from the homogeneous nRP equations (blue circles) for the $\beta = 1$ fluid when $\dot{\gamma}_0 = 10$ and $\omega = [10^{0.5}, 10]$. We show the results when using the applied strain rate (left) and the local strain rate for the $\dot{\gamma}$ observable.

In Fig. 7.6 and Fig. 7.7 we show the results from rheoKIC from using the shear banding data $\omega = \{10^{0.5}, 10\}$ when $\beta = 0.4$ and $\beta = 1$, respectively. When using the applied shear rate $\bar{\gamma}$, we see significant errors for our predicted coefficients, in particular when predicting the coefficients for the Σ_{xy} evolution equation and when $\omega = 10^{0.5}$. Once the local strain rate is used instead, we find the same high level of accuracy for our coefficients as in Fig. 7.5 where the data is spatially homogeneous. We can choose to avoid handling spatial inhomogeneity if we have access to strain rate measurements at the same wall as the stress measurements since this ensures that, if shear banding is present, we are using input and output data from the same

shear banding regions with the same dynamics.

In Table 7.1 we present the reconstructed constitutive laws when combining the data for each value of ω and using the local strain rate for the $\dot{\gamma}$ observable. We apply thresholding iteratively to the results using the combined higher order data which is able to successfully identify the correct observables in all cases. Most of the coefficient errors are around 2% or less, with the largest error being 8% for the $\dot{\gamma}\Sigma_{xy}\Sigma_{yy}$ observable in the $\beta = 0.4$ case.

Correct, $\beta = 0.4$	
$\dot{\Sigma}_{xy} =$	$-1.000\Sigma_{xy} + 1.000\dot{\gamma} + 1.000\dot{\gamma}\Sigma_{yy} - 0.933\dot{\gamma}\Sigma_{xy}^2$
$\dot{\Sigma}_{yy} =$	$-1.000\Sigma_{yy} - 0.667\dot{\gamma}\Sigma_{xy} - 0.933\dot{\gamma}\Sigma_{xy}\Sigma_{yy}$
Predicted, $\beta = 0.4$	
$\dot{\Sigma}_{xy} =$	$-1.000\Sigma_{xy} + 1.000\dot{\gamma} + 0.993\dot{\gamma}\Sigma_{yy} - 0.951\dot{\gamma}\Sigma_{xy}^2$
$\dot{\Sigma}_{yy} =$	$-1.000\Sigma_{yy} - 0.677\dot{\gamma}\Sigma_{xy} - 1.012\dot{\gamma}\Sigma_{xy}\Sigma_{yy}$
Correct, $\beta = 1$	
$\dot{\Sigma}_{xy} =$	$-1.000\Sigma_{xy} + 1.000\dot{\gamma} + 1.000\dot{\gamma}\Sigma_{yy} - 1.333\dot{\gamma}\Sigma_{xy}^2$
$\dot{\Sigma}_{yy} =$	$-1.000\Sigma_{yy} - 0.667\dot{\gamma}\Sigma_{xy} - 1.333\dot{\gamma}\Sigma_{xy}\Sigma_{yy}$
Predicted, $\beta = 1$	
$\dot{\Sigma}_{xy}$	$-0.976\Sigma_{xy} + 1.000\dot{\gamma} + 0.999\dot{\gamma}\Sigma_{yy} - 1.335\dot{\gamma}\Sigma_{xy}^2$
$\dot{\Sigma}_{yy}$	$-1.000\Sigma_{yy} - 0.666\dot{\gamma}\Sigma_{xy} - 1.332\dot{\gamma}\Sigma_{xy}\Sigma_{yy}$

Table 7.1: Final reconstructed equations when using the combined data sets from the wall of the rheometer, where the fluid within the rheometer may be experiencing shear banding.

Taking the SVD of the observables individually is unnecessary when there is only one data point per snapshot: we would find the left singular vector to be a scalar value, and also equal to one since the vectors are orthonormal by construction. If only one data point is available, evidence for shear banding being present can be found by plotting the flow curve from a constant shear scenario, as illustrated in Fig. 7.2, and determining whether the stress response plateaus or is non-monotonic for a region of shear rates.

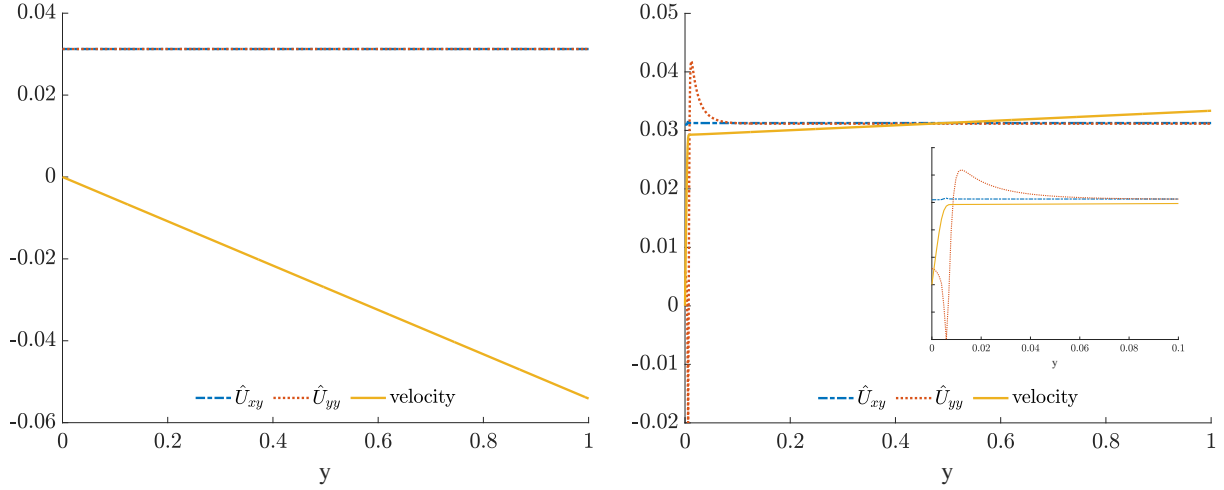


Figure 7.8: First spatial modes for Σ'_{xy} , Σ'_{yy} , and $u(y)$ for the $\beta = 0.4$ fluid when $\omega = 10^{0.5}$ and $\dot{\gamma}_0 = 10^{1.75}$. (Left) The fluid is spatially homogeneous. (Right) The fluid has shear banding behaviour, with inset zoomed in to the high shear banding region.

We can directly determine the level of spatial inhomogeneity when more data points per snapshot are available by looking at shape of the first left singular vectors of Σ_{xy} , Σ_{yy} , and the velocity field $u(y)$ computed across the width of the channel. In Fig. 7.8 we show these modes from data both with and without shear banding. When there is no shear banding, as expected we find straight lines for all the modes, indicating spatial homogeneity. Any spatial variation without structure, perhaps due to measurement noise, would be contained within the higher order modes. With shear banding, we see there that the high shear rate region near the wall has been represented with each spatial mode, and the inset figure shows the shape of these modes within this narrow layer. Analysing just the first spatial mode of this data, regardless of the number of spatial measurements in total, could therefore be a useful guide for determining whether any variation in the fluid response across the rheometer has an underlying structure.

7.3.1 Applying rheoKIC to each band separately

A key assumption behind the type of shear banding we have chosen to focus on is that there are exactly two disparate regions with different dynamics, separated according to the lever

rule given in Eq. 7.1. Previous work in the field of identifying the mechanisms behind shear banding has in fact treated them as two entirely different fluids [175], while particle simulations undergoing dynamics that result in shear banding have shown that it is possible to produce different particle concentrations within two different regions of the system [176].

In this section we will apply rheoKIC to data collected from each of the two regions from a fluid separately to see how their dynamics are reflected in the predicted coefficients. We focus on data from a simulation of a fluid where $\beta = 1$, $\omega = 10$, and $\dot{\gamma} = 10^{1.75}$. We take points recorded from within each region, with some tolerance around the band interface so that any effects from the diffusion region are not incorporated, and such that the data is adequately modelled with a single spatial mode. This results in region L_1 (the high shear rate band) being represented by points 1 : 60, while the low shear rate band L_2 is represented by points 100 : 512 from the total of $J = 512$ measurements.

We then apply rheoKIC separately to each of these sets of points, using either the local shear rate recorded at the same points as the stress data within each region or the applied shear rate $\bar{\dot{\gamma}}$. Since we retain only one spatial mode for each observable and the output data, all the approximated coefficients will be scalar and so we are able to use the more complex generalised coefficient $\check{\check{\mathbf{C}}}_k$ without suffering from difficulties in interpretability.

Observable	Correct	$L_1, \bar{\dot{\gamma}}$	$L_1, \dot{\gamma}$	$L_2, \bar{\dot{\gamma}}$	$L_2, \dot{\gamma}$
$\dot{\gamma}\Sigma_{yy}$	1.000	0.820	0.998	1.008	0.997
$\dot{\gamma}\Sigma_{xy}^2$	-1.333	-1.538	-1.335	-1.438	-1.340
$\dot{\gamma}\Sigma_{yy}$	-0.667	-0.760	-0.668	-1.005	-0.663
$\dot{\gamma}\Sigma_{xy}\Sigma_{yy}$	-1.333	-1.484	-1.336	-2.261	-1.323

Table 7.2: Reconstructed constitutive laws using spatially inhomogeneous data where the dimensions of the coefficients are enforced to be scalar.

Table 7.2 shows the coefficients from our reconstructed constitutive laws for each region. We find that using the local shear rate to construct the set of candidate observables is crucial for extracting good approximations of the coefficients for each observable. The predicted coeffi-

cients when using the local shear rate are consistent across both bands, while they can differ by up to a factor of two when the imposed shear rate $\bar{\dot{\gamma}}$ is used instead. We are able to determine that the entire fluid can be modelled with a single constitutive law by using the local shear rate when creating the candidate observables. RheoKIC applied to data from a fluid that has developed different properties within each band, for example due to differing particle concentrations within each region [176], would produce constitutive laws with different coefficients and potentially also different observables for each banded region.

7.4 Generalised coefficients for shear banding data

We now look at how the coefficients for the observables generalise when spatial measurements spanning the entire rheometer channel are included within the data, to see how our method generalises to include the effects of multiple regions with different dynamics. We will focus on data from the following two simulations:

1. $\omega = 10^{0.5}$, $\dot{\gamma}_0 = 10^{1.75}$, $G = \lambda = \beta = 1$.
2. $\omega = 10$, $\dot{\gamma}_0 = 10^{1.75}$, $G = \lambda = \beta = 1$.

The spatial modes we have retained for Σ_{xy} and Σ_{yy} using $e = 0.99$ for both simulations are displayed in Fig. 7.9. We have chosen to use data from these simulation for analysis as both bands are clearly visible: Simulation 1 has bands that are close to equal in size with a diffusive region taking up around 10% of the channel, while Simulation 2 has a smaller high-shear rate channel with $f \approx 0.15$ and a much narrower diffusive region. The shape of the spatial modes coincides with the two different banding regions in the fluid as expected. One mode suffices to represent all the data apart from Σ_{yy} for Simulation 2: here, the first mode represents 98.86% of the data while the second mode represents 0.9%. We will investigate the results from each simulation separately in the following subsections.

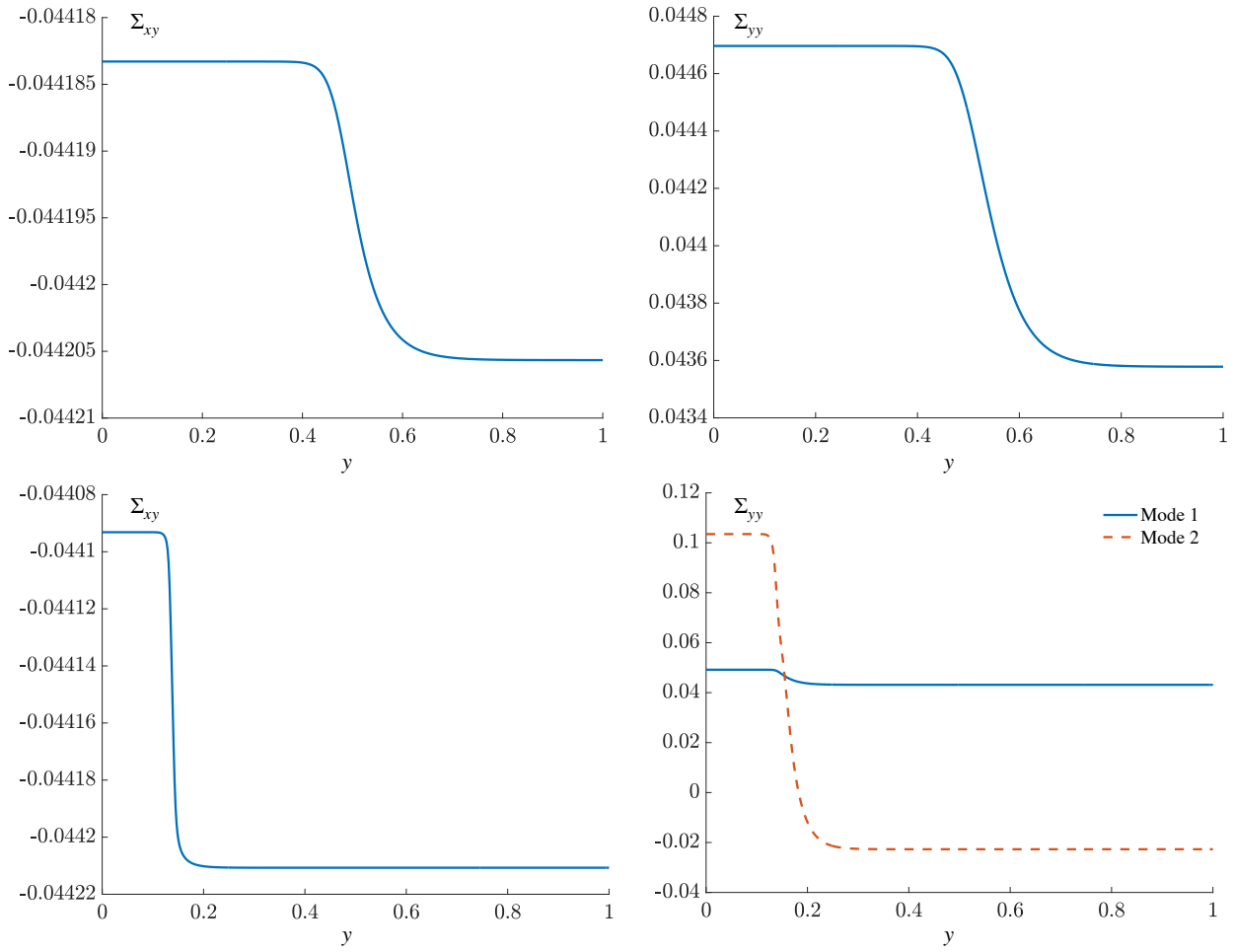


Figure 7.9: Primary spatial modes needed to represent more than 99% of the Σ_{xy} and Σ_{yy} data for (top row) Simulation 1 and (bottom row) Simulation 2.

Table 7.3 shows how many spatial modes are retained for each observable for each simulation while we continue to fix $e = 0.99$. The dimensions for each coefficient can be interpreted from this table: the number of rows depends on the modes required for the observable acting as the input to the equation, while the number of columns depends on the output data Σ_{xy} or Σ_{yy} . While a rank-1 approximation is sufficient for some of the observables, others require up to 6 modes to meet our 99% reconstruction criteria.

$\dot{\Sigma}_{xy}$ equation	Φ_{xy}	Σ'_{xy}	Σ_{xy}	$\dot{\gamma}$	$\dot{\gamma}\Sigma_{yy}$	$\dot{\gamma}\Sigma_{xy}^2$
Simulation 1	5	1	1	3	3	3
Simulation 2	6	1	1	6	6	6
$\dot{\Sigma}_{yy}$ equation	Φ_{yy}	Σ'_{yy}	Σ_{yy}	$\dot{\gamma}\Sigma_{xy}$	$\dot{\gamma}\Sigma_{xy}\Sigma_{yy}$	
Simulation 1	4	1	1	3	3	
Simulation 2	6	2	2	6	6	

Table 7.3: Number of spatial modes required to represent each observable for Simulation 1 and Simulation 2, using $e = 0.99$ in both cases.

7.4.1 Analysis of Simulation 1

For Simulation 1 there are $n = 1$ spatial modes for the output data, which allows us to simplify Eq. 7.39 for both Σ'_{xy} and Σ'_{yy} to

$$\frac{\partial\sigma(t + \Delta t)}{\partial t} = \left[-\frac{1}{\lambda} - D \int_0^L \left| \frac{\partial b}{\partial y} \right|^2 \partial y \right] \sigma(t) + \sum_k \alpha_k \sum_{q_k} \varphi_{q_k}^k(t) \langle a_{q_k}^k(y), b(y) \rangle. \quad (7.43)$$

We first focus on the coefficients for the Σ_{xy} and Σ_{yy} observables, which are 1×1 scalars since $n = 1$ and are found via the square bracket in Eq. 7.43. We compute the integral term numerically for both equations and find it to be very small - $O(10^{-12})$ for Σ_{xy} and $O(10^{-9})$ for Σ_{yy} - so it has negligible impact on the final predicted coefficients. Furthermore, since there is only one spatial mode, we can directly compare the scalar coefficients for the Σ_{xy} and Σ_{yy} observables to their counterparts from the underlying nRP equations as we did in the previous chapters.

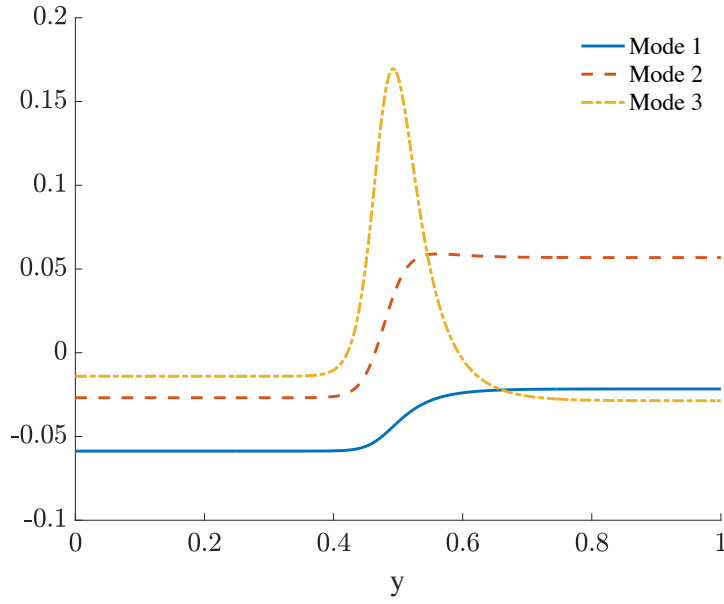


Figure 7.10: Spatial modes needed to represent more than 99% of the $\dot{\gamma}$ data for Simulation 1.

All of the other observables have three spatial modes. The actual shape of the spatial modes themselves will differ between each observable. We take the generalised coefficient for the $\dot{\gamma}$ observable as an example and plot the first three spatial modes of $\dot{\gamma}$ in Fig. 7.10. Modes 1-3 represent 84.21%, 12.67%, and 2.35% of the total data, respectively, calculated using Eq. 7.42. Interestingly, the third spatial mode is very reminiscent of the spatial gradient of the first mode.

Using the method which produces $r \times 1$ generalised coefficient vectors \hat{c}_k will result in approximated coefficients that are scalar for all observables. These predicted coefficients are displayed in Table 7.4 alongside the inner products $\langle a_{q_k}^k(y), b(y) \rangle$ between the spatial mode of the output data and the spatial modes from the observables. Aside from the prediction for the $\dot{\gamma}\Sigma_{yy}$ coefficient which has $\sim 5\%$ error, all other coefficients have been found with $< 1\%$ error.

Observable	From nRP equations	Inner product correlations	$\hat{\underline{c}}_k$
Σ_{xy}	1.000	1.000	0.998
Σ_{yy}	1.000	1.000	0.998
$\dot{\gamma}$	1.000	[0.919, -0.390, 0.062]	0.9830
$\dot{\gamma}\Sigma_{yy}$	1.000	[-0.912, 0.404, -0.073]	0.9464
$\dot{\gamma}\Sigma_{xy}^2$	-1.333	[0.915, -0.395, 0.073]	-1.3552
$\dot{\gamma}\Sigma_{xy}$	-0.667	[-0.921, 0.384, -0.067]	-0.6669
$\dot{\gamma}\Sigma_{xy}\Sigma_{yy}$	-1.333	[0.915, -0.395, -0.075]	-1.3341

Table 7.4: Spatial mode vector correlations and approximated scalar coefficients for each observable from Simulation 1.

The entries for each of the generalised coefficients are shown in Table 7.5 for Simulation 1. It is difficult to find a relation between the non-scalar generalised coefficients and the original coefficients also provided in the table. The approximations for the original coefficients using $\hat{\underline{c}}_k$ were found by enforcing the linear operators to be rank one matrices. Here, the $J \times J$ linear operators $\tilde{\mathbf{C}}_k$ within each entry of $\check{\mathbf{C}}_k$ are in fact rank four matrices. From this we may conclude that the cause of the discrepancy is the spatial complexity of $\tilde{\mathbf{C}}_k$, for which we do not have a clear method of interpretation.

Observable	From nRP equations	$\check{\mathbf{C}}$
Σ_{xy}	1.000	0.998
$\dot{\gamma}$	1.000	[0.107, -0.050, 0.028]
$\dot{\gamma}\Sigma_{yy}$	1.000	[0.032, -0.018, 0.023]
$\dot{\gamma}\Sigma_{xy}^2$	-1.333	[-0.135, 0.053, 0.011]
Σ_{yy}	1.000	0.999
$\dot{\gamma}\Sigma_{xy}$	-0.667	[0.010, -0.010, 0.033]
$\dot{\gamma}\Sigma_{xy}\Sigma_{yy}$	-1.333	[-0.001, -0.004, -0.033]

Table 7.5: Generalised coefficients for each observable for Simulation 1, alongside the original coefficient for that term in nRP equations.

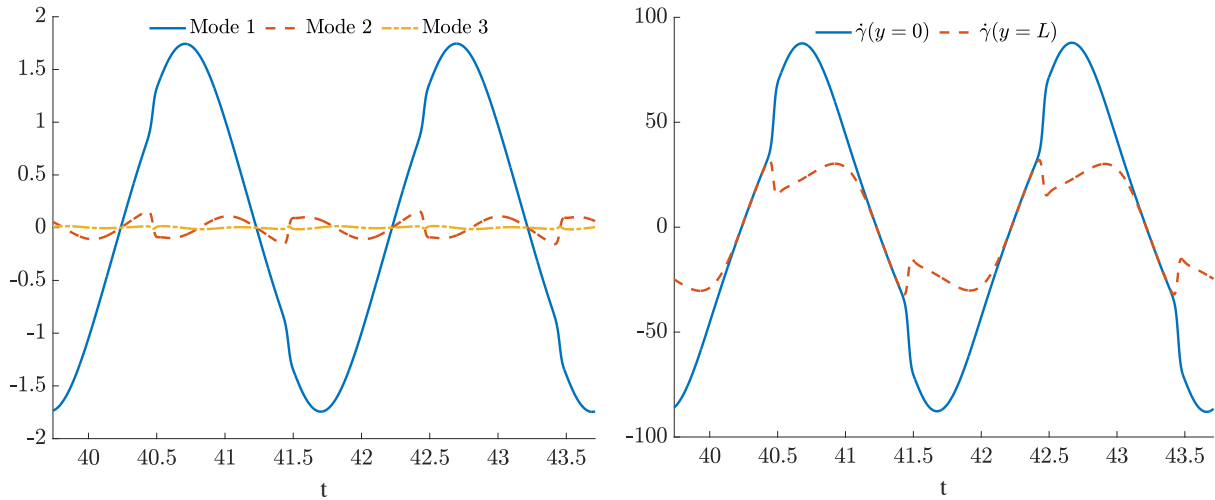


Figure 7.11: (Left) Reconstructed modes for the $\dot{\gamma}$ observable. (Right) Values for $\dot{\gamma}$ at each of the wall edges.

Our generalised coefficients $\check{\check{\mathbf{C}}}_k$ multiplied by their corresponding spatial modes for the case of the $\dot{\gamma}$ observable are displayed in Fig. 7.11, alongside $\dot{\gamma}$ recorded at each of the rheometer walls in the simulation for comparison. We can see that the first entry emulates the shape of $\dot{\gamma}$ for the larger, lower shear rate region, while the second entry emulates the smaller, high-shear rate region. Based on our observation from Fig. 7.10, we expect the third entry to represent the spatial gradient of $\dot{\gamma}$ between the regions. Similar behaviour can be found for the reconstructed modes across the other observables. We therefore find overall that the 1×3 generalised coefficients from Simulation 1 appear to correspond to the low shear rate band, the high shear rate band, and the diffusive region, in that order. The level of ‘importance’ of each entry is dictated by the percentage that its corresponding mode approximates the observable, rather than the value of the entry itself.

7.4.2 Analysis of Simulation 2

For Simulation 2, again we may compute the $r \times 1$ generalised coefficient vectors $\hat{\mathbf{c}}_k$ as described in Section 7.2.1. These are displayed in Table 7.6. There are two predictions for the observables

involving Σ_{yy} as we find one prediction per spatial mode of the output data. The largest error is $\sim 5\%$ for the $\dot{\gamma}\Sigma_{yy}$ observable coefficient, while all of the other predictions are highly accurate. Interestingly, there is very little change in accuracy for the predicted material coefficient when using the data from the second spatial mode of the Σ'_{yy} output data instead of the first.

Observable	nRP Eq.	Inner product correlations				$\hat{\mathcal{C}}_k$
Σ_{xy}	1	1.000				0.999
Σ_{yy}	1	1.000				$\begin{bmatrix} 0.999 \\ 1.000 \end{bmatrix}$
$\dot{\gamma}$	1	$\begin{bmatrix} 0.479 & -0.874 & -0.078 & -0.021 & -0.024 & 0.012 \end{bmatrix}$				0.983
$\dot{\gamma}\Sigma_{yy}$	1	$\begin{bmatrix} -0.459 & -0.876 & 0.133 & 0.034 & 0.034 & -0.024 \end{bmatrix}$				0.946
$\dot{\gamma}\Sigma_{xy}^2$	-1.333	$\begin{bmatrix} 0.462 & 0.865 & -0.185 & -0.037 & -0.046 & 0.024 \end{bmatrix}$				-1.3541
$\dot{\gamma}\Sigma_{xy}$	-0.667	$\begin{bmatrix} -0.507 & -0.851 & 0.132 & 0.024 & 0.030 & -0.014 \\ -0.832 & 0.452 & -0.207 & -0.124 & -0.150 & 0.114 \end{bmatrix}$				$\begin{bmatrix} -0.6673 \\ -0.6649 \end{bmatrix}$
$\dot{\gamma}\Sigma_{xy}\Sigma_{yy}$	-1.333	$\begin{bmatrix} 0.494 & 0.843 & -0.202 & -0.037 & -0.045 & 0.024 \\ 0.839 & -0.415 & 0.235 & 0.124 & 0.151 & -0.124 \end{bmatrix}$				$\begin{bmatrix} -1.3351 \\ -1.3298 \end{bmatrix}$

Table 7.6: Spatial mode vector correlations and predicted scalar coefficients for each observable from Simulation 2.

We now turn to the analysis of the generalised coefficients $\check{\mathbf{C}}_k$ with dimensions $r \times q_k$. As in Simulation 1, we find that the coefficient for the Σ_{xy} observable will be scalar. The contribution to the predicted coefficient from the magnitude of the diffusive region is $O(10^{-10})$, again leaving behind only the contribution from the material parameter $\frac{1}{\lambda}$. As we have explained the mechanism behind the generalised coefficients with scalar and vector dimensions in Section 7.4.1, here we will focus on interpreting the results from the Σ_{yy} equation which have generalised coefficients in the form of matrices.

We first look at the coefficient for the Σ_{yy} observable, which produces a generalised coefficient

with dimensions 2×2 that is nearly diagonal. The fact that it is diagonal is evident since each entry contains the inner product between the corresponding spatial modes of Σ_{yy} , which are orthogonal by construction:

$$\check{\mathbf{C}}_{\Sigma_{yy}} = \frac{1}{\lambda} \mathbf{I} - D \cdot \begin{bmatrix} \langle b_1(y), b_1(y) \rangle \int_0^L \left| \frac{\partial b_1(y)}{\partial y} \right|^2 dy & \langle b_1(y), b_2(y) \rangle \int_0^L \left| \frac{\partial b_1(y)}{\partial y} \right|^2 dy \\ \langle b_2(y), b_1(y) \rangle \int_0^L \left| \frac{\partial b_2(y)}{\partial y} \right|^2 dy & \langle b_2(y), b_2(y) \rangle \int_0^L \left| \frac{\partial b_2(y)}{\partial y} \right|^2 dy \end{bmatrix} \quad (7.44a)$$

$$= \frac{1}{\lambda} \mathbf{I} - 4 \cdot 10^{-4} \cdot \begin{bmatrix} 1 \cdot 10^{-7} & 10^{-16} \cdot 10^{-7} \\ 10^{-16} \cdot 10^{-5} & 1 \cdot 10^{-5} \end{bmatrix} \quad (7.44b)$$

$$= \frac{1}{\lambda} \mathbf{I} - \begin{bmatrix} 4 \cdot 10^{-11} & 4 \cdot 10^{-27} \\ 4 \cdot 10^{-25} & 4 \cdot 10^{-9} \end{bmatrix}. \quad (7.44c)$$

It is apparent that the contribution from the term representing the diffusive region has negligible impact on our final prediction, and the difference between the two diagonal terms in our generalised coefficient can be accredited to errors accumulated during the rheoKIC process.

We can visualise the behaviour of each entry from the 2×2 generalised coefficient by looking at their reconstructed modes, shown in Fig. 7.12. By comparing them to Σ_{yy} at each of the rheometer walls (also shown in Fig. 7.12), we can see that the entry in the first row and column of $\check{\mathbf{C}}_k$ matches with the shape of Σ_{yy} for both shear banding regions, which is also represented by the first projected spatial mode of Σ'_{yy} . The second diagonal entry in Eq. 7.44 and the second projected spatial mode of Σ'_{yy} appear to correspond to the diffusive region, based on its shape in comparison to the entries we saw in Section 7.4.1. Unlike previously, there is not a one-to-one correspondence between an entry in the generalised coefficient and a specific spatial behaviour. The off-diagonal terms from the generalised coefficient appear to make little to no impact on the reconstruction of the output data from the equation.

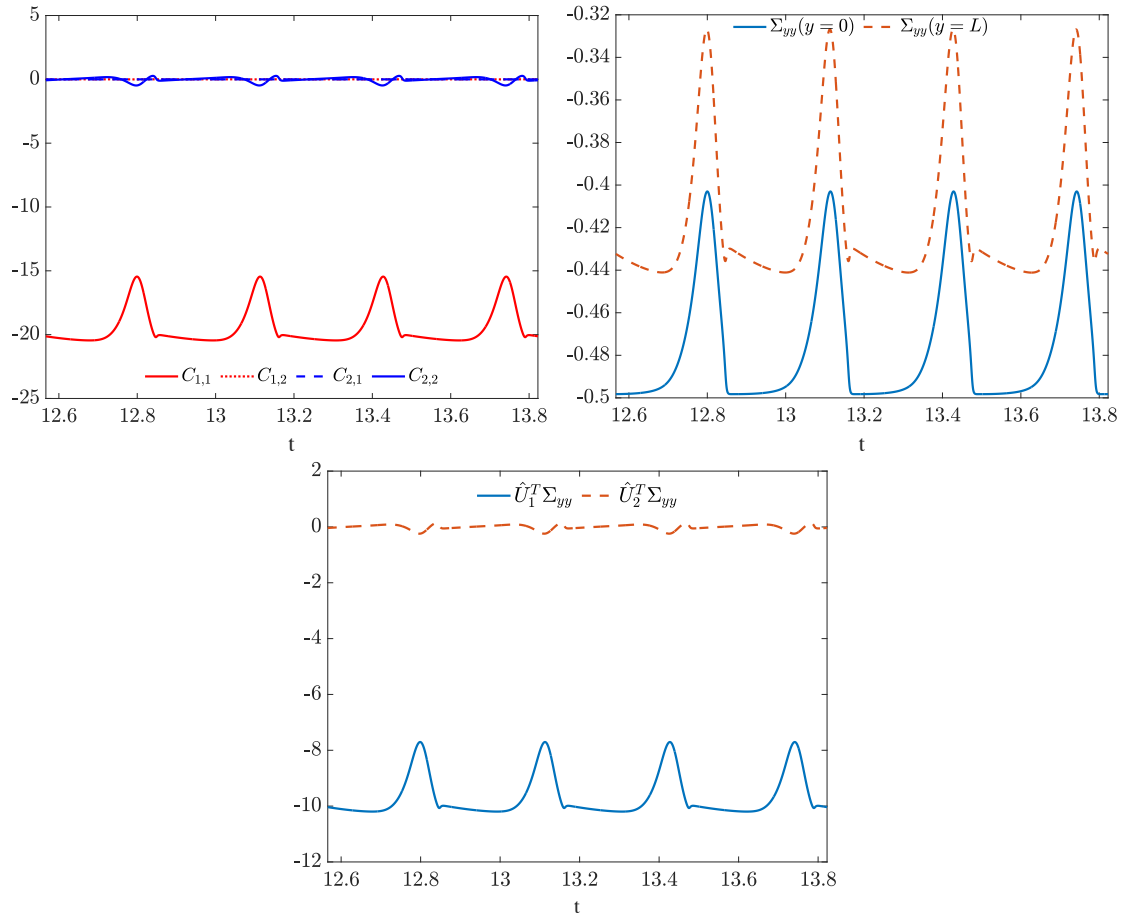


Figure 7.12: (Top-left) Reconstructed modes for the Σ_{yy} observable. (Top-right) Σ_{yy} recorded at each wall of the rheometer. (Bottom) First two projected spatial modes for Σ'_{yy} .

Table 7.7 shows the generalised coefficients $\check{\tilde{\mathbf{C}}}$ for all of the observables in Simulation 2. Again, we find that the non-scalar approximations cannot be directly related to the coefficients from the original homogeneous equations. In this case, we find that linear operator approximations $\check{\tilde{\mathbf{C}}}_k$ have rank six for all observables in both the Σ_{xy} and Σ_{yy} equations. The linear operator is therefore still expressing spatial features of the data which we are not able to separate from the scalar coefficient.

Observable	From nRP equations	$\check{\mathbf{C}}$
Σ_{xy}	1.000	1.000
$\dot{\gamma}$	1.000	[0.086, -0.170, -0.020, -0.005, -0.019, 0.008]
$\dot{\gamma}\Sigma_{yy}$	1.000	[0.049, 0.071, -0.012, -0.000, -0.014, 0.006]
$\dot{\gamma}\Sigma_{xy}^2$	-1.333	[-0.131, -0.197, 0.034, 0.006, -0.006, 0.003]
Σ_{yy}	1.000	0.999
$\dot{\gamma}\Sigma_{xy}$	-0.667	$\begin{bmatrix} 0.0028 & 0.0252 & -0.012 & -0.005 & 10^{-4} & 10^{-5} \\ 0.002 & 0.016 & -0.004 & 0.006 & -0.029 & 0.035 \end{bmatrix}$
$\dot{\gamma}\Sigma_{xy}\Sigma_{yy}$	-1.333	$\begin{bmatrix} 10^{-4} & 0.0018 & -0.012 & -0.005 & 10^{-4} & 10^{-6} \\ -0.002 & -0.029 & 0.008 & 0.011 & -0.022 & 0.0341 \end{bmatrix}$

Table 7.7: Generalised coefficients for each observable for Simulation 2, alongside the original coefficient for that term in nRP equations.

Focusing on the 2×6 generalised coefficients, we show the reconstructed modes for each entry in the coefficient for the $\dot{\gamma}\Sigma_{xy}$ observable in Fig. 7.13. The first spatial modes align with the low shear rate region containing the $y = 0$ measurements, the second spatial modes align with the high shear rate region lying next to the $y = L$ wall, and the third spatial mode represents the diffusive region. We can check the correlations between the spatial modes for each entry in the coefficient, which are found to be

$$\begin{bmatrix} -0.507 & -0.851 & 0.132 & 0.024 & 0.030 & -0.013 \\ -0.832 & 0.452 & -0.207 & -0.124 & -0.150 & 0.114 \end{bmatrix}. \quad (7.45)$$

There are no very small values indicating there are spatial modes orthogonal to each other. Instead, we find that the two values with the largest magnitudes are the off-diagonal entries in the first two columns. From this we can conclude that the second spatial mode of the $\dot{\gamma}\Sigma_{xy}$ observable is correlated to the first spatial mode of Σ'_{yy} , and vice versa.

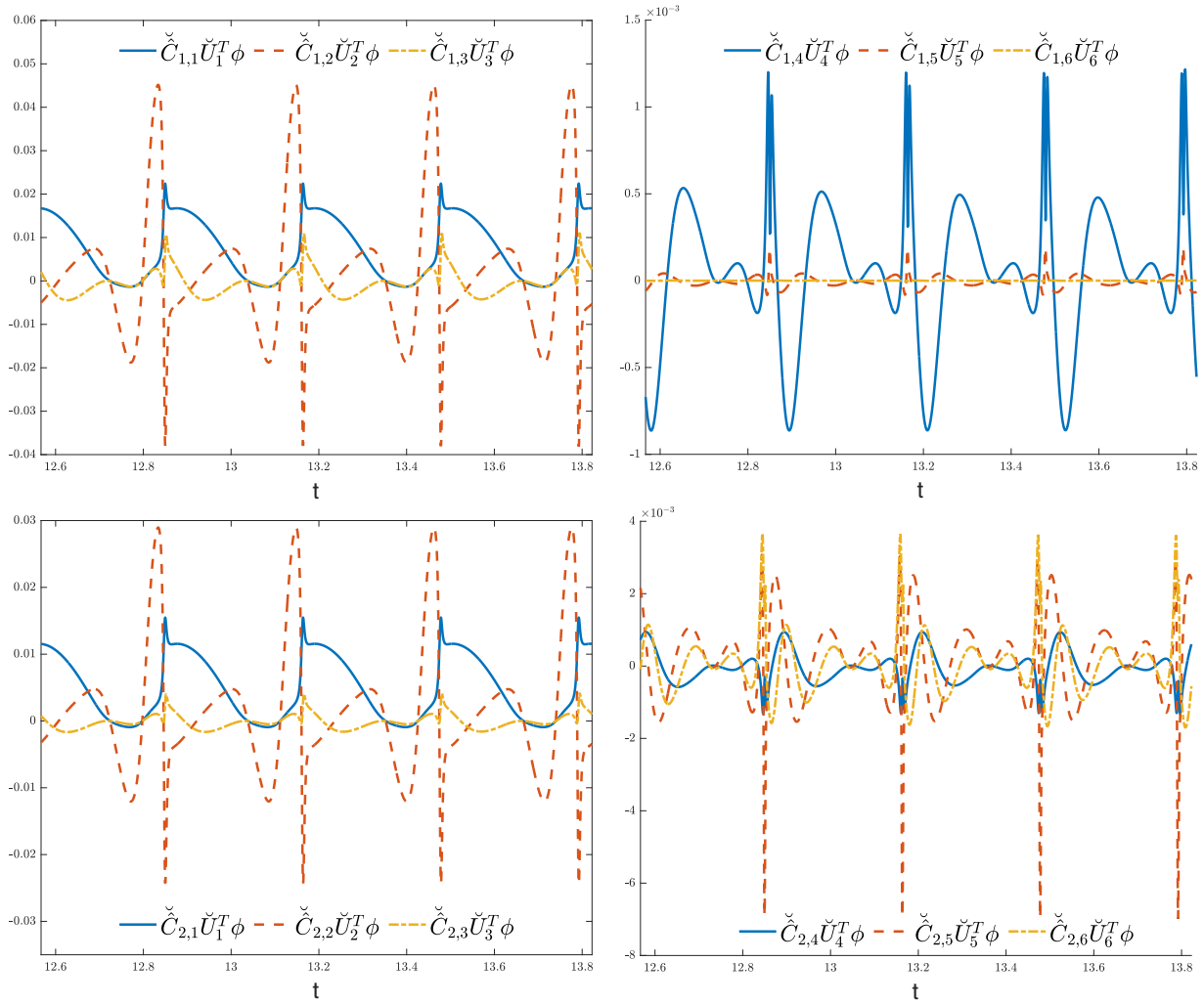


Figure 7.13: Reconstructed modes for the $\dot{\gamma}\Sigma_{yy}$ observable where each of the entries in the generalised coefficient has been multiplied by its corresponding entry in $\check{\mathbf{U}}_k^T \phi_k$.

7.5 Conclusions

While the existence of shear banding has been known for a long time, it is still an emerging topic in rheology as only recently has it been possible to record data from rheological experiments in multiple dimensions and at high fidelity. Nonlinear rheological analysis is able to avoid the subject of spatial heterogeneity through the implicit assumption that the fluid response is affine, which in turn justifies the decision to consider time series data exclusively.

Our intention for this chapter is to demonstrate that the mathematics behind rheoKIC and

Koopman methods extends to incorporate spatial behaviour within a data set. We continue to use the nRP equations introduced in Chapter 6 but use a simulation that allows for shear banding to occur. If measurements across the rheometer gap are not available, we show that rheoKIC can successfully reconstruct the constitutive law from time series measurements at the rheometer wall, regardless of whether shear banding is present or not, by using the local shear rate when constructing the set of candidate observables. Previous chapters demonstrated that combining multiple data sets which exhibit nonlinear behaviour improves the accuracy of the results from rheoKIC with respect to the higher order observables. Here, we show that this result holds even when data sets with and without spatial homogeneity are combined. We also suggest that the spatial modes from multidimensional data sets could be used as a tool for determining whether any underlying spatial structure in the data is present, as it will filter out any unstructured spatial variation from measurement noise. When measurements from within each band are available, we demonstrate that we are able to determine whether the fluid has the same properties in both regions despite their differing dynamics. We highlight that this could be used on both experimental and particle simulation data to identify and construct different constitutive laws for different regions of the system.

Lastly, we looked at how rheoKIC responds to a data set that contains measurements across the entire rheometer gap where shear banding is present. The existence of shear banding is reflected in the number of spatial modes required to reconstruct each observable and the stress response data, and thus the dimensions of each generalised coefficient. We found that these coefficients reduce to approximately the identity matrix for the Σ_{xy} and Σ_{yy} observables where the input and output data have the same spatial modes.

For the other observables, the computation for each entry in the generalised coefficient contains a linear operator approximation for the dynamics of the system which acts on the spatial modes of the observable. Our methodology for interpreting the results of spatial rheoKIC assumes that this operator can be written as a rank-one matrix. In fact, when we enforce the structure of the linear operator to be as such by solving the system as a matrix-vector problem, we retrieve the underlying coefficients remarkably successfully, with $< 1\%$ error in most cases.

When we look to interpret the generalised coefficients without enforcing structure, we find that we can use the values of the inner products of the spatial modes between the input and output data to understand how each entry relates to the different regions of behaviour within the fluid. Looking at the entries of the generalised coefficients themselves, we find that the linear operator approximations are no longer rank one, and therefore encode spatial information which is then projected onto the spatial modes of the observable. We are hopeful that further analysis of this operator in the future could be used for understanding the dynamics of more complex rheological data, for example when transitioning to or undergoing elasto-inertial turbulence.

Chapter 8: Conclusions and future work

This thesis is concerned with applying an existing branch of methods in data analysis to the field of rheology. The effect of small amplitude deformations and the subsequent response from a viscoelastic fluid is well characterised, but establishing material parameters in the nonlinear regime is still an open problem. We have conceived of and developed a method based on the Koopman with Inputs and Control (KIC) technique [20], which we call rheoKIC, for the identification of viscoelastic constitutive laws using linear and nonlinear data. We believe rheoKIC to be the first application of Koopman operator-type methods to constitutive law identification for rheological data.

By fitting the equation for the constitutive law rather than its solution, our method is able to interface with data from many standard rheological measurements, and throughout the thesis we explore how the choice of data set affects the performance of rheoKIC. A crucial aspect of these types of system identification methods is the selection of a dictionary of observables: by using the terms from a generalised constitutive framework [70] as our dictionary, we tailor rheoKIC to the identification of constitutive laws lying within this framework. Chapters 4-7 describe the development the steps underpinning the rheoKIC method in response to increasingly complex data. The results from each of these chapters are laid out below.

Chapter 4 We showed how rheoKIC simplifies to Dynamic Mode Decomposition with Control (DMDc) when applied to data from within the linear viscoelastic regime, in this case from the linear Maxwell model. We quantified the effects of the Euler approximation for the time derivative and determined that a minimum of 512 snapshots per oscillatory period suitably balanced the accuracy of our

approximations with the level of data resolution we expect from rheological experiments. Using this measurement interval retrieved approximations for our coefficients with $< 1\%$ error. We then found that supplying higher order observables when analysing linear data can be shown to be redundant via a negligible decrease in data reconstruction error when these terms are additionally supplied to rheoKIC. By exploiting the known analytic solution to the Maxwell model, we proved that rheoKIC reduced to a standard Fourier basis expansion when applied to linear data from small amplitude oscillatory shear (SAOS) simulations. Lastly, by combining data sets which emulated the data of standard linear experiments - stress relaxation, shear startup, and SAOS - we found approximations for the material parameters λ and G with $< 0.5\%$ error.

Chapter 5 We increased the problem complexity by augmenting the Maxwell model with a cubic order term to produce the simple/scalar fluidity model (SFM). Applying rheoKIC directly to this data resulted in large errors in the approximations for the nonlinear observables. Inspired by the ω -MAOS experimental protocol, we showed that fixing $\dot{\gamma}_0$ across an oscillatory frequency sweep ensured that the cubic order term stayed relevant in the rheoKIC reconstruction of the model, which was additionally reflected in the rank of the set of candidate observables. We introduced a sequential approach which first identifies the linear coefficients using linear data with excellent accuracy. We then used the approximated relaxation time from the linear data to inform our simulation parameters for a nonlinear data set, with which we located approximations for the higher order observable with $< 1\%$ error. We then compared this approach, which used three data sets in total, to rheoKIC applied to a single MAPS data set with high shear rate amplitude, and found the results to be quantitatively similar while the MAPS data set also allowed us to remove all the unwanted observables. Finally, we confirmed that the performance of rheoKIC was not affected by Gaussian noise for signal-to-noise ratios as low as $100 : 1$. We found that a simple low-pass filter dramatically improved our approximations for higher noise levels than this,

and described how our knowledge of the imposed shear rate could be used to determine an appropriate filter attenuation point.

Chapter 6 We extended the complexity of the constitutive law to the non-stretching Rolie-Poly (nRP) system of equations for two components of the stress tensor, which in turn increased the number of candidate observables to twenty. This left a naive application of rheoKIC exposed to overfitting. We recognised that attempting to include terms involving the solvent viscosity exacerbated this issue as they were several orders of magnitude smaller, and concluded that these terms should not be considered within the constitutive law reconstruction. The increase in the number of observables heightened the need for effective application of the thresholding process. Through a combination of the sequential method, combined nonlinear data sets, and thresholding, we correctly identified the observables from the underlying constitutive law and found the corresponding coefficients with $< 3\%$ error. Lastly, applying thresholding to a MAPS data at high strain rate amplitude retrieved the results with a similar level of accuracy.

Chapter 7 We explored the potential for rheoKIC to be used on data sets with multiple data points per measurement and where the fluid demonstrates shear banding behaviour. After first producing data sets for the nRP equations that allow for spatial inhomogeneity, we showed that the quality of results from rheoKIC was unaffected if only data from the rheometer wall was supplied and that rheoKIC successfully determined that the fluid has the same properties in each region when data from each of the banded regions was provided to rheoKIC separately. Finally, we generalised the rheoKIC analysis so that it could be applied to spatially varying data, and found that each entry in the generalised coefficient contained information about the relationship between the spatial modes for each observable and the output data. We showed how we can extract the coefficients for the constitutive law from this data with $< 5\%$ error, and explained how the generalised coefficients contain further information regarding the evolution of the system dynamics which may be useful for future rheological analysis.

8.1 Future work

We have brought together two areas of research for what we believe to be the first time and so it is natural to separate our thoughts regarding extensions of the work into two main areas: those broadening the applications in rheology, and those extending the methodology itself.

8.1.1 Extensions within Rheology

From the outset, we restricted the scope of the fluids under analysis to viscoelastic fluids whose constitutive law falls within the GNMM framework. Viscoelastic behaviour often coincides with yield stress behaviour [177], where the fluid behaves as an elastic solid below a critical stress but behave as a solid above this point [178], and the corresponding constitutive laws are often two different equations depending on the regime [179]. Carrying out rheoKIC on a data set from above and below the critical stress value would in theory construct two different constitutive laws, while carrying out rheoKIC on combined data sets spanning both regimes has the potential to create a unified equation representing both types of material behaviour.

We have also restricted our focus to models assuming a single relaxation time for the fluid. The initial derivation of the GNMM framework allows for the inclusion of multiple relaxation times [70], and analysis of MAOS data using Chebyshev basis functions has already been extended to this aim [180, 181] by using nonlinear regression with a regularisation term to determine the number of modes to retain. We imagine a similar procedure during an initial iteration of rheoKIC could similarly determine how many relaxation modes to use in the analysis.

A key component in the motivation behind this thesis is that rheoKIC should be applicable to experimental data sets with minimal modifications. Applying rheoKIC to experimental data should therefore be a priority for future work. A comparison of the results using multiple data sets from the same experiment but with varying dimensions (for example, stress data from the wall of a rheometer coupled with PIV data of the fluid dynamics within the rheometer [150]) could also prove very enlightening. We have focused on data regarding the applied strain rate

and the stress response, but an important additional channel of information is the presence of any normal stress differences [182], particularly because extracting the individual diagonal elements of the stress tensor may prove to be challenging [183]. We believe that, given the right data is provided, rheoKIC could reconstruct an equation for the normal stress differences analogously to how we use it at present for the stress evolution equation.

We have looked at data sets that emulate the results from several rheometry experiments which probe both the linear and nonlinear viscoelastic regimes. Further work could be carried out in analysing the results from other recently introduced experimental protocols, such as the superposition rheometry experiments [64, 65] and chirp experiments [76, 78] introduced in Chapter 2. Regarding more interesting data sets from simulations, we would be interested to see how rheoKIC would construct a constitutive law for a particle simulation where the constitutive law has not been specified explicitly, and if rheoKIC could be used as a method for combined analysis of data from low-fidelity and high-fidelity simulations [184].

Koopman-inspired methods such as KIC and DMDC are often used for open loop control and model predictive-control type problems [132], where the stability of the computed linear operator determines how the input to the system should be adapted in real time [126]. An ‘interrogation system’ approach has already been proposed for the identification of ordinary differential equations [185]: data from an initial experiment is used to produce a battery of candidate models, then new sets of initial conditions for subsequent experiments are proposed to probe the regions where the candidate models disagree most. Over a longer time horizon, we imagine utilising the control-related attributes of the rheoKIC approach, which have yet to be explored, as an interrogation method during rheological experiments to produce the best possible data sets for analysis.

8.1.2 Extensions within the methodology

The original paper presenting the KIC method was published in 2018 [20], ten years after the initial release of the Dynamic Mode Decomposition (DMD) [95] method which first demonstrated how the Koopman operator could be approximated with finite dimensions. Within this

decade, there has been a constellation of modifications and extensions to the original DMD method, of which comprehensive reviews are available [85]. There are undoubtedly features from these efforts which could be incorporated into future extensions of rheoKIC. More generally, the question of identifying an equation driving the underlying dynamics of a system generally falls under the area of *inverse problems*; this is a field of research within its own right, of which there are a huge quantity of methods, applications, and entire journals dedicated to studying [186, 187].

We first noted within Chapter 4 that the Euler approximation for the time derivative required by DMD introduces numerical error of the order of the time step size. A way of mitigating this problem is by introducing time delay embedding of the data sets. This has been introduced within ‘higher order DMD’ [133, 134] and in deep learning approaches to learning system dynamics [113, 188], and which have strong connections to Takens’ embedding theorem [189]. Another extension to rheoKIC would be to replace the SVD step, which computes a linear subspace for the nonlinear data to lie on, with a nonlinear autoencoder, where the final subspace can remain nonlinear [188, 190]. This results in a simpler and more accurate final model at the cost of significantly more complex computation [191]. Finally, it would be beneficial to incorporate further techniques within rheoKIC that account for measurement noise above the methods discussed in this thesis, for which several methods have already been proposed [103, 104]. This would allow for the inclusion of confidence intervals to accompany the resulting terms and coefficients for the reconstructed constitutive law [136], which would be highly advantageous during practical applications of rheoKIC.

By using the GNMM framework to inform our set of observables, and by using a sequential method that enforces the presence of linear terms in the model, we intend for constitutive laws built using rheoKIC to be physically admissible by default. Future work could be carried out to confirm this theoretically. It would also be highly interesting to investigate how further constraints could be incorporated within the methodology, such as the range of values each parameter can take, by taking advantage of extensions to DMD which already exist with this goal in mind [192]. Neural network (NN) models [193] have already been modified to include physical constraints as ‘physics-informed neural networks’ (PINNs) [194–196], to preserve symmetries

within the underlying dynamics [197], and even with a particular focus on learning constitutive laws [198] as well as learning and representing the set of candidate observables [116, 120]. However, these techniques require large amounts of training data and the final representation is usually difficult to interpret [199]. As yet unpublished work claims to have combined a constitutive law framework with a NN to maintain admissibility and intelligibility of the final model while allowing flexibility to represent data from different environments [200].

Finally, while we established the theoretical framework behind constructing the Koopman operator for a nonlinear constitutive law, in this thesis we did not move onto applying this framework to scenarios where its benefits can be fully understood - namely, in the interpretation of complex nonlinear dynamics that may be evolving over time and space. We believe that rheoKIC could be used for understanding the formation of coherent structures in systems undergoing transition or experiencing elasto-inertial turbulence, as it has the potential to disambiguate nonlinearities due to turbulence from those arising naturally due to the constitutive law of the fluid.

8.2 Closing remarks

We hope that the work presented in this thesis has shown that the rheoKIC method is a novel, powerful, and generalisable method for interpreting rheological data. The underlying mathematics behind the rheoKIC method is simple - the singular value decomposition is often taught to second-year mathematics undergraduates - but it has deep strong connections to both well-established and cutting-edge methods of studying fluid dynamics. The simplicity of the approach allows for the unification of linear and nonlinear analysis, using data from multiple experiments and under different experimental protocols. We see a huge number of potential avenues for further investigation of this approach within the field of rheology, and we hope that any rheologists reading this conclusion feels similarly.

Bibliography

- [1] Vojtěch Kumbár, Veronika Kouřilová, Renáta Dufková, Jiří Votava, and Luděk Hřivna. Rheological and Pipe Flow Properties of Chocolate Masses at Different Temperatures. *Foods*, 10(11):2519, October 2021.
- [2] D Balzer, S Varwig, and M Weihrauch. Viscoelasticity of personal care products. *Colloids and Surfaces A: Physicochemical and Engineering Aspects*, 99(2-3):233–246, June 1995.
- [3] R.B. Bird, R.C. Armstrong, and O. Hassager. *Dynamics of Polymeric Liquids. Vol. 1, 2nd Ed. : Fluid mechanics*. Wiley, 2nd edition, 1987.
- [4] Nikola Bosnjak, Siva Nadimpalli, Dai Okumura, and Shawn A. Chester. Experiments and modeling of the viscoelastic behavior of polymeric gels. *Journal of the Mechanics and Physics of Solids*, 137:103829, April 2020.
- [5] Noreen Sher Akbar and S. Nadeem. Carreau fluid model for blood flow through a tapered artery with a stenosis. *Ain Shams Engineering Journal*, 5(4):1307–1316, December 2014.
- [6] M.O. Chevrel, T. Platz, E. Hauber, D. Baratoux, Y. Lavallée, and D.B. Dingwell. Lava flow rheology: A comparison of morphological and petrological methods. *Earth and Planetary Science Letters*, 384:109–120, December 2013.
- [7] Jonathan B. Freund and Randy H. Ewoldt. Quantitative rheological model selection: Good fits versus credible models using Bayesian inference. *Journal of Rheology*, 59(3):667–701, May 2015. Publisher: Society of Rheology.

- [8] M. T. Gallagher, R. A.J. Wain, S. Dari, J. P. Whitty, and D. J. Smith. Non-identifiability of parameters for a class of shear-thinning rheological models, with implications for haematological fluid dynamics. *Journal of Biomechanics*, 2019.
- [9] Sandra Lerouge and Peter D. Olmsted. Non-local Effects in Shear Banding of Polymeric Flows. *Frontiers in Physics*, 7:246, January 2020.
- [10] Robyn L. Moorcroft, Michael E. Cates, and Suzanne M. Fielding. Age-Dependent Transient Shear Banding in Soft Glasses. *Physical Review Letters*, 106(5):055502, February 2011.
- [11] K. Sato, I. Kunita, Y. Takikawa, D. Takeuchi, Y. Tanaka, T. Nakagaki, and H. Orihara. Direct observation of orientation distributions of actin filaments in a solution undergoing shear banding. *Soft Matter*, 13(14):2708–2716, 2017.
- [12] A. Chiuso and G. Pillonetto. System Identification: A Machine Learning Perspective. *Annual Review of Control, Robotics, and Autonomous Systems*, 2(1):281–304, May 2019.
- [13] Bernard Koopman. Hamiltonian Systems and Transformation in Hilbert Space. *Proceedings of the National Academy of Sciences*, 17(5):315–318, May 1931.
- [14] Marko Budišić, Ryan Mohr, and Igor Mezić. Applied Koopmanism. *Chaos*, 22(4), October 2012. Publisher: American Institute of Physics Inc.
- [15] Peter J. Schmid. Dynamic mode decomposition of numerical and experimental data. *Journal of Fluid Mechanics*, 2010. ISBN: 1469-7645.
- [16] P. J. Schmid, L. Li, M. P. Juniper, and O. Pust. Applications of the dynamic mode decomposition. *Theoretical and Computational Fluid Dynamics*, 2011. ISBN: 0935-4964.
- [17] Neethu Mohan, K.P. Soman, and Kumar S Sachin. A Data-driven Approach for Estimating Power System Frequency and Amplitude Using Dynamic Mode Decomposition. In *2018 International Conference and Utility Exhibition on Green Energy for Sustainable Development (ICUE)*, pages 1–9, October 2018.

- [18] Joshua L. Proctor and Philip A. Eckhoff. Discovering dynamic patterns from infectious disease data using dynamic mode decomposition. *International Health*, 7(2):139–145, March 2015.
- [19] Jordan Mann and J. Nathan Kutz. Dynamic mode decomposition for financial trading strategies. *Quantitative Finance*, 2016.
- [20] Joshua L. Proctor, Steven L. Brunton, and J. Nathan Kutz. Generalizing Koopman Theory to Allow for Inputs and Control. *SIAM Journal on Applied Dynamical Systems*, 17(1):909–930, January 2018.
- [21] Alexander Morozov and Saverio E. Spagnolie. Introduction to Complex Fluids. In Saverio E. Spagnolie, editor, *Complex Fluids in Biological Systems: Experiment, Theory, and Computation*, Biological and Medical Physics, Biomedical Engineering, pages 3–52. Springer, New York, NY, 2015.
- [22] J. G. Oldroyd. An approach to non-newtonian fluid mechanics. *Journal of Non-Newtonian Fluid Mechanics*, 14:9–46, January 1984. Publisher: Elsevier BV.
- [23] A. S. Lodge. On the use of convected coordinate systems in the mechanics of continuous media. *Mathematical Proceedings of the Cambridge Philosophical Society*, 47(3):575–584, July 1951.
- [24] Alan D. Freed and Shahla Zamani. On the use of convected coordinate systems in the mechanics of continuous media derived from a QR factorization of F . *International Journal of Engineering Science*, 127:145–161, June 2018.
- [25] J. G. Oldroyd. On the Formulation of Rheological Equations of State. *Proceedings of the Royal Society A: Mathematical, Physical and Engineering Sciences*, 1950. ISBN: 0080-4630.
- [26] John Hinch and Oliver Harlen. Oldroyd B, and not A? *Journal of Non-Newtonian Fluid Mechanics*, 298:104668, December 2021.

- [27] M. Lemou, M. Picasso, and P. Degond. Viscoelastic Fluid Models Derived from Kinetic Equations for Polymers. *SIAM Journal on Applied Mathematics*, 62(5):1501–1519, January 2002.
- [28] Lifei Zhao, Zhen Li, Bruce Caswell, Jie Ouyang, and George Em Karniadakis. Active learning of constitutive relation from mesoscopic dynamics for macroscopic modeling of non-Newtonian flows. *Journal of Computational Physics*, 2018.
- [29] Malcolm M. Cross. Rheology of non-Newtonian fluids: A new flow equation for pseudoplastic systems. *Journal of Colloid Science*, 20(5):417–437, June 1965.
- [30] J. Kim, P.K. Singh, J.B. Freund, and R.H. Ewoldt. Uncertainty Propagation in Simulation Predictions of Generalized Newtonian Fluid Flows. *Journal of Non-Newtonian Fluid Mechanics*, July 2019.
- [31] T. Kirchdoerfer and M. Ortiz. Data Driven Computing with noisy material data sets. *Computer Methods in Applied Mechanics and Engineering*, 2017. ISBN: 9783319608853.
- [32] T. Kirchdoerfer and M. Ortiz. Data-driven computational mechanics. *Computer Methods in Applied Mechanics and Engineering*, 2016. ISBN: 0045-7825.
- [33] T. Kirchdoerfer and M. Ortiz. Data-driven computing in dynamics. *International Journal for Numerical Methods in Engineering*, 2018.
- [34] Mouldi Ben Azzouna, Pierre Feissel, and Pierre Villon. Robust identification of elastic properties using the Modified Constitutive Relation Error. *Computer Methods in Applied Mechanics and Engineering*, 2015. ISBN: 0045-7825.
- [35] Biswanath Banerjee, Timothy F. Walsh, Wilkins Aquino, and Marc Bonnet. Large scale parameter estimation problems in frequency-domain elastodynamics using an error in constitutive equation functional. *Computer Methods in Applied Mechanics and Engineering*, 2013. ISBN: 0045-7825.
- [36] Frédéric Barbaresco and Frank Nielsen, editors. *Geometric Structures of Statistical Physics, Information Geometry, and Learning: SPIGL’20, Les Houches, France, July*

- 27–31, volume 361 of *Springer Proceedings in Mathematics & Statistics*. Springer International Publishing, Cham, 2021.
- [37] Anthony N Beris. Simple non-equilibrium thermodynamics: applications to polymer rheology. *Rheology Reviews*, pages 37–75, 2003.
- [38] Hao-Hsun Hsu and Jia-Lin Tsai. Characterizing the hyper-viscoelastic behavior of adhesive films. *Journal of Mechanics*, 37:446–453, June 2021.
- [39] Ya Zhao, Simon J. Haward, and Amy Q. Shen. Rheological characterizations of wormlike micellar solutions containing cationic surfactant and anionic hydrotropic salt. *Journal of Rheology*, 59(5):1229–1259, September 2015.
- [40] Th.F. Tadros. Fundamental principles of emulsion rheology and their applications. *Colloids and Surfaces A: Physicochemical and Engineering Aspects*, 91:39–55, November 1994.
- [41] J. R. Gillmor, R. H. Colby, E. Hall, and C. K. Ober. Viscoelastic properties of a model main-chain liquid crystalline polyether. *Journal of Rheology*, 38(5):1623–1638, September 1994.
- [42] K. R. Rajagopal and A. R. Srinivasa. A thermodynamic frame work for rate type fluid models. *Journal of Non-Newtonian Fluid Mechanics*, 88(3):207–227, January 2000. Publisher: Elsevier Science Publishers B.V.
- [43] Rui Xiao, Hongguang Sun, and Wen Chen. An equivalence between generalized Maxwell model and fractional Zener model. *Mechanics of Materials*, 100:148–153, September 2016.
- [44] Qinwu Xu and Björn Engquist. A mathematical model for fitting and predicting relaxation modulus and simulating viscoelastic responses. *Proceedings of the Royal Society A: Mathematical, Physical and Engineering Sciences*, 474(2213):20170540, May 2018.
- [45] J. G. Oldroyd. Non-Newtonian effects in steady motion of some idealized elastico-viscous liquids. *Proceedings of the Royal Society of London. Series A. Mathematical and Physical Sciences*, 245(1241):278–297, June 1958.

- [46] Alan Jeffrey Giacomini and Chaimongkol Saengow (Image). Ongoing relevance of Oldroyd 8-constant fluids. *Journal of Non-Newtonian Fluid Mechanics*, 299:104653, January 2022.
- [47] Kyle R. Lennon, Gareth H. McKinley, and James W. Swan. The medium amplitude response of nonlinear Maxwell–Oldroyd type models in simple shear. *Journal of Non-Newtonian Fluid Mechanics*, 295:104601, September 2021.
- [48] A J M Spencer and R S Rivlin. The Theory of Matrix Polynomials and its Application to the Mechanics of Isotropic Continua. *Archive for Rational Mechanics and Analysis*, 2:309–336, 1958.
- [49] K. A. Carter, J. M. Girkin, and S. M. Fielding. Shear banding in large amplitude oscillatory shear (LAOS strain and LAOS stress) of polymers and wormlike micelles. *Journal of Rheology*, 60(5):883–904, September 2016.
- [50] Martin Laun, Dietmar Auhl, Rüdiger Brummer, Dirk J. Dijkstra, Claus Gabriel, Marc A. Mangnus, Maximilian Rüllmann, Wim Zoetelief, and Ulrich A. Handge. Guidelines for checking performance and verifying accuracy of rotational rheometers: viscosity measurements in steady and oscillatory shear (IUPAC Technical Report). *Pure and Applied Chemistry*, 86(12):1945–1968, December 2014.
- [51] J.D. Ferry. *Viscoelastic Properties of Polymers*. John Wiley, New York, 3rd edition, 1980.
- [52] Hyeon Yong Song, Hyo Jae Kong, Si Yoon Kim, and Kyu Hyun. Evaluating predictability of various constitutive equations for MAOS behavior of entangled polymer solutions. *Journal of Rheology*, 64(3):673–707, May 2020.
- [53] Edgar Volpert, Joseph Selb, and Françoise Candau. Associating behaviour of polyacrylamides hydrophobically modified with dihexylacrylamide. *Polymer*, 39(5):1025–1033, March 1998.
- [54] Roney L. Thompson, Alexandra A. Alicke, and Paulo R. de Souza Mendes. Model-based material functions for SAOS and LAOS analyses. *Journal of Non-Newtonian Fluid Mechanics*, 2015.

- [55] Manfred Wilhelm. Fourier-Transform Rheology. *Macromolecular Materials and Engineering*, 287(2):83–105, February 2002.
- [56] Kyu Hyun, Manfred Wilhelm, Christopher O. Klein, Kwang Soo Cho, Jung Gun Nam, Kyung Hyun Ahn, Seung Jong Lee, Randy H. Ewoldt, and Gareth H. McKinley. A review of nonlinear oscillatory shear tests: Analysis and application of large amplitude oscillatory shear (LAOS). *Progress in Polymer Science*, 36(12):1697–1753, December 2011.
- [57] Kwang Soo Cho, Kyu Hyun, Kyung Hyun Ahn, and Seung Jong Lee. A geometrical interpretation of large amplitude oscillatory shear response. *Journal of Rheology*, 49(3):747–758, May 2005. Publisher: Society of Rheology.
- [58] Paulo R. de Souza Mendes, Roney L. Thompson, Alexandra A. Alicke, and Ricardo T. Leite. The quasilinear large-amplitude viscoelastic regime and its significance in the rheological characterization of soft matter. *Journal of Rheology*, 58(2):537–561, March 2014.
- [59] Christopher O. Klein, Hans W. Spiess, Andreea Calin, Corneliu Balan, and Manfred Wilhelm. Separation of the Nonlinear Oscillatory Response into a Superposition of Linear, Strain Hardening, Strain Softening, and Wall Slip Response. *Macromolecules*, 40(12):4250–4259, June 2007.
- [60] Simon A. Rogers. A sequence of physical processes determined and quantified in LAOS: An instantaneous local 2D/3D approach. *Journal of Rheology*, 56(5):1129–1151, September 2012.
- [61] Jana Zelenkova, Radek Pivokonsky, and Petr Filip. Two Ways to Examine Differential Constitutive Equations: Initiated on Steady or Initiated on Unsteady (LAOS) Shear Characteristics. *Polymers*, 9(12):205, June 2017.
- [62] Randy H. Ewoldt, A. E. Hosoi, and Gareth H. McKinley. New measures for characterizing nonlinear viscoelasticity in large amplitude oscillatory shear. *Journal of Rheology*, 52(6):1427–1458, November 2008. Publisher: Society of Rheology.

- [63] Giulio G. Giusteri and Ryohei Seto. A theoretical framework for steady-state rheometry in generic flow conditions. *Journal of Rheology*, 62(3):713–723, May 2018.
- [64] R. I. Tanner. Comparative Studies of Some Simple Viscoelastic Theories. *Transactions of the Society of Rheology*, 12(1):155–182, March 1968.
- [65] D.J. Curtis and A.R. Davies. Volterra kernels, Oldroyd models, and interconversion in superposition rheometry. *Journal of Non-Newtonian Fluid Mechanics*, 293:104554, July 2021.
- [66] J Vermant, L Walker, P Moldenaers, and J Mewis. Orthogonal versus parallel superposition measurements. *Journal of Non-Newtonian Fluid Mechanics*, 79(2-3):173–189, November 1998.
- [67] Erik E Holly, Sundar K Venkataraman, Francois Chambon, and H Henning. Fourier transform mechanical spectroscopy of viscoelastic materials with transient structure. *Journal of Non-Newtonian Fluid Mechanics*, pages 17–26, 1988.
- [68] Etienne Ghiringhelli, Denis Roux, Didier Bleses, Helene Galliard, and Francois Caton. Optimal fourier rheometry: Application to the gelation of an alginate. *Rheologica Acta*, 51(5):413–420, May 2012.
- [69] D.J. Curtis, A. Holder, N. Badiei, J. Claypole, M. Walters, B. Thomas, M. Barrow, D. Deganello, M.R. Brown, P.R. Williams, and K. Hawkins. Validation of Optimal Fourier Rheometry for rapidly gelling materials and its application in the study of collagen gelation. *Journal of Non-Newtonian Fluid Mechanics*, 222:253–259, August 2015.
- [70] Kyle R. Lennon, Gareth H. McKinley, and James W. Swan. Medium amplitude parallel superposition (MAPS) rheology. Part 1: Mathematical framework and theoretical examples. *Journal of Rheology*, 64(3):551–579, May 2020. Publisher: Society of Rheology.
- [71] Kyle R. Lennon, Michela Geri, Gareth H. McKinley, and James W. Swan. Medium amplitude parallel superposition (MAPS) rheology. Part 2: Experimental protocols and data analysis. *Journal of Rheology*, 64(5):1263–1293, September 2020.

- [72] Kyle R. Lennon, Gareth H. McKinley, and James W. Swan. Medium amplitude parallel superposition (MAPS) rheology of a wormlike micellar solution. *Rheologica Acta*, 60(12):729–739, December 2021.
- [73] P. T. Madsen and A. Surlykke. Functional Convergence in Bat and Toothed Whale Biosonars. *Physiology*, 28(5):276–283, September 2013.
- [74] Whitlow W. L. Au and James A. Simmons. Echolocation in dolphins and bats. *Physics Today*, 60(9):40–45, September 2007.
- [75] Xiang-gen Xia. System identification using chirp signals and time-variant filters in the joint time-frequency domain. *IEEE Transactions on Signal Processing*, 45(8):2072–2084, August 1997.
- [76] Michela Geri, Bavand Keshavarz, Thibaut Divoux, Christian Clasen, Daniel J. Curtis, and Gareth H. McKinley. Time-Resolved Mechanical Spectroscopy of Soft Materials via Optimally Windowed Chirps. *Physical Review X*, 8(4):041042, December 2018.
- [77] P. Fausti and A. Farina. Acoustic measurements in opera houses: comparison between different techniques and equipment. *Journal of Sound and Vibration*, 232(1):213–229, April 2000.
- [78] Joshua David John Rathinaraj, Jan Hendricks, Gareth H. McKinley, and Christian Clasen. OrthoChirp: A fast spectro-mechanical probe for monitoring transient microstructural evolution of complex fluids during shear. *Journal of Non-Newtonian Fluid Mechanics*, page 104744, January 2022.
- [79] Alejandro F. Villaverde, Nikolaos Tsiantis, and Julio R. Banga. Full observability and estimation of unknown inputs, states and parameters of nonlinear biological models. *Journal of The Royal Society Interface*, 16(156):20190043, July 2019.
- [80] Igor Mezić. Analysis of Fluid Flows via Spectral Properties of the Koopman Operator. *Annual Review of Fluid Mechanics*, 45(1):357–378, October 2012. Publisher: Annual Reviews.

- [81] Jonathan H. Tu, Clarence W. Rowley, Dirk M. Luchtenburg, Steven L. Brunton, and J. Nathan Kutz. On Dynamic Mode Decomposition: Theory and Applications. *Journal of Computational Dynamics*, 1(2):391–421, 2014. arXiv: 1312.0041.
- [82] Steven L. Brunton, Marko Budišić, Eurika Kaiser, and J. Nathan Kutz. Modern Koopman Theory for Dynamical Systems. *SIAM Review*, 64(2):229–340, May 2022.
- [83] Carl Eckart and Gale Young. The approximation of one matrix by another of lower rank. *Psychometrika*, I(3), 1936.
- [84] Gal Berkooz, Philip Holmes, and John L Lumley. The proper orthogonal decomposition in the analysis of turbulent flows. *Annual Review of Fluid Mechanics*, 25:539–75, 1993. Publication Title: Annu. Rev. Fluid Mech Volume: 25.
- [85] Kunihiro Taira, Steven L. Brunton, Scott T. M. Dawson, Clarence W. Rowley, Tim Colonius, Beverley J. McKeon, Oliver T. Schmidt, Stanislav Gordeyev, Vassilios Theofilis, and Lawrence S. Ukeiley. Modal Analysis of Fluid Flows: An Overview. *AIAA Journal*, 55(12):4013–4041, December 2017.
- [86] Paloma Gutierrez-Castillo and Becca Thomases. Proper Orthogonal Decomposition (POD) of the flow dynamics for a viscoelastic fluid in a four-roll mill geometry at the Stokes limit. *Journal of Non-Newtonian Fluid Mechanics*, 2019.
- [87] Paloma Gutierrez-Castillo, Adam Kagel, and Becca Thomases. Three-dimensional viscoelastic instabilities in a four-roll mill geometry at the Stokes limit. *Physics of Fluids*, 32(2):023102, February 2020.
- [88] V. Algazi and D. Sakrison. On the Optimality of the Karhunen-Loeve Expansion. *IEEE Transactions on Information Theory*, 15(2), 1969.
- [89] Clarence W. Rowley and Scott T.M. Dawson. Model Reduction for Flow Analysis and Control. *Annual Review of Fluid Mechanics*, 49(1):387–417, January 2017. Publisher: Annual Reviews.

- [90] Lawrence Sirovich. Turbulence and the dynamics of coherent structures. Part I: Cpheren structures. *Quarterly of Applied Mathematics*, 45:12, 1987.
- [91] C W Rowley. Model Reduction for Fluids, Using Balanced Proper Orthogonal Decomposition. *International Journal on Bifurcation and Chaos*, 15(3):97–1013, 2005.
- [92] Sanjay Lall, Jerrold E. Marsden, and Sonja Glavaski. A subspace approach to balanced truncation for model reduction of nonlinear control systems. *International Journal of Robust and Nonlinear Control*, 12(6):519–535, May 2002.
- [93] Aaron Towne, Oliver T. Schmidt, and Tim Colonius. Spectral proper orthogonal decomposition and its relationship to dynamic mode decomposition and resolvent analysis. *Journal of Fluid Mechanics*, 2018.
- [94] Kevin K. Chen, Jonathan H. Tu, and Clarence W. Rowley. Variants of dynamic mode decomposition: Boundary condition, Koopman, and fourier analyses. *Journal of Nonlinear Science*, 22(6):887–915, December 2012.
- [95] Peter Schmid and Joern Sesterhenn. Dynamic Mode Decomposition of numerical and experimental data. In *APS division of fluid dynamics meeting abstracts*, volume 61 of *APS meeting abstracts*, page MR.007, November 2008. tex.adsnote: Provided by the SAO/NASA Astrophysics Data System tex.adsurl: <https://ui.adsabs.harvard.edu/abs/2008APS..DFD.MR007S> tex.eid: MR.007.
- [96] Stefan Klus, Feliks Nüske, Péter Koltai, Hao Wu, Ioannis Kevrekidis, Christof Schütte, and Frank Noé. Data-Driven Model Reduction and Transfer Operator Approximation. *Journal of Nonlinear Science*, 28(3):985–1010, June 2018. Publisher: Springer New York LLC.
- [97] Mihailo R. Jovanović, Peter J. Schmid, and Joseph W. Nichols. Sparsity-promoting dynamic mode decomposition. *Physics of Fluids*, 26(2):024103, February 2014.
- [98] M. A. Mendez, M. Balabane, and J.-M. Buchlin. Multi-scale proper orthogonal decomposition of complex fluid flows. *Journal of Fluid Mechanics*, 870:988–1036, July 2019.

- [99] Ziyou Wu, Steven L. Brunton, and Shai Revzen. Challenges in dynamic mode decomposition. *Journal of The Royal Society Interface*, 18(185):20210686, December 2021.
- [100] Jonathan H. Tu, Clarence W. Rowley, J. Nathan Kutz, and Jessica K. Shang. Spectral analysis of fluid flows using sub-Nyquist-rate PIV data. *Experiments in Fluids*, 55(9):1805, September 2014.
- [101] Daniel Duke, Julio Soria, and Damon Honnery. An error analysis of the dynamic mode decomposition. *Experiments in Fluids*, 52(2):529–542, February 2012.
- [102] Chong Pan, Dong Xue, and Jinjun Wang. On the accuracy of dynamic mode decomposition in estimating instability of wave packet. *Experiments in Fluids*, 56(8):164, August 2015.
- [103] Scott T.M. Dawson, Maziar S. Hemati, Matthew O. Williams, and Clarence W. Rowley. Characterizing and correcting for the effect of sensor noise in the dynamic mode decomposition. *Experiments in Fluids*, 2016.
- [104] Maziar S. Hemati, Clarence W. Rowley, Eric A. Deem, and Louis N. Cattafesta. De-biasing the dynamic mode decomposition for applied Koopman spectral analysis of noisy datasets. *Theoretical and Computational Fluid Dynamics*, 31(4):349–368, August 2017. Publisher: Springer New York LLC.
- [105] Travis Askham and J. Nathan Kutz. Variable Projection Methods for an Optimized Dynamic Mode Decomposition. *SIAM Journal on Applied Dynamical Systems*, 17(1):380–416, January 2018.
- [106] Naoya Takeishi, Yoshinobu Kawahara, and Takehisa Yairi. Subspace dynamic mode decomposition for stochastic Koopman analysis. *Physical Review E*, 96(3):033310, September 2017.
- [107] Joshua L. Proctor, Steven L. Brunton, and J. Nathan Kutz. Dynamic mode decomposition with control. *SIAM Journal on Applied Dynamical Systems*, 15(1):142–161, 2016. Publisher: Society for Industrial and Applied Mathematics Publications.

- [108] Clarence W. Rowley, Igor Mezi, Shervin Bagheri, Philipp Schlatter, and Dan S. Henningson. Spectral analysis of nonlinear flows. *Journal of Fluid Mechanics*, 641:115–127, December 2009.
- [109] Stefan Klus, Peter Koltai, and Christof Schutte. On the numerical approximation of the Perron-frobenius and Koopman operator. *Journal of Computational Dynamics*, 3(1):51–79, 2016.
- [110] Adam R. Gerlach, Andrew Leonard, Jonathan Rogers, and Chris Rackauckas. The Koopman Expectation: An Operator Theoretic Method for Efficient Analysis and Optimization of Uncertain Hybrid Dynamical Systems, August 2020. arXiv:2008.08737 [math].
- [111] Igor Mezić. Spectral Properties of Dynamical Systems, Model Reduction and Decompositions. *Nonlinear Dynamics*, 41(1-3):309–325, August 2005.
- [112] Steven L Brunton, Bingni W Brunton, Joshua L Proctor, and J Nathan Kutz. Koopman Invariant Subspaces and Finite Linear Representations of Nonlinear Dynamical Systems for Control. *PLOS ONE*, page 19, 2016.
- [113] Naoya Takeishi, Yoshinobu Kawahara, and Takehisa Yairi. Learning Koopman Invariant Subspaces for Dynamic Mode Decomposition. In *NIPS’17: Proceedings of the 31st International Conference on Neural Information Processing Systems*, pages 1130–1140, Long Beach, California, USA, 2017. Curran Associates Inc.
- [114] Alexandre Mauroy and Jorge Goncalves. Koopman-Based Lifting Techniques for Nonlinear Systems Identification. *IEEE Transactions on Automatic Control*, 65(6):2550–2565, June 2020.
- [115] Eurika Kaiser, J Nathan Kutz, and Steven L Brunton. Data-driven discovery of Koopman eigenfunctions for control. *Machine Learning: Science and Technology*, 2(3):035023, September 2021.
- [116] Lu Shi and Konstantinos Karydis. ACD-EDMD: Analytical Construction for Dictionaries of Lifting Functions in Koopman Operator-Based Nonlinear Robotic Systems. *IEEE Robotics and Automation Letters*, 7(2):906–913, April 2022.

- [117] Matthew O. Williams, Ioannis G. Kevrekidis, and Clarence W. Rowley. A Data-Driven Approximation of the Koopman Operator: Extending Dynamic Mode Decomposition. *Journal of Nonlinear Science*, 25:1307–1346, 2015.
- [118] Matthew O. Williams, Clarence W. Rowley, and Ioannis G. Kevrekidis. A kernel-based method for data-driven koopman spectral analysis. *Journal of Computational Dynamics*, 2(2):247–265, 2015.
- [119] Julien Mairal, Francis Bach, Jean Ponce, and Guillermo Sapiro. Online dictionary learning for sparse coding. In *Proceedings of the 26th Annual International Conference on Machine Learning - ICML '09*, pages 1–8, Montreal, Quebec, Canada, 2009. ACM Press.
- [120] Qianxiao Li, Felix Dietrich, Erik M. Bollt, and Ioannis G. Kevrekidis. Extended dynamic mode decomposition with dictionary learning: A data-driven adaptive spectral decomposition of the koopman operator. *Chaos*, 27(103111), 2017.
- [121] Matthew O. Williams, Maziar S. Hemati, Scott T.M. Dawson, Ioannis G. Kevrekidis, and Clarence W. Rowley. Extending Data-Driven Koopman Analysis to Actuated Systems. *IFAC-PapersOnLine*, 49(18):704–709, 2016.
- [122] Matthew O. Williams, Clarence W. Rowley, Igor Mezić, and Ioannis G. Kevrekidis. Data fusion via intrinsic dynamic variables: An application of data-driven Koopman spectral analysis. *EPL*, 109(4), February 2015. Publisher: Institute of Physics Publishing.
- [123] Pan, Shaowu and Duraisamy, Karthik. Data-Driven Discovery of Closure Models. *SIAM Journal on Applied Dynamical Systems*, 17(4):2381–2413, 2018.
- [124] Steven L. Brunton, Joshua L. Proctor, and J. Nathan Kutz. Discovering governing equations from data by sparse identification of nonlinear dynamical systems. *PNAS*, 113(15):3932–3937, 2015. ISBN: 1091-6490 (Electronic) 0027-8424 (Linking).
- [125] Kadierdan Kaheman, Steven L Brunton, and J Nathan Kutz. Automatic differentiation to simultaneously identify nonlinear dynamics and extract noise probability distributions from data. *Machine Learning: Science and Technology*, 3(1):015031, March 2022.

- [126] Steven L. Brunton, Joshua L. Proctor, and J. Nathan Kutz. Sparse Identification of Nonlinear Dynamics with Control (SINDYc). *IFAC-PapersOnLine*, 49(18):710–715, December 2016. Publisher: Elsevier BV.
- [127] Seth M. Hirsh, David A. Barajas-Solano, and J. Nathan Kutz. Sparsifying priors for Bayesian uncertainty quantification in model discovery. *Royal Society Open Science*, 9(2):211823, February 2022.
- [128] N. M. Mangan, J. N. Kutz, S. L. Brunton, and J. L. Proctor. Model selection for dynamical systems via sparse regression and information criteria. *Proceedings of the Royal Society A: Mathematical, Physical and Engineering Sciences*, 473(2204), August 2017. Publisher: Royal Society Publishing.
- [129] Sheng Zhang and Guang Lin. Robust data-driven discovery of governing physical laws with error bars. *Proceedings of the Royal Society A: Mathematical, Physical and Engineering Sciences*, 474(2217), September 2018. Publisher: Royal Society Publishing.
- [130] Markus Quade, Markus Abel, J. Nathan Kutz, and Steven L. Brunton. Sparse identification of nonlinear dynamics for rapid model recovery. *Chaos*, 28(6), June 2018. Publisher: American Institute of Physics Inc.
- [131] Samuel H. Rudy, Steven L. Brunton, Joshua L. Proctor, and J. Nathan Kutz. Data-driven discovery of partial differential equations. *Science Advances*, 3(4):e1602614, April 2017.
- [132] Milan Korda and Igor Mezić. Linear predictors for nonlinear dynamical systems: Koopman operator meets model predictive control. *Automatica*, 93:149–160, July 2018.
- [133] Soledad Le Clainche and José M. Vega. Higher Order Dynamic Mode Decomposition. *SIAM Journal on Applied Dynamical Systems*, 16(2):882–925, January 2017.
- [134] Soledad Le Clainche and José M. Vega. Analyzing Nonlinear Dynamics via Data-Driven Dynamic Mode Decomposition-Like Methods. *Complexity*, 2018, 2018. Publisher: Hindawi Limited.

- [135] Piyush K. Singh, Johannes M. Soulages, and Randy H. Ewoldt. Frequency-sweep medium-amplitude oscillatory shear (MAOS). *Journal of Rheology*, 62(1):277–293, January 2018. Publisher: Society of Rheology.
- [136] O. Nelles. *Nonlinear system identification: From classical approaches to neural networks and fuzzy models*. Engineering online library. Springer, 2001. tex.lccn: 00064122.
- [137] Piyush K Singh and Randy H Ewoldt. On simultaneous fitting of nonlinear and linear rheology data: Preventing a false sense of certainty. *arXiv:2202.02867*, page 46, 2022.
- [138] Manfred Wilhelm, Pierre Reinheimer, and Martin Ortseifer. High sensitivity Fourier-transform rheology. *Rheologica Acta*, 38(4):349–356, October 1999.
- [139] Vito Volterra. *Theory of functionals and of integral and integro-differential equations*. Dover Publications, New York, 1959.
- [140] Shada Abuhattum, Hui-Shun Kuan, Paul Müller, Jochen Guck, and Vasily Zaburdaev. Unbiased retrieval of frequency-dependent mechanical properties from noisy time-dependent signals. *Biophysical Reports*, 2(3):100054, September 2022.
- [141] Richard S. Graham, Alexei E. Likhtman, Tom C. B. McLeish, and Scott T. Milner. Microscopic theory of linear, entangled polymer chains under rapid deformation including chain stretch and convective constraint release. *Journal of Rheology*, 47(5):1171–1200, September 2003.
- [142] Alexei E. Likhtman and Richard S. Graham. Simple constitutive equation for linear polymer melts derived from molecular theory: Rolie–Poly equation. *Journal of Non-Newtonian Fluid Mechanics*, 114(1):1–12, September 2003.
- [143] Richard S. Graham, Ewan P. Henry, and Peter D. Olmsted. Comment on “New Experiments for Improved Theoretical Description of Nonlinear Rheology of Entangled Polymers”. *Macromolecules*, 46(24):9849–9854, December 2013.

- [144] Jerry Westerweel, Gerrit E. Elsinga, and Ronald J. Adrian. Particle Image Velocimetry for Complex and Turbulent Flows. *Annual Review of Fluid Mechanics*, 45(1):409–436, March 2011. Publisher: Annual Reviews.
- [145] M.G. Romano, F. Alberini, L. Liu, M.J.H. Simmons, and E.H. Stitt. 3D-PTV flow measurements of Newtonian and non-Newtonian fluid blending in a batch reactor in the transitional regime. *Chemical Engineering Science*, 246:116969, December 2021.
- [146] Mumtaz Hussain Qureshi, Wei-Hsin Tien, and Yi-Jiun Peter Lin. Performance comparison of particle tracking velocimetry (PTV) and particle image velocimetry (PIV) with long-exposure particle streaks. *Measurement Science and Technology*, 32(2):024008, February 2021.
- [147] A Gurung, J W Haverkort, S Drost, B Norder, J Westerweel, and C Poelma. Ultrasound image velocimetry for rheological measurements. *Measurement Science and Technology*, 27(9):094008, September 2016.
- [148] Jennifer R. Brown and Paul T. Callaghan. Changing micellar order, lever rule behavior and spatio-temporal dynamics in shear-banding at the onset of the stress plateau. *Soft Matter*, 7(21):10472, 2011.
- [149] Thibaut Divoux, Marc A. Fardin, Sebastien Manneville, and Sandra Lerouge. Shear Banding of Complex Fluids. *Annual Review of Fluid Mechanics*, 48(1):81–103, January 2016.
- [150] Laura Casanellas, Christopher J. Dimitriou, Thomas J. Ober, and Gareth H. McKinley. Spatiotemporal dynamics of multiple shear-banding events for viscoelastic micellar fluids in cone-plate shearing flows. *Journal of Non-Newtonian Fluid Mechanics*, 222:234–247, August 2015.
- [151] Pierre Ballesta, M. Paul Lettinga, and Sébastien Manneville. Superposition rheology of shear-banding wormlike micelles. *Journal of Rheology*, 51(5):1047–1072, September 2007.

- [152] C.-Y. David Lu, Peter D. Olmsted, and R. C. Ball. Effects of Nonlocal Stress on the Determination of Shear Banding Flow. *Physical Review Letters*, 84(4):642–645, January 2000.
- [153] Shweta Sharma, V. Shankar, and Yogesh M. Joshi. Onset of transient shear banding in viscoelastic shear start-up flows: Implications from linearized dynamics. *Journal of Rheology*, 65(6):1391–1412, November 2021.
- [154] J. D. Goddard. Material Instability in Complex Fluids. *Annual Review of Fluid Mechanics*, 35(1):113–133, January 2003.
- [155] T. W. Wright. *The physics and mathematics of adiabatic shear bands*. Cambridge monographs on mechanics. Cambridge University Press, Cambridge, UK ; New York, 2002.
- [156] Kapilanjani Krishan and Michael Dennin. Viscous shear banding in foam. *Physical Review E*, 78(5):051504, November 2008.
- [157] Pouyan E. Boukany and Shi-Qing Wang. Shear banding or not in entangled DNA solutions depending on the level of entanglement. *Journal of Rheology*, 53(1):73–83, January 2009.
- [158] Stylianos Varchanis, Simon J. Haward, Cameron C. Hopkins, John Tsamopoulos, and Amy Q. Shen. Evaluation of constitutive models for shear-banding wormlike micellar solutions in simple and complex flows. *Journal of Non-Newtonian Fluid Mechanics*, 307:104855, September 2022.
- [159] Simon J. Haward and Amy Q. Shen. Chapter 9. Microfluidic Flows and Confinement of Wormlike Micelles. In Cecile A Dreiss and Yujun Feng, editors, *Soft Matter Series*, pages 236–278. Royal Society of Chemistry, Cambridge, 2017.
- [160] Y. T. Hu and A. Lips. Kinetics and mechanism of shear banding in an entangled micellar solution. *Journal of Rheology*, 49(5):1001–1027, September 2005.
- [161] Erik Miller and Jonathan P. Rothstein. Transient evolution of shear-banding wormlike micellar solutions. *Journal of Non-Newtonian Fluid Mechanics*, 143(1):22–37, April 2007.

- [162] Joseph Yerushalmi, Stanley Katz, and Reuel Shinnar. The stability of steady shear flows of some viscoelastic fluids. *Chemical Engineering Science*, 25(12):1891–1902, December 1970.
- [163] Jean-Baptiste Salmon, Annie Colin, Sébastien Manneville, and François Molino. Velocity Profiles in Shear-Banding Wormlike Micelles. *Physical Review Letters*, 90(22):228303, June 2003.
- [164] Sandra Lerouge. Flow of wormlike micelles: From shear banding to elastic turbulence. *Science Talks*, 3:100050, August 2022.
- [165] Marc-Antoine Fardin, Laura Casanellas, Brice Saint-Michel, Sébastien Manneville, and Sandra Lerouge. Shear-banding in wormlike micelles: Beware of elastic instabilities. *Journal of Rheology*, 60(5):917–926, September 2016.
- [166] M. A. Fardin, D. Lopez, J. Croso, G. Grégoire, O. Cardoso, G. H. McKinley, and S. Lerouge. Elastic Turbulence in Shear Banding Wormlike Micelles. *Physical Review Letters*, 104(17):178303, April 2010.
- [167] Devranjan Samanta, Yves Dubief, Markus Holzner, Christof Schäfer, Alexander N. Morozov, Christian Wagner, and Björn Hof. Elasto-inertial turbulence. *Proceedings of the National Academy of Sciences*, 110(26):10557–10562, June 2013.
- [168] Katherine Anne Carter. *Shear banding in polymeric fluids under large amplitude oscillatory shear flow*. PhD thesis, Durham University, 2016.
- [169] R G Owens and T N Phillips. *Computational Rheology*. Imperial College Press, May 2002.
- [170] Ardith W. El-Kareh and L. Gary Leal. Existence of solutions for all Deborah numbers for a non-Newtonian model modified to include diffusion. *Journal of Non-Newtonian Fluid Mechanics*, 33(3):257–287, January 1989.
- [171] John C. Strikwerda. 6. Parabolic Partial Differential Equations. In *Finite Difference Schemes and Partial Differential Equations, Second Edition*, Other Titles in Applied

- Mathematics, pages 137–163. Society for Industrial and Applied Mathematics, January 2004.
- [172] Yanfei Li, Miao Hu, Gregory B. McKenna, Christopher J. Dimitriou, Gareth H. McKinley, Rebecca M. Mick, David C. Venerus, and Lynden A. Archer. Flow field visualization of entangled polybutadiene solutions under nonlinear viscoelastic flow conditions. *Journal of Rheology*, 57(5):1411–1428, September 2013.
- [173] O Radulescu, P. D Olmsted, J. P Decruppe, S Lerouge, J.-F Berret, and G Porte. Time scales in shear banding of wormlike micelles. *Europhysics Letters (EPL)*, 62(2):230–236, April 2003.
- [174] M. Paul Lettinga and Sébastien Manneville. Competition between Shear Banding and Wall Slip in Wormlike Micelles. *Physical Review Letters*, 103(24):248302, December 2009.
- [175] Joseph D. Peterson, Michael Cromer, Glenn H. Fredrickson, and L. Gary Leal. Shear banding predictions for the two-fluid Rolie-Poly model. *Journal of Rheology*, 60(5):927–951, September 2016.
- [176] A. van den Noort and W.J. Briels. Brownian dynamics simulations of concentration coupled shear banding. *Journal of Non-Newtonian Fluid Mechanics*, 152(1-3):148–155, June 2008.
- [177] P. Coussot. Yield stress fluid flows: A review of experimental data. *Journal of Non-Newtonian Fluid Mechanics*, 211:31–49, September 2014.
- [178] Christopher J. Dimitriou, Randy H. Ewoldt, and Gareth H. McKinley. Describing and prescribing the constitutive response of yield stress fluids using large amplitude oscillatory shear stress (LAOStress). *Journal of Rheology*, 2012.
- [179] R. K. Dash, K. N. Mehta, and G. Jayaraman. Effect of yield stress on the flow of a Casson fluid in a homogeneous porous medium bounded by a circular tube. *Applied Scientific Research*, 57(2):133–149, June 1996.

- [180] Luca Martinetti, Johannes M. Soulares, and Randy H. Ewoldt. Continuous relaxation spectra for constitutive models in medium-amplitude oscillatory shear. *Journal of Rheology*, 62(5):1271–1298, September 2018.
- [181] J. Honerkamp and J. Weese. A nonlinear regularization method for the calculation of relaxation spectra. *Rheologica Acta*, 32(1):65–73, January 1993.
- [182] Jung Gun Nam, Kyu Hyun, Kyung Hyun Ahn, and Seung Jong Lee. Prediction of normal stresses under large amplitude oscillatory shear flow. *Journal of Non-Newtonian Fluid Mechanics*, 2008. ISBN: 0377-0257.
- [183] Anugrah Singh and Prabhu R. Nott. Experimental measurements of the normal stresses in sheared Stokesian suspensions. *Journal of Fluid Mechanics*, 490:293–320, September 2003.
- [184] Seungjoon Lee, Felix Dietrich, George E. Karniadakis, and Ioannis G. Kevrekidis. Linking Gaussian process regression with data-driven manifold embeddings for nonlinear data fusion. *Interface Focus*, 9(3), 2019. Publisher: Royal Society Publishing.
- [185] Josh Bongard and Hod Lipson. Automated reverse engineering of nonlinear dynamical systems. *PNAS*, 104(24):9943–9948, 2007. ISBN: 1.00390.0011.
- [186] Pierre C. Sabatier. Past and future of inverse problems. *Journal of Mathematical Physics*, 41(6):4082–4124, June 2000.
- [187] Andreas Kirsch. *An Introduction to the Mathematical Theory of Inverse Problems*, volume 120 of *Applied Mathematical Sciences*. Springer New York, New York, NY, 2011.
- [188] Bethany Lusch, J. Nathan Kutz, and Steven L. Brunton. Deep learning for universal linear embeddings of nonlinear dynamics. *Nature Communications*, 9(1), December 2018. Publisher: Nature Publishing Group.
- [189] Floris Takens. Detecting strange attractors in turbulence. In David Rand and Lai-Sang Young, editors, *Dynamical systems and turbulence, warwick 1980*, pages 366–381, Berlin, Heidelberg, 1981. Springer Berlin Heidelberg.

- [190] Israr Ul Haq, Tomoharu Iwata, and Yoshinobu Kawahara. Dynamic mode decomposition via convolutional autoencoders for dynamics modeling in videos. *Computer Vision and Image Understanding*, 216:103355, February 2022.
- [191] Toby R. F. Phillips, Claire E. Heaney, Paul N. Smith, and Christopher C. Pain. An autoencoder-based reduced-order model for eigenvalue problems with application to neutron diffusion. *International Journal for Numerical Methods in Engineering*, 122(15):3780–3811, August 2021.
- [192] Florian De Vuyst and Pierre Villon. Identification of nonlinear dynamical system equations using dynamic mode decomposition under invariant quantity constraints. *Comptes Rendus Mécanique*, 347(11):882–890, November 2019.
- [193] Zichao Long, Yiping Lu, Xianzhong Ma, and Bin Dong. PDE-Net: Learning PDEs from Data. In *Proceedings of the 35th International Conference on Machine Learning*, pages 3208–3216, Stockholm, Sweden, 2018.
- [194] M. Raissi, P. Perdikaris, and G. E. Karniadakis. Physics-informed neural networks: A deep learning framework for solving forward and inverse problems involving nonlinear partial differential equations. *Journal of Computational Physics*, 378:686–707, February 2019. Publisher: Academic Press Inc.
- [195] Brandon Reyes, Amanda A. Howard, Paris Perdikaris, and Alexandre M. Tartakovsky. Learning unknown physics of non-Newtonian fluids. *Physical Review Fluids*, 6(7):073301, July 2021.
- [196] Dongkun Zhang, Ling Guo, and George Em Karniadakis. Learning in Modal Space: Solving Time-Dependent Stochastic PDEs Using Physics-Informed Neural Networks. *SIAM Journal on Scientific Computing*, 42(2):A639–A665, January 2020.
- [197] Peter J. Baddoo, Benjamin Herrmann, Beverley J. McKeon, and Steven L. Brunton. Kernel learning for robust dynamic mode decomposition: linear and nonlinear disambiguation optimization. *Proceedings of the Royal Society A: Mathematical, Physical and Engineering Sciences*, 478(2260):20210830, April 2022.

- [198] Mohammadamin Mahmoudabadbozchelou and Safa Jamali. Rheology-Informed Neural Networks (RhINNs) for forward and inverse metamodeling of complex fluids. *Scientific Reports*, 11(1):12015, December 2021.
- [199] Antoine Garcon, Julian Vexler, Dmitry Budker, and Stefan Kramer. Deep neural networks to recover unknown physical parameters from oscillating time series. *PLOS ONE*, 17(5):e0268439, May 2022.
- [200] Kyle R. Lennon. Learning Physically Informed Differential Viscoelastic Constitutive Models from Data, August 2021.

Appendices

Appendix A: GNMM equation

Eq. 2.13 written in terms of the evolution of σ_{xx} , σ_{yy} , and σ_{xy} .

$$\begin{aligned}
& \lambda_1 \dot{\sigma}_{xx} + (1 + \zeta) \sigma_{xx} + \zeta \sigma_{yy} + (\nu_1 - \mu_1 - \lambda_1) \dot{\gamma} \sigma_{xy} \\
& + ((\alpha_1 - \alpha_0 + \beta_0 - \beta_1/2)/\eta_0) \sigma_{xx}^2 + ((\alpha_1 - \beta_1)/\eta_0) \sigma_{xy}^2 + ((\beta_0 - \beta_1/2)/\eta_0) \sigma_{yy}^2 \\
& + ((2\beta_0 - \alpha_0)/\eta_0) \sigma_{xx} \sigma_{yy} - (c_3 + f_3) (\lambda_1/\eta_0^2) \sigma_{xx}^3 \\
& - 2\lambda_1 ((c_3 + 2f_3)/\eta_0^2) \sigma_{xy}^2 \sigma_{xx} - (2f_3 \lambda_1/\eta_0^2) \sigma_{xy}^2 \sigma_{yy} - (c_3 \lambda_1/\eta_0^2) \sigma_{yy}^2 \sigma_{xx} \\
& - 2\lambda_1 (c_2 + f_2) \dot{\gamma}^2 \sigma_{xx} - (2(f_1 + c_1) \lambda_1/\eta_0) \dot{\gamma} \sigma_{xx} \sigma_{xy} - (2f_1 \lambda_1/\eta_0) \dot{\gamma} \sigma_{xy} \sigma_{yy} \\
& = -\eta_0 (\lambda_2 + \mu_2 - \nu_2) \dot{\gamma}^2.
\end{aligned} \tag{A.1}$$

$$\begin{aligned}
& \lambda_1 \dot{\sigma}_{yy} + (1 + \zeta) \sigma_{yy} + \zeta \sigma_{xx} + (\nu_1 - \mu_1 + \lambda_1) \dot{\gamma} \sigma_{xy} \\
& + ((\beta_0 - \beta_1/2)/\eta_0) \sigma_{xx}^2 + ((\alpha_1 - \beta_1)/\eta_0) \sigma_{xy}^2 + ((\alpha_1 - \alpha_0 + \beta_0 - \beta_1/2)/\eta_0) \sigma_{yy}^2 \\
& + ((2\beta_0 - \alpha_0)/\eta_0) \sigma_{xx} \sigma_{yy} - \lambda_1 (c_3 + 2f_3) (\lambda_1/\eta_0^2) \sigma_{yy}^3 - (c_3 \lambda_1/\eta_0^2) \sigma_{xx}^2 \sigma_{yy} \\
& - (2f_3 \lambda_1/\eta_0^2) \sigma_{xy}^2 \sigma_{xx} - (2(c_3 + 2f_3) \lambda_1/\eta_0^2) \sigma_{xy}^2 \sigma_{yy} \\
& - 2\lambda_1 (c_2 + f_2) \dot{\gamma}^2 \sigma_{yy} - (2f_1 \lambda_1/\eta_0) \dot{\gamma} \sigma_{xx} \sigma_{xy} - 2(c_1 + f_1) \lambda_1/\eta_0 \dot{\gamma} \sigma_{xy} \sigma_{yy} \\
& = \eta_0 (\lambda_2 - \mu_2 + \nu_2) \dot{\gamma}^2.
\end{aligned} \tag{A.2}$$

$$\begin{aligned}
& \lambda_1 \dot{\sigma}_{xy} + \sigma_{xy} + 0.5(\mu_0 + \lambda_1 - \mu_1) \dot{\gamma} \sigma_{xx} + 0.5(\mu_0 - \lambda_1 - \mu_1) \dot{\gamma} \sigma_{yy} \\
& + ((\alpha_1 - \alpha_0)/\eta_0) \sigma_{xx} \sigma_{xy} + ((\alpha_1 - \alpha_0)/\eta_0) \sigma_{xy} \sigma_{yy} - 2\lambda_1 ((c_3 + f_3)/\eta_0^2) \sigma_{xy}^3 \\
& - ((c_3 + 2f_3)\lambda_1/\eta_0^2) \sigma_{xx}^2 \sigma_{xy} - ((c_3 + 2f_3)\lambda_1/\eta_0^2) \sigma_{yy}^2 \sigma_{xy} - (2f_3\lambda_1/\eta_0^2) \sigma_{xx} \sigma_{xy} \sigma_{yy} \quad (\text{A.3}) \\
& - 2(c_2 + d_2 + f_2)\lambda_1 \dot{\gamma}^2 \sigma_{xy} - ((d_1 + f_1)\lambda_1/\eta_0) \dot{\gamma} \sigma_{xx}^2 - (2(c_1 + d_1 + f_1)\lambda_1/\eta_0) \dot{\gamma} \sigma_{xy}^2 \\
& - ((d_1 + f_1)\lambda_1/\eta_0) \dot{\gamma} \sigma_{yy}^2 = \eta_0 \dot{\gamma} + 4d_3 f_4 \eta_0 \lambda_1^2 \dot{\gamma}^3 + \eta_0 \lambda_2 \ddot{\gamma}.
\end{aligned}$$

Appendix B: Full transformation of GNMM observables to Fourier basis functions

In Chapter 4, we showed a transformation matrix between a set of observables containing the linear and cubic order combinations of σ and $\dot{\gamma}$ and a Fourier basis containing only odd terms. Here we show the complete transformation with the inclusion of quadratic order observables and the even terms of the Fourier basis.

$$\begin{bmatrix} \sigma & \dot{\gamma} & \sigma^2 & \sigma\dot{\gamma} & \dot{\gamma}^2 & \sigma^3 & \sigma^2\dot{\gamma} & \sigma\dot{\gamma}^2 & \dot{\gamma}^3 \end{bmatrix}^T = \mathbf{Q} \begin{bmatrix} \cos(\omega t) \\ \sin(\omega t) \\ \cos(2\omega t) \\ \sin(2\omega t) \\ \cos(3\omega t) \\ \sin(3\omega t) \end{bmatrix} \quad (\text{B.1})$$

where

$$\mathbf{Q} = \begin{bmatrix} 0 & B & A & 0 & 0 & 0 \\ 0 & \dot{\gamma}_0 & 0 & 0 & 0 & 0 \\ \frac{1}{2}(A^2 + B^2) & 0 & 0 & \frac{1}{2}(A^2 - B^2) & AB & 0 \\ \frac{1}{2}A\dot{\gamma}_0 & 0 & 0 & \frac{1}{2}A\dot{\gamma}_0 & \frac{1}{2}B\dot{\gamma}_0 & 0 \\ \frac{1}{2}\dot{\gamma}_0^2 & 0 & 0 & \frac{1}{2}\dot{\gamma}_0^2 & 0 & 0 \\ 0 & \frac{3}{4}A(A^2 + B^2) & \frac{3}{4}B(A^2 + B^2) & 0 & \frac{1}{4}A(A^2 - 3B^2) & \frac{1}{4}B(3A^2 - B^2) \\ 0 & \frac{1}{4}(3A^2 + B^2)\dot{\gamma}_0 & \frac{1}{2}AB\dot{\gamma}_0 & 0 & \frac{1}{4}(A^2 - B^2)\dot{\gamma} & \frac{1}{2}AB\dot{\gamma}_0 \\ 0 & \frac{3}{4}A\dot{\gamma}_0^2 & \frac{1}{4}B\dot{\gamma}_0^2 & 0 & \frac{1}{4}A\dot{\gamma}_0^2 & \frac{1}{4}B\dot{\gamma}_0^2 \\ 0 & \frac{3}{4}\dot{\gamma}_0^3 & 0 & 0 & \frac{1}{4}\dot{\gamma}_0^3 & 0 \end{bmatrix}. \tag{B.2}$$

It is entirely possible to choose Φ to be the terms from a Fourier expansion explicitly. However, it should be noted that this will not produce exactly the same results as FT-rheology described in Section 2.5.2. We can show this explicitly for the case where σ is generated from the linear Maxwell model. Using the analytic solution of σ , we find

$$\begin{aligned}
 \sigma_n &= A \cos_n + B \sin_n \\
 \longrightarrow \sigma_{n+1} &= [A \cos(\omega \Delta t) + B \sin(\omega \Delta t)] \cos_n + [B \cos(\omega \Delta t) - A \sin(\omega \Delta t)] \sin_n \\
 &= A' \cos_n + B' \sin_n.
 \end{aligned} \tag{B.3}$$

Using the Fourier basis as the set of observables does not locate A and B exactly because we are relating the data from time n to $n + 1$, whereas standard FT-rheology involves taking the Fourier transform of the entirety of the σ signal.